GENERAL PURPOSE AND SCOPE: The Applied Computational Electromagnetics Society *(ACES)* Journal hereinafter known as the *ACES Journal* is devoted to the exchange of information in computational electromagnetics, to the advancement of the state-of-the art, and the promotion of related technical activities. The primary objective of the information exchange is to inform the scientific community on the developments of new computational electromagnetics tools and their use in electrical engineering, physics, or related areas. The technical activities promoted by this publication include code validation, performance analysis, and input/output standardization; code or technique optimization and error minimization; innovations in solution technique or in data input/output; identification of new applications for electromagnetics modeling codes and techniques; integration of computational electromagnetics techniques with new computer architectures; and correlation of computational parameters with physical mechanisms.

SUBMISSIONS: The *ACES Journal* welcomes original, previously unpublished papers, relating to applied computational electromagnetics. Typical papers will represent the computational electromagnetics aspects of research in electrical engineering, physics, or related disciplines. However, papers which represent research in applied computational electromagnetics itself are equally acceptable.

Manuscripts are to be submitted through the upload system of *ACES* web site http://www.aces-society.org See "Information for Authors" on inside of back cover and at *ACES* web site. For additional information contact the Editor-in-Chief:

Dr. Atef Elsherbeni
Department of Electrical Engineering
The University of Mississippi
University, MS 386377 USA
Phone: 662-915-5382
Email: atef@olemiss.edu

SUBSCRIPTIONS: All members of the Applied Computational Electromagnetics Society are entitled to access and download the *ACES Journal* any published journal article available at http://www.aces-society.org. Printed issues of the *ACES Journal* are delivered to institutional members. Each author of published papers receives a printed issue of the *ACES Journal* in which the paper is published.

Back issues, when available, are $50 each. Subscription to *ACES* is through the web site. Orders for back issues of the *ACES Journal* and change of address requests should be sent directly to *ACES* office at:

Department of Electrical Engineering
The University of Mississippi
University, MS 386377 USA
Phone: 662-915-7231

Allow four weeks advance notice for change of address. Claims for missing issues will not be honored because of insufficient notice, or address change, or loss in the mail unless the *ACES* office is notified within 60 days for USA and Canadian subscribers, or 90 days for subscribers in other countries, from the last day of the month of publication. For information regarding reprints of individual papers or other materials, see "Information for Authors".

APPLIED

COMPUTATIONAL

ELECTROMAGNETICS

SOCIETY

JOURNAL

June 2013

Vol. 28 No. 6

ISSN 1054-4887

JUNE 2013 REVIEWERS

Ahmed Abdelrahman
Ayman Al-Zayed
Rodolfo Araneo
Ahmed Boutejdar
C. Poongodi
Ali Çetin
Vijay Devabhaktuni
Roland Gilbert
Mousa Hussein
Lai Sheng Jian
Lokman Kuzu
George Kyriacou
Mun Soo Lee
Yipeng Li

Angelo Liseno
Zi-Liang Liu
Mohammad Nikkhah
Mohammad Ojaroudi
Andrew Peterson
Lionel Pichon
Alain Reineix
Luca Roselli
César Méndez Ruiz
Ping Jack Soh
Joshua Wilson
Hua Zeng
Jun Zhou
Lei Zhao

THE APPLIED COMPUTATIONAL ELECTROMAGNETICS SOCIETY

JOURNAL

TABLE OF CONTENTS

Equivalent Circuit Models for Propagation Analysis of In-Building Power line Communications Systems

Azlan Hakimi and Grant A. Ellis

Department of Electrical and Electronics Engineering
Universiti Teknologi Petronas, Tronoh, Perak 31750, Malaysia
azlan.hakimi@yahoo.com and grant.ellis@gmail.com

Abstract ─ In-building power line transmission measurements show potential for low attenuation propagation above 30 MHz. These measurements show that frequency bands can exist having low or minimum attenuation above 100 MHz. A simple high-frequency propagation model for analysis of in-building communications up to 900 MHz, which can be implemented using a commercial circuit simulator, is described. This physics-based model is extracted using broadband data from both time- and frequency-domain network transmission (S_{21}) measurements. The novelty of this modeling approach is that different propagation modes such as electromagnetic coupling, waveguide propagation through the wiring conduit, and fading are included. An RF circuit model in a simulator environment is useful for analyzing a wide range of communication problems at the circuit, subsystem, and system levels.

Index Terms - Frequency response, modeling, power line communications, propagation, transmission line, and waveguide.

I. INTRODUCTION

The power line network is a low-cost alternative to existing wired and wireless systems for wideband or broadband data communications. Broadband power line communications (PLC) is a system that uses existing power distribution lines and is characterized by a carrier system connected to power lines to transmit radio frequency signals for broadband communications. PLC is an alternative mode of communication and differs from other wired and wireless systems and is preferred due to the wide availability and easy implementation using the existing power line networks in a designated area [1, 2]. PLC was initially used as a remote monitoring system in the high voltage portion of the power line system for unmanned sites for the purpose of controlling and monitoring the power network [3]. One of the main uses of PLC is carrier transmissions over power line (CTP), which covers three basic functions including operations management, electric line monitoring and limitation, and removal of failures [4]. It is gradually being applied to the medium and low voltage lines especially in home networks due to the wide availability of power lines [5, 6]. This is due to the existing power line system, which can greatly reduce the cost of deploying a new communication system since it does not require additional infrastructure. Another advantage is that it can penetrate areas that are remote or rural and do not have a readily available connection [4, 7]. A number of research trials have been carried out at different locations and show that broadband power line is a possible technique for data communications [8−11].

Most of the PLC research to date only covers the frequency band up to 30 MHz [12]. Although this is sufficient at present, it is necessary to increase the transmission rates due to the requirements for higher data rates and higher speed. Since the introduction of PLC there has been promising research for evaluation at frequencies above 30 MHz [5]. Commissions and regulatory bodies around the world such as the federal communications commission (FCC) have set up guidelines and regulations for operators regarding broadband PLC [12]. It is stated in the FCC guidelines that frequencies above 40 MHz

requires further research and development. In [13], a technique to provide Wi-Fi coverage to users within a physical or "fenced" boundary is proposed. Power line communications can be utilized to perform the same purpose since it supports relatively short distances such as in a room or on an office floor. A model of the PLC channel transfer function is derived for the frequency range of 1 MHz to 30 MHz by using a two-wire transmission approximation and derivation of characteristic impedance and propagation constant are done analytically [14, 15]. A broadband power line model based on transmission line theory is validated by comparing transfer function response with actual measurements for frequencies up to 100 MHz. Above 30 MHz, the experimental and modeled results begin to deviate [16]. The power line network is modeled using a multiconductor transmission line and the network is simulated with ABCD matrices. The results are however, validated using a laboratory setup and do not use an actual power line system [17, 18].

The focus of this paper is to develop a model, which can be used to evaluate the feasibility of higher frequency broadband PLC circuits and systems. This model is useful for simulating circuit configurations in a PLC environment. Since the model is physics-based, effects such as time delay, multipath, and dispersion are included. This model is broadband so that effects at harmonic frequencies can also be simulated. Time-varying effects such as fading can also be included using random simulation of varying attenuation in the model.

To develop a model for PLC for use above 30 MHz, in-building measurements were taken to determine the transmission parameters (S_{21}) of the network. The neutral line was chosen instead of the phase line for transmission because it is believed to have less loading and to minimize the presence of high voltage on the measurement equipment [19]. Different locations and times of the day were chosen for measurements. From the measured data, it is shown that potential PLC systems have significant attenuation and that the transmission characteristics can vary significantly during the day. Electric field emission measurements were also taken and to comply with FCC specifications, the input power to the PLC must be limited to keep the emissions to

acceptable levels [20]. The broadband propagation model is fitted to measured data, which can be implemented using Agilent ADS [21]. The availability of an RF model in a circuit simulator environment is especially useful for analyzing a wide range of communications problems at the circuit, subsystem, and system levels.

This paper is organized as follows: section II describes the methodology used for measurements, section III describes the measurement results, section IV describes the methodology for extraction of an equivalent RF circuit model for the PLC, and finally the paper is concluded.

II. MEASUREMENT METHODOLOGY AND CONFIGURATION

The in-building power line system is utilized by exciting the neutral and ground lines in a transmission line mode where the signal is fed into the neutral line and the ground is used as the signal return. The neutral and ground run separately as parallel wires and are connected only at the incoming service main circuit breaker or transformer. In order to develop the broadband models for in-building power line system, S_{21} (transmission) parameter measurements were carried out to determine the attenuation and return loss. These measurements were taken using a network analyzer and include high pass filters connected to the neutral and ground using shielded cables at the power sockets in the measurement setup shown in Fig. 1.
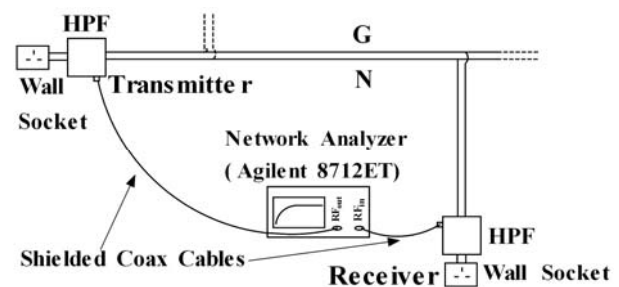
Fig. 1. S_{21} transmission measurement setup.

The high pass filters have a cutoff frequency of 5 MHz and are located at each end of the path. The filters are necessary to protect the measurement equipment since the power line network is constantly active and supports many loads including lighting, air conditioning, computers, printers, and elevators all of which can

contribute noise, transients, and even faults in the power system. The high-pass filter schematic diagram is shown in Fig. 2. The high pass filter circuit with the power socket is shown in Fig. 3.
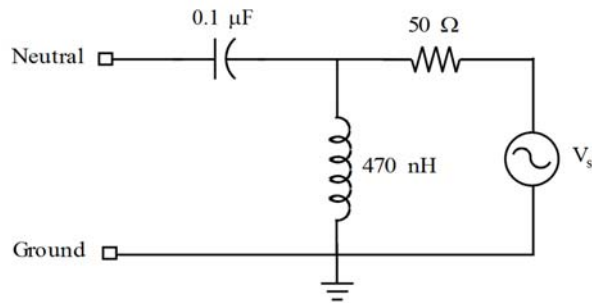
Fig. 2. High-pass filter used for isolating measurement equipment.

Fig. 3. High pass filter circuit (top and bottom socket).

Several locations in building Block 22 at Universiti Teknologi Petronas located in Tronoh Malaysia were chosen for these measurements. Block 22 has four floors including the ground and was constructed in 2003. Path A in room 22-02-02 has a length of 11 m (in the same room), path B is in room 22-02-02 with approximate length of 9 m (from inside to outside of the room), path C is in room 22-02-05 with approximate length of 6 m (from inside to outside of the room), path D is in room 22-02-02 with approximate length of 3 m (in the same room), and path E is from Wing 1 to Wing 2 with approximate length of 45 m. There are several panels distributed nearly evenly throughout each wing. All of the ground, neutral, and phase lines in each room pass through a PVC duct and are collected at the panel located adjacent to that room. These panel locations are shown in the diagram in Fig. 4. All of the ground, neutral, and phase lines from the panels then pass through an overhead metallic conduit to the end of each wing to the riser.

The simulated and measured transmission (S_{21}) and reflection (S_{11}) coefficients for the high pass filter for $Z_0 = 50\ \Omega$ are shown in Fig. 5. The measured insertion loss for the filter is less than 4 dB below 0.8 GHz. Also shown in the figure is the return loss (Γ) of the high pass filter connected to the power line network. The measured return loss is better than 10 dB for several frequencies below 500 MHz.
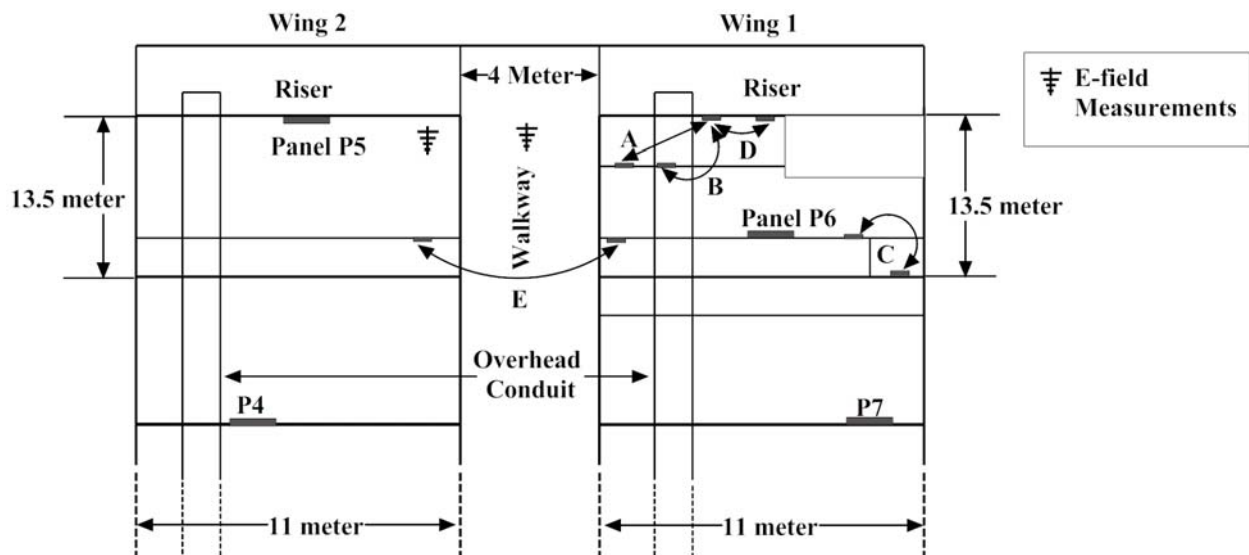
Fig. 4. Building diagram for paths A, B, C, D, and E.

The neutral-ground transmission line configuration has an average input impedance of about 70 Ω. The filters were connected to the wall socket and the transmission parameters (S_{21}) were measured using a calibrated Agilent 8712ET network analyzer. As will be evident in the S_{21} measurements, as the path length increases, the received signal attenuates and a power amplifier is required to increase the transmission of the system. The field measurements were carried out by injecting RF signals into the power line through a power amplifier and high pass filter and the field emissions were measured using an AFJ EBA-01 log periodic dipole and an Advantest R3132 spectrum analyzer located a distance of 3 meters from the power line feed points (Fig. 6).
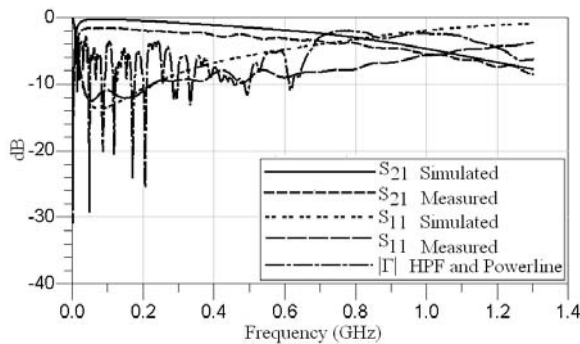
Fig. 5. S_{21} and S_{11} for the high pass filter ($Z_0 = 50$ Ω).
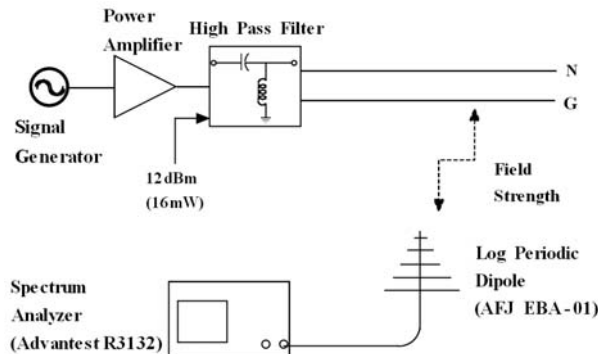
Fig. 6. Electric field measurement setup.

III. MEASUREMENT RESULTS

In this section, the measurement setup described in the previous section is used to measure the transmission coefficient S_{21} for the paths shown in Fig. 4. The measurements were taken at 10 am, 12 pm, 3 pm, 5 pm, and 8 pm over a span of nearly one month to determine the attenuation and amount of fading in the PLC. Broadband measurements were taken to estimate the impulse response of the power line system. Field probe measurements were taken and the results are compared with the transmission data to identify any possible coupling. In the next section, this measurement data is used to extract an equivalent RF circuit model of the power line system.

A. Different times of day

The measured S_{21} for paths A, B, and E are shown in Figs. 7 - 9. The response for each path shows that the transmission can vary with the time of the day and that a frequency band having minimum attenuation or resonance exists between 400 MHz and 700 MHz. This is strongly evident in path A and path E at different times of the day while for path B the location of the resonance is nearly constant. The measurement data shown in Figs. 7 and 8 were measured at 5 pm on separate days for both paths and show almost no difference in resonance frequency. The electrical line loads vary at different times, which also affect the RF S_{21} transmission.
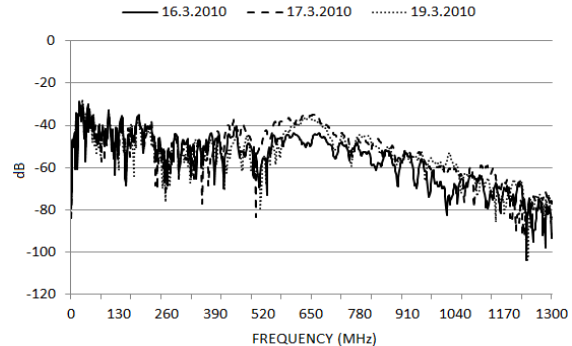
Fig. 7. S_{21} measured at 5pm on separate days for path A.

At 5 pm, the S_{21} measured for path A shows resonance between 400 MHz and 500 MHz and between 500 MHz and 715 MHz. The measurement for path B shows nearly constant S_{21} from 400 MHz to 715 MHz with the exception of a slight variation in the peak in the range of 600 MHz to 715 MHz. The wing-to-wing (path E) measurements in Fig. 9 show a peak in S_{21} between 244 MHz and 650 MHz. The maximum variation in the measured S_{21} or fading is about 20 dB. In each case the resonant frequency range is nearly constant.
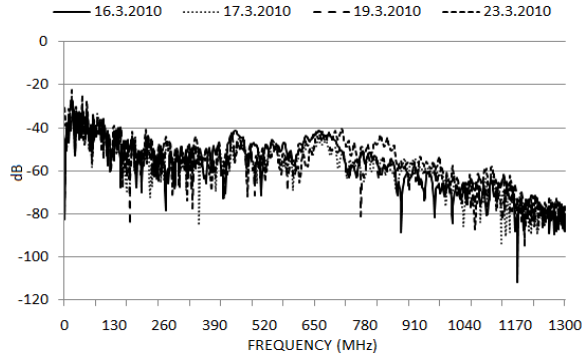
Fig. 8. S_{21} measured at 5pm on separate days for path B.
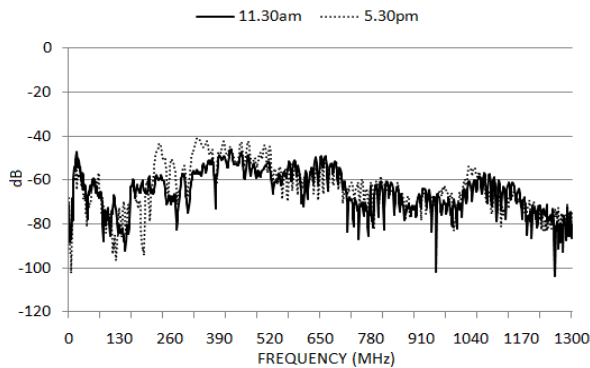
Fig. 9. S_{21} measured at different times for path E.

B. Field emission measurements

The average measured transmission, S_{21} for path E (wing to wing) and electric field intensity near the center of the walkway are shown in Fig. 10. The field probe is located at a distance of 3 meters from the input to the power line (see Fig. 4). The input power to the high pass filter is 16 mW. These measurements reveal that there is a correlation between peaks in both S_{21} and the resulting electric field intensity. For some frequencies e.g. 450 MHz there is both low attenuation in S_{21} and a minimum field emission level.
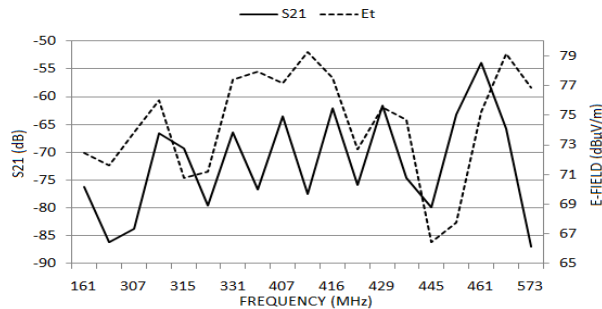
Fig. 10. S_{21} and electric field measurements (161 MHz to 572.5 MHz).

The measured total electric field levels are higher than permitted by FCC (40 dBμV/m for frequencies above 40 MHz) and are due to the configuration of the power line network in the building. Here, asymmetries in distribution of the neutral and ground lines generate common mode currents resulting in radiation [20]. Simply lowering the input power to the PLC however, can lower these emission levels. The measured input power to the high pass filter required to maintain a field emission of 40 dBμV/m is only -15 dBm at 700 MHz. From the FCC and other commission guidelines, frequencies above 40 MHz are subjected to further development and deployment scenarios.

C. Frequency response and estimation of impulse response of power line system

The measurement setup described in the previous section and shown in Fig. 1 was also used to estimate the impulse response of the PLC. The data was obtained for the transmission paths in Block 22 (Fig. 4). The S_{21} was first measured for each path and then converted into real and imaginary parts. The frequency range used was 0.3 MHz to 1.3 GHz. Next, the data was loaded into MATLAB[TM] [22] and expanded by using complex conjugation into a set of positive and negative frequencies. Finally, the data was inverse fast Fourier transformed using the IFFT command to estimate the (real) impulse response.

Figure 11 is the original transmission (S_{21}) magnitude data in frequency domain and Fig. 12 is the estimated impulse response for path A. A number of reflections are present on the line and from 400 MHz – 600 MHz there is a small increase in S_{21}. This is believed to be primarily due to the conduit. Figure 13 is the original transmission (S_{21}) magnitude data in frequency and Fig. 14 is the impulse response for path B. For this path, there are also several reflections present and another small peak in S_{21} occurs near 600 MHz. Figure 15 – 18 are the original transmission (S_{21}) magnitude data in frequency and impulse response for paths C and D.

Transmission paths C and D have the shortest path lengths or propagation distances and have the fewest reflections. Figure 16 (path C) response shows that the signal is damped for t > 200 nsec. Figure 18 (path D) response shows that the signal is damped for t > 75 nsec. The time required for

the reflections to decay is inversely proportional to the path length. Path C and path D have a shorter distance compared to path A, B, and E, which show the least damping.
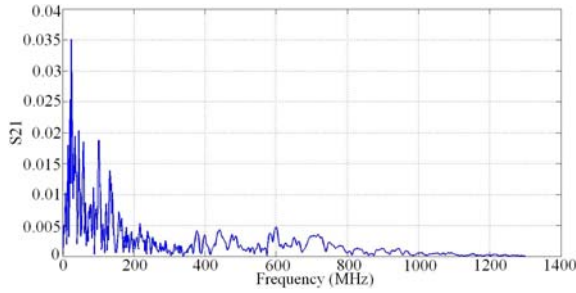
Fig. 11. Frequency magnitude response for transmission path A.
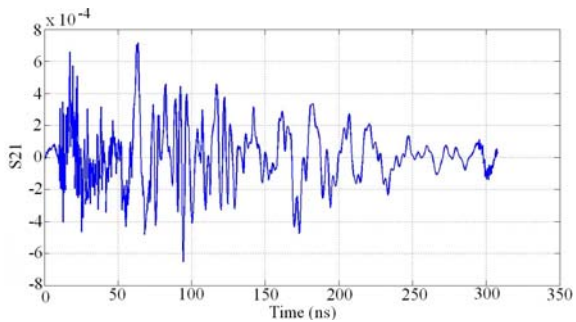
Fig. 12. Impulse response for transmission path A.
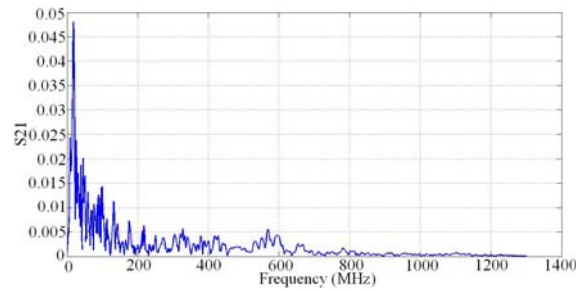
Fig. 13. Frequency magnitude response for transmission path B.
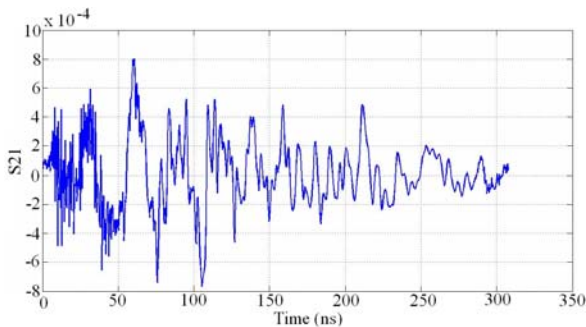
Fig. 14. Impulse response for transmission path B.
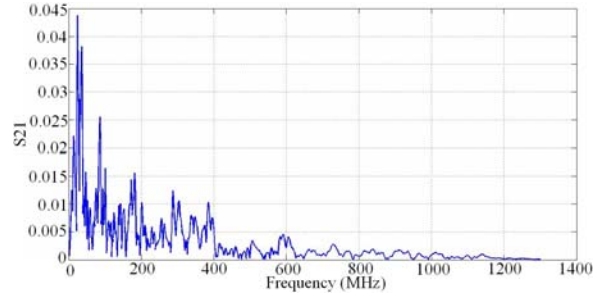
Fig. 15. Frequency magnitude response for transmission path C.
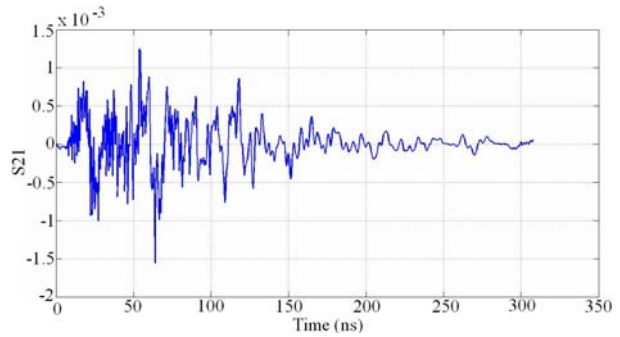
Fig. 16. Impulse response for transmission path C.
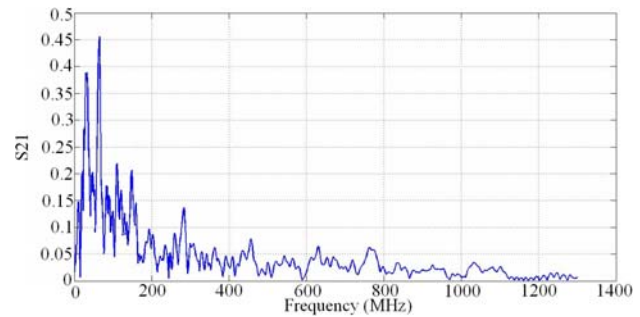
Fig. 17. Frequency magnitude response for transmission path D.
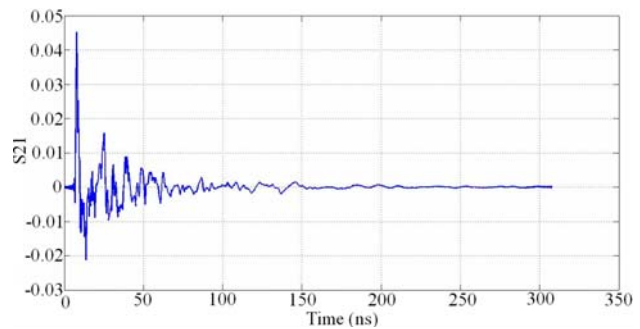
Fig. 18. Impulse response for transmission path D.

Figures 19 and 20 show the S_{21} responses for path E (wing to wing). Figure 19 is the measured transmission (S_{21}) magnitude data in frequency domain and Fig. 20 is the estimated impulse response. Figure 20 shows damping in the signal and some reflections and a peak at t = 280 nsec. In the frequency response, above 400 MHz there are several peaks. The corresponding impulse response shows peaks at 30 and 280 nsec. These peaks can be identified as direct electromagnetic coupling between the two wings and a high frequency waveguide mode due to propagation through the conduit.
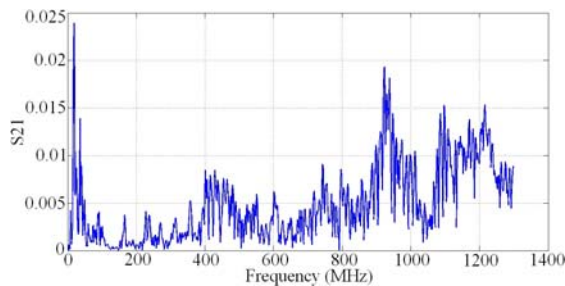
Fig. 19. Frequency response for transmission path E (wing to wing).
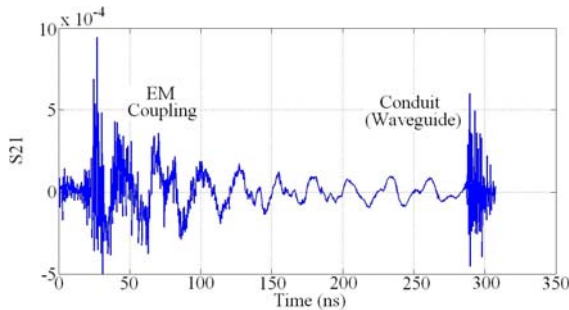
Fig. 20. Impulse response for path E (wing to wing).

Field probe measurements were taken to provide further insight into electromagnetic coupling into the power line. Figure 21 shows the measured S_{21} for the wing-to-wing (path E) wall socket to wall socket (N-G to N-G) and wing-to-wing wall socket (N-G) to a field probe located adjacent to the second wall socket. The distance between the field probe and first wall socket is 9 m. The wall socket to wall socket transmission data (N-G to N-G) shows both low and high frequencies present (> 400 MHz). From the field probe measurement data, low frequencies couple the most and the high frequency data is not present. Figure 22 shows the corresponding time domain wing-to-wing measurements. Comparison of the impulse response for wall socket to wall socket and wall socket to field probe show that propagation through the ground-neutral lines for t > 250 nsec is due to the waveguide mode in the conduit only. Also, the field probe measurements show a response for t > 28 nsec, which suggests coupling from the wall socket. From the foregoing analysis of the frequency- and time-domain responses, the primary propagation components through the power lines are direct electromagnetic coupling and a waveguide mode through the conduit.
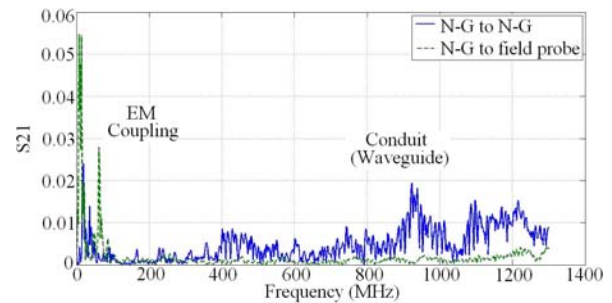
Fig. 21. Frequency response for transmission path E (wing to wing): direct and field probe.
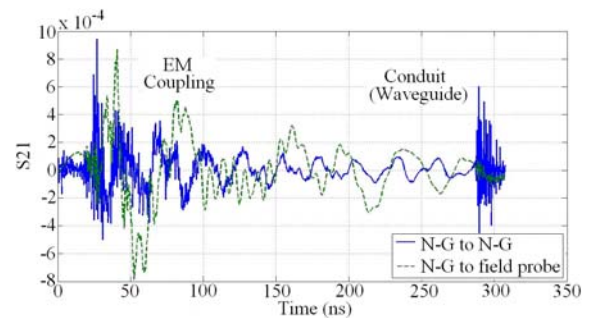
Fig. 22. Impulse response for transmission path E (wing to wing): direct and field probe.

IV. EQUIVALENT RF CIRCUIT MODEL FOR POWER LINES

During measurement of the power line network in the previous section, it was observed that there could be several transmission paths. There is a direct path and additional paths that result in reflections. When the source and receiver are located in different wings, electromagnetic (EM) coupling can also occur. Also, the signal can propagate in modes other than the neutral-ground

(TEM) type mode. In Block 22 for distances greater than 5 meters, the wires must travel through an overhead conduit where the transmission coefficient (S_{21}) can increase instead of decrease with frequency. At certain frequencies, this increase in S_{21} was found to be caused by exciting a waveguide mode inside the conduit. From the dimensions of the conduit, it was calculated that the waveguide cutoff frequency for the lowest order TE_{10} mode is about 750 MHz. For other locations where the path length is less than 5 meters and the wires do not pass through a conduit (waveguide) the S_{21} shows a response that decreases monotonically with frequency.

For power line connections with path lengths greater than 5 meters and where the neutral and ground lines pass through a conduit, a simple model was developed using ADS^{TM} and CST^{TM} [23] to estimate the power distribution between the conduit represented by TE_{10} mode and the neutral-ground wires represented by the TEM mode. This model decomposes the propagation into TEM and TE_{10} propagating modes and is shown in Fig. 23.
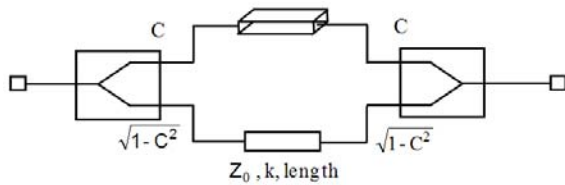
Fig. 23. Equivalent circuit model for propagation through conduit.

To create the conduit model for implementation in a circuit simulator such as ADS^{TM}, a numerical procedure was first used to estimate the coupling (C) for 2-wire transmission through a rectangular waveguide. The power coupled into each mode is conduit $= C$, and for the neutral-ground wires $= \sqrt{(1-C^2)}$. For the model, parameters varied are the spacing (d) between the 2 wires and the height (h) of the wires inside the waveguide as shown in Fig. 24. Simulations were carried out with varying parameters d and h using CST^{TM} and the resulting coupling parameter value C was extracted. In the simulations, the conduit length is 5 meters and wire diameters are 1 mm. The values for Z_0 and k (relative dielectric constant) used in the transmission line model are assumed to be 200 Ω and 1.8. The spacing (d) and the height (h) are varied and simulated

accordingly. The neutral and ground wires inside the conduit with spacing, d are varied between 1 and 5 cm. The estimated coupling, C is extracted using the following procedure:

1. Set the d and h values.
2. EM-simulate the structure shown in Fig. 24 from 0.3 MHz to 900 MHz using CST^{TM}.
3. Import the resulting S-parameters into the circuit simulator.
4. Fit the S-parameters to the circuit shown in Fig. 23 to extract C value.

For height (h) value of 0.1 mm, the value for C is lowest since the neutral and ground wires are placed near the bottom of the conduit and become nearly short-circuited. The coupling value C for this work occurs for the neutral and ground located at least 10 mm from the bottom of the conduit and the neutral and ground are spaced at least 20 mm apart. When the height (h) is 10 mm to 20 mm and spacing (d) is 20 mm to 50 mm, the range for the coupling, C is $0.18 < C < 0.23$.

A frequency dependent coupling can also be used. Here, the coupling increases with frequency and has the form $C = \alpha f$ where f is frequency. Using the procedure described above $\alpha = 0.6 - 0.8$ GHz^{-1} for the height (h) between 10 mm and 20 mm and spacing (d) between 20 mm and 50 mm.
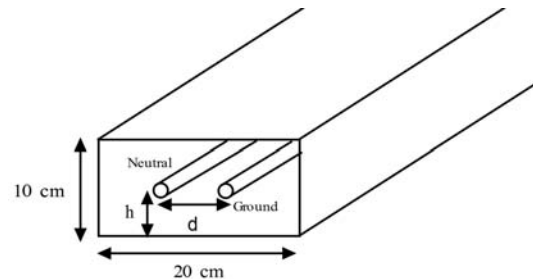
Fig. 24. Conduit cross-sectional view including neutral and ground.

From the layout given in Fig. 4, the equivalent RF circuit model for the wing-to-wing path consists of high pass filters at the transmitter and receiver, an equivalent circuit model for the conduit in each wing, a transmission line for the riser that connects both wings, and a short section of high attenuation transmission line used to model the coupling between the wings. Frequency dependant coupling between the TEM and TE_{10} modes in the conduit is included using $\alpha = 0.7$ GHz^{-1}. Figure 25 shows the equivalent circuit

propagation model for path E for implementation using ADS^{TM}. The final component values are determined by optimizing the model parameters with the frequency- and time-domain S_{21} data using ADS^{TM}. Time-varying attenuation or fading can be included in the model for random or Monte Carlo type analysis by varying the transmission line "*atw*" parameter. For 20 dB variation in attenuation, the range $0.4 < atw < 0.8$ is used.
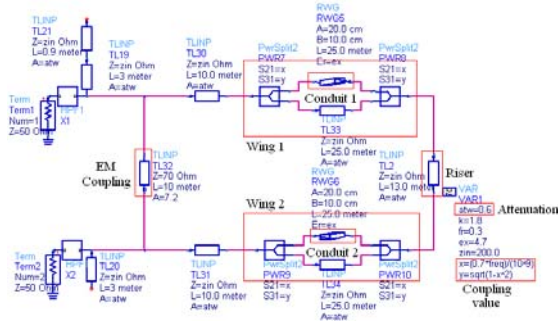
Fig. 25. ADS Schematic diagram for path E (wing to wing).

Figure 26 shows the measured and simulated S_{21} for the wing-to-wing transmission in the frequency- and time-domains. The measured data and simulated model compare well in both domains. For wing-to-wing transmission, the signal propagates through two conduits and the riser as well as direct coupling between the wings and is evident in the time domain response at 28 nsec and 290 nsec in Fig. 26 (b). Figure 26 (a) shows that the frequency response for measurement and simulation are similar up to 900 MHz. As mentioned earlier, the response for frequencies above 400 MHz is primarily due to the TE mode excited in the conduits.

V. CONCLUSION

The transmission measurements in an office building at different locations and times show that the power line system can have low attenuation for frequencies above 30 MHz. These measurements show that frequency bands exist that are nearly fixed with only 40 – 50 dB attenuation and maximum variation of 20 dB. Field strength measurements of the broadband power line were taken and demonstrate that in order to not exceed field levels required by FCC regulations, a low input power level must be used. A simple broadband propagation model for analysis of the

PLC up to 900 MHz is extracted by using both frequency- and time-domain representations of the measured S_{21} parameters. Analysis of S_{21} in both domains is not only helpful in fitting the measured response to a useful model but is also helpful in identifying the various propagation modes. The RF propagation model can be implemented using a standard circuit simulator and provide a unified analysis capability for in-building PLC at the component, sub-system, and system levels. The model is easily modified to account for fading.
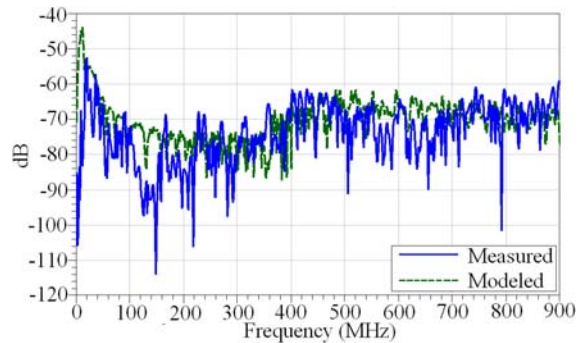
(a) Frequency response.
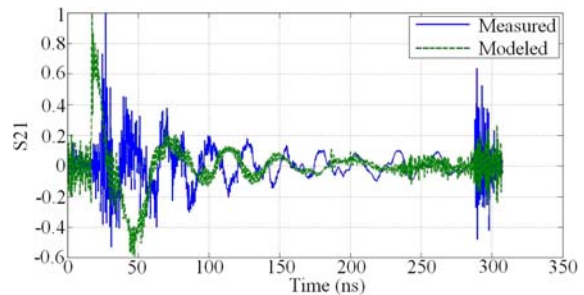
(b) Impulse response.

Fig. 26. Comparison of measured versus modeled S_{21} for path E (wing to wing).

REFERENCES

[1] A. Papaioannou and F. N. Pavlidou, "Evaluation of power line communication equipment in home networks," *IEEE Systems Journal*, vol. 3, no. 3, pp. 288-294, Sept. 2009.

[2] N. A. Pavlidou, H. Vinck, J, Yazdani, and B. Honary, "Power line communications: state of the art and future trends," *IEEE Commun. Mag.*, vol. 41, pp. 34-40, 2003.

[3] K. Dostert, *Power Line Communications*, Prentice Hall PTR, NJ, Upper Saddle River , pp. 1-2, 2000.

[4] S. Ntuli, H. N. Muyingi, A. Terzoli, and G. S. V. R. K. Rao, "Power line networking as an

alternative networking solution: A South African experience," *IEEE Power India Conference*, 2006.

[5] S. Chen, M. Setta, X. Chen, and C. G. Parini, "Ultra wideband power line communication (PLC) above 30 MHz," *IET Comm.*, vol. 3, no. 10, pp. 1587-1596, 2009.

[6] R. G. Olsen, "Technical considerations for wideband power line communication," *IEEE Power Engineering Society Summer Meeting*, vol. 3, pp. 1186-1191, Feb. 2002.

[7] D. Fink and R. J. Jaeung, "Feasible connectivity solutions of PLC for rural and remote areas," *IEEE Int. Sym. on Power Line Comm. and Its Appl.*, pp. 158-163, 2008.

[8] Y. J. Yang and C. M. Arteaga, "Broadband over power line field trial for commercial in-building application in a multi-dwelling-unit environment," *IEEE Int. Sym. on Power Line Comm. and Its Appl.*, pp. 342-346, 2009.

[9] C. M. Arteaga and Y. J. Yang, "Large scale broadband over power line field trial on medium voltage overheard circuits," *IEEE Int. Sym. on Power Line Comm. and Its Appl.*, pp. 289-292, 2008.

[10] T. Esmailian, F. R. Kschischang, and P. G. Gulak, "Characteristics of in-building power lines at high frequencies and their channel capacity," *IEEE Int. Sym. on Power Line Comm. and Its Appl.*, pp. 52-59, 2000.

[11] H. Philipps, "Performance measurements of power line channels at high frequencies," *IEEE Int. Sym. on Power Line Comm. and Its Appl.*, pp. 229-237, March 1998.

[12] A. Leimer and S. Martin, *Carrier Current Systems (CCS) and Broadband over Power Line (BPL)*, Office of Engineering and Technology, FCC Laboratory, May 2004.

[13] A. Sheth, S. Seshan, and D. Wetherall, "Geo-fencing: confining Wi-Fi coverage to physical boundaries," *Proc. Pervasive*, pp. 274-290, 2009.

[14] H. Meng, S. Chen, Y. L. Guan, C. L. Law, P. L. So, E. Gunawan, and T. T. Lie, "A transmission line model for high-frequency power line communication channel," *International Conference on Power System Technology*, vol. 2, pp. 1290-1295, 2002.

[15] H. Meng, S. Chen, Y. L. Guan, C. L. Law, P. L. So, E. Gunawan, and T. T. Lie, "Modeling of transfer characteristics for the broadband power line communication channel," *IEEE Trans. on Power Delivery*, vol. 19, no. 3, pp. 1057-1064, July 2004.

[16] J. Anatory, N. Theethayi, R. Thottappillil, M. M. Kissaka, and N. H. Mvungi, "An experimental validation for broadband powerline communication (BPLC) model," *IEEE Trans. on Power Delivery*, vol. 23, no. 3, pp. 1380-1383, July 2008.

[17] T. Banwell and S. Galli, "A novel approach to the modeling of the indoor power line channel-Part I: circuit analysis and companion model," *IEEE Trans. on Power Delivery*, vol. 20, no. 2, pp. 655-663, 2005.

[18] S. Galli and T. Banwell, "A novel approach to the modeling of the indoor power line channel-Part II: transfer function and its properties," *IEEE Trans. on Power Delivery*, vol. 20, no.3, pp. 1869-1878, July 2005.

[19] T. Zhong, "A new power line modem and its performance in power line channels," M. S. thesis, Dept. Elect. Eng., British Columbia Univ., Vancouver, Canada, 1996.

[20] L. B. Wang, S. Lam, S. K. Yak, O. Manish, and P. T. Seng, "Investigation of radiated emissions in power line communications networks," *Int. Journal of Emerging Electric Power Systems*, vol. 9, no. 3, Article 4, 2008.

[21] Agilent EEsof EDA, Agilent Design System (ADS) version 2008, Agilent Technologies Inc, California, USA.

[22] MATLAB version R2009a, Mathworks Inc, Massachusetts, USA.

[23] CST Microwave Studio version 2011, Computer Simulation Technology, Darmstadt, Germany.

Azlan Hakimi Yahaya Rashid was born in Kuala Lumpur, Malaysia in 1984. He received the Bachelor Degree in Electrical Engineering from University Teknologi Mara, Shah Alam, Malaysia, in November 2008 and is currently working toward the M.Sc. at Universiti Teknologi Petronas, Tronoh, Perak, Malaysia.

Grant Andrew Ellis received the PhD degree in Electrical Engineering from the University of Washington, Seattle, in 1995. He has more than 25 years of professional experience in the areas of RF and Microwave design and antenna analysis and design. Dr Ellis has written over 30 papers and publications and holds 5 US patents. Dr. Ellis is the founding chairman of the IEEE MTT/ED/AP Penang Chapter. He is a registered professional engineer in the State of California and is a Senior Member of the IEEE.

Discontinuous Galerkin Time Domain Method for Scattering Analysis of Air-Inlets

S. Gao [1], M. Liu [2], and Q. Cao [1]

[1] College of Electronic and Information Engineering
Nanjing University of Aeronautics and Astronautics, Nanjing, 210016, People's Republic of China
gaosiping@gmail.com, qunsheng@gmail.com

[2] Shanghai Institute of Satellite Engineering
Shanghai, 200240, People's Republic of China
liumeilin.cn@gmail.com

Abstract ─ In this paper, a high-order three dimensional (3-D) discontinuous Galerkin time domain (DGTD) method has been introduced for the first time for the efficient scattering analysis of air-inlets. This method combines the geometrical versatility of finite element method (FEM) with the explicit time-stepping of finite volume time domain (FVTD) method, thus having the advantages of handling electrically large, arbitrarily shaped, and complex media objects. To validate the capability of this method, the radar cross section (RCS) of three typical air-inlet models have been simulated. The results of the DGTD method agree well with that of the method of moments (MoM), which proves the DGTD method a useful alternative to the traditional methods to solve the scattering problems.

Index Terms ─ Air-inlets, DGTD, and RCS.

I. INTRODUCTION

Scattering properties of air-inlets is of great importance in radar signature analysis [1], as the air-inlets could significantly affect the overall RCS from jetfighters. Therefore, the development of accurate and efficient methods to evaluate the RCS from such structures is an important task and has attracted much attention in the computational electromagnetics community.

Classic frequency methods of scattering analysis include high frequency methods and low frequency methods. However, the high frequency methods employing ray tracing techniques [2] are less accurate when dealing with cavity structures, while the low frequency methods like the MoM [3] is hard to deal with electrically large and complex objects with dielectric coating. Moreover, as the increasing needs for the wideband scattering information, time domain method is more efficient, nonetheless, classic time domain methods such as the finite difference time domain (FDTD) method [4] and the finite element method time domain (FEMTD) [5] suffer from low accuracy or great resource consumption. As a result, new time domain method for efficiently solving the electrically large and complex scattering problem is highly desirable.

Recently a set of high-order DGTD methods has been developed [6-9], which commonly combines the geometrical versatility of the FEM [5] and the explicit time-stepping of the FVTD method [10]. It exceeds FDTD and FEMTD in accuracy and efficiency respectively [11], thus becoming a very suitable method for the electrically large, arbitrarily shaped, and complex media targets. Therefore, in this paper, for the first time, the high-order 3-D DGTD method is applied for the RCS evaluation of air-inlets. To validate the capability of this method to solving scattering problem, three typical air-inlet models have been simulated. The results of them have shown good agreement with that of the MoM, which proves the DGTD method a useful alternative to the other numerical methods.

The remaining parts of the paper are organized as follows. In section II, the DGTD method is briefly presented. In section III, several numerical results of air-inlet models are given to verify the accuracy of the method. Finally, conclusions are drawn in section IV.

II. DGTD FUNDAMENTALS

To introduce the high-order 3D DGTD method simply, the Maxwell's curl equations in linear, isotropic, and homogeneous media are presented in conservation form first,

$$\mathcal{Q} \cdot \partial_t q + \nabla \cdot \boldsymbol{F}(q) = 0, \tag{1}$$

where the material matrix $\mathcal{Q}$, the state vector q, and the flux $\boldsymbol{F}$ are denoted as follows,

$$\mathcal{Q} = \begin{bmatrix} \varepsilon & \\ & \mu \end{bmatrix}, \qquad q = \begin{bmatrix} \boldsymbol{E} \\ \boldsymbol{H} \end{bmatrix},$$

$$\boldsymbol{F}_i(q) = \begin{bmatrix} -\hat{\boldsymbol{e}}_i \times \boldsymbol{H} \\ \hat{\boldsymbol{e}}_i \times \boldsymbol{E} \end{bmatrix}, i = x, y, z.$$

Then, considering a 3D physical domain Ω, which is discretized by K non-overlapping elements (tetrahedrons in 3D), Ω^k, $k=1…K$. In an arbitrary element Ω^k, the fields can be expanded using Lagrange interpolation polynomials $L_i(\boldsymbol{r})$

$$q^k(\boldsymbol{r},t) \approx \sum_{i=1}^{N_p} \hat{q}_i^k(t) L_i(\boldsymbol{r}), \tag{2}$$

where N_p represents the number of the local expansion. $\hat{q}^k$ contains a N_p-vector of expansion coefficients to be solved. The relationship between N_p and the polynomial expansion order N for tetrahedron is $N_p = (N+1)(N+2)(N+3)/6$. A carefully chosen set of the interpolation nodes $\boldsymbol{r}_i$ could lead to good numerical behaviour [12].

Next, using the classic Galerkin method, equation (1) is sampled with test function $L_i(\boldsymbol{r})$ as shown,

$$\int_{\Omega^k} \left(\mathcal{Q}^k \cdot \partial_t \hat{q}^k + \nabla \cdot \boldsymbol{F}(\hat{q}^k) \right) \cdot L_i(\boldsymbol{r}) d\boldsymbol{r} = 0. \tag{3}$$

In order to couple with the neighbouring elements, the divergence part of the integral in equation (3) is first manipulated by an integration by parts as

$$\int_{\Omega^k} \left(\mathcal{Q}^k \cdot \partial_t \hat{q}^k \cdot L_i(\boldsymbol{r}) - \boldsymbol{F}(\hat{q}^k) \cdot \nabla L_i(\boldsymbol{r}) \right) d\boldsymbol{r} =$$
$$-\int_{\partial\Omega^k} \left(\hat{\boldsymbol{n}}^k \cdot \boldsymbol{F}(\hat{q}^k) \right) \cdot L_i(\boldsymbol{r}) d\boldsymbol{r},$$

where $\hat{\boldsymbol{n}}^k$ denotes the unit outward-pointing vector normal to the contour of element Ω^k denoted by $\partial\Omega^k$. Then, replace the flux $\boldsymbol{F}$ on the RHS by the

numerical flux $\boldsymbol{F}^*$ and perform another integration by parts, the strong variational formulation of equation (3) can be obtained as,

$$\int_{\Omega^k} \left(\mathcal{Q}^k \cdot \partial_t \hat{q}^k + \nabla \cdot \boldsymbol{F}(\hat{q}^k) \right) \cdot L_i(\boldsymbol{r}) d\boldsymbol{r} =$$
$$\int_{\partial\Omega^k} \hat{\boldsymbol{n}}^k \cdot \left(\boldsymbol{F}(\hat{q}^k) - \boldsymbol{F}^*(\hat{q}^k) \right) \cdot L_i(\boldsymbol{r}) d\boldsymbol{r}. \tag{4}$$

The numerical flux $\boldsymbol{F}^*$ on the surface $\partial\Omega^k$ is to exchange the coupling between neighboring elements. It can be obtained properly by solving a local Riemann problem [6]. Here, the pure upwind flux [13] is used, which could strongly damp the unphysical modes [6],

$$\hat{\boldsymbol{n}} \cdot \left(\boldsymbol{F}(\hat{q}^k) - \boldsymbol{F}^*(\hat{q}^k) \right) =$$
$$\begin{bmatrix} -\overline{Z}^{-1}\hat{\boldsymbol{n}} \times (Z^+[\boldsymbol{H}^k] - \hat{\boldsymbol{n}} \times [\boldsymbol{E}^k]) \\ \overline{Y}^{-1}\hat{\boldsymbol{n}} \times (Y^+[\boldsymbol{E}^k] + \hat{\boldsymbol{n}} \times [\boldsymbol{H}^k]) \end{bmatrix}, \tag{5}$$

where $[\boldsymbol{E}] = \boldsymbol{E}^- - \boldsymbol{E}^+$ and $[\boldsymbol{H}] = \boldsymbol{H}^- - \boldsymbol{H}^+$ measure the jump in the field values across element interfaces; i.e., superscript "+" refers to field values from the neighbor element while the "−" refers to field values local to the element. For the possible difference of material properties between two elements, local impedance and conductance, $Z^\pm = (Y^\pm)^{-1} = \sqrt{\mu^\pm/\varepsilon^\pm}$ and local sums $\overline{Z} = Z^+ + Z^-$, $\overline{Y} = Y^+ + Y^-$ has to be defined.

Finally, by substituting the expansions in equation (2) with the numerical flux of equation (5) into equation (4) and assuming parameters ε and μ constant in each element, the explicit expressions of the DGTD can be easily obtain as follows,

$$\frac{\partial \boldsymbol{E}^k}{\partial t} = \frac{(\mathcal{M}^k)^{-1}}{\varepsilon^k} \begin{pmatrix} \mathcal{S}^k \times \boldsymbol{H}^k - \\ \mathcal{F}^k \dfrac{\hat{\boldsymbol{n}} \times (Z^+[\boldsymbol{H}^k] - \hat{\boldsymbol{n}} \times [\boldsymbol{E}^k])}{\overline{Z}} \end{pmatrix},$$

$$\frac{\partial \boldsymbol{H}^k}{\partial t} = \frac{(\mathcal{M}^k)^{-1}}{\mu^k} \begin{pmatrix} -\mathcal{S}^k \times \boldsymbol{E}^k + \\ \mathcal{F}^k \dfrac{\hat{\boldsymbol{n}} \times (Y^+[\boldsymbol{E}^k] + \hat{\boldsymbol{n}} \times [\boldsymbol{H}^k])}{\overline{Y}} \end{pmatrix}. \tag{6}$$

Here, $\boldsymbol{E}^k$ and $\boldsymbol{H}^k$ are N_p-vectors. The mass matrix $\mathcal{M}^k$, the stiffness matrices $\mathcal{S}^k$, and the face mass matrix $\mathcal{F}^k$ with respect to the element contour $\partial\Omega k$ are defined as shown below

$$(\mathcal{M}^k)_{ij} = \int_{\Omega^k} L_i(\boldsymbol{r}) L_j(\boldsymbol{r}) d\boldsymbol{r},$$

$$(\mathcal{S}_m^k)_{ij} = \int_{\Omega^k} L_i(\boldsymbol{r}) \partial_m L_j(\boldsymbol{r}) d\boldsymbol{r}, m \in \{x, y, z\},$$

$$(\mathcal{F}^k)_{ij} = \int_{\partial\Omega^k} L_i(\boldsymbol{r}) L_j(\boldsymbol{r}) d\boldsymbol{r}, \quad j \in \{j \mid \boldsymbol{r}_j \in \partial\Omega^k\}.$$

Since equation (6) are ordinary differential

equations with respect to time, a 4th-order, five-stage, low-storage Runge-Kutta scheme [14] is employed for the time integration.

III. NUMERICAL RESULTS

In this section, we present several numerical results to validate the accuracy of the DGTD method while solving the scattering problem of air-inlets. The 3rd-order Lagrange polynomial is employed as the basis function. And a commercial MoM is employed for comparison. Figure 1 shows the computational setup of the air-inlet model. For simplicity here, the electrically large air-inlet is considered as a long perfect electric conducting cylindrical waveguide with a closed-end (deep cavity). It is placed in the center of the total field (TF). A two-cell perfectly matched layer (not depicted here) is wrapped around the scattering field (SF) in order to truncate the computational area. A modulation Gaussian pulse ($\varphi = 180°$, $\theta = 0°$, polarization angle $= 0°$) is injected using the TF/SF technique [4].
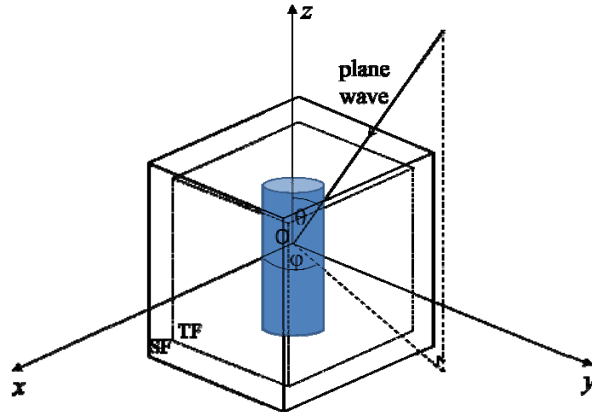
Fig. 1. Computational setup of the air-inlet model.

Figures 2 to 4 show three numerical results and their corresponding model insets. The models are the straight, the frustum, and the bending air-inlet models as shown in Figs. 2b to 4b, respectively. Each model is 10λ length and 0.5λ radius, except that the radius of frustum one varies from 0.5λ to 0.25λ, and the bending one bends $90°$ from the z-direction at the rear. They are all meshed with tetrahedrons of 0.1λ edge-length.

Two comparable bistatic RCS results at 300 MHz are shown in Figs. 2a to 4a, which are the blue circle curves by the DGTD method and the red line curves by the MoM using FEKO v6.1. All the RCS values are evaluated at the direction of φ

$= 0°$, θ from $0°$ to $360°$ with $1°$ increment. From these values, although the air-inlets models are various and electrically long, we could observe great agreement between the results of these two methods. Among these values, the majors mainly appear at the front ($\theta = 0°$) and back ($\theta = 180°$) of the air-inlet models. It could be caused by the direction of the incident plane wave and its multiple reflections by the deep cavity.
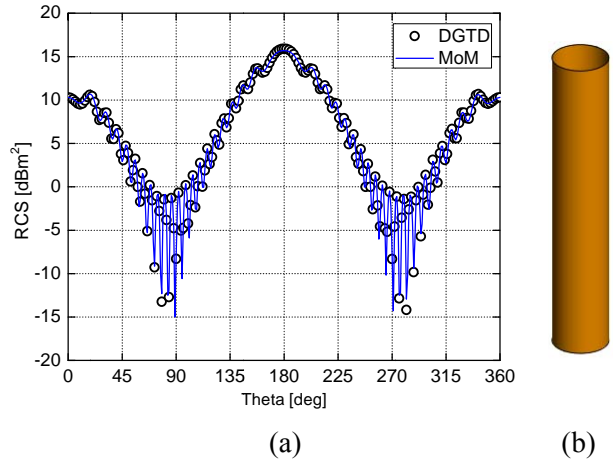
Fig. 2. (a) the bistatic RCS results and (b) the inset of the straight air-inlet model.
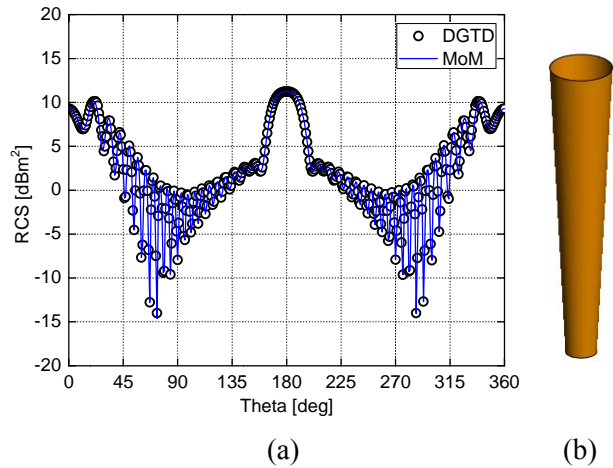
Fig. 3. (a) the bistatic RCS results and (b) the inset of the frustum air-inlet model.

The time consumed by the numerical examples using the DGTD method is a bit longer than the commercial MoM under the same circumstance, which is the platform of the ThinkPad T420 with the Intel® Core™ i7-2640M CPU with 2.80 GHz (only one core is used) and 4.0 GB RAM. However, considering the MoM is a

frequency domain method and the models in FEKO are meshed with 0.1λ edge-length on surface, the DGTD method would be a potential tool when dealing with wideband scattering problems of electrically larger and complex media air-inlet.
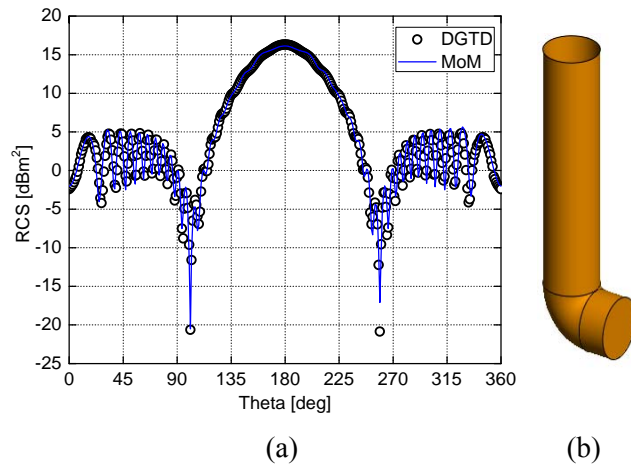
Fig. 4. (a) the bistatic RCS results and (b) the inset of the bending air-inlet model.

IV. CONCLUSION

In this article, the high-order 3-D DGTD method has been introduced for the first time for the scattering analysis of air-inlets. This method has the advantages of handling electrically large, arbitrarily shaped, and complex media composition objects. The results of DGTD agree well with those of the MoM, which proves it to be a useful alternative to the traditional methods to solve the scattering problem. Considering the advantages of this method, it may be a promising method for electrically large and complex air-inlet in future work.

ACKNOWLEDGMENT

REFERENCES

[1] J. Jin, "Electromagnetic scattering from large, deep, and arbitrarily-shaped open cavities," *Electromagnetics,* vol. 18, pp. 3-34, 1997.

[2] H. Ling, S.-W. Lee, and R.-C. Chou, "High-frequency RCS of open cavities with rectangular and circular cross sections," *IEEE Transactions on Antennas and Propagation,* vol. 5, pp. 648-654, 1992.

[3] C. C. Lu and C. Luo, "Comparison of iteration convergences of SIE and VSIE for solving electromagnetic scattering problems for coated objects," *Radio Science,* vol. 38, pp. 11/1-11/9, 2003.

[4] A. Taflove and S. C. Hagness, *Computational Electrodynamics: The Finite-Difference Time-Domain Method*: Artech House, 2005.

[5] J. M. Jin, *The Finite Element Method in Electromagnetics*: Wiley, 2002.

[6] J. S. Hesthaven and T. Warburton, *Nodal Discontinuous Galerkin Methods: Algorithms, Analysis, and Applications*: Springer, 2008.

[7] N. Canouet, L. Fezoui, and S. Piperno, "Discontinuous Galerkin time-domain solution of Maxwell's equations on locally-refined nonconforming Cartesian grids," *COMPEL - The International Journal for Computation and Mathematics in Electrical and Electronic Engineering,* vol. 24, pp. 1381-1401, 2005.

[8] E. Gjonaj and T. Weiland, "A projection penalization approach for the high-order DG-FEM in the time domain," *Radio Science,* vol. 46, 2011.

[9] S. D. Gedney, C. Luo, J. A. Roden, R. D. Crawford, B. Guernsey, J. A. Miller, T. Kramer, and E. W. Lucas, "The discontinuous Galerkin finite-element time-domain method solution of Maxwell's equations," *Applied Computational Electromagnetics Society Journal,* vol. 24, pp. 129-142, 2009.

[10] R. J. LeVeque, *Finite Volume Methods for Hyperbolic Problems*: Cambridge University Press, 2002.

[11] J. Alvarez, S. G. Garcia, L. D. Angulo, and A. R. Bretones, "Computational electromagnetic tools for EMC in aerospace," Marrakesh, 2011, pp. 1840-1844.

[12] T. Warburton, "An explicit construction of interpolation nodes on the simplex," *Journal of Engineering Mathematics,* vol. 56, pp. 247-262, 2006.

[13] J. S. Hesthaven and T. Warburton, "Nodal high-order methods on unstructured grids. I. Time-domain solution of Maxwell's equations," *Journal of Computational Physics,* vol. 181, pp. 186-221, 2002.

[14] M. H. Carpenter and C. A. Kennedy, "Fourth-order 2N-storage Runge-Kutta schemes," NASA Technical Memorandum 109112, 1994.

Analytical Solution of Scattering by a 2D Dielectric Filled Crack in a Ground Plane Coated by a Dielectric Layer: TM Case

B. Ghalamkari [1], A Tavakoli [1, 2], and M. Dehmollaian[3]

[1] Department of Electrical Engineering,
[2] Institute of Communications Technology and Applied Electromagnetics
Amirkabir University of Technology, Tehran, 15914, Iran
B.Ghalamkari@aut.ac.ir, Tavakoli@aut.ac.ir

[3] Department of Electrical and Computer Engineering
University of Tehran, Tehran, 14395-515, Iran
M.Dehmollaian@ece.ut.ac.ir

Abstract ─ In this paper, KP method is applied to study the scattering of a 2D loaded crack on a ground plane, coated by a dielectric layer for TM case. For simplicity, the geometry is divided into three regions, whose fields are expressed in terms of Bessel eigen functions. The governing equations involve several infinite summations with infinite number of unknown coefficients. By the use of Weber-Schafheitlin discontinuous integrals, these infinite summations could efficiently be truncated with high numerical accuracy. Boundary conditions are applied to determine unknown coefficients. We employ finite element method (FEM) and convergence analysis to confirm our results. Finally, the influence of coating dielectric layer and filling material is investigated on the scattered field.

Index Terms ─ 2D coated crack, dielectric layer, Kobayashi and Nomura method, plane wave scattering, and Weber-Schafheitlin discontinuous integrals.

I. INTRODUCTION

An assessment of the surface cracks is a significant area under discussion in nondestructive testing and evaluation (NDT/NDE). There are two main near-field category techniques reported by the engineering community for crack detection. These methods are based on waveguide techniques [1-3] and the resonator method [4-6]. These techniques are not applicable to the non-accessible cracks like those on boilers or blast furnaces, thus, far-field electromagnetic (EM) scattering measurement is recommended.

The scattering from the rectangular crack can be approached in a variety of ways including the method of moment (MoM) [7], quasi-static approach [8, 9], approximate boundary conditions (ABC) [10, 11], Fourier spectrum analysis [12], finite element boundary integral method (FE-BI) [13], transparent boundary condition (TBC) [14], and overlapping T-block method [15-17]. Additionally, Morgan and Schwering utilized mode expansion scattering solution for wide rectangular cracks in 2D [18] and cavities in 3D [19]. Deek et al. extracted the natural frequency poles with matrix pencil method (MPM) for detecting cracks in buried pipes [20]. Bozorgi *et al.* reported a direct integral equation solver (DIES) method for determining the backscattering signatures of a crack in a metallic surface by omitting singularities in hyper singular integrals [21, 22]. Honarbakhsh *et al.* presented mesh free collocation method for 2D filled crack in infinite ground [23].

The Kobayashi potential (KP) is an analytical technique for solving mixed boundary problems and it has been applied to various EM scattering problems [24-32]. KP utilizes the discontinuity properties of Weber-Schafheitlin's integrals and is closely related to MoM approach. Some of the advantages of KP method are cited here. First, the

KP method is accurate and simple in the sense of not dealing with singularity of the Green's functions. Second, the solution converges rapidly due to the satisfaction of a part of the boundary condition by each basis function involved in the integrand [31].

Hongo *et al.* used KP method to find scattering of EM spherical wave from a PEC disk [24]. Imran *et al.* utilized this method to compute diffraction of plane wave from a perfectly electromagnetic conductor (PEMC) strip [25]. Sato *et al.* used KP method to analyze TM plane wave scattering by a 2D filled rectangular crack on a ground plane without any dielectric coating [26]. They applied KP method to two rectangular troughs on a ground plane [27] with a standard impedance boundary condition (SIBC) [28] and estimated the depth of the crack [29]. They also used KP method to model the propagation through slits array [30].

In most cases, paint, primer, rust, and oil coat the corrosion (crack) and it cannot be visually detected. Near-field techniques for detecting cracks under paint were applied [1, 3] but a fast, accurate and rigorous method for analyzing the scattering signature of the coating crack with far-field methods is in demand. Previously, EM plane wave scattering by a 2D rectangular gap in a PEC ground plane, coated by a dielectric layer was reported for TE case [32]. In this paper, the TM case of this problem is investigated.

The paper is organized as follows. In section II the KP method is used to derive the governing field equations with unknown excitation coefficients and truncated unknown excitation coefficients are computed. The numerical results and validations are shown in section III. Conclusion remarks are provided in section IV. Here, the time harmonic factor $e^{-i\omega t}$ is assumed throughout the context.

II. PROBLEM DISCRIPTION AND FORMULATION

We assume a dielectric rectangular crack that is filled by a dielectric material and is coated by a dielectric slab. The cross section for the crack is $2a \times b$ and the height of the slab is y_t as shown in Fig. 1. The relative permittivity and permeability of the filling material are ε_r and μ_r, respectively, and (ε_1, μ_1) are of the coating material. The filling

and the coating materials could be both lossy, meaning that ε_r, μ_r, ε_1, and μ_1 could be complex.
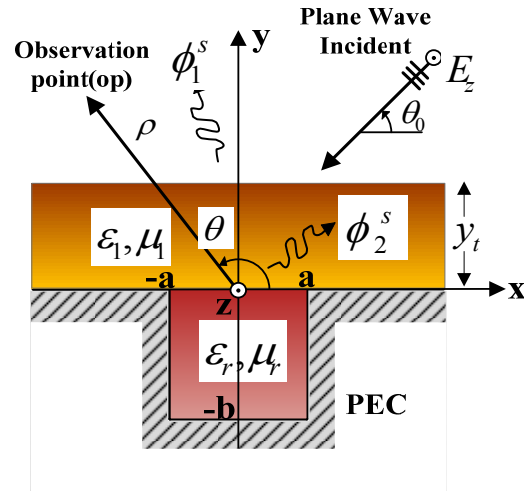
Fig. 1. Geometry of the filled rectangular crack underneath a coating layer in an infinite ground plane.

The incident angle is θ_0 and the observation point is represented by ρ and θ in the cylindrical coordinate system. Assuming ψ is the total electric field in a dielectric slab. The crack is filled by a material with relative permittivity and permeability of ε_r and μ_r, respectively. The relative permittivity and permeability of the slab are ε_1 and μ_1, respectively.

A. Expansion of electromagnetic fields

The geometry of the problem is divided into three regions, which are described as follows.

Region I: Semi-infinite half space $(y > y_t)$

In this region the total z-component of the electric field is denoted by $\phi_i^1 = E_z$ which is,

$$\phi_1^t = \phi^i + \phi^r + \phi_1^s, \tag{1}$$

where, ϕ^i and ϕ^r represent the incident and the reflected field, respectively. Additionally, ϕ_1^s characterizes the scattering contribution of the crack in this region. The material in this region is free space (ε_0, μ_0).

Region II: Slab Region $(y_t > y > 0)$

The total z-component of the electric field in this region is given by,

$$\phi_2^t = \psi + \phi_2^s. \tag{2}$$

Here, ψ is the total electric field in the dielectric slab and its calculation is given in the Appendix. Scattering contribution of the crack in this region is denoted by ϕ_2^s.

Region III: Cavity Region $\left(-b \leq y < 0, |x| < a\right)$

This region is like a parallel plate waveguide. Therefore, the total field is expressed by a summation of waveguide modal eigenfunctions. Considering the boundary conditions at $x = \pm a$ and $y = -b$, ϕ_3^t is given by,

$$\phi_3^t = \sum_{n=0}^{\infty} L_n \left\{ e^{-ih_n y} - e^{ih_n(y+2b)} \right\} \sin\left(\frac{n\pi}{2}\left(1 - \frac{x}{a}\right)\right) \tag{3}$$

where $h_n = \sqrt{\varepsilon_r \mu_r k_0^2 - (n\pi/w)^2}$ stands for the propagation constant of the nth parallel plate waveguide mode and L_n is the excitation coefficient inside cavity region.

B. Applying KP method for scattering fields

In this section, the scattering fields ϕ_i^s ($i = 1, 2$) are derived by utilizing the KP method and the boundary conditions are applied to find the unknown coefficients. Since the scattering fields ϕ_i^s ($i = 1, 2$) satisfy the homogeneous Helmholtz equation, they could be represented as an integral of the general solutions by using the separation of variables method [26]. Without loss of generality, all variables and parameters are normalized with respect to a as follows,

$$u = \frac{x}{a}, \quad v = \frac{y}{a}, \quad k_0 = \frac{\kappa_0}{a}, k_1 = \frac{\kappa_1}{a}, t = \frac{y_t}{a}, \quad (4)$$

therefore,

$$\phi_1^s = \frac{1}{a} \int_0^{\infty} \left\{ d(\xi/a)\cos(\xi\, u) + e(\xi/a)\sin(\xi\, u) \right\} e^{-v\sqrt{\xi^2 - \kappa_0^2}} d\xi \tag{5}$$

and

$$\phi_2^s = \frac{1}{a} \int_0^{\infty} \left\{ f(\xi/a)\cos(\xi\, u) + g(\xi/a)\sin(\xi\, u) \right\} e^{-v\sqrt{\xi^2 - \kappa_1^2}} d\xi$$

$$+ \frac{1}{a} \int_0^{\infty} \left\{ h(\xi/a)\cos(\xi\, u) + k(\xi/a)\sin(\xi\, u) \right\} e^{(v-t)\sqrt{\xi^2 - \kappa_1^2}} d\xi, \tag{6}$$

where, $d(.), e(.), f(.), g(.), h(.),$ and $k(.)$ denote the

unknown weighting functions. It is notable that ϕ_1^s includes only the up-going wave, while ϕ_2^s contains both up-going and down-going waves. Noting the relation between trigonometric and Bessel functions,

$$\begin{cases} \cos(\xi u) = \sqrt{\dfrac{\pi \xi u}{2}} J_{-\frac{1}{2}}(\xi u), \\[3mm] \sin(\xi u) = \sqrt{\dfrac{\pi \xi u}{2}} J_{\frac{1}{2}}(\xi u). \end{cases} \tag{7}$$

The weighting functions are expanded in term of the Bessel functions. Thus,

$$\begin{Bmatrix} d \\ f \\ h \end{Bmatrix}(\xi/a) = \sum_{m=0}^{\infty} \begin{Bmatrix} D_m \\ F_m \\ H_m \end{Bmatrix} \frac{J_{2m+1}(\xi)}{\xi} a, \tag{8}$$

and

$$\begin{Bmatrix} e \\ g \\ k \end{Bmatrix}(\xi/a) = \sum_{m=0}^{\infty} \begin{Bmatrix} E_m \\ G_m \\ K_m \end{Bmatrix} \frac{J_{2m+2}(\xi)}{\xi} a. \tag{9}$$

By substituting equations (8) and (9) into equations (5) and (6) we have,

$$\phi_1^s =$$

$$\sqrt{\frac{\pi u}{2}} \sum_{m=0}^{\infty} \int_0^{\infty} \frac{1}{\sqrt{\xi}} \left\{ \begin{array}{c} D_m J_{2m+1}(\xi) J_{-\frac{1}{2}}(\xi\, u) \\ + E_m J_{2m+2}(\xi) J_{\frac{1}{2}}(\xi\, u) \end{array} \right\} e^{-v\sqrt{\xi^2 - \kappa_0^2}} d\xi, \tag{10}$$

and

$$\phi_2^s = \sqrt{\frac{\pi u}{2}} \sum_{m=0}^{\infty} \int_0^{\infty} \frac{1}{\sqrt{\xi}} \left\{ \begin{array}{c} F_m J_{2m+1}(\xi) J_{-\frac{1}{2}}(\xi u) \\ + G_m J_{2m+2}(\xi) J_{\frac{1}{2}}(\xi u) \end{array} \right\} e^{-v\sqrt{\xi^2 - \kappa_1^2}} d\xi$$

$$+ \sqrt{\frac{\pi u}{2}} \sum_{m=0}^{\infty} \int_0^{\infty} \frac{1}{\sqrt{\xi}} \left\{ \begin{array}{c} H_m J_{2m+1}(\xi) J_{-\frac{1}{2}}(\xi u) \\ + K_m J_{2m+2}(\xi) J_{\frac{1}{2}}(\xi u) \end{array} \right\} e^{(v-t)\sqrt{\xi^2 - \kappa_1^2}} d\xi. \tag{11}$$

In equations (10) and (11), all integrals are identified as a class of Weber-Schafheitlin integrals, which automatically satisfy the zero tangential electric field boundary condition on a part of the ground plane where $|u| > 1, v = 0$.

C. Boundary conditions

The unknown coefficients of the fields consisting of D_m, E_m, F_m, G_m, H_m, K_m, and L_n are determined by applying the boundary conditions.

The boundary conditions at the interface between regions *I* and *II*, where $v = t(y = y_t)$, are given by,

$$\begin{cases} \phi_1^s = \phi_2^s & BC.1 \\ \dfrac{\partial}{\partial v}\phi_1^s = \dfrac{\partial}{\mu_1 \partial v}\phi_2^s. & BC.2 \end{cases} \quad (12)$$

Also the boundary conditions at the interface between regions *II* and *III*, where $v = 0(y = 0)$, are

$$\begin{cases} \phi_2^t = \phi_3^t & BC.3 \\ \dfrac{\partial}{\mu_1 \partial v}\phi_2^t = \dfrac{\partial}{\mu_r \partial v}\phi_3^t. & BC.4 \end{cases} \quad (13)$$

By substituting equations (12) and (13) and equations (7) and (9) into equations (10) and (11) and after some mathematical manipulation, the following equations are derived,

$BC.1$:

$$\sum_{m=0}^{\infty}\int_0^{\infty}\frac{1}{\xi}\left\{ D_m G_{2m+1}^C(\xi) + E_m G_{2m+2}^S(\xi)\right\}e^{-t\sqrt{\xi^2-\kappa_0^2}}d\xi$$
$$=\sum_{m=0}^{\infty}\int_0^{\infty}\frac{1}{\xi}\left\{ F_m G_{2m+1}^C(\xi) + G_m G_{2m+2}^S(\xi)\right\}e^{-t\sqrt{\xi^2-\kappa_1^2}}d\xi \quad , \quad (14)$$
$$+\sum_{m=0}^{\infty}\int_0^{\infty}\frac{1}{\xi}\left\{ H_m G_{2m+1}^C(\xi) + K_m G_{2m+2}^S(\xi)\right\}d\xi$$

$BC.2$:

$$\mu_1\sum_{m=0}^{\infty}\int_0^{\infty}\frac{\sqrt{\xi^2-\kappa_0^2}}{\xi}\left\{ D_m G_{2m+1}^C(\xi) + E_m G_{2m+2}^S(\xi)\right\}e^{-t\sqrt{\xi^2-\kappa_0^2}}d\xi$$
$$=\sum_{m=0}^{\infty}\int_0^{\infty}\frac{\sqrt{\xi^2-\kappa_1^2}}{\xi}\left\{ F_m G_{2m+1}^C(\xi) + G_m G_{2m+2}^S(\xi)\right\}e^{-t\sqrt{\xi^2-\kappa_1^2}}d\xi \quad , \quad (15)$$
$$-\sum_{m=0}^{\infty}\int_0^{\infty}\frac{\sqrt{\xi^2-\kappa_1^2}}{\xi}\left\{ H_m G_{2m+1}^C(\xi) + K_m G_{2m+2}^S(\xi)\right\}d\xi$$

$BC.3$:

$$\sum_{k=0}^{\infty}(-1)^k\left\{ \begin{matrix} L_{2k+1}\gamma_{2k+1}\cos\left(\dfrac{2k+1}{2}\pi u\right) \\ +L_{2k+2}\gamma_{2k+2}\sin\left((k+1)\pi u\right) \end{matrix}\right\}=$$
$$\sum_{m=0}^{\infty}\int_0^{\infty}\frac{1}{\xi}\left\{ F_m G_{2m+1}^C(\xi) + G_m G_{2m+2}^S(\xi)\right\}d\xi \quad , \quad (16)$$
$$+\sum_{m=0}^{\infty}\int_0^{\infty}\frac{1}{\xi}\left\{ H_m G_{2m+1}^C(\xi) + K_m G_{2m+2}^S(\xi)\right\}e^{-t\sqrt{\xi^2-\kappa_1^2}}d\xi$$

$BC.4$:

$$-\frac{\mu_1}{\mu_r}\sum_{k=0}^{\infty}(-1)^k\left\{ \begin{matrix} L_{2k+1}(ih_{2k+1}a)\beta_{2k+1}\cos\left(\dfrac{2k+1}{2}\pi\ u\right) \\ +L_{2k+2}(ih_{2k+2}a)\beta_{2k+2}\sin\left((k+1)\pi\ u\right) \end{matrix}\right\}=$$
$$-i2A\kappa_1\sin\theta_t e^{ik_1 y_t \sin\theta_t}e^{-ik_0\cos\theta_0 x}$$
$$-\sum_{m=0}^{\infty}\int_0^{\infty}\frac{\sqrt{\xi^2-\kappa_1^2}}{\xi}\left\{ F_m G_{2m+1}^C(\xi) + G_m G_{2m+2}^S(\xi)\right\}d\xi$$
$$+\sum_{m=0}^{\infty}\int_0^{\infty}\frac{\sqrt{\xi^2-\kappa_1^2}}{\xi}\left\{ H_m G_{2m+1}^C(\xi) + K_m G_{2m+2}^S(\xi)\right\}e^{-t\sqrt{\xi^2-\kappa_1^2}}d\xi,$$
$$(17)$$

where $\gamma(.) = \left\{1 - e^{ih(.)2b}\right\}$, $\beta(.) = \left\{1 + e^{ih(.)2b}\right\}$, Gc and Gs are

$$\begin{cases} G_\tau^C(\xi) = J_\tau(\xi)\cos(\xi u) \\ G_\tau^S(\xi) = J_\tau(\xi)\sin(\xi u) \ . \end{cases} \quad (18)$$

These equations are solved by KP method and separated into odd and even groups in accordance with Euler's formula. One may end up with the following simultaneous equations.

$BC.1 : Even\ Identity$:

$$\sum_{m=0}^{\infty}D_m\int_0^{\infty}P(\xi)e^{-t\sqrt{\xi^2-\kappa_0^2}}d\xi = \sum_{m=0}^{\infty}F_m\int_0^{\infty}P(\xi)e^{-t\sqrt{\xi^2-\kappa_1^2}}d\xi + \sum_{m=0}^{\infty}H_m\int_0^{\infty}P(\xi)d\xi. \quad (19)$$

$BC.1 : Odd\ Identity$:

$$\sum_{m=0}^{\infty}E_m\int_0^{\infty}Q(\xi)e^{-t\sqrt{\xi^2-\kappa_0^2}}d\xi = \sum_{m=0}^{\infty}G_m\int_0^{\infty}Q(\xi)e^{-t\sqrt{\xi^2-\kappa_1^2}}d\xi + \sum_{m=0}^{\infty}K_m\int_0^{\infty}Q(\xi)d\xi. \quad (20)$$

$BC.2 : Even\ Identity$:

$$\mu_1\sum_{m=0}^{\infty}D_m\int_0^{\infty}\sqrt{\xi^2-\kappa_0^2}\,P(\xi)e^{-t\sqrt{\xi^2-\kappa_0^2}}d\xi =$$
$$\sum_{m=0}^{\infty}F_m\int_0^{\infty}\sqrt{\xi^2-\kappa_1^2}\,P(\xi)e^{-t\sqrt{\xi^2-\kappa_1^2}}d\xi - \sum_{m=0}^{\infty}H_m\int_0^{\infty}\sqrt{\xi^2-\kappa_1^2}\,P(\xi)d\xi. \quad (21)$$

$BC.2 : Odd\ Identity$:

$$\mu_1\sum_{m=0}^{\infty}E_m\int_0^{\infty}\sqrt{\xi^2-\kappa_0^2}\,Q(\xi)e^{-t\sqrt{\xi^2-\kappa_0^2}}d\xi =$$
$$\sum_{m=0}^{\infty}G_m\int_0^{\infty}\sqrt{\xi^2-\kappa_1^2}\,Q(\xi)e^{-t\sqrt{\xi^2-\kappa_1^2}}d\xi - \sum_{m=0}^{\infty}K_m\int_0^{\infty}\sqrt{\xi^2-\kappa_1^2}\,Q(\xi)d\xi. \quad (22)$$

$BC.3 : Even\ Identity$:

$$(-1)^k\{L_{2k+1}\gamma_{2k+1}\} = \frac{2}{2k+1}\sum_{m=0}^{\infty}J_{2m+1}\left((2k+1)\frac{\pi}{2}\right)\left\{ \begin{matrix} F_m \\ e^{-t\sqrt{\left((2k+1)\frac{\pi}{2}\right)^2-\kappa_1^2}}H_m \end{matrix}\right\}. \quad (23)$$

BC.3 : *Odd Identity*:

$$(-1)^k\{L_{2k+2}\gamma_{2k+2}\}=\frac{1}{k+1}\sum_{m=0}^{\infty}J_{2m+2}\big((k+1)\pi\big)\begin{Bmatrix}G_m\\e^{-t\sqrt{((k+1)\pi)^2-\kappa_1^2}}K_m\end{Bmatrix}.$$ (24)

BC.4 : *Even Identity*:

$$\frac{\mu_1}{\mu_r}\sum_{k=0}^{\infty}(-1)^k\left\{L_{2k+1}\beta_{2k+1}(ih_{2k+1}a)\frac{J_{2n+1}\big((2k+1)\frac{\pi}{2}\big)}{(2k+1)\frac{\pi}{2}}\right\}=$$

$$i2Ak_1\sin\theta_t e^{ik_1y_t\sin\theta_t}\frac{J_{2n+1}(\kappa_0\cos\theta_0)}{\kappa_0\cos\theta_0}$$

$$+\sum_{m=0}^{\infty}F_m\int_0^{\infty}\sqrt{\xi^2-\kappa_1^2}\,P(\xi)d\xi-\sum_{m=0}^{\infty}H_m\int_0^{\infty}\sqrt{\xi^2-\kappa_1^2}\,P(\xi)e^{-t\sqrt{\xi^2-\kappa_1^2}}d\xi.$$ (25)

BC.4 : *Odd Identity*:

$$\frac{\mu_1}{\mu_r}\sum_{k=0}^{\infty}(-1)^k\left\{L_{2k+2}\beta_{2k+2}(ih_{2k+2}a)\frac{J_{2n+2}\big((k+1)\pi\big)}{(k+1)\pi}\right\}=$$

$$2Ak_1\sin\theta_t e^{ik_1y_t\sin\theta_t}\frac{J_{2n+2}(\kappa_0\cos\theta_0)}{\kappa_0\cos\theta_0}$$

$$+\sum_{m=0}^{\infty}G_m\int_0^{\infty}\sqrt{\xi^2-\kappa_1^2}\,Q(\xi)d\xi-\sum_{m=0}^{\infty}K_m\int_0^{\infty}\sqrt{\xi^2-\kappa_1^2}\,Q(\xi)e^{-t\sqrt{\xi^2-\kappa_1^2}}d\xi.$$ (26)

where

$$P(\xi)=\frac{J_{2m+1}(\xi)J_{2n+1}(\xi)}{\xi^2}$$
$$Q(\xi)=\frac{J_{2m+2}(\xi)J_{2n+2}(\xi)}{\xi^2}.$$ (27)

Equations (19) to (26) are eight sets of equations to be solved for eight sets of unknown coefficients D_m, E_m, F_m, G_m, H_m, K_m, L_{2k}, L_{2k+1}. In a cylindrical coordinate system where the observation point is represented by ρ and θ the far-field scattering is [29],

$$\phi_1^s=\sqrt{\frac{\pi}{2k_0\rho}}e^{i_1(k_0\rho+\pi/4)}\sum_{m=0}^{\infty}\begin{Bmatrix}D_mJ_{2m+1}(k_0a\cos\theta)\\-iE_mJ_{2m+2}(k_0a\cos\theta)\end{Bmatrix}.$$ (28)

The above summations are all convergent and therefore, n and m are limited to N and M, respectively.

III. VALIDATION AND NUMERICAL RESULTS

In this section different simulations for both filled and coated cracks are given. Two approaches are utilized for validation of this method. First, FEM calculates the equivalent magnetic current density $|M_x|$ on the aperture for several incident angles. Second, for rigorous validation, convergence analysis is performed by changing the truncation numbers N and M [33]. Different cases of the simulations are listed in Table 1.

A. Magnetic current density analysis

Referring to Fig. 1 and Table 1, in the case (a), the non-filled crack is coated by a dielectric layer with a complex permittivity and permeability, while in the case (b); the crack is additionally filled by a complex material. Figure 2 shows the equivalent magnetic current density distribution, $|M_x|$ on the crack ($|x| < a$, $y = 0$) for various incident angles ($\theta_0 = 15^o$, 30°, 45°, 60°, 75°, 90°). In this figure, truncation number of the series is assumed to be N, $M = 14$. Comparison of the results with the FEM solution demonstrates the accuracy of the method for all incident angles. We plot the electric field distribution, calculated by KP method, at normal incident angle for case (b) (see Fig. 3). As shown, the boundary conditions are satisfied at the edges of the crack ($x / \lambda_0 = \pm 1$, $y / \lambda_0 = 0$), while the field maximum occurs near the slab layer ($y / \lambda_0 = 1$). It can also be observed that the field values at $y / \lambda_0 = 1$ is equal to the black solid line in Fig. 2 where $\theta_0 = 90^o$.

Table 1: Different scenarios of coated/filled cracks.

	$2a$	b	ε_r	μ_r	ε_1	μ_1	y_t
a	$2\lambda_0$	$1\lambda_0$	1	1	$2+0.1i$	$1.4+0.1i$	$\lambda_0/10$
b	$2\lambda_0$	$1\lambda_0$	$2.5+0.2i$	$1.8+0.1i$	$2+0.1i$	$1.4+0.1i$	$\lambda_0/10$
c	$0.5\lambda_0$	$0.2\lambda_0$	$3+0.1i$	$1.2+0.02i$	$2.1+1.53i$	$1.4+0.1i$	$\lambda_0/6$
d	$0.8\lambda_0$	$0.3\lambda_0$	$2.7+0.03i$	$1.8+0.1i$	$5.33+1.53i$	$1.4+0.1i$	$\lambda_0/7$
e	$0.9\lambda_0$	$0.5\lambda_0$	$8.42+1.03i$	$1.6+0.1i$	$3.48+0.12i$	$1.2+0.2i$	$\lambda_0/5$
f	$2\lambda_0$ [26]	$1\lambda_0$	$2.5+0.2i$	$1.8+0.1i$	1	1	---
g	$2\lambda_0$ [26]	$1\lambda_0$	1	1	1	1	---
h	$1.5\lambda_0$	$10\lambda_0$	$3.48+0.12i$	$1.2+0.02i$	1	1	---

B. Convergence analysis

For rigorous validation, the error analysis is carried out and the convergence curves are represented in Fig. 4 for various cases c, d, and e. The error function and Euclidean norm are

$$\begin{cases} e_r = \left\| M_{x_k}^{i+1} - M_{x_k}^{i} \right\| / \left\| M_{x_k}^{i} \right\|, \quad i = 1..N, \\ \left\| M_{x_k}^{i} \right\| = \sqrt{\sum_{k=1}^{K} \left| M_{x_k}^{i} \right|^2} \end{cases} \quad (29)$$

where x_k denotes the position of the kth point on the crack and K represents the total number of the observation points. The results are calculated using $K = 25$ for all three cases.

According to Fig. 4, the summations converge rapidly, such that for N and M close to 8~10, the error is equal to $10^{-1.7} = 0.02$. This result is expectable due to the fact that Weber-Schafheitlin type integrals satisfy the boundary condition on the PEC ($|x| > a$, $v = 0$) automatically. The rapid convergence of the analytic method makes it desirable for efficient calculation of the scattered field in the inverse problems.

C. Results

In this section, we compute backscattered RCS, bistatic RCS, and far-field scattering patterns for several filled and coated cracks. We make comparisons with other computed results of the backscattered RCS for the simpler geometry, such as the case of no coating layer. Figure 5 shows the normalized backscattered RCS of cases f and g from Table 1 and compare the results of this method with those on [26]. A very good agreement is observed between these methods. Cases of coated layer with height $y_t = \lambda_0 / 3$ and relative permittivity $\varepsilon_1 = 3 + 0.1i$ and relative permeability $\mu_1 = 1.6 + 0.2i$ are also simulated. Black dash line and cyan dot line depict the results of proposed method for coated cases f and g, respectively. Observation shows that coating layer on the crack alters the RCS signature significantly.

Figure 6 shows the variation of the normalized RCS versus observation angle for case g where the crack is coated by various materials. The crack is illuminated by an incident plane wave at $\theta_0 = 45^o$. Additionally, the depth of the dielectric layer is assumed $y_t = 0.6 \, \lambda_0$ for all of the coating layers. As shown the dielectric constant of the layer does not have a monotonic effect on RCS. Additionally, RCS drops down when very lossy material coats the crack (solid pink line with diamonds).

Next, to show the validity of the proposed method for narrow cracks the normalized backscattering RCS of the case g is presented in

Fig. 7. We also coat this case by a material with $\varepsilon_1 = 2.7 + 0.03i$, $\mu_1 = 1.4 + 0.1i$ and the thickness of $y_t = \lambda_0/4$.
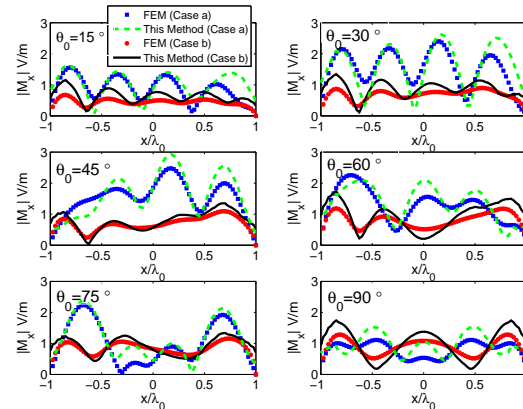

Fig. 2. Magnetic current densities on the crack ($|x| < a$, $y = 0$) computed by the proposed method and FEM for cases a and b.
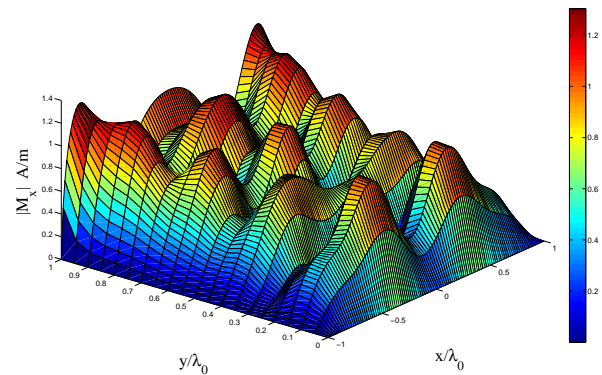

Fig. 3. Distribution of magnetic current density in the crack computed by the KP method for crack of case b.
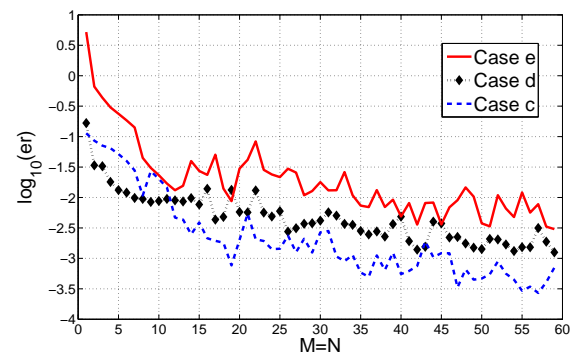
Fig. 4. Convergence curves for cases c, d, and e.
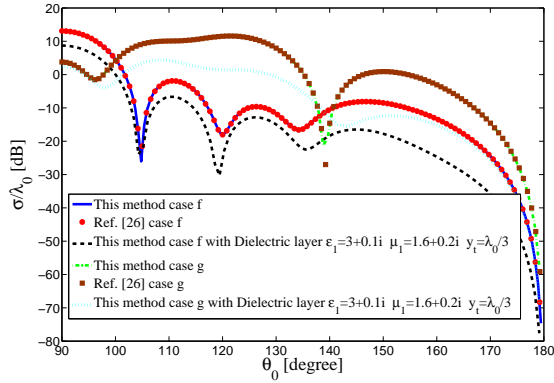
Fig. 5. Normalized RCS as a function of incident angles for case e, and with a dielectric layer of case f.
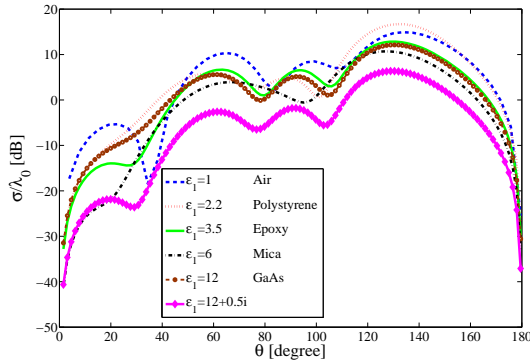
Fig. 6. Normalized bistatic RCS of the crack versus observation angle for various coated dielectric materials of case g.

The variation of the normalized RCS versus the dielectric layer thickness for various permittivity and permeability are shown in Figs. 8 and 9, respectively. The parameters of the crack are $w = 0.2 \lambda_0$ and $b = 0.2 \lambda_0$, also it is illuminated by normal plane wave. In addition, the cracks in all cases are filled by rust with $\varepsilon_r = 2.7 + 0.03i$ and $\mu_r = 1$. As shown in Fig. 8 when the dielectric constant increases, normalized RCS almost increases. According to Figs. 8 and 9, by increasing the dielectric slab thickness RCS has oscillatory behaviour.

Next, the scattering far-field pattern for an empty and covered crack with $w = b$ and $2ka = 15$ is shown in Fig. 10. We compare our results with those on [26] for non-coated crack. The crack is coated by a common paint with relative dielectric constant $\varepsilon_1 = 3 + 0.1i$ and height of $y_t = 0.6 \lambda_0$ for

plane-wave incident angle of $\theta_0 = 30^o$. Also, the crack is coated by a layer of salt rust with relative dielectric of $\varepsilon_1 = 5.33 + 1.53i$ height of $y_t = 0.5 \lambda_0$ for plane-wave incident angle of $\theta_0 = 75^o$.
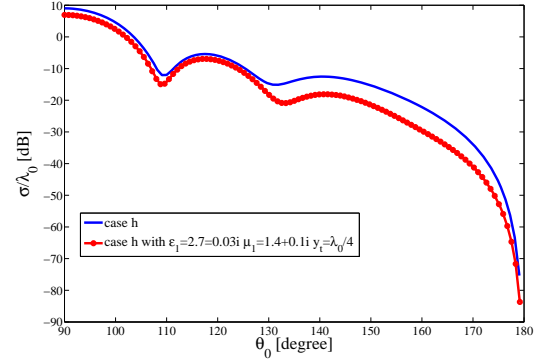
Fig. 7. Normalized backscattering RCS of the narrow crack of case h and this case with a $\lambda_0 / 4$ dielectric layer of $\varepsilon_1 = 2.7 + 0.03i$ and $\mu_1 = 1.4 + 0.1i$.
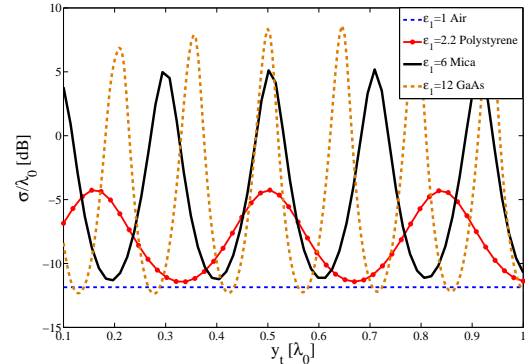
Fig. 8. Normalized RCS of the crack with $w = 0.2\lambda_0$, $b = 0.2\lambda_0$ as a function of coating thickness for different permittivities.
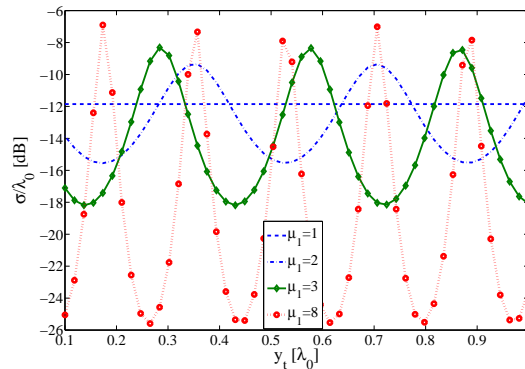
Fig. 9. Normalized RCS of the crack with $w = 0.2\lambda_0$, $b = 0.2\lambda_0$, $\varepsilon_r = 2.7 + 0.03i$, $\mu_r = 1$ versus paint thickness for different permeabilities.
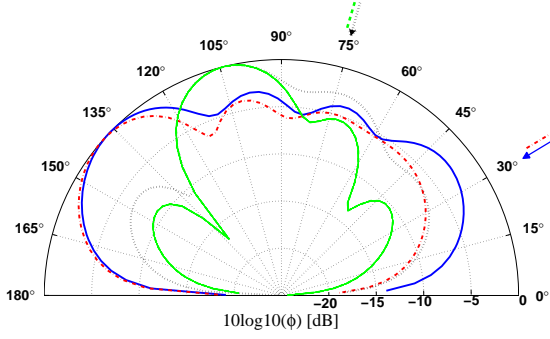
Fig. 10. Scattering far-field pattern for an empty crack where $w = b$ and $2ka = 15$.

——: $(\theta_0 = 30°, \varepsilon_1 = 1, \mu_1 = 1)$, Ref.[26],

— · ·: $(\theta_0 = 30°, \varepsilon_1 = 3 + 0.1i, \mu_1 = 1, y_t = 0.6\lambda_0)$,

........: $(\theta_0 = 75°, \varepsilon_1 = 1, \mu_1 = 1)$, Ref.[26],

— —: $(\theta_0 = 75°, \ \varepsilon_1 = 5.33 + 1.53i, \mu_1 = 1, y_t = 0.5\lambda_0)$.

As shown a thin layer of lossy dielectric alters the scattering pattern significantly. The maximum scattering peak value occurs at the vicinity of the corresponding specular direction for both cases of incident angles. Finally, in Fig. 11, the scattering far-field pattern for a crack with $w = b$ and $2ka = 5$ is shown. We compare our results with those on [26] for non-coated crack. Relative permittivity and relative permeability of $\varepsilon_r = 2.5 + 0.2i$ and $\mu_r = 1.8 + 0.1i$ are used to fill the crack and Fe_2O_3 powder (Rust) with relative dielectric constant $\varepsilon_1 = 2.7 + 0.03i$ and height of $y_t = 0.7 \ \lambda_0$ is utilized to cover the crack. Additionally, the results are shown for two incident angles $\theta_0 = 15°, 60°$. As shown in Fig. 11, scattering pattern varies significantly even for a thin layer of coating layer.

IV. CONCLUSION

In this paper, we analyzed the EM plane wave scattering of a 2D rectangular filled and coated crack on a ground plane by the use of KP method for the TM case. The validation of the proposed method was accomplished by utilizing two techniques; consisting of FEM to investigate the equivalent magnetic current density on the aperture and the convergence analysis. The proposed method is shown to be accurate for both narrow and wide cracks and also is applicable to all lossy and lossless materials for filled and coated cracks. In addition, the sensitivity of RCS

to permittivity, permeability, and thickness of the overlaying layer was presented.
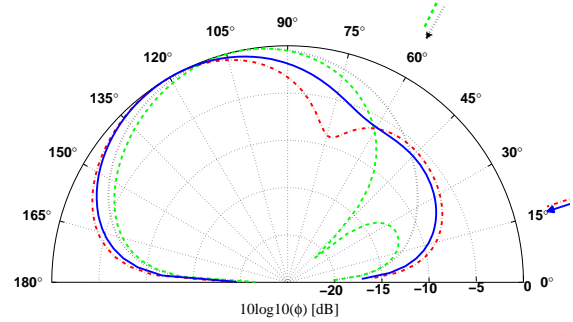
Fig. 11. Scattering far-field pattern for a crack where $w = b$, $2ka = 5$, $y_t = \lambda_0 / 7$, and dielectric filled material characteristics are depicted in the figure legend

——: $(\theta_0 = 15°, \varepsilon_1 = 1, \mu_1 = 1)$, non-filled, Ref.[26],

— · ·: $(\theta_0 = 15°, \varepsilon_1 = 2.7 + 0.03i, \mu_1 = 1, y_t = 0.7\lambda_0)$, filled,

........: $(\theta_0 = 60°, \varepsilon_1 = 1, \mu_1 = 1)$, non-filled, Ref.[26],

— —: $(\theta_0 = 60°, \varepsilon_1 = 2.7 + 0.03i, \mu_1 = 1, y_t = 0.7\lambda_0)$, filled.

APPENDIX
STANDING WAVES IN THE SLAB

A dielectric slab on an infinite PEC ground is shown in Fig. A. The height of the slab is y_t and the relative permittivity and relative permeability of ε_1 and μ_1, respectively are the material characterization of the slab. Here, $k_0 = \omega\sqrt{\varepsilon_0\mu_0}$ and $k_1 = k_0\sqrt{\varepsilon_1\mu_1}$ are respectively the free space and the dielectric slab wave numbers. The slab is illuminated by a TM polarized EM plane wave,

$$\phi^i\left(= E_z^i\right) = e^{-ik_0(x\cos\theta_0 + y\sin\theta_0)}, \tag{A.1}$$

and the reflected plane wave is,

$$\phi^r\left(= E_z^r\right) = \text{R}e^{-ik_0(x\cos\theta_0 - y\sin\theta_0)}, \tag{A.2}$$

where, R is the reflection coefficient, θ_0 is the incident angle, θ_t is the transmission angle. Assuming ψ is the total electric field in the dielectric slab. Therefore,

$$\psi = \left[Ae^{-ik_1\sin\theta_t(y-y_t)} + Be^{+ik_1\sin\theta_t y}\right]e^{-ik_1\cos\theta_t x}, \qquad \text{(A.3)}$$

where A and B are unknown coefficients. The first term and the second term in (A.3) describe the down-going and the up-going wave, respectively. In order to find the aforementioned unknowns first, we note that the tangential electric field is zero over the PEC boundary ($y = 0$), thus,

$$B = -Ae^{ik_1 y_t \sin\theta_t}, \qquad \text{(A.4)}$$

Second, imposing the continuity of the tangential field components E_z and H_x at $y = y_t$ yields,

$$A = \frac{2e^{-ik_0 y_t(\sin\theta_0)}}{1 + \dfrac{k_1\sin\theta_t}{\mu_1 k_0 \sin\theta_0} + e^{ik_1 2y_t(\sin\theta_t)}\left[-1 + \dfrac{k_1\sin\theta_t}{\mu_1 k_0 \sin\theta_0}\right]}, \qquad \text{(A.5)}$$

and

$$R = \frac{\dfrac{k_1\sin\theta_t}{\mu_1 k_0 \sin\theta_0}\left[1 + e^{ik_1 2y_t(\sin\theta_t)}\right] - 1 + e^{ik_1 2y_t(\sin\theta_t)}}{-\dfrac{k_1\sin\theta_t}{\mu_1 k_0 \sin\theta_0}\left[1 + e^{ik_1 2y_t(\sin\theta_t)}\right] - 1 + e^{ik_1 2y_t(\sin\theta_t)}} \qquad \text{(A.6)}$$
$$\cdot e^{-ik_0 2y_t(\sin\theta_0)}.$$

Thus, the electric field in dielectric slab can be expressed as,

$$\psi = A\left[e^{-ik_1(y-y_t)\sin\theta_t} - e^{+ik_1(y+y_t)\sin\theta_t}\right]e^{-ik_1\cos\theta_t x}. \qquad \text{(A.7)}$$

where A is given in equation (A.5).
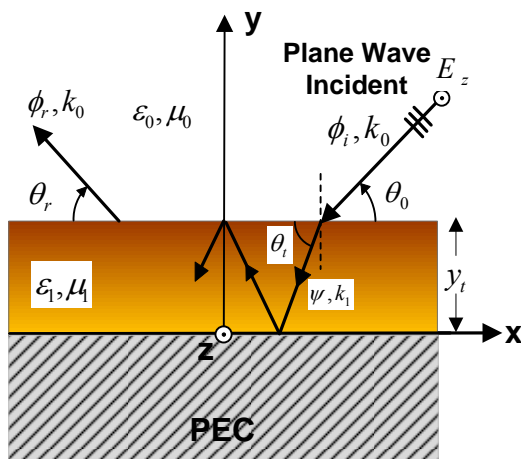
Fig. A. Geometry of a dielectric slab on an infinite ground plane.

REFERENCES

[1] M. T. Ghasr, S. Kharkovsky, and R. Zoughi, "Comparison of near-field millimeter-wave probes for detecting corrosion precursor pitting under paint," *IEEE Trans. on Instrumentation and Measurement*, vol. 54, no. 4, pp. 1497-1504, August 2005.

[2] A. McClanahan, S. Kharkovsky, A. R. Maxon, R. Zoughi, and D. D. Palmer, "Depth evaluation of shallow surface cracks in metals using rectangular waveguides at millimeter-wave frequencies," *IEEE Trans. on Instrumentation and Measurement*, vol. 59, no. 6, pp. 1693-1704, June 2010.

[3] N. Qaddoumi, A. Shroyer, and R. Zoughi, "Microwave detection of rust under paint and composite laminates," *Taylor and Francis Journal: Research in Nondestructive Evaluation*, vol. 9, no. 4, pp. 201-212, June 1997.

[4] A. M. Albishi, M. S. Boybay, and O. M. Ramahi, "Complementary split-ring resonator for crack detection in metallic surfaces," *IEEE Microw. Wireless Compon. Lett.*, vol. 22, no. 6, pp. 330-332, June 2012.

[5] J. Kerouedan, P. Queffelec, P. Talbot, C. Quendo, and A. L. Brun, "Detecting of micro-cracks on metal surfaces using near field microwave dual behaviour resonators," *Springer, New Developments and App. in Sen. Tech*, vol. 83, pp. 1-13, 2011.

[6] S. Kharkovsky, A. McClanahan, R. Zoughi, and D. D. Palmer, "Microwave dielectric-loaded rectangular waveguide resonator for depth evaluation of shallow flaws in metals," *IEEE Trans. on Instrumentation and Measurement*, vol. 60, no. 12, pp. 3923-3930, Dec. 2011.

[7] W. D. Wood and A. W. Wood, "Development and numerical solution of integral equations for electromagnetic scattering from a trough in a ground plane," *IEEE Trans. Antennas Propagat.*, vol. 47, no. 8, pp. 1318-1322, August 1999.

[8] T. B. A. Senior, K. Sarabandi, and J. R. Natzke, "Scattering by a narrow gap," *IEEE Trans. Antennas Propagat.*, vol. 38, no. 7, pp. 1102-1111, July 1990.

[9] T. B. A. Senior and J. L.Volakis, "Scattering by gaps and cracks," *IEEE Trans. Antennas Propagat.*, vol. 37, no. 6, pp. 744-750, June 1989.

[10] K. Barkeshli and J. L. Volakis, "TE scattering by a two-dimensional groove in a ground plane using higher order boundary conditions," *IEEE Trans. Antennas Propagat.*, vol. 38, no. 9, pp. 1421-1428, Sep. 1990.

[11] K. Barkeshli and J. L. Volakis, "Scattering from narrow rectangular filled grooves," *IEEE Trans. Antennas Propagat.*, vol. 39, no. 6, pp. 804-810, June 1991.

[12] T. J. Park, H. J. Eom, and K. Yoshitomi, "An analytic solution for transverse-magnetic scattering from a rectangular channel in a conducting plane," *Journal of Appl. Phys.*, vol. 73, no. 7, pp. 3571-3573, April 1993.

[13] J. Jin, *The Finite Element Method in Electromagnetics*: John Wiley & Sons, 2002.

[14] K. Du, "Two transparent boundary conditions for the electromagnetic scattering from two-dimensional overfilled cavities," *Elsevier Journal of Computational Physics* pp. 5822-5835 2011.

[15] Y. H. Cho, "TM scattering from finite rectangular grooves in a conducting plane using overlapping T-block analysis," *IEEE/ACES Conf. on Wireless Commun. and Appl. Comp. Electro.*, *Society (ACES)*, pp. 744-747, 2005.

[16] Y. H. Cho, "TM plane-wave scattering from finite rectangular grooves in a conducting plane using overlapping T-block method," *IEEE Trans. Antennas Propagat.*, vol. 54, no. 2, pp. 746-749, Feb. 2006.

[17] Y. H. Cho, "Transverse magnetic plane-wave scattering equations for infinite and semi-infinite rectangular grooves in a conducting plane," *IET Microwaves, Antennas & Propagation*, vol. 2, no. 7, pp. 704-710, March 2008.

[18] M. A. Morgan and F. K. Schwering, "Mode expansion solution for scattering by a material filled rectangular groove," *Progress in Electromagnetics Research (PIER)*, vol. 18, pp. 1-17, 1998.

[19] G. Bao, J. Gao, J. Lin, and W. Zhang, "Mode matching for the electromagnetic scattering from three-dimensional large cavities," *IEEE Trans. Antennas Propag.*, vol. 60, no. 4, pp. 2004-2010, April 2012.

[20] F. Deek and M. El-Shenawee, "Microwave detection of cracks in buried pipes using the complex frequency technique," *Appl. Comp. Electro. Society (ACES) Journal*, vol. 25, no. 10, pp. 894-902 2010.

[21] M. Bozorgi and A. Tavakoli, "Backscattering from a two dimensional rectangular crack using FIE," *IEEE Trans. Antennas Propag.*, vol. 58, no. 2, pp. 552-564, Feb. 2010.

[22] M. Bozorgi and A. Tavakoli, "Polarimetric scattering from a 3-D rectangular crack in a PEC covered by a dielectric layer," *Appl. Comp. Electro. Society (ACES) Journal*, vol. 26, no. 6, pp. 502-510, June 2011.

[23] B. Honarbakhsh and A. Tavakoli, "Scattering by a 2D crack: The mesh free collocation approach," *Appl. Comp. Electro. Society (ACES) Journal*, vol. 27, no. 3, pp. 278-284, March 2012.

[24] K. Hongo, A. D. U. Jafri, and Q. A. Naqvi, "Scattering of electromagnetic spherical wave by a perfect conducting disk," *Progress In Electromagnetics Research (PIER)*, vol. 129, pp. 315-343, 2012.

[25] A. Imran, Q. A. Naqvi, and K. Hongo, "Diffraction of electromagnetic plane wave from a PEMC strip," *International Journal of Applied Electromagnetics and Mechanics*, vol. 34, no. 3, pp. 181-193, Jan. 2010.

[26] R. Sato and H. Shirai, "Electromagnetic wave scattering by a trough on a ground --E polarization case--," *Memoirs of The Faculty of Education, Niigata University*, vol. 39, no. 1, pp. 1-9, Sep. 1997.

[27] R. Sato and H. Shirai, "Electromagnetic wave scattering by two rectangular troughs on a ground plane," *IEEE AP-S International Symposium and USNC/URSI National Radio Science URSI Meeting*, Utah USA, 2000.

[28] R. Sato and H. Shirai, "EM scattering analysis by a loaded trough on a ground plane using SIBC-E polarization case," *IEEE Antennas and Propagation Society Int. Symp. Digest*, 1999.

[29] H. Shirai and H. Sekiguchi, "A simple crack depth estimation method from backscattering response," *IEEE Trans. on Instrumentation and Measurement*, vol. 53, no. 4, pp. 1249-1254, Aug. 2004.

[30] R. Sato and H. Shirai, "Propagation analysis for a simplified indoor/outdoor interface model," *IEEE Antennas and Propagation Society Int. Symp. Digest, AP-S*. Nigata, Japan, 2010.

[31] K. Hongo and Q. A. Naqvi, "Similarities between moment method and Kobayashi potential," *IEICE General Conference*, Kusatsu, Japan, 2001.

[32] B. Ghalamkari, M. Dehmollian, and A. Tavakoli, "Analytical solution of scattering by a 2D dielectric filled crack in a ground plane coated by a dielectric layer: TE case," *To Be Published in Appl. Comp. Electro. Society (ACES) Journal*.

[33] J. C. Rautio, "The microwave point of view on software validation," *IEEE Antennas Propagat. Mag.*, vol. 38, no. 2, pp. 68-71, April 1996.

Behbod Ghalamkari was born in Tehran, Iran, on December 5, 1981. He received B.Sc. degree in Electrical Engineering from Semnan University of Semnan, Semnan, Iran, in 2005, the M.Sc. degree from the Amirkabir University of Technology (Tehran Polytechnic), Tehran, Iran, in 2007, both in Electrical Engineering. He is currently working toward the Ph.D. degree in Electrical Engineering in Amirkabir University of Technology. His main interest

lies in the electromagnetic wave propagation, scattering and optimization in electromagnetic problems.

Ahad Tavakoli was born in Tehran, Iran, on March 8, 1959. He received the B.Sc. and M.Sc. degrees from the University of Kansas, Lawrence, and the Ph.D. degree from the University of Michigan, Ann Arbor, all in Electrical Engineering, in 1982, 1984, and 1991, respectively.

He is currently a Professor in the Department of Electrical Engineering at Amirkabir University of Technology. His research interests include EMC, scattering of electromagnetic waves and microstrip antennas.

Mojtaba Dehmollaian was born in Iran in 1978. He received the B.Sc. and M.Sc. degrees in Electrical Engineering from the University of Tehran, Tehran, Iran, in 2000 and 2002, respectively. He received the M.Sc. degree in applied mathematics and Ph.D. degree in Electrical Engineering from the University of Michigan, Ann Arbor, in 2007.

Currently, he is an Assistant Professor with the Department of Electrical and Computer Engineering, University of Tehran. His research interests are applied electromagnetics, radar remote sensing, electromagnetic wave propagation, and scattering.

Scattering by a Metallic Sphere Coated with Chiral Metamaterials

Mao Y. Wang[1], Nan Yang[1], Si C. Ye[1], Hai L. Li[1], Jun Xu[1], Cui L. Zhong[2], and Hu Zheng[1]

[1] School of Physical Electronics
University of Electronic Science and Technology of China, Cheng du, 610054, P.R. China
wmybrimlhl@163.com, yangnan1205@163.com, yesichao@gmail.com, hailong703@163.com,
xujun@uestc.edu.cn, huberyzheng@gmail.com.

[2] Centre of Integrated Electronics
Shenzhen Institutes of Advanced Technology, Chinese Academy of Sciences, Shenzhen, 518055, China
zhongcuilin@hotmail.com

Abstract — Co-polarized and cross-polarized electromagnetic scattering of a metallic sphere coated with chiral metamaterials (CMMs) are simulated with Mie series solution. Firstly, based on Bohren's decomposition technique, electromagnetic fields inside and outside of the sphere are expanded in spherical harmonics vector function. Then, the expanded coefficients are obtained in a suitable form for computation by applying the boundary conditions on the interfaces of all regions. The validity of Mie series solution is shown by computing backward scattering for a ferrite-coated metallic sphere. The effects to bistatic, forward and backward scattering caused by incident wave frequency, media parameters of a metallic sphere coated with CMMs are investigated in details.

Index Terms — Chiral, metamaterials, metallic, Mie series, and scattering.

I. INTRODUCTION

Recently, chiral metamaterials (CMMs) [1-6], which are artificial materials with large optical activity and circular dichroism have been proposed and made for polarization control applications at microwave and optical frequencies. CMMs lack any planes of mirror symmetry and possess strong ability to rotate the plane of polarization of electromagnetic waves. Due to geometric asymmetry, the cross-coupling between the electric and magnetic fields exists at the resonance. The chirality parameter β is used to describe the strength of the cross-coupling effect. Several geometric structures have been proposed to excite cross coupling, such as helices, Y structure, double-layered rosettes and crosswire structure and so on. Meanwhile negative refraction can be achieved by a chiral route. Due to the potential applications ranging from cloaking devices, sub-wavelength optical waveguides, to circular polarizer etc., interest in the study of CMMs has been growing both theoretically and experimentally. Analytical and numerical methods have been used to investigate wave propagation in chiral media [2-6] or metamaterials [7-9] such as Mie series solution, invariant embedding method, finite-difference time-domain method [10], and method of moments, etc. For three-dimensional structures, analytical Mie series solution [11-19] is more efficient and accurate than the others.

This paper is organized as follows: according to Bohren's decomposition technique, Mie series solution for a metallic sphere coated with chiral metamaterials is firstly deduced by applying electromagnetic fields expanded in spherical harmonics vector function inside and outside of the CMMs-coated metallic sphere to boundary conditions. Meanwhile, how to overcome the numerical instability of the Bessel function in the Mie series formula is presented. In section 3, co-polarized and cross-polarized bistatic forward and backward scattering of a metallic sphere coated with chiral metamaterials are calculated with Mie series solution to study its application in the cloak. Finally, conclusions are given.

II. THEORY

Figure 1 presents the geometry of the electromagnetic wave incident on a coated sphere with inner radius b and outer radius a [13, 16]. The time harmonic dependence $e^{(-i\omega t)}$ is assumed for all fields. The incident electromagnetic wave can be expanded in the vector spherical harmonics functions as,

$$\boldsymbol{E}^{inc} = \sum_{n=1}^{\infty} E_n \left[\boldsymbol{M}_{o1n}^{(1)}(k_0) - i\boldsymbol{N}_{e1n}^{(1)}(k_0) \right]$$

$$\boldsymbol{H}^{inc} = \frac{-k_3}{\omega\mu_3} \sum_{n=1}^{\infty} E_n \left[\boldsymbol{M}_{e1n}^{(1)}(k_0) + i\boldsymbol{N}_{o1n}^{(1)}(k_0) \right], \quad (1)$$

where $E_n = i^n E_0(2n+1)/[n(n+1)]$. The notations $o1n$ and $e1n$ mean the summation form of both, the even and odd modes, respectively.
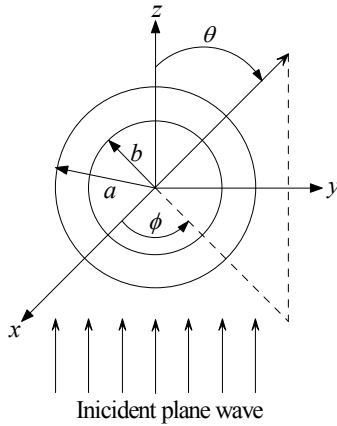

Fig. 1. A plane wave is incident on a metallic sphere coated with chiral metamaterials.

According to the Bohren's decomposition technique [13], the eigenfunction expansion in asymmetry chiral metamaterials can be written as a superposition of a left-handed and right-handed circularly polarized wave functions $\boldsymbol{v}_{o1n}^{(i)} = \boldsymbol{M}_{o1n}^{(i)} + \boldsymbol{N}_{o1n}^{(i)}$, $\boldsymbol{w}_{o1n}^{(i)} = \boldsymbol{M}_{o1n}^{(i)} - \boldsymbol{N}_{o1n}^{(i)}$, where i equals 1 or 3. The superscript "1" relates to the first type of spherical Bessel function and "3" relates the first kind of spherical Hankel function. The expansions of the scattered electromagnetic fields ($\boldsymbol{E}^s$, $\boldsymbol{H}^s$), and the electromagnetic fields ($\boldsymbol{E}^{chiral}$, $\boldsymbol{H}^{chiral}$) in the CMMs region $b < r < a$ are,

$$\boldsymbol{E}^s = \sum_{n=1}^{\infty} E_n \left[a_n^o \boldsymbol{M}_{o1n}^{(3)}(k_0) - ib_n^e \boldsymbol{N}_{e1n}^{(3)}(k_0) \right.$$
$$\left. + a_n^e \boldsymbol{M}_{e1n}^{(3)}(k_0) - ib_n^o \boldsymbol{N}_{o1n}^{(3)}(k_0) \right]$$

$$\boldsymbol{H}^s = -\frac{k_3}{\omega\mu_3} \sum_{n=1}^{\infty} E_n \left[b_n^e \boldsymbol{M}_{e1n}^{(3)}(k_0) + ia_n^o \boldsymbol{N}_{o1n}^{(3)}(k_0) \right.$$
$$\left. + b_n^o \boldsymbol{M}_{o1n}^{(3)}(k_0) + ia_n^e \boldsymbol{N}_{e1n}^{(3)}(k_0) \right],$$

$$\boldsymbol{E}^{chiral} = \sum_{n=1}^{\infty} E_n \left\{ \left[c_{1n}^o \boldsymbol{v}_{o1n}^{(1)}(k_L) + c_{2n}^o \boldsymbol{v}_{o1n}^{(3)}(k_L) \right. \right.$$
$$\left. + c_{1n}^e \boldsymbol{v}_{e1n}^{(1)}(k_L) + c_{2n}^e \boldsymbol{v}_{e1n}^{(3)}(k_L) \right]$$
$$- i\eta_c \left[d_{1n}^o \boldsymbol{w}_{o1n}^{(1)}(k_R) + d_{2n}^o \boldsymbol{w}_{o1n}^{(3)}(k_R) \right.$$
$$\left. \left. + d_{1n}^e \boldsymbol{w}_{e1n}^{(1)}(k_R) + d_{2n}^e \boldsymbol{w}_{e1n}^{(3)}(k_R) \right] \right\},$$

$$\boldsymbol{H}^{chiral} = \sum_{n=1}^{\infty} E_n \left\{ -i\left[c_{1n}^o \boldsymbol{v}_{o1n}^{(1)}(k_L) + c_{2n}^o \boldsymbol{v}_{o1n}^{(3)}(k_L) \right. \right.$$
$$\left. + c_{1n}^e \boldsymbol{v}_{e1n}^{(1)}(k_L) + c_{2n}^e \boldsymbol{v}_{e1n}^{(3)}(k_L) \right]/\eta_c$$
$$+ \left[d_{1n}^o \boldsymbol{w}_{o1n}^{(1)}(k_R) + d_{2n}^o \boldsymbol{w}_{o1n}^{(3)}(k_R) \right. \quad (2)$$
$$\left. \left. + d_{1n}^e \boldsymbol{w}_{e1n}^{(1)}(k_R) + d_{2n}^e \boldsymbol{w}_{e1n}^{(3)}(k_R) \right] \right\},$$

where $\eta_c = (\mu/\varepsilon)^{1/2}$, $k = \omega(\varepsilon_r\varepsilon_0\mu_r\mu_0)^{1/2}$, $k_R = k/(1+\beta k)$, $k_L = k/(1-\beta k)$, ε_r, μ_r and β are the relative permittivity, relative permeability and chirality parameter of CMMs, respectively.

The unknown coefficients a_n^o, b_n^o, a_n^e, b_n^e of the scattered fields can be obtained by applying the boundary conditions of continuous tangential electric and magnetic fields at $r = a$ and the tangential electric field of the metallic boundary being vanished at $r = b$ [8]. In order to avoid computing Bessel functions with complex components that produce numerical instabilities, the coefficients of the scattered fields can be rearranged in a suitable form for computation as below,

$$a_n^o = \frac{-\psi_n(x)}{\xi_n(x)}$$

$$\cdot \frac{\left[\eta_c' P_{1n}^{(1)}(R) D_n(x) - P_{2n}^{(2)}(R)\right]\left[P_{2n}^{(1)}(L) F_n(x) - \eta_c' P_{1n}^{(2)}(L)\right]}{\left[\eta_c' P_{1n}^{(1)}(R) F_n(x) - P_{2n}^{(2)}(R)\right]\left[P_{2n}^{(1)}(L) F_n(x) - \eta_c' P_{1n}^{(2)}(L)\right]}$$

with the additional terms:
$$+\left[\eta_c' P_{1n}^{(1)}(L) D_n(x) - P_{2n}^{(2)}(L)\right]\left[P_{2n}^{(1)}(R) F_n(x) - \eta_c' P_{1n}^{(2)}(R)\right]$$
$$+\left[\eta_c' P_{1n}^{(1)}(L) F_n(x) - P_{2n}^{(2)}(L)\right]\left[P_{2n}^{(1)}(R) F_n(x) - \eta_c' P_{1n}^{(2)}(R)\right]$$

$$b_n^o = \frac{\left[P_{1n}^{(2)}(L)P_{2n}^{(1)}(R) - P_{1n}^{(2)}(R)P_{2n}^{(1)}(L)\right]\psi_n(x)}{\left[P_{1n}^{(1)}(L)P_{2n}^{(2)}(R) - P_{1n}^{(1)}(R)P_{2n}^{(2)}(L)\right]\xi_n(x)}$$

$$\cdot \frac{\begin{array}{l}\left[\eta_c'P_{1n}^{(1)}(R)D_n(x) - P_{2n}^{(2)}(R)\right]\left[-\eta_c'P_{1n}^{(1)}(L)F_n(x) + P_{2n}^{(2)}(L)\right] + \\ \left[\eta_c'P_{1n}^{(1)}(L)D_n(x) - P_{2n}^{(2)}(L)\right]\left[\eta_c'P_{1n}^{(1)}(R)F_n(x) - P_{2n}^{(2)}(R)\right]\end{array}}{\begin{array}{l}\left[\eta_c'P_{1n}^{(1)}(R)F_n(x) - P_{2n}^{(2)}(R)\right]\left[-\eta_c'P_{1n}^{(2)}(L) + P_{2n}^{(1)}(L)F_n(x)\right] + \\ \left[\eta_c'P_{1n}^{(1)}(L)F_n(x) - P_{2n}^{(2)}(L)\right]\left[-\eta_c'P_{1n}^{(2)}(R) + P_{2n}^{(1)}(R)F_n(x)\right]\end{array}},$$

$$a_n^e = -\frac{\left[P_{1n}^{(1)}(R)P_{2n}^{(2)}(L) - P_{1n}^{(1)}(L)P_{2n}^{(2)}(R)\right]\psi_n(x)}{\left[P_{1n}^{(2)}(R)P_{2n}^{(1)}(L) - P_{1n}^{(2)}(L)P_{2n}^{(1)}(R)\right]\xi_n(x)}$$

$$\cdot \frac{\begin{array}{l}\left[P_{2n}^{(1)}(R)D_n(x) - \eta_c'P_{1n}^{(2)}(R)\right]\left[P_{2n}^{(1)}(L)F_n(x) - \eta_c'P_{1n}^{(2)}(L)\right] + \\ \left[\eta_c'P_{1n}^{(2)}(L) - P_{2n}^{(1)}(L)D_n(x)\right]\left[P_{2n}^{(1)}(R)F_n(x) - \eta_c'P_{1n}^{(2)}(R)\right]\end{array}}{\begin{array}{l}\left[P_{2n}^{(2)}(L) - \eta_c'P_{1n}^{(1)}(L)F_n(x)\right]\left[P_{2n}^{(1)}(R)F_n(x) - \eta_c'P_{1n}^{(2)}(R)\right] + \\ \left[P_{2n}^{(2)}(R) - \eta_c'P_{1n}^{(1)}(R)F_n(x)\right]\left[P_{2n}^{(1)}(L)F_n(x) - \eta_c'P_{1n}^{(2)}(L)\right]\end{array}},$$

$$b_n^e = \frac{\psi_n(x)}{\xi_n(x)}$$

$$\cdot \frac{\begin{array}{l}\left[P_{2n}^{(1)}(R)D_n(x) - \eta_c'P_{1n}^{(2)}(R)\right]\left[\eta_c'P_{1n}^{(1)}(L)F_n(x) - P_{2n}^{(2)}(L)\right] \\ +\left[P_{2n}^{(1)}(L)D_n(x) - \eta_c'P_{1n}^{(2)}(L)\right]\left[\eta_c'P_{1n}^{(1)}(R)F_n(x) - P_{2n}^{(2)}(R)\right]\end{array}}{\begin{array}{l}\left[P_{2n}^{(1)}(R)F_n(x) - \eta_c'P_{1n}^{(2)}(R)\right]\left[\eta_c'P_{1n}^{(1)}(L)F_n(x) - P_{2n}^{(2)}(L)\right] \\ +\left[P_{2n}^{(1)}(L)F_n(x) - \eta_c'P_{1n}^{(2)}(L)\right]\left[\eta_c'P_{1n}^{(1)}(R)F_n(x) - P_{2n}^{(2)}(R)\right]\end{array}},$$

$$\tag{3}$$

with

$$P_{2n}^{(1)}(R) = \frac{\psi_n(x_R^a)}{x_R^a} - Q_n(R)\frac{\xi_n(x_R^a)}{x_R^a} - G_n(R)\frac{\xi_n(x_L^a)}{x_L^a},$$

$$P_{2n}^{(2)}(R) = \frac{\psi_n'(x_R^a)}{x_R^a} - Q_n(R)\frac{\xi_n'(x_R^a)}{x_R^a} + G_n(R)\frac{\xi_n'(x_L^a)}{x_L^a},$$

$$P_{1n}^{(1)}(R) = \frac{\psi_n(x_R^a)}{x_R^a} - Q_n(R)\frac{\xi_n(x_R^a)}{x_R^a} + G_n(R)\frac{\xi_n(x_L^a)}{x_L^a},$$

$$P_{1n}^{(2)}(R) = \frac{\psi_n'(x_R^a)}{x_R^a} - Q_n(R)\frac{\xi_n'(x_R^a)}{x_R^a} - G_n(R)\frac{\xi_n'(x_L^a)}{x_L^a},$$

$$P_{2n}^{(1)}(L) = \frac{\psi_n(x_L^a)}{x_L^a} - Q_n(L)\frac{\xi_n(x_L^a)}{x_L^a} - G_n(L)\frac{\xi_n(x_R^a)}{x_R^a},$$

$$P_{2n}^{(2)}(L) = \frac{\psi_n'(x_L^a)}{x_L^a} - Q_n(L)\frac{\xi_n'(x_L^a)}{x_L^a} + G_n(L)\frac{\xi_n'(x_R^a)}{x_R^a},$$

$$P_{1n}^{(1)}(L) = \frac{\psi_n(x_L^a)}{x_L^a} - Q_n(L)\frac{\xi_n(x_L^a)}{x_L^a} + G_n(L)\frac{\xi_n(x_R^a)}{x_R^a},$$

$$P_{1n}^{(2)}(L) = \frac{\psi_n'(x_L^a)}{x_L^a} - Q_n(L)\frac{\xi_n'(x_L^a)}{x_L^a} - G_n(L)\frac{\xi_n'(x_R^a)}{x_R^a},$$

$$Q_n(R) = \frac{\left[F_n(x_L^b) - \dfrac{n}{x_R^b}\right]\psi_n(x_R^b) + \psi_{n-1}(x_R^b)}{\left[F_n(x_L^b) - \dfrac{n}{x_R^b}\right]\xi_n(x_R^b) + \xi_{n-1}(x_R^b)},$$

$$Q_n(L) = \frac{\left[F_n(x_R^b) - \dfrac{n}{x_L^b}\right]\psi_n(x_L^b) + \psi_{n-1}(x_L^b)}{\left[F_n(x_R^b) - \dfrac{n}{x_L^b}\right]\xi_n(x_L^b) + \xi_{n-1}(x_L^b)},$$

$$G_n(R) = \left(\frac{x_L^b}{x_R^b}\right)\frac{\left[F_n(x_R^b) + \dfrac{n}{x_R^b}\right]\psi_n(x_R^b) - \psi_{n-1}(x_R^b)}{\left[\dfrac{n}{x_L^b} - F_n(x_R^b)\right]\xi_n(x_L^b) - \xi_{n-1}(x_L^b)},$$

$$G_n(L) = \left(\frac{x_R^b}{x_L^b}\right)\frac{\left[F_n(x_L^b) + \dfrac{n}{x_L^b}\right]\psi_n(x_L^b) - \psi_{n-1}(x_L^b)}{\left[\dfrac{n}{x_R^b} - F_n(x_L^b)\right]\xi_n(x_R^b) - \xi_{n-1}(x_R^b)},$$

$$x_L^a = k_L a \,, \quad x_R^a = k_R a \,,$$

$$x_L^b = k_L b \,, \quad x_R^b = k_R b \,,$$

$$\psi_n(x) = x j_n(x),$$

$$\xi_n(x) = x h_n^{(1)}(x),$$

$$\eta_c' = \eta_c / \sqrt{\mu_0 / \varepsilon_0}\,,$$

$$D_n(x) = \psi_n'(x) / \psi_n(x),$$

$$F_n(x) = \xi_n'(x) / \xi_n(x), \tag{4}$$

$$D_{n-1}(\sigma) = \frac{\psi_{n-1}'(\sigma)}{\psi_{n-1}(\sigma)} = \frac{n}{\sigma} - \frac{1}{D_n + n/\sigma}, \tag{5}$$

$$F_n(\sigma) = \xi_n'(\sigma) / \xi_n(\sigma) = \xi_{n-1}(\sigma) / \xi_n(\sigma) - n/\sigma.$$

D_n can be stably computed by downward recursion, while F_n can be stably computed by forward recursion [8]. With the assumption that the plane of interest is defined by $\phi = 0^o$, the co-polarized bistatic radar cross section (RCS) $\sigma_{\theta\theta}$, $\sigma_{\phi\phi}$, and the cross-polarized bistatic RCS $\sigma_{\phi\theta}$ of a metallic sphere coated with CMMs can be obtained as,

$$\sigma_{\theta\theta} = \frac{\lambda_0^2}{\pi}\left|\sum_{n=1}^{\infty}\left[\frac{2n+1}{n(n+1)}(b_n^e\tau_n + a_n^o\pi_n)\right]\right|^2$$

$$\sigma_{\phi\phi} = \frac{\lambda_0^2}{\pi}\left|\sum_{n=1}^{\infty}\left[\frac{2n+1}{n(n+1)}(b_n^e\pi_n + a_n^o\tau_n)\right]\right|^2,$$

$$\sigma_{\phi\theta} = \frac{\lambda_0^2}{\pi}\left|\sum_{n=1}^{\infty}\left[\frac{2n+1}{n(n+1)}(b_n^o\pi_n - a_n^e\tau_n)\right]\right|^2, \tag{6}$$

with

$$\pi_n = P_n^1(\cos\theta)/\sin\theta,$$

$$\tau_n = -\sin\theta P_n^{1\prime}(\cos\theta), \qquad (7)$$

where P_n^1 is the Legendre function.

III. NUMERICAL RESULTS

In this section, numerical results about scattering by a metallic sphere coated with CMMs are illustrated. Bistatic, forward and backward radar cross sections, which are generally dependent upon various parameters characterizing the geometry, material properties, and incident fields, are discussed below.

A. Example verification

The validity of Mie series solution in the paper is verified with the results in reference [11]. Figure 2 presents the backward scattering versus the radius for a 0.01 m depth metallic sphere coated with different kinds of media. The wavelength of the incident wave λ_0 is chosen to be 0.01 m, the thickness $t = a-b$ of the media coating layer is $0.05\lambda_0$. The curve consisting of crosses represent backward scattering of a bald metallic sphere. The solid line, dash line, dotted line, and circular curve represents the backward scattering of a metallic sphere coated with lossless ferrite ($\varepsilon_r = 2.5$, $\mu_r = 1.6$), lossy ferrite ($\varepsilon_r = 2.5+i1.25$, $\mu_r = 1.6+i0.8$), lossy metamaterials ($\varepsilon_r = -2.5+i1.25$, $\mu_r = -1.6+i0.8$), and lossy chiral media ($\varepsilon_r = 2.5+i1.25$, $\mu_r = 1.6+i0.8$, $\beta = 9\times10^{-4}$), respectively.

In Fig. 2, the dash line has an excellent agreement with the asterisk for the backward scattering data in reference [11]. Lossy ferrite, metamaterials, and chiral media can make backward scattering decrease at relatively wide electrical size. The backward RCS of a metallic sphere coated with lossy metamaterials and lossy chiral media vary relatively slower as the radius increases. Though the skin depth of each kinds of media coating and the incident wave frequency are numerically identical, it may be noted in Fig. 2 that the backward scattering of a metallic sphere coated with lossy chiral media is significantly smaller than the other media coating.
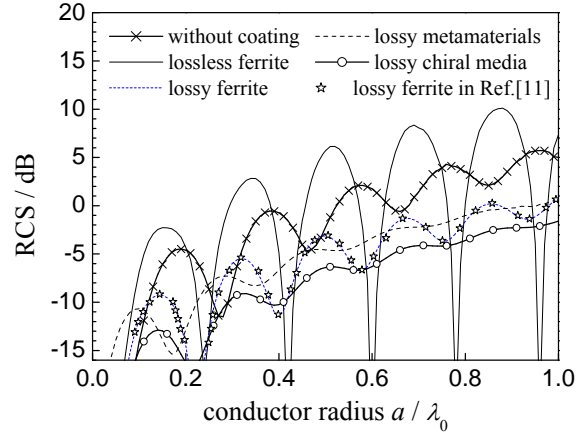

Fig. 2. Backward scattering versus radius for a metallic sphere with ferrite, metamaterials, or chiral media coating.

B. Bistatic RCS

Figure 3 presents the bistatic co-polarized E-plane with a bistatic RCS of $\sigma_{\theta\theta}$ and a co-polarized H-plane with a bistatic RCS of $\sigma_{\phi\phi}$. In addition to the cross-polarized RCS patterns for a metallic sphere coated with CMMs, having $\varepsilon_r = -4.0$, $\mu_r = -1.0$, and $\beta = 0.006$. The radius b of the metallic sphere is 0.382 cm and the outer radius a of the chiral metamaterials shown in Fig. 1 is 1.528 cm [20]. The arrow indicates the direction of the plane wave incidence. The Mie series solution spans incident wave frequencies 3 GHz, 9.375 GHz, and 18 GHz. For the sake of brevity in the paper, only half of the bistatic scattering patterns are shown.

As shown in Fig. 3, the co-polarized and cross-polarized bistatic radar cross sections are relatively smaller at most angles as the 3GHz electromagnetic wave incident. When the incident wave frequency increase, both co-polarized forward scattering and resonant characteristic of a metallic sphere coated with CMMs obviously increase.


(a)
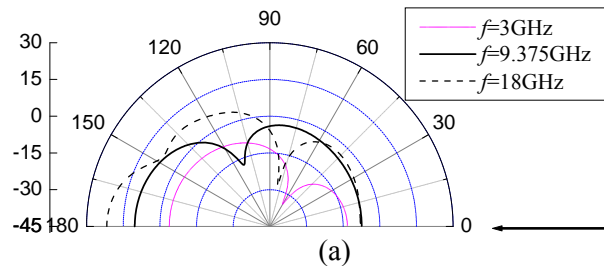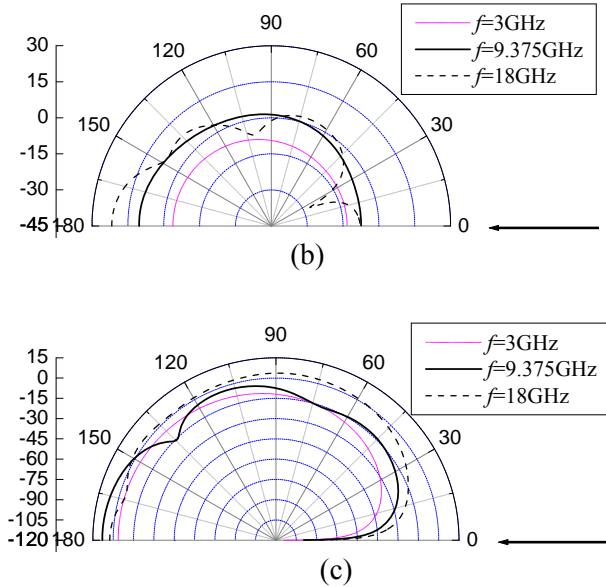
Fig. 3. Bistatic RCS patterns for a metallic sphere coated with CMMs for the (a) co-polarized E-plane, (b) co-polarized H-plane, and (c) cross-polarized RCS.

C. Forward RCS

Figure 4 compares the forward scattering response of a 10 cm radius metallic sphere and a 10 cm radius metallic sphere coated with 1 cm thickness CMMs as a function of electrical size. The cross-polarized scattering of a bald metallic is zero. The circular curve, curve consisting of crosses, solid line, and dotted line represent the imposed condition without the coating layer, coated with lossy chiral metamaterials case I ($\varepsilon_r = \mu_r = -1$, $\beta = 0.001$), case II ($\varepsilon_r = \mu_r = -2$, $\beta = 0.001$), case III ($\varepsilon_r = \mu_r = -0.5$, $\beta = 0.001$), respectively. As can be seen from Fig. 4, a metallic sphere coated with CMMs cast a larger shadow than a metallic sphere. Though the introduction of chiral parameter destroy the impedance match characteristic of matched metamaterials with $\varepsilon_r = \mu_r$, $\beta = 0$, the co-polarized, and cross-polarized forward scattering of a metallic sphere coated with lossy CMMs case I has a well-defined trend, in a manner consistent with the forward scattering of a metallic sphere. Compared to the co-polarized, the cross-polarized forward scattering is relatively smaller. A metallic sphere coated with chiral metamaterials case III ($\varepsilon_r = \mu_r = -0.5$, $\beta = 0.001$) has relatively more surface modes, due to the resonant effect related to the Mie scattering coefficients.
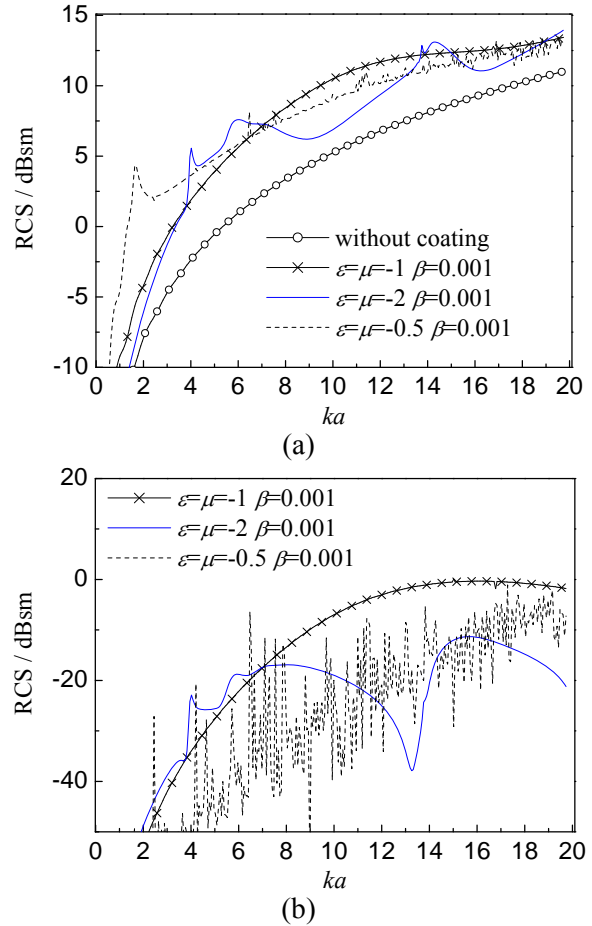

Fig. 4. Forward scattering from a 10 cm radius metallic sphere coated with CMMs for both the (a) co-polarized and the (b) cross-polarized.

D. Backward RCS

Figure 5 illustrates the co-polarized and cross-polarized backward scattering of a relatively large 10 cm radius metallic sphere coated with 1 cm thickness for different kinds of media. In Fig. 5 (a), the curve consisting of crosses and circular curve represent the co-polarized backward scattering of a bald metallic sphere and a metallic sphere coated with chiral metamaterials ($\varepsilon_r = -2.5$, $\mu_r = -1.6$, and $\beta = 0.005$). From 2.2 GHz to 2.7 GHz, the chiral metamaterials make the backward RCS of metallic sphere evidently decrease. One of the possible reasons is the negative refractive properties of the chiral metamaterials, which makes the refracted wave go back to the front surface of the metallic sphere and produce a shadowing effect on the back region. The other possible reason is the chirality parameter, which

induces the cross-polarized wave. The cross-polarized scattering in Fig. 5 (b) is nearly negligible as the value of chirality parameter β is relatively small.


(a)

(b)
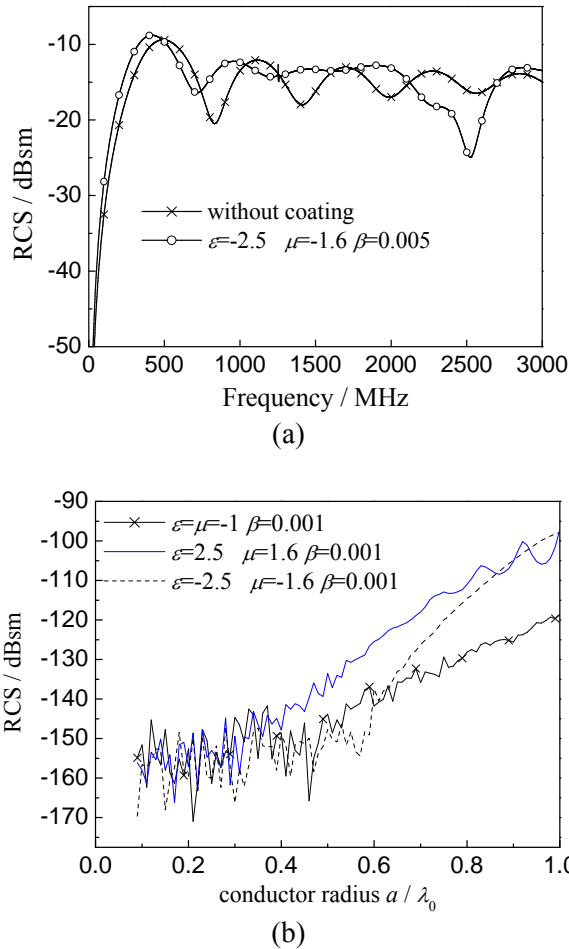
Fig. 5. Backward scattering response of a metallic sphere coated with different kinds of media for both (a) co-polarized and (b) cross-polarized.

IV. CONCLUSIONS

This paper presents Mie theory for electromagnetic scattering by a perfectly metallic sphere with a uniform coating of chiral metamaterials. How to overcome the numerical instability of the Bessel function in the series formula is given. Co-polarized and cross-polarized bistatic scattering patterns, forward and backward radar cross section of a metallic sphere coated with chiral metamaterials are illustrated. Numerical results show that the co-polarized forward scattering and the resonant surface modes of a

metallic sphere coated with CMMs increase with increasing the frequency of the incident wave. Compared to the co-polarized scattering, the cross-polarized scattering are relatively smaller. Due to the negative refractive property and giant optical activity, CMMs can make the echo of a metallic sphere decrease to a certain degree.

REFERENCES

[1] J. B. Pendry, "A chiral route to negative refraction," *Science*, vol. 306, no. 5700, pp. 1353-1355, 2004.

[2] E. K. Yung and B. J. Hu, "Scattering by conducting sphere coated with chiral media," *Microw. Opt. Techn. Let.*, vol. 35, no. 4, pp. 288-293, 2002.

[3] S. Tretyakov, I. Nefedov, A. Sihvola, S. Maslovski, and C. Simovski, "Waves and energy in chiral nihility," *J. Electro. Wave*, vol. 17, no. 5, pp. 695-706, 2003.

[4] D. V. Guzatov and V. V. Klimov, "Chiral particles in a circularly polarised light field: new effects and applications," *Quantum Electronics*, vol. 41, no. 6, pp. 526-533, 2011.

[5] A. M. Attiya, "Coupled mode analysis of two-dimensional chiral grating," *Appl. Comp. Electro. Society*, vol. 26, no. 4, pp. 303-311, 2011.

[6] S. T. Imeci, F. Altunkilic, J. R. Mautz, and E. Arvas, "Transmission through an arbitrarily shaped aperture in a conducting plane separating air and a chiral medium," *Appl. Comp. Electro. Society*, vol. 25, no. 7, pp. 587-599, 2010.

[7] J. M. Taboada, M. G. Araújo, J. Rivero, L. Landesa, and F. Obelleiro, "Surface integral equation solvers for large-scale conductors, metamaterials and plasmonic nanostructures," *Appl. Comp. Electro. Society*, vol. 27, no. 2, pp. 189-197, 2012.

[8] L. Gaoa and Y. Y. Huang, "Extinction properties of a coated sphere containing a left-handed material," *Opt. Commun.*, vol. 239, no. 1-3, pp. 25-31, 2004.

[9] M. I. Aksun, A. Alparslan, E. P. Karabulut, E. Irci, and V. B. Ertürk, "Determining the effective constitutive parameters of finite periodic structures: photonic crystals and metamaterials," *IEEE Trans. Microwave Theory and Tech.*, vol. 56, no. 6, pp. 1423-1434, 2010.

[10] J. A. Pereda, A. Grande, O. González, and Á. Vegas,

"FDTD modeling of chiral media by using the mobius transformation technique," *IEEE Antennas and Wireless Propagation Letters*, vol. 5, no. 3, pp. 327-330, 2006.

[11] J. H. Richmond, "Scattering by a ferrite-coated conducting sphere," *IEEE Trans. Antennas Propagat.*, vol. 35, no. 1, pp. 73-79, 1987.

[12] D. J. Ross and R. Sigel, "Mie scattering by soft core-shell particles and its applications to ellipsometric light scattering," *Phys. Rev. E*, vol. 85, no. 5, pp. 1-13, 2012.

[13] C. F. Bohren and D. R. Huffman, *Absorption and scattering of light by small particles*, Wiley, New York, 1983.

[14] Z. S. Wu and Y. P. Wang, "Electromagnetic scattering for multilayered sphere: recursive algorithms," *Radio Sci.*, vol. 26, no. 6, pp. 1393-1401, 1991.

[15] Z. W. Zhao, Z. S. Wu, and Q. Z. Xue, "An algorithm for electromagnetic scattering of large absorptive homogeneous sphere," *Chinese Journal of Radio Science*, vol. 14, no. 4, pp. 422-425, 1999.

[16] V. Demir, A. Elsherbeni, and D. Worasawate, "A graphical user interface (GUI) for plane wave scattering from a conducting, dielectric or a chiral Sphere," *IEEE Antenn. Propag. Mag.*, vol. 46, no. 5, pp. 94-99, 2004.

[17] Y. L. Geng and S. L. He, "Analytical solution for electromagnetic scattering from a sphere of uniaxial left-handed material," *J. Zhejiang Univ.-Sc. A*, vol. 17, no. 1, pp. 99-104, 2006.

[18] Z. W. Zhao, Z. S. Wu, and Q. Z. Xue, "An algorithm for electromagnetic scattering of large absorptive homogeneous sphere," *Chinese Journal of Radio Science*, vol. 14, no. 4, pp. 422-425, 1999.

[19] M. Y. Wang, C. W. Qiu, J. Xu, Y. L. Dong, H. Zheng, and H. L. Li, "MIE series for electromagnetic scattering of chiral metamaterials sphere," *Journal of Systems Engineering and Electronics*, vol. 22, no. 6, pp. 885-891, 2011.

[20] D. B. Ge and Y. B. Yan, "Finite-difference time-domain method for electromagnetic waves," *Xi'an University Press*, 2011.

Mao Yan Wang was born in Shandong, China, 1979. She is currently an Associate Professor with University of Electronic Science and Technology of China (UESTC). Her research interests include millimeter wave circuit and systems, computation electromagnetic and metamaterials.

Nan Yang was born in Shandong, China, 1990. She is currently working toward the Master degree in Radio Physics at UESTC. Her research interest is millimeter wave circuit and systems.

Si Chao Ye was born in Si chuan,China,1990. He is currently working toward the M.Sc. degree in Radio physics at UESTC. His research interest is millimeter wave systems.

Hai Long Li was born in Shandong, China, in 1979. He is currently an Associate Professor with UESTC. His research interests include dusty plasma and high-power microwave technique.

Jun Xu was born in 1963. He is currently a Professor with UESTC. His research interests include millimeter wave hybrid integrated technology, communication and radar RF technology.

Cui Lin Zhong was born in Hunan, China, 1975. His current research interests include microwaves, antenna techniques, and radio technology of wireless communication and radar.
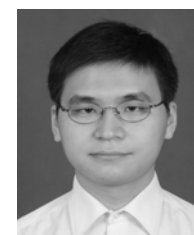
Hu Zheng was born in 1979. He is an Associate Professor with UESTC. His research interests include EM theory and microwave technology and computation electromagnetic etc.

A Novel Wilkinson Power Divider Using Open Stubs for The Suppression of Harmonics

Mohsen Hayati [1,2] and Saeed Roshani [1]

[1]Electrical Engineering Department, Faculty of Engineering
Razi University, Kermanshah, 67149, Iran
mohsen_hayati@yahoo.com, roshany@ieee.org

[2] Computational Intelligence Research Centre
Razi University, Kermanshah, 67149, Iran

Abstract ─ In this paper, the design process of a novel Wilkinson power divider is presented. The proposed power divider features a simple structure with open stubs at each port. With slight changes of the dimensions of open stubs, designed power divider can suppress combinations of each two desired order harmonic simultaneously. From the measured results, 45 dB and 43 dB suppression for 3rd and 5th harmonics is obtained, respectively. The proposed power divider has an insertion loss less than 0.1 dB, input return loss better than 31 dB, output return loss better than 51 dB, and better than 43 dB of isolation at 1.65 GHz.

Index Terms ─ Harmonic suppression, open stub, and Wilkinson power divider.

I. INTRODUCTION

Wilkinson power dividers are widely applied in microwave communication such as power amplifiers, mixers, and frequency multipliers. Wilkinson power divider is designed for the single/dual band applications [1-2].

In many applications, the unwanted harmonics caused by nonlinear property of the active circuit dluohs be removed. Minimizing harmonics distortion is a great challenge in modern wireless communications with the high data-rate. It is cost-effective if the unwanted harmonics are suppressed in the power divider or the combiner structure [3]. Several methods have been proposed so far to design miniaturized harmonic suppressed power dividers with improved performance [3-17].

In [3-6] power dividers with two microstrip electromagnetic band-gap (EBG) cells for harmonics suppression are presented. In [7, 8] harmonics suppression is demonstrated with defected ground structure (DGS). Nevertheless, DGS and EBG, need etching process on backside ground plane and accurate position calibration, which improve time-consumption and difficulty in machining [9]. Nowadays resonators, filters [10-12] and shunt open stubs elements have been widely used to suppress the unwanted harmonics and size reduction. In [13, 14] a compact size Wilkinson power divider, based on non-uniform transmission lines is presented and in [15-17], Π- and T-shaped shunt open-stubs are used for harmonics suppression.

However, in these works, obtaining harmonics suppression with high level of attenuation is still subject of discussion and challenge. In this paper, a novel Wilkinson power divider for harmonics suppression with high level of attenuation is presented. This structure has significant advantages in terms of simple topology and superior harmonic suppression. The major advantage of the new structure is its high flexibility capability. The power divider is fabricated based on 3rd and 5th harmonics suppression. Moreover, simulation results show that the proposed structure can suppress the 2nd and 3rd harmonics.

II. POWER DIVIDER DESIGN

Figure 1 (a) shows the conventional Wilkinson

power divider that consists of two quarter-wavelength transmission lines ($\sqrt{2}\ Z_0$) and an isolation resistor (100 ohms). Figure 1 (b) shows the structure of the proposed Wilkinson power divider. It consists of two quarter-wavelength transmission lines, two branch-lines (θ_3), three open shunt stubs (two θ_2 and one θ_1) and an isolation resistor. This power divider is symmetric, so the odd- and even-mode analyses can be used to determine the circuit parameters for harmonic suppression [18].

A. Odd-mode analysis

With referring to the diagram shown in Fig. 2 (a), the output admittance of the half-circuit is simply equal to,

$$Y_A = -\frac{j\cot 90^0}{Z} = 0 \tag{1}$$

$$Y_B = \frac{j\tan\theta_2}{Z}\ , \tag{2}$$

$$Y_C = \frac{Z + j\frac{R}{2}\tan\theta_3}{\frac{R}{2}Z + jZ^2\tan\theta_3}\ , \tag{3}$$

$$Y_0 = Y_A + Y_B + Y_C\ . \tag{4}$$

The real part of equation (4) becomes,

$$R = 2Z_0(1 - \tan\theta_2\tan\theta_3)\ , \tag{5}$$

while the imaginary part yields

$$Z^2\tan\theta_3 = \frac{R}{2}Z_0(\tan\theta_2 + \tan\theta_3)\ . \tag{6}$$

Substituting equation (5) into equation(6), results in,

$$Z = Z_0\sqrt{(\tan\theta_2 + \tan\theta_3)(\cot\theta_3 - \tan\theta_2)}\ . \tag{7}$$

B. Even-mode analysis

According to Figure 2 (b) under even mode excitation, the ABCD matrix can be expressed for the equivalent circuit of the proposed power divider as follows,

$$\begin{bmatrix} 1 & 0 \\ \frac{jY\tan\theta_1}{2} & 1 \end{bmatrix} \times \begin{bmatrix} 0 & jZ \\ jY & 0 \end{bmatrix} \times$$

$$\begin{bmatrix} 1 & 0 \\ jY\tan\theta_2 + jY\tan\theta_3 & 1 \end{bmatrix} = \begin{bmatrix} A & B \\ C & D \end{bmatrix}\ . \tag{8}$$

Subsequently, the ABCD parameters can be obtained as,

$$A = -(\tan\theta_2 + \theta_3) \tag{9}$$

$$B = jZ\ , \tag{10}$$

$$C = jY - j\frac{Y}{2}\tan\theta_1\tan\theta_2 - j\frac{Y}{2}\tan\theta_1\tan\theta_3\ , \tag{11}$$

$$D = -\frac{\tan\theta_1}{2}\ . \tag{12}$$


(a)

(b)
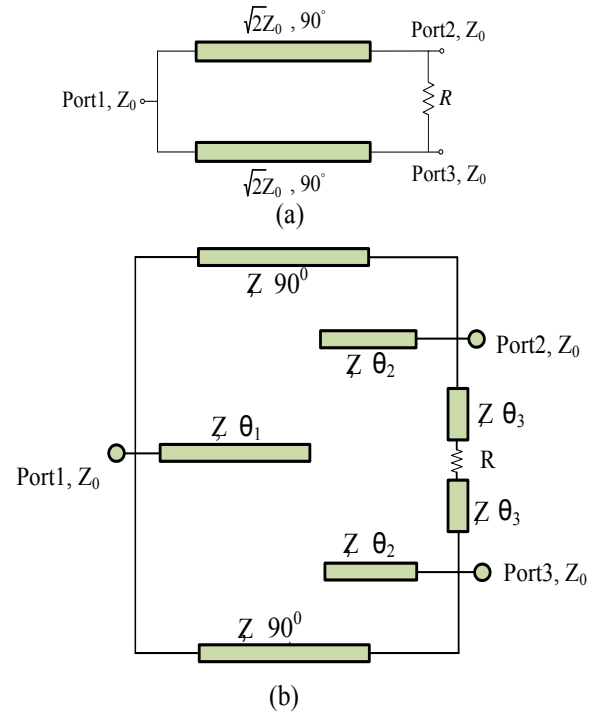
Fig. 1. Schematic diagram of the (a) conventional Wilkinson power divider and the (b) proposed power divider.

The input impedance of the even mode equivalent circuit is expressed as [18],

$$Z_{in} = 2Z_0 = \frac{AZ_0 + B}{CZ_0 + D}\ . \tag{13}$$

Assuming the network is reciprocal and lossless, then equation (13) can be written as,

$$A = 2D \tag{14}$$

and

$$A^2 - \left(\frac{B}{Z_0}\right)^2 = 2\ . \tag{15}$$

Using equations (9) - (12), equations (14) and (15) can then be modified as follows,

$$\tan\theta_1 = \tan\theta_2 + \tan\theta_3 \tag{16}$$

and

$$(\tan\theta_2 + \tan\theta_3)^2 + \frac{Z^2}{Z_0^2} = 2\ . \tag{17}$$

Substituting equations (16) and (7) into equation (17), yields,

$$\tan\theta_1^2 + \tan\theta_1(\cot\theta_3 - \tan\theta_2) = 2\ . \tag{18}$$

Since n^{th} harmonic suppression is desired, θ_1 and θ_2 are assigned to be $\pi/2n$ [19]. For the 3rd and 5th

harmonic suppressions, θ_1 and θ_2 are obtained to be $\pi/6$ and $\pi/10$, respectively. Substituting these values into equation (16), θ_3 is obtained, which is $14.1°$. The value of R and Z are obtained from equations (5) and (7), as 92 ohms and 72 ohms, respectively.


(a)

(b)
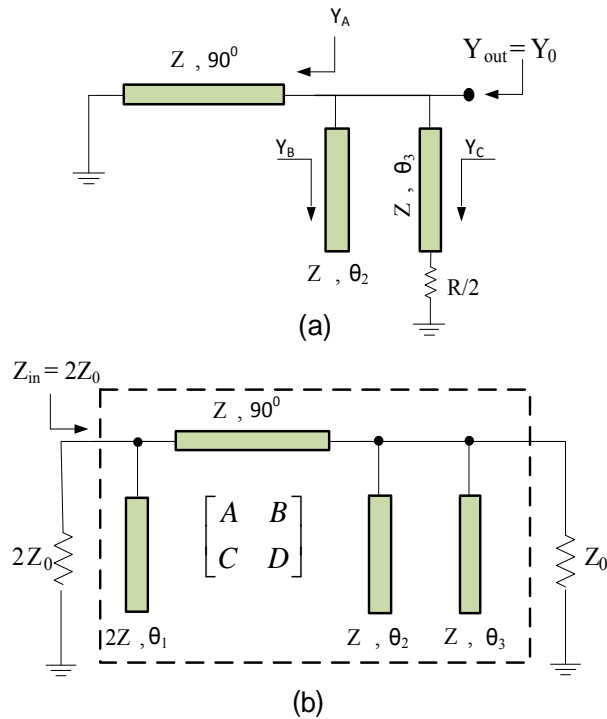
Fig. 2. Half-circuit of the proposed power divider for the (a) odd mode and the (b) even mode.

III. IMPLEMENTATION AND RESULTS

To demonstrate the proposed circuit, a power divider with a center frequency fixed at 1.65 GHz for harmonics suppression was designed and implemented, as shown in Fig. 3. It was fabricated on an RT/Duorid 5880 substrate with a relative permittivity of 2.2, thickness of 0.381 mm and loss tangent of 0.0009. The overall dimension of the circuit was about 24 mm × 16 mm (384 mm^2), which demonstrates a 35% size reduction compared to the conventional microstrip Wilkinson power divider with the same center frequency. The S-parameters were measured using an Agilent N5230A network analyzer. Figure 4 illustrates the simulated and measured S_{21} as a function of frequency.
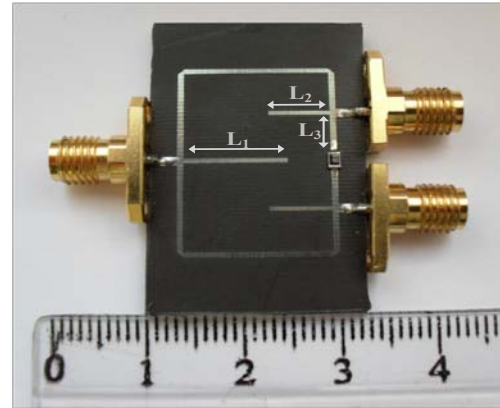

Fig. 3. Photograph of the fabricated power divider.
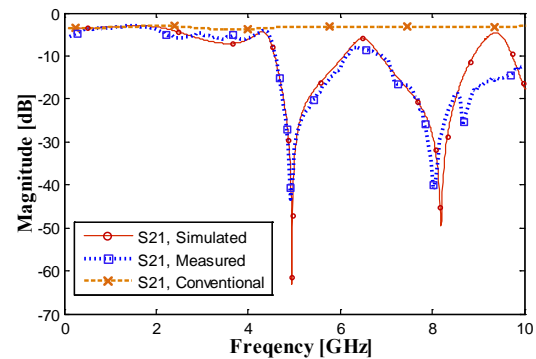
Fig. 4. Measured and simulated insertion loss of power divider for the 3rd and 5th harmonics suppression mode.

The simulations were performed using ADS (advanced design system by Agilent technologies). From the measured results, it can be found that the power divider passes the 1.65 GHz fundamental signal and suppresses the 4.95 GHz third-order harmonic and the 8.25 GHz fifth-order harmonic, simultaneously. From Fig. 4, the insertion loss at 1.65 GHz is 0.1 dB, the suppression for the third- and fifth-order harmonics are 43 dB and 41 dB, respectively. However, the measured S-parameter is shifted from 8.25 GHz to 8 GHz for the fifth-order harmonic suppression. This error is due to the high-frequency parasitic effect [3].

The S_{21} response of the conventional Wilkinson power divider is also shown in Fig. 4. From the simulated and measured results, as shown in Fig. 5, the circuit provides good input return loss. The measured S_{11} is about 31 dB at the operation frequency of 1.65 GHz. Figure 6,

demonstrates the simulated and measured output return loss. As seen from Fig. 6, the measured S_{22} is better than 51 dB at the operation frequency of 1.65 GHz.

Therefore, the designed circuit is well matched to the input and two output ports. In Fig. 7, the simulated and measured isolations of the two output ports are shown.
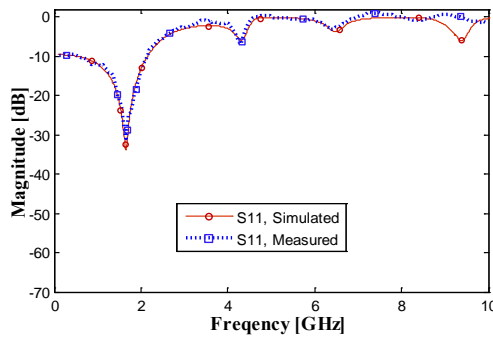

Fig. 5. Measured and simulated input return loss of power divider for the 3rd and 5th harmonics suppression mode.

The measured isolation between ports 2 and 3 is better than 43 dB. A comparison of the power dividers for the nth harmonics suppression is summarized in Table 1. As the results show, this work presents significant third- and fifth-order harmonic suppressions as compared to the reported works. The most significant advantage of this structure is that only by changing the dimensions of θ_1 and θ_2, it can suppress each two desired harmonics. With $\theta_1 = 45°$ ($L_1 = 15.3$ mm) and $\theta_2 = 22.5°$ ($L_2 = 7.6$ mm), 2nd and 4th harmonics are suppressed.
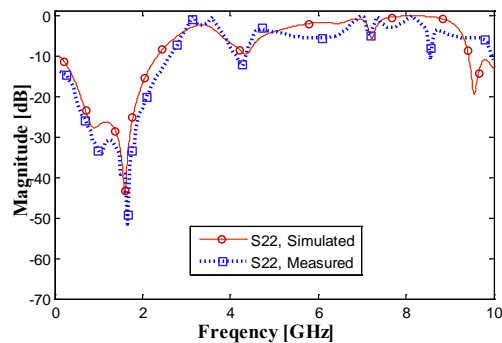

Fig. 6. Measured and simulated output return loss of power divider for 3rd and 5th harmonics suppression mode.
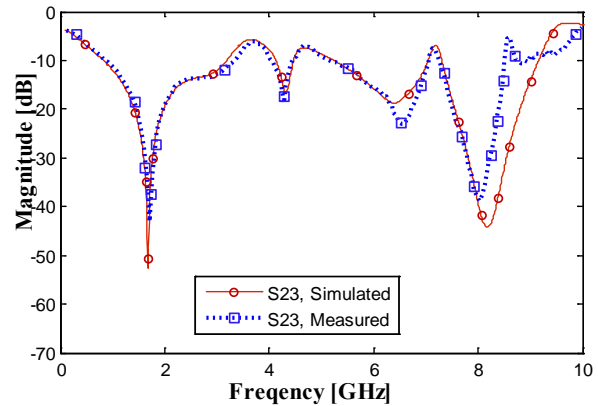

Fig. 7. Measured and simulated isolation of power divider for 3rd and 5th harmonics suppression mode.

Moreover, 3rd and 4th harmonics suppression is achieved with $\theta_1 = 30°$ ($L_1 = 10.2$ mm) and $\theta_2 = 22.5°$ ($L_2 = 7.6$ mm). With $\theta_1 = 45°$ ($L_1 = 15.3$ mm) and $\theta_2 = 30°$ ($L_2 = 10.2$ mm), after fine adjustment 2nd and 3rd harmonics suppression is occurred as shown in Fig. 8. The power divider passes the same fundamental signal (1.65 GHz) and suppresses the 3.3 GHz second-order harmonic and the 4.95 GHz third-order harmonic, simultaneously. The simulated S_{21} parameter at 1.65 GHz shows a power split of 3.04 dB. Furthermore, over than 70 dB suppression for the second- and third-order harmonic is obtained. Figure 9 shows that the isolation between the two ports, which is over 34 dB and the output return loss is more than 36 dB.
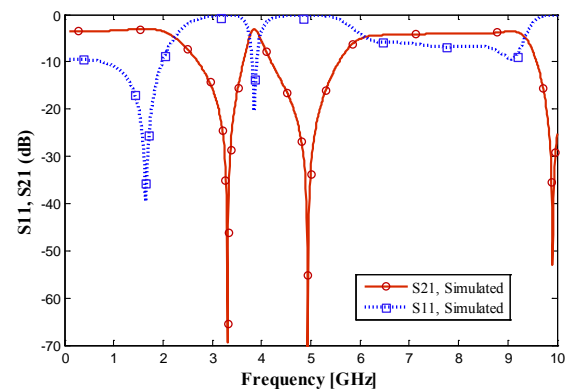

Fig. 8. The simulated results of S_{11}, S_{21} for 2nd and 3rd harmonics suppression mode.
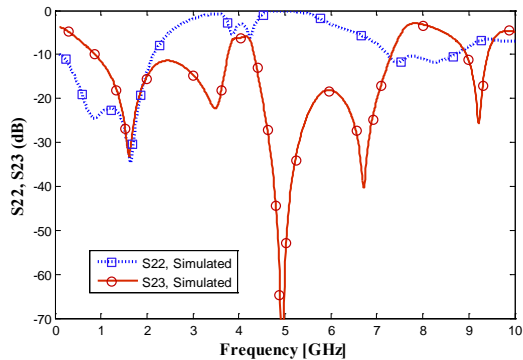
Fig. 9. Simulated results of S_{22} and S_{23} for 2nd and 3rd harmonic suppression modes.

Table 1: Performance comparison of the proposed power divider with other works.

Ref.	Freq.	Nth Harmonics Suppression	
[3]	2.4 GHz	3rd	32.5 dB
		5th	12 dB
[4]	1.8 GHz	2nd	26 dB
		3rd	25 dB
[5]	2.65 GHz	2nd	30 dB
		3rd	18 dB
[6]	1.25 GHz	2nd	17 dB
		3rd	25 dB
		4th	22 dB
[7]	1.5 GHz	2nd	18 dB
		3rd	15 dB
[11]	2.4 GHz	3rd	46 dB
		5th	37 dB
[20]	2.05 GHz	3rd	44 dB
[21]	0.9 GHz	2nd	13 dB
		3rd	35 dB
[22]	2.4 GHz	2nd	20 dB
		3rd	40 dB
[23]	1.5 GHz	3rd	37 dB
This Works	**1.65 GHz**	**3rd**	**45 dB**
		5th	**43 dB**

IV. CONCLUSION

A new Wilkinson power divider with novel structure for harmonics suppression is designed, simulated, and measured. This structure enables the power divider to work as harmonics suppresser with capability of suppressing each two desired harmonics. The proposed power divider with such performance can answer the demands of modern communication systems.

REFERENCES

[1] Z. Sun, L. Zhang, Y. Liu, and X. Tong, "Modified Gysel power divider for dual-band aApplications," *IEEE Microw. Wireless Compon. Lett.*, vol. 21, pp.16-18, 2011.

[2] J. C. Chiu, C. P. Chang, M. P. Houng, and Y. H. Wang, "A 12–36 GHz PHEMT MMIC balanced frequency tripler," *IEEE Microw. Wireless Compon. Lett.,* vol. 16, pp.19-21, 2006.

[3] C. M. Lin, H. H. Su, J. C. Chiu, and Y. H. Wang, "Wilkinson power divider using microstrip EBG cells for the suppression of harmonics," *IEEE Microw. Wireless Compon. Lett.*, vol. 17, pp. 700-702, 2007.

[4] F. Zhang and C. F. Li, "Power divider with microstrip electromagnetic bandgap element for miniaturisation and harmonic rejection," *Electron. Lett.,* vol. 44, pp. 422-424, 2008.

[5] C. F. Zhang, "Miniaturized and harmonics-rejected slow-wave branch-line coupler based on microstrip electromagnetic bandgap element," *Microw. Opt. Technol. Lett.*, vol. 51, pp. 1080-1084, 2009.

[6] C. F. Zhang, "planar rat-race coupler with microstrip electromagnetic band gap element," *Microw. Opt. Technol. Lett.*, vol. 53, pp. 2619-2622, 2011.

[7] D. J. Woo and T. K. Lee "Suppression of harmonics in Wilkinson power divider using dual-band rejection by asymmetric DGS," *IEEE Trans. Microw. Theory Tech.,* vol. 53, pp. 2139-2144, 2005.

[8] Y. Xu, S. H. Gong, and Y. Guan, "Coaxially fed microstrip antenna for harmonic suppression," *Electron. Lett.,* vol. 48, pp. 895-896, 2012.

[9] H. W. Liu, R. Cao, W. Hu, and M. Wu, "Harmonics suppression of Wilkinson power divider using spurlines with adjustable rejection bands," *IEEE MTT-S. Symposium Dig.,* Atlanta, pp. 189-192, 2008.

[10] J. Y. Shao, S. C. Huang, and Y. H. Pang, "Wilkinson power divider incorporating quasi-elliptic filters for improved out-of-band rejection," *Electron. Lett.,* vol. 47, pp. 1288-1289, 2011.

[11] Z. Zhang, Y. C. Jiao, and Z. B. Weng, "Design of 2.4 GHz power divider with harmonic

suppression," *Electron. Lett.,* vol. 48, pp. 705-707, 2012.

[12] M. Gil, J. Bonache, and F. Martin, "Synthesis and applications of new left handed microstrip lines with complementary split-ring resonators etched on the signal strip," *IET Microw. Antennas Propag.*, vol. 2, pp. 324-330, 2008.

[13] D. Hawatmeh, K. A. Shamaileh, and N. Dib, "Design and analysis of multi-frequency Unequal-split Wilkinson power divider using non-uniform transmission lines," *Appl. Comp. Electro. Society (ACES) Journal*, vol. 27, pp. 248-255, 2012.

[14] K. A. Shamaileh, A. Qaroot, N. Dib, and A. Sheta, "Design of miniaturized unequal split Wilkinson power divider with harmonics suppression using non-uniform transmission lines," *Appl. Comp. Electro. Society (ACES) Journal*, vol. 26, pp. 530-538, 2011.

[15] V. K. Velidi, A. Pal, and S. Sanyal, "Harmonics and size reduced microstrip branch-line baluns using shunt open-stubs," *Int. J. RF Microwave Comput. Aided Eng.,* vol. 21, pp. 199-205, 2011.

[16] D. H. Lee, Y. B. Park, and Y. Yun, "Highly miniaturised Wilkinson power divider employing pi-type multiple coupled microstrip line structure," *Electronic Letters*, vol. 42, pp. 763-765, 2006.

[17] C. H. Tseng and C. H. Wu, "Compact planar Wilkinson power divider using pi-equivalent shunt-stub-based artificial transmission lines," *Electron. Lett.,* vol. 46, pp. 1327-1328, 2010.

[18] D. M. Pozar, *Microwave Engineering*, Wiley, New York, 2005.

[19] K. M. Cheng and W. C. Ip, "A novel power divider design with enhanced spurious suppression and simple structure," *IEEE Trans. Microw. Theory Tech.,* vol. 58, pp. 3903-3908, 2010.

[20] K. H. Yi and B. Kang, "Modified Wilkinson power divider for nth harmonic suppression," *IEEE Microw. Wireless Compon. Lett.,* vol. 13, pp. 178-180, 2003.

[21] J. Yang, C. Gu, and W. Wu, "Design of novel compact coupled microstrip power divider with harmonic suppression," *IEEE Microw. Wireless Compon. Lett.,* vol. 18, pp. 572-574, 2008.

[22] J. Z. Gu, X. J. Yu, and X. W. Sun, "A compact harmonic-suppressed Wilkinson power divider using C-SCMRC resonators," *Microw. Opt. Technol. Lett.*, vol. 48, pp. 2382-2384, 2006.

[23] J. -S. Kim, M. -J. Park, and K. -B. Kong, "Modified design of Wilkinson power divider for harmonic suppression," *Electronics Letters*, vol. 45, pp. 1174-1175 2009.

Mohsen Hayati received the B.Eng. in Electronics and Communication Engineering from Nagarjuna University, India, in 1985, and the M.Eng. and PhD in Electronics Engineering from Delhi University, Delhi, India, in 1987 and 1992, respectively. He joined the Electrical Engineering Department, Razi University, Kermanshah, Iran, as an assistant professor in 1993. At present, he is an associate professor with the Electrical Engineering Department, Razi University. He has published more than 120 papers in international and domestic journals and conferences. His current research interests include a Microwave and millimeter wave devices and circuits, application of computational intelligence, artificial neural networks, fuzzy systems, neuro-fuzzy systems, electronic circuit synthesis, modeling and simulations.

Saeed Roshani received the B.Eng. in Razi University, Kermanshah, Iran, in 2008, M.Eng. in Electrical Engineering in 2011, Shahed University, Tehran, Iran. He is currently working towards the Ph.D. degree in Electrical Engineering at the Razi University and he joined the Electrical Engineering Department, Islamic Azad University of Kermanshah, Iran, in 2012. His research interest includes the low-power and low-size integrated circuit design, Microwave and millimeter wave devices and circuits.

A Linear-to-Circular Polarizer Using Split Ring Resonators

Juan Chen and Anxue Zhang

The Key Laboratory for Physical Electronics and Devices of the Ministry of Education,
Xi'an Jiaotong University, Xi'an, Shanxi, 710049, China
chenjuan0306@yahoo.com.cn

Abstract ─ A transmission polarizer with one layer of splitting ring resonator to realize a linear-to-circular polarization rotator is presented. Based on the accurate design of anisotropic metamaterials, high conversion efficiency and 8 % frequency band are achieved. Microwave experiments were performed to realize these ideas successfully and results are in excellent agreement with numerical simulations.

Index Terms ─ Circularly polarized, linearly polarized, metamaterial, polarizer, and split ring resonators.

I. INTRODUCTION

Polarization is an important characteristic of electromagnetic (EM) waves and is often utilized in microwave and optical systems. It is always desirable to have full control of polarization in transmission and reflection of waves. Conventional methods to manipulate polarization include using optical gratings, dichroic crystals, or employing the Brewster and birefringence effects [1, 2]. Recently, metamaterials have been proposed to manipulate EM wave polarizations [3-8]. Metamaterials have drawn much attention recently due to its many fascinating properties, such as the negative refraction, the in-phase reflection, and the axially frozen modes, etc [9, 10]. A metamaterial reflector has been employed to manipulate the polarization state of an incident EM wave [6]. A near-complete cross polarization conversion has been achieved with anisotropic metamaterials. It is duo to the reflection phase difference in the two orthogonal polarizations. The disadvantage of the reflector polarizer is that the incoming and outgoing waves are difficult to separate. To overcome this, a metamaterial

transmission polarizer has been proposed [7]. It can complete conversions from a linear polarization to a circular polarization and to its cross linear polarization effectively. Compared to the reflector polarizer, the incoming and outgoing waves in the transmission polarizer are naturally well separated, and therefore do not interfere with each other. However, in the transmission polarizer, it needs two (for the liner-to-circular polarizer) or four (for the liner-to-liner polarizer) pieces of substrate fixed with certain spacing. These substrates bring many reflections, which make the transmission efficiency of the polarizer restricted. Another alternative approach to the polarization conversion is by using a bilayered chiral metamaterials [8]. It is composed of a substrate coated on both surface with some enantiomeric patterns. In this polarization rotator, a 90° polarization rotation with high polarization conversion efficiency is obtained, but the bandwidth is only about 3 %.

In this paper, we propose a new transmission polarizer in which only one layer of splitting ring resonator (SRR) is fabricated. It completes the conversion from a linearly polarized wave to a circularly polarized wave successfully. The transmission efficiency of the polarizer can be controlled and the frequency band is extended to about 8%. Microwave experiments were performed and the results are in agreement with numerical simulations. Both the results of the simulations and the experiments show that highly efficient conversion from a linear polarization to a circular polarization has been accomplished.

II. NUMERICAL ANALYSIS

Figure 1 (a) shows the schematic diagram of one unit cell of the present polarizer. The

dimension of the unit cell is 11×11 mm^2. The dielectric constant of the substrate is $\varepsilon_r = 2.65$ and its thickness t is 1 mm. The SRR with 0.1 mm thick is coated on one side of the substrate. Both the length l and width w of the SRR are 9 mm. The width of the wires is $w_1 = 0.75$ mm. The air gap g between two adjacent cut-wires is 1.2 mm. The incident wave $\vec{E}^{in}$ normally impinged on the sample can be decomposed into two modes with the electric fields along the x axis and the y axis ($\vec{E}^{in} = \hat{x}E_x^{in} + \hat{y}E_y^{in}$, as shown in Fig. 1 (b)). The incident wave is linearly polarized with,

$$\left|E_x^{in}\right| = \left|E_y^{in}\right| \tag{1}$$

$$\arg\left(E_x^{in}\right) = \arg\left(E_y^{in}\right). \tag{2}$$

(a)

(b)
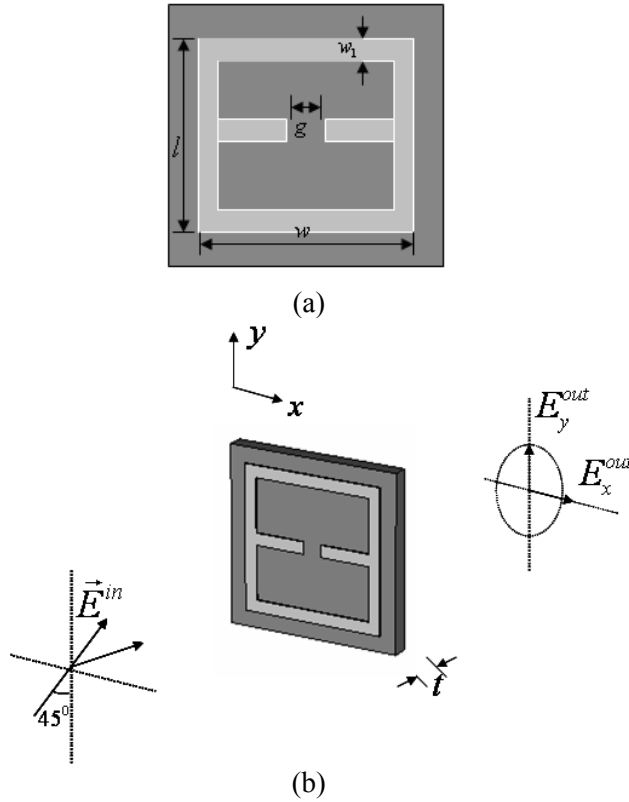
Fig. 1. (a) Unite cell of the polarizer and (b) the schematic picture of the polarization state of the incident and transmitted waves.

The transmitted wave is $\vec{E}^{out} = \hat{x}E_x^{out} + \hat{y}E_y^{out}$. For the two wave modes, the transmission coefficients T_x and T_y are defined as,

$$T_x = \left|E_x^{out}\right|/\left|E^{in}\right| \tag{3}$$

$$T_y = \left|E_y^{out}\right|/\left|E^{in}\right|. \tag{4}$$

The axial ration p and phase difference of the transmitted wave are defined as [11],

$$p = 20\log\left(\left|E_x^{out}\right|/\left|E_y^{out}\right|\right) \tag{5}$$

$$phase\ difference = \left|\arg\left(E_x^{out}\right) - \arg\left(E_y^{out}\right)\right|, \tag{6}$$

when $p = 0$ and $phase\ difference = \pi/2$, the transmitted wave becomes circularly polarized wave. The transmission coefficients T_x and T_y represent the conversion efficiency of the polarizer. If we are able to control T_x and T_y to be close to -3 dB, nearly all the energy will be transmitted and no wave will be reflected.

We use the commercial software CST Microwave Studio to simulate the unite cell shown in Fig. 1. The SRR is modeled as perfect electrically conducting material. Along the x and y axes, periodic boundary conditions are applied. The calculated transmission coefficients and the axial ratio of the transmitted wave are shown in Fig. 2 (a). It can be seen from this figure that both the transmission coefficients of T_x and T_y are close to -3 dB in the frequency range 12 GHz - 13 GHz, which is a direct evidence of small loss and little reflections of the polarizer. The axial ratio of the transmitted wave is below 2 dB in this frequency range. Meanwhile, an obvious zero value in the axial ratio can be observed around 12.6 GHz, which indicates that the two wave modes of the transmitted waves have equal amplitudes. The phases of the two modes of the transmitted wave obtained using CST calculations are shown in Fig. 2 (b). The phase difference between the E_x^{out} and E_y^{out} is also shown in the same figure. It can be seen from this figure that in the frequency range of 12 GHz - 13 GHz near 90° phase difference in the two orthogonal components is achieved. These simulated results confirm a fact that in the frequency range of 12 GHz - 13 GHz the linearly polarized wave is conserved to a circularly polarized wave by the transmission polarizer. The bandwidth can reach to 8 %.

The conversion efficiency (defined as $\sqrt{\left(E_x^{out}\right)^2 + \left(E_y^{out}\right)^2}/E^{in}$) is plotted in Fig. 3. It

can be seen from this figure that the conversion efficiency of the polarizer exceeds 99 % in the frequency range of 12 GHz - 13 GHz and reaches its maximum value at around 12.6 GHz, which shows that highly efficient conversion from a linearly polarized wave to a circularly polarized wave has been accomplished.


(a)

(b)
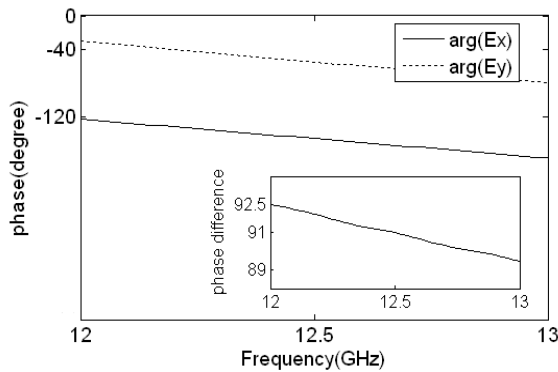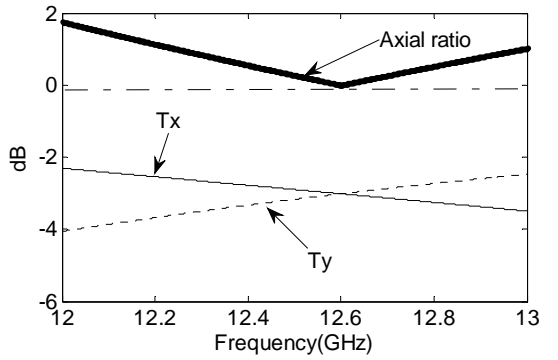
Fig. 2. (a) The simulated transmission and axial ration of the transmitted wave and (b) the simulated phase difference of the two wave modes of the transmitted wave.
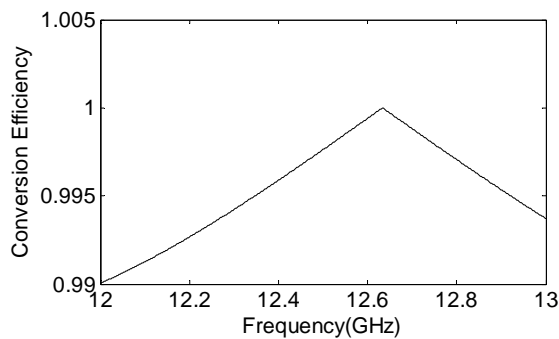

Fig. 3. The conversion efficiency of the polarizer.

III. EXPERIMENT VALIDATION

In order to confirm this expected behavior experimentally, we have fabricated a sample composed of 30×30 unit cells (see Fig. 4 (a)). The picture of the experimental setup is shown in Fig. 4 (b). The reflection and transmission waves were measured using a pair of horn antennas connected to the vector network analyzer (Agilent E83638). The horns antennas was fixed on a fixator, which had angle calibration to ensure that horn alignments were at the exact angles. The electric field of the transmitting antenna was polarized to the direction illustrated in Fig. 1 (b), which had a 45° angle with respect to the vertical direction, so that the electric fields of the two modes for incident waves were related by $|E_x^{in}| = |E_y^{in}|$ and arg $(E_x^{in}) = $ arg (E_y^{in}) and. A calibration was conducted by removing the sample and having the receiving antenna aligned at the same direction with the transmitting antenna. Then we rotated the receiving antenna from 0° to 90° to achieve the E_x^{out} and E_y^{out} of the transmitted wave. All the measurements were performed in an anechoic chamber.


(a)
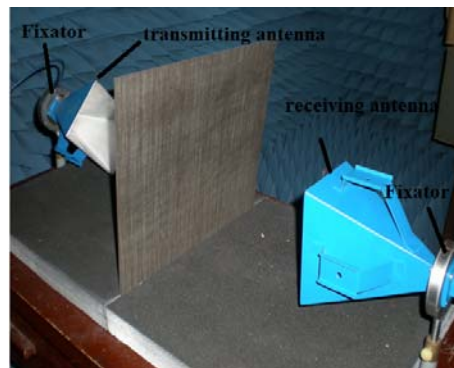
(b)

Fig. 4. (a) The top view of the fabricated sample and (b) the picture of the experimental setup.

The measured axial ratio of the electric field is shown in Fig. 5 (a). For circular polarization, the amplitude of the electric field is supposed to be invariant and in our measurement the variation is less than 2 dB. The measured phase difference between the E_x^{out} and E_y^{out} components is shown in Fig. 5 (b). It can be seen from this figure that the phase difference is also around 90°. For the sake of comparison, the simulated results of the axial ratio and phase difference are also plotted in Fig. 5. It can be seen from this figure that although the measured result deviates from the simulated result in some frequencies (in fact, it revolves around the simulation result), it also indicates a fact that a full conversion from a linearly polarized wave to a circularly polarized wave is achieved. The deviations between the simulated value and the measured result are mainly due to the fact that, in the simulated model, the unit cells are periodically arranged and the substrate is infinite, while, in the experiment, the sample is composed of 30 × 30 unit cells and its size is only 33 × 33 cm^2, which is slightly larger than the aperture of the horn antenna. The small size of the sample results is due to the fact that some diffracted wave from the transmitting antenna reaches the receiving antenna directly. If we increase the size of the sample, the deviation between the simulated value and the measured result will be reduced.

IV. THE APPLICATION OF THE POLARIZER TO A HORN ANTENNA

To demonstrate the function of the metamaterial as a circular polarizer, we integrate the polarizer to a conventional horn antenna. The aperture of the horn antenna is 19.05 mm × 9.525 mm. It radiates a linearly polarized wave at 12.6 GHz. We arrange the structure periodically on the aperture of the antenna, as shown in Fig. 6. The horn needs to be rotated 45° to the x-axis to make sure that the electronic field has the same component along the x and y directions.

The simulated normalized radiation pattern of the integrated horn antenna is shown in Fig. 7. The simulation frequency is 12.6 GHz. For the sake of comparison, the radiation pattern of the conventional horn antenna is also plotted in this figure. It can be seen from this figure that the

novel integrated horn has almost the same gain with the conventional horn, but it radiates a left handed circularly polarized (LHCP) wave. The gain-difference between the LHCP wave and the right handed circularly polarized (RHCP) wave of the integrated horn is 21.9 dB in the E-plane, and 20.3 dB in the H-plane.


(a)

(b)
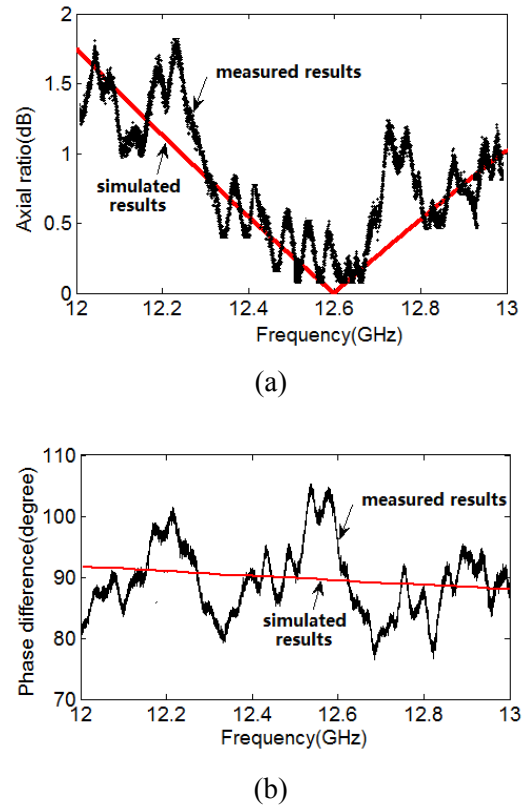
Fig. 5. (a) The measured axial ration of the transmitted wave and (b) the measured phase difference of the transmitted wave.
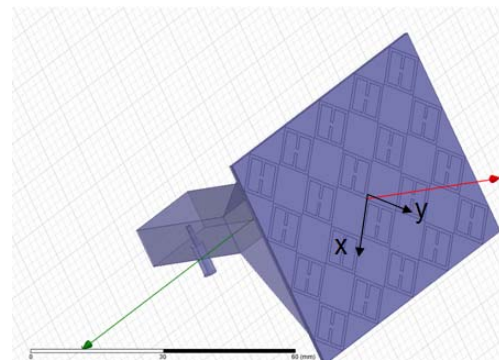

Fig. 6. The schematic picture of the polarizer integration to a horn antenna.

(a)

(b)
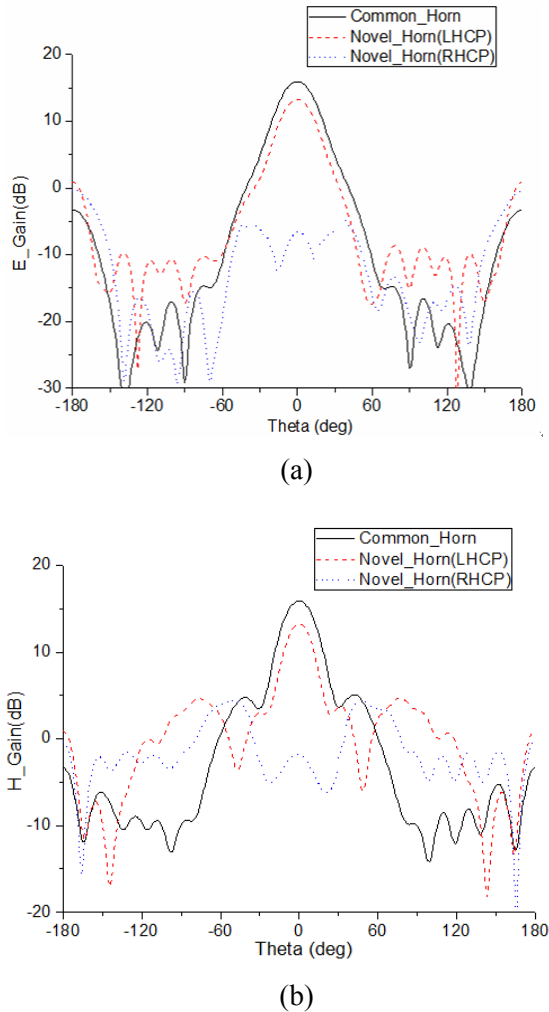
Fig. 7. (a) The simulated radiation patterns in the E-plane at 12.6 GHz and (b) the simulated radiation patterns in the H-plane at 12.6 GHz.

The simulated axial ratio of the integrated horn in both E- and H-planes are shown in Fig. 8. The axial ratio is bellow 3 dB from about -10° ~10° at 12.6 GHz and the 3 dB angle band covers the main lobe. The results in the presented simulations demonstrate the function of the metamaterial as a circular polarizer. It can turn a conventional horn antenna, which radiate linearly polarized wave into a circularly polarized antenna.

V. CONCLUSION

This paper presents a new transmission polarizer with one layer of SRR to realize a linear-to-circular polarization rotator. Both the simulated and the measured results show that highly efficient conversion is achieved. Due to its thin thickness and high polarization conversion efficiency, the present polarizer may have potential applications in many situations and will find broad applications in various radio frequency and optical devices.
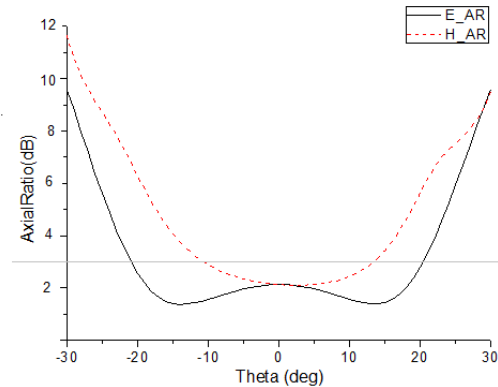

Fig. 8. The axis ratio of the circular polarized horn at 12.6 GHz.

REFERENCES

[1] M. Born and E. Wolf, *Principles of Optics,* Cambridge University Press, Cambridge, England, 1999.

[2] J. B. Pendry, A. J. Holden, D. J. Robbins, and W. J. Stewart, "Magnetism from conductors and enhanced nonlinear phenomena," *IEEE Trans. Microwave and Theory Tech.,* vol. 47, no. 11, pp. 2075-2084, Nov. 1999.

[3] J. Y. Chin, L. Mingzhi, and C. Tie Jun, "A transmission polarizer by anisotropic metamaterials," *IEEE Antennas and Propagation Society International Symposium, APS,* pp. 1-4, 2008.

[4] X. L. Ma, C. Huang, M. B. Pu, C. G. Hu, Q. Feng, and X. G. Luo, "Single-layer circular polarizer using metamaterial and its application in antenna," *Microwave and Optical Technology Letters,* vol. 54, pp. 1770-1774, 2012.

[5] J. Kaschke, J. K. Gansel, and M. Wegener, "On metamaterial circular polarizers based on metal N-helices," *Optics Express*, vol. 20, pp. 26012-26020, 2012.

[6] J. Hao, Y. Yuan, L. Ran, T. Jiang, J. A. Kong, C. T. Chan, and L. Zhou, "Manipulating electromagnetic wave polarizations by anisotropic metamaterials," *Physical Reviews letters*, vol. 99, no. 6, 063908, 2007.

[7] J. Y. Chin, M. Lu, and T. J. Cui, "Metamaterial polarizers by electric-field-coupled resonators," *Applied Physics Letters*, vol. 93, 251903, 2008.

[8] Y. Ye and S. He, "90° polarization rotator using a bilayered chiral metamaterial with giant optical activity," *Applied Physics Letters*, vol. 96, 203501, 2010.

[9] H. F. Ma and T. J. Cui, "Three-dimensional broadband ground-plane cloak made of metamaterials," *Nature Communications*, vol. 1, no. 21, June 2010.

[10] D. R. Smith and N. Kroll, "Negative refractive index in left-handed materials," *Physical Reviews letters*, vol. 85, no. 14, pp. 2933-2936, 2000.

[11] B. E. A. Saleh and M. C. Teich, *Fundamentals of Photonics*, John Wiley & Sons. Inc., Hoboken, New Jersey, 2007.

Compact Microstrip Lowpass Filter with Wide Stopband and Sharp Roll-off using Triple Radial Stubs Resonator

M. Hayati [1,2], H. AL. Memari [1], and H. Abbasi[1]

[1] Electrical Engineering Department, Faculty of Engineering, Razi University,
Tagh-E-Bostan, Kermanshah-67149, Iran
Mohsen_Hayati@yahoo.com

[2] Computational Intelligence Research Center, Faculty of Engineering, Razi University
Tagh-E-Bostan, Kermanshah-67149, Iran
Mohsen_Hayati@yahoo.com

Abstract ─ A novel microstrip lowpass filter with good specifications such as sharp cutoff, wide stopband, low insertion loss, and high return loss is proposed. The proposed lowpass filter is realized using triple radial stubs resonator, i.e., three 60° radial stubs and harmonic attenuator, i.e., T shaped cell loaded by the semicircle. The cutoff frequency of the proposed filter is adjusted to 1.39 GHz. The transition band is approximately 0.21 GHZ from 1.39 GHz to 1.6 GHz with corresponding attenuation levels of -3 dB and -20 dB. The stopband with better than -20 dB rejection is from 1.6 GHz to 12.36 GHz, insertion loss in the passband is less than 0.1 dB, return loss is less than -25 dB and the overall size of the filter is $0.0074\ \lambda g^2$ ($15 \times 12.3\ mm^2$). The proposed filter is fabricated and measured. The simulation and measurement results are in good agreement.

Index Terms ─ Lowpass filter, microstrip, radial stub, sharp roll-off, and wide stopband.

I. INTRODUCTION

Due to increasing constraint of reduction in size with optimum performance such as sharp cut-off, wide stopband, low insertion loss, and high return loss designs of lowpass filters are done with different methods. The sharp cut-off shows a sharper transition band, which indicates the higher selectivity; wide stopband shows the band with more than -20 dB harmonic suppression; low insertion loss shows high passing signals in the passband and high return loss refer to low return signals in the passband.

The conventional filter design method is normally not used, due to inherited deficiencies like the slow roll-off, poor frequency response in the passband and narrow stopband [1]. The Radial patches are presented in [2], which has good specification such as sharp roll-off and wide stopband, but the return loss in the pass band and the size of the filter is not satisfactory. A compact LPF using front coupled tapered compact microstrip resonator cell (FCTCMRC) is presented in [3], which despite the small size, neither the passband performance nor the stopband widths are good. Another method is to use complementary split ring resonators [4], which present sharp response and compact size, but fabrication of this structure because of its 3D configuration is difficult. A LPF with wide stopband using coupled line hairpin unit is demonstrated in [5]. In this filter, the insertion loss and return loss in the passband and the attenuation level in the stopband is not adequate. Later, LPF with novel patch resonator in [6] has been presented, while this filter has large circuit size. New ultra wide stopband LPF using transformed radial stubs (TRS) is introduced and investigated in [7], which has bad return loss in both passband and stopband, and the insertion loss in the passband is not good. A new compact defected ground structure (DGS) lowpass filter using a crescent shape structure etched in the ground plan is introduced in [8]. This filter has a gradual roll-off and narrow stopband.

In this paper, a microstrip LPF having compact size, sharp roll-off, wide stopband, low insertion loss, and high return loss in the passband is presented.

II. FILTER DESIGN

The design process for the proposed filter is as follows:

1- Design of the proposed three 60° radial stub resonator to achieve sharp roll-off response and to eliminate harmonics that appear near the cutoff frequency.

2- Suppressing Cells design and its addition to the proposed resonator in order to extend the stopband.

3- Combination of the proposed resonator and suppressing the cell to have a LPF with a wide stopband, sharp response, and good passband performance.

A detailed description of these steps is presented.

A. Proposed resonator

The 180° radial stub resonator and its LC equivalent circuit are shown in Figs. 1 and 2, respectively. The capacitance of Cr in Fig.2 would be lumped capacitor or other circuit's capacitance like straight or radial stubs.
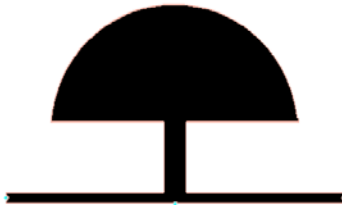

Fig. 1. The 180° radial stub resonator.
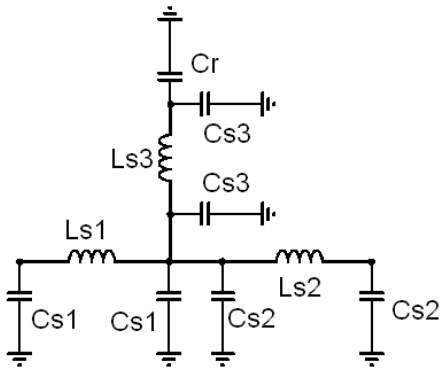
Fig. 2. LC equivalent circuit of the 180° radial stub resonator.

Figure 3 shows two types of capacitive elements, i.e., radial and straight stubs and their equivalent circuit. The parameter of the distributed stub section, which includes radial and the straight stubs of Fig. 3, can be modeled approximately as a lumped element.
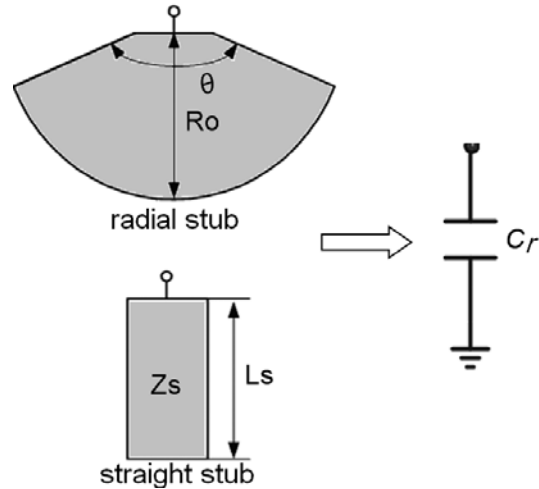

Fig. 3. Two types of capacitive elements and their model.

A distributed transmission line, when the effective electric length is less than a quarter wavelength, can be modeled as a lumped elements. The proposed three 60° radial stub is shown in Fig. 4. The simulated S-parameters of the proposed resonator with different dimension of W, L and, R are illustrated in Figs. 5, 6, and 7, respectively. As seen in Fig. 5, by increasing W from 0.1 mm to 0.5 mm with steps of 0.2 mm, the inductance of the resonator will be decreased, which makes the transmission zero move away from the lower frequency. Similarly, as shown in Fig. 6, when L increases from 10.5 mm to 12.5 mm with step of 1 mm, the inductance of the resonator will be increased, which result in moving the transmission zero to the lower frequency. As shown in Fig. 7, when R decreases from 3 mm to 2.2 mm with steps of 0.4 mm, the capacitance of the proposed resonator decreases so the cutoff frequency move to the higher frequency.
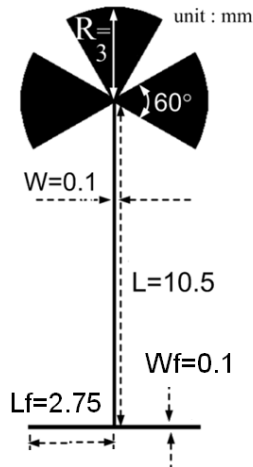
Fig. 4. The proposed three 60° radial stub resonator.
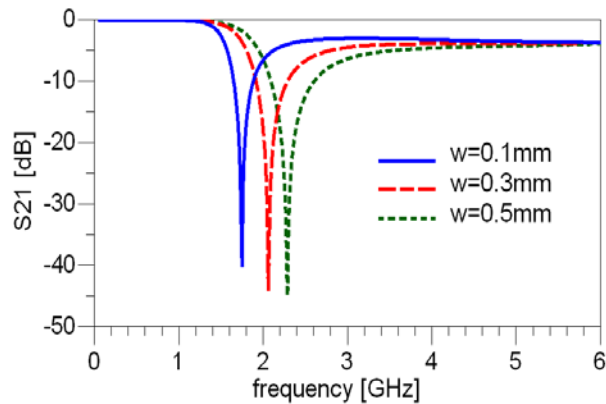
Fig. 5. Frequency response of the proposed resonator with different dimensions of W.
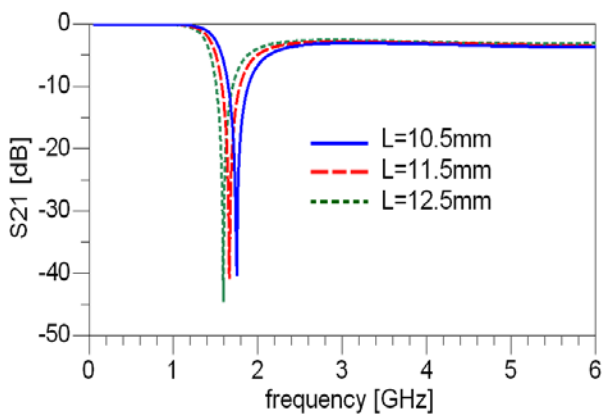

Fig. 6. Frequency response of the proposed resonator with different dimensions of L.
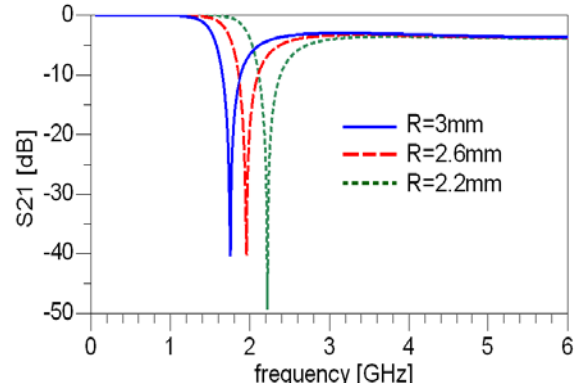

Fig. 7. Frequency response of the proposed resonator with different dimensions of R.

Frequency response of the proposed resonator with different dimensions of Lf is shown in Fig. 8. As it is seen, when Lf increases the suppression level increases without change in the location of the transmission zero. But increment of Lf result in the size increment. The decrement of Wf increment the inductance of the transmission line, which result in the increment of suppressing level as shown in Fig. 9. Therefore, the optimum value for Wf and Lf with respect to suppression level and filter size are selected.
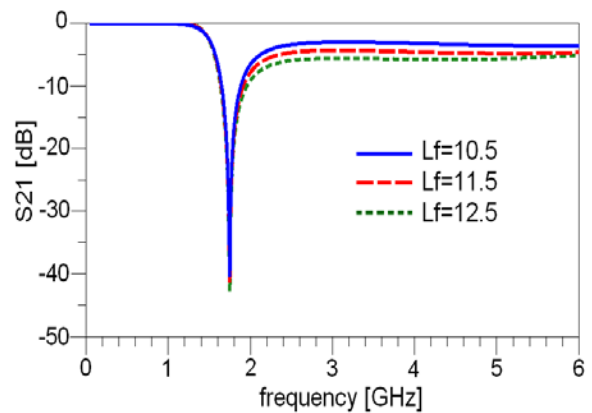
Fig. 8. Frequency response of the proposed resonator with different dimensions of Lf.

As seen in Fig. 10 the cut-off frequency of the proposed resonator is adjusted to 1.49 GHz and the transition band is approximately 0.2 GHz from 1.5 GHz to 1.7 GHz with corresponding attenuation levels of -3 dB and -20 dB. The dimensions of the proposed resonator are as follows: R = 3 mm, W = 0.1 mm, L = 10.5 mm, Lf = 2.75 mm, Wf = 0.1 mm.
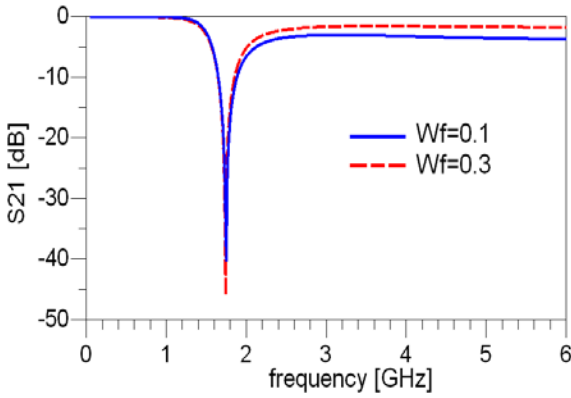
Fig. 9. Frequency response of the proposed resonator with different dimensions of Wf.
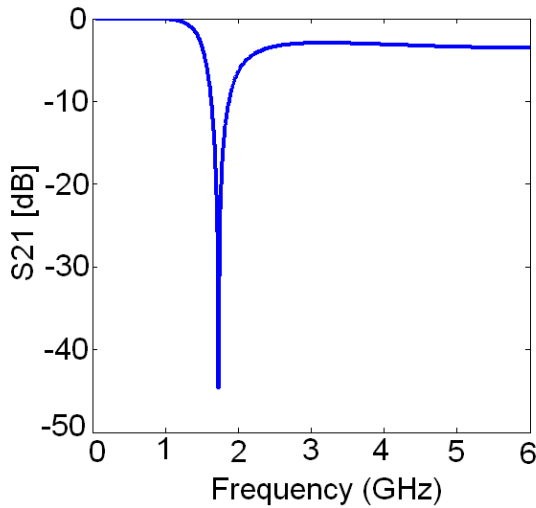

Fig. 10. The frequency response of the proposed three 60° radial stub resonator.

B. Suppressing cell design

To obtain a LPF with wide stopband, a suppressing cell to suppress the harmonics in the stopband is required. It is realized by a T shaped cell that is loaded by the semicircle. Figure 11 shows the single T shaped cell and T shaped cell loaded by the semicircle. Their frequency response is shown in Fig. 12. As it is seen from Fig. 12, when T shaped cell is loaded by the semicircle, the suppression level in the stopband is increased.

C. Proposed filter

To have a LPF with a wide stopband, sharp response and good passband performance, the

proposed suppressing cell and the proposed resonator are combined. The proposed filter and its frequency response are shown in Figs. 13 and 14, respectively.

T shaped cell

T shaped cell loaded by semicircle ended
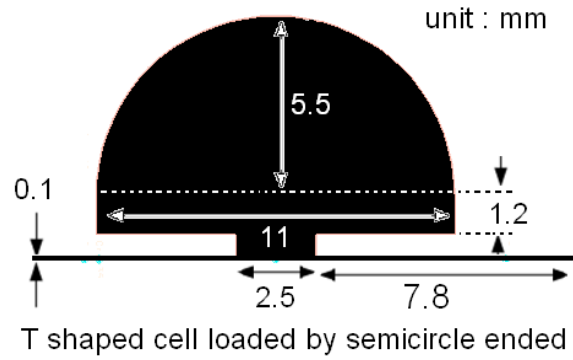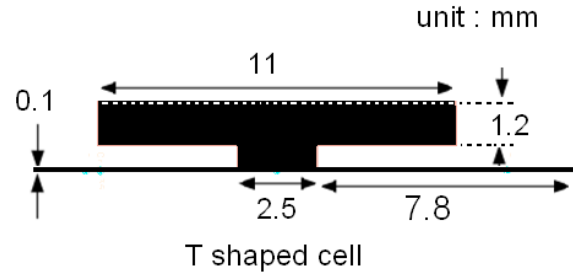
Fig. 11. The single T shaped cell and T shaped cell loaded by semicircle.
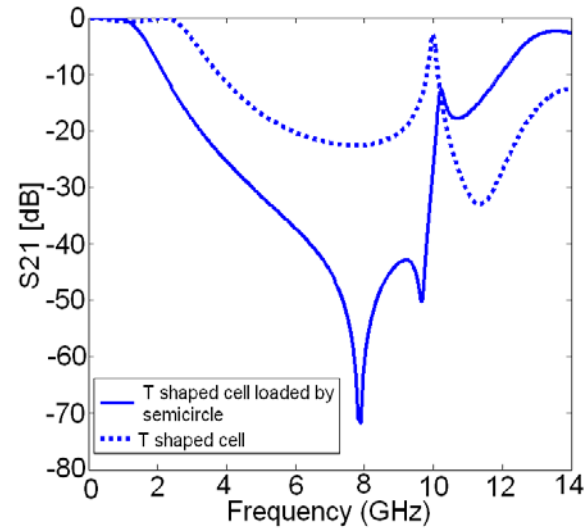
Fig. 12. Frequency response of the single T shaped cell and T shaped cell loaded by semicircle.

As shown in Fig. 15 when Lt is increased from 10.95 mm to 19.95 mm with steps of 3 mm, the stopband will be increased but the return loss and the insertion loss performance is decreased. Therefore, the optimum value for Lt with respect to its passband and stopband performance is selected.

The main transmission line in the proposed filter is bended, which results in size reduction. This work increases the inductance effect in the main transmission line, so the rejection level in the stopband is increased. Bending the transmission line has reduced the overall filter size by 52 % and increased the suppression level in the stopband. The proposed LPF with bended transmission line and its frequency response are shown in Figs. 16 and 17, respectively.
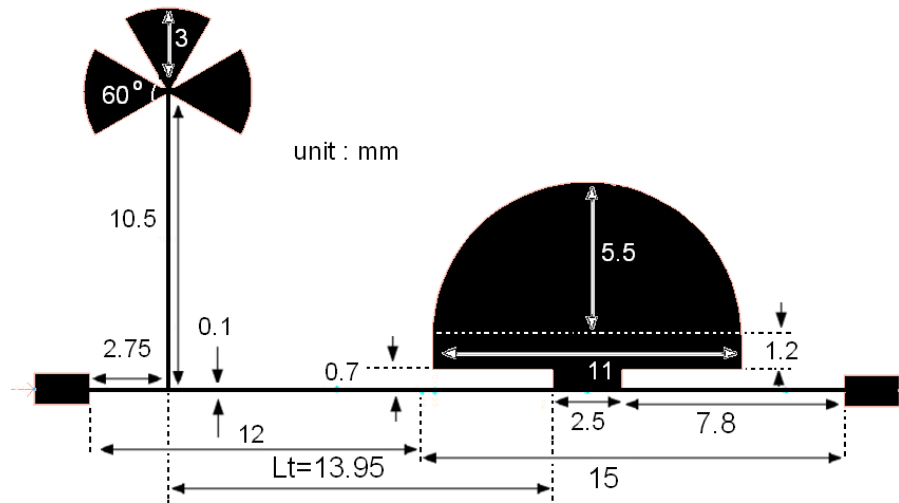
Fig. 13. The proposed filter in the straight form.
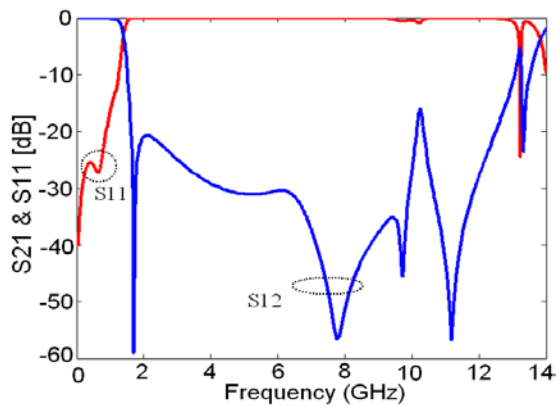
Fig. 14. Frequency response of the proposed filter in the straight form.
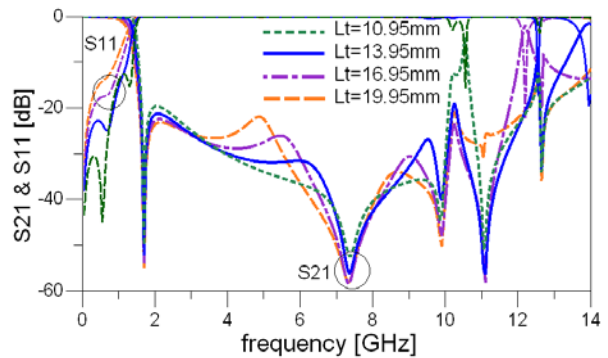
Fig. 15. Frequency response of the proposed filter in the straight form with different dimensions of Lt.
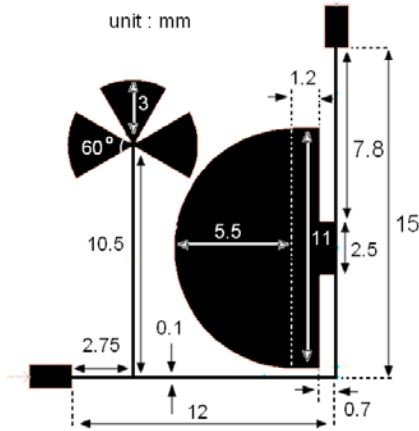
Fig. 16. The proposed filter in the bended form.
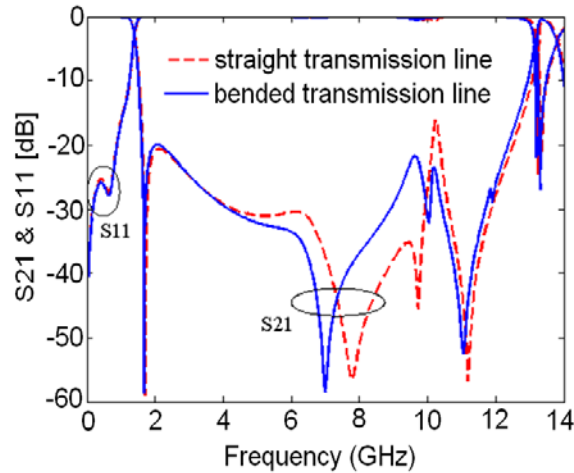
Fig. 17. Frequency response of the proposed filter in the both straight and bended form.

III. SIMULATION AND MEASUREMENT

The proposed LPF is designed and optimized using EM-simulator of ADS. The main transmission line has been bended, which results in size reduction. The microstrip LPF is fabricated on a substrate with dielectric constant of $\varepsilon_r = 2.2$, thickness of $h = 15$ mil and loss tangent equal to 0.0009. The source and the load of the structure have characteristic impedance of Z_0 equal to $50\,\Omega$ with width of 1.1 mm. The photograph and the simulated and measured results of the proposed filter are illustrated in Figs. 18 and 19, respectively. It is seen that the attenuation level in the stopband is higher than -20 dB, which is achieved from 1.6 GHz to 12.36 GHz and present

the wide stopband. The proposed filter has low insertion loss of less than 0.1 dB and return loss of more than 25 dB in the passband. The frequency response of the filter is very sharp with the transition band equal to 0.21 GHz from 1.39 GHz to 1.6 GHz with corresponding attenuation levels of -3 dB and -20 dB.
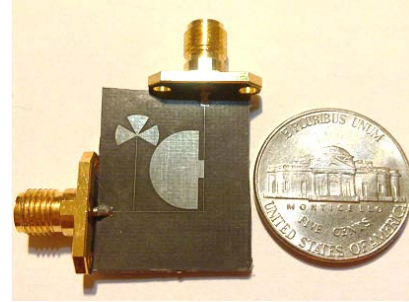
Fig. 18. The photograph of the proposed filter.
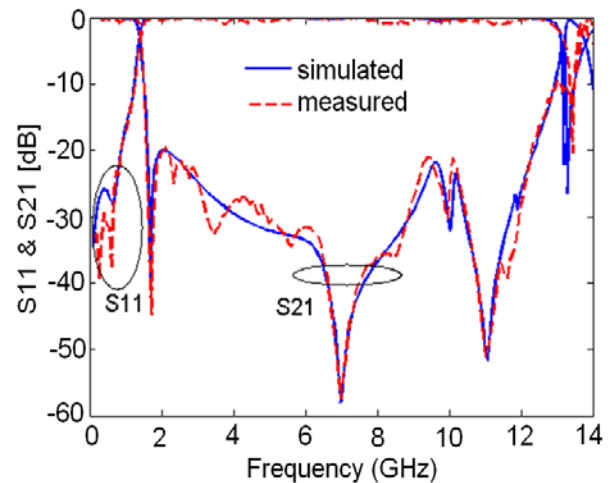
Fig. 19. The simulated and measured results of the proposed filter.

The performance comparison between the proposed LPF and other works is presented in Table 1, where ξ, RSB, NCS, SF, AF, FOM, RL, and IL correspond to the Roll-off rate, relative stopband width, normalized circuit size, suppressing factor, architecture factor, figure of merit, return loss, and insertion loss, respectively. These parameters are defined as follows:
Roll-off rate ξ is

$$\xi = \frac{\alpha_{max} - \alpha_{min}}{f_s - f_c}, \tag{1}$$

where α_{max} is the -20 dB attenuation point; α_{min} is the -3 dB attenuation point; f_s is the -20 dB stopband frequency, and f_c is the -3 dB cut-off frequency. Therefore, the high roll off rate shows a sharper transition band, which indicates the higher selectivity.

The relative stopband width (RSB) is

$$RSB = \frac{stopband \ (-20dB)}{stopband \ center \ frequency}, \quad (2)$$

where the high RSB shows the high stopband that is the band with more than -20 dB harmonic suppression.

The normalized circuit size (NCS) is

$$NCS = \frac{physical \ size \ (lenght \times width)}{\lambda_g^2}, \quad (3)$$

where the lower NCS indicates the size of the filter is compact. The suppressing factor (SF) is based on the suppression in the stopband and is calculated as,

$$SF = \frac{rejection \ level}{10}. \quad (4)$$

The architecture factor (AF) for a planar and 3-D structure is defined as 1 and 2, respectively. Finally, the figure of merit (FOM) is defined as,

$$FOM = \frac{\xi \times RSB \times SF}{NCS \times AF}. \quad (5)$$

The FOM shows the overall performance of a LPF, where the filter with compact size, sharp transition band, high suppression level, and high stopband leads to a high FOM.

Table 1: Performance comparison between the proposed LPF and other works.

Ref.	ξ	RSB	NCS	SF	AF	FOM	RL (dB)	IL (dB)
[2]	56.66	1.355	0.037	3	1	6099	11	0.1
[3]	35.5	0.71	0.028	2	1	1800	12	1
[5]	62.06	1.42	0.022	2	1	7978	16.3	0.5
[6]	30.35	1.35	0.055	2	1	1487	11.54	0.33
[7]	72	1.71	0.074	2.5	1	4159	12	1.5
Proposed filter	**80.95**	**1.59**	**0.0074**	**2**	**1**	**34550**	**25**	**0.1**

In the structure of the proposed filter, the three 60^0 radial stub resonator is used to control the transition band, which result in increasing roll-off rate (ξ) i.e., equal to 80.95. The stopband is extended to 12.36 GHz using T shaped cell loaded by semicircle as suppressing cell, so the RSB is increased. By bending the transmission lines the overall size of the filter is reduced to about 52 % that makes NCS to have a lower value among the referred filters. Finally, the comparison shows that the proposed filter has the best figure of merit (FOM), ξ, NCS, return loss (RL), and insertion loss (IL) among the referred filters.

IV. CONCLUSION

A microstrip LPF with good specifications such as sharp roll-off, wide stopband, low insertion loss, and high return loss is designed and optimized. The three 60° radial stubs resonator added to the T shaped cell loaded by the semicircle, results in sharp cutoff and wide stopband.   The measurement results are in good agreement with the simulation results, and the proposed filter has very high FOM in comparison with the other works that is presented in recent years. This Filter with such features is a good candidate for modern communication system.

REFERENCES

[1] J. S. Hong and M. J. Lancaster, *Microstrip Filters for RF/Microwave Applications*, New York: Wiley, 2001.

[2] J. L. Li, S. W. Qu, and Q. Xue, "Compact microstrip lowpass filter with sharp roll-off and wide stop-band," *Electron. Lett.*, vol. 45, no. 2, pp. 110-111, 2009.

[3] M. Hayati and A. Lotfi, "Compact lowpass filter with high and wide rejection in stopband using front coupled tapered CMRC," *Electron. Lett.*, vol. 45, no. 2, pp. 846-848, 2010.

[4] M. K. Mandal, P. Mondal, S. Sanyal, and A. Chakrabarty, "Low insertion-loss, sharp-rejection and compact microstrip low-pass filters," *IEEE Microw. and Wireless Compon. Lett.*, vol. 16, no. 11, pp. 600-602, Nov. 2006.

[5] V. K. Velidi and S. Sanyal, "Sharp roll-off lowpass filter with wide stopband using stub-loaded coupled-line hairpin unit," *IEEE Microw. Wireless Compon. Lett.,* vol. 21, no. 6, pp. 301-303, 2011.

[6] M. Hayati, A. Sheikhi, and A. Lotfi, "Compact lowpass filter with wide stopband using modified semi-elliptic and semi-circular microstrip patch resonator," *Electron. Lett.*, vol. 46, no. 22, pp. 1507-1509, Oct. 2010.

[7] K. Ma and K. S. Yeo, "New ultra wide stopband lowpass filter using transformed radial stubs," *IEEE Trans. Microw. Theory Tech.,* vol. 59, no. 3, pp. 604-611, 2011.

[8] M. Al Sharkawy, A. Boutejdar, F. Alhefnawi, and O. Luxor, "Improvement of compactness of lowpass/bandpass filter using a new electromagnetic coupled crescent defected ground structure resonators," *Appl. Comp. Electro. Society Journal (ACES)*, vol. 25, no. 7, July 2010.

Mohsen Hayati received the B.Eng. in Electronics and Communication Engineering from Nagarjuna University, India, in 1985, and the M.Eng. and PhD in Electronics Engineering from Delhi University, Delhi, India, in 1987 and 1992, respectively. He joined the Electrical Engineering Department, Razi University, Kermanshah, Iran, as an assistant professor in 1993. At present, he is an associate professor with the Electrical Engineering Department, Razi University. He has published more than 120 papers in international and domestic journals and conferences. His current research interests include microwave and millimeter wave devices and circuits, application of computational intelligence, artificial neural networks, fuzzy systems, neuro-fuzzy systems, electronic circuit synthesis, modeling and simulations.

Hessam Al-Din Memari was born in Kermanshah, Iran in 1985. He received the B.Sc. and M.Sc. degree in Electrical Engineering from the Razi University, Kermanshah, Iran. His research interests include design and analysis of the microstrip filters, and antennas.

Hamed Abbasi was born in Kermanshah, Iran in 1987. He received the B.Sc. in Electronics Engineering from the Islamic Azad University of the Kermanshah, Iran in 2008 and received the M.Sc. degree in Electrical Engineering from the Razi University, Kermanshah, Iran in July 2012. His research interests include design and analysis of the microstrip filters, couplers and antennas.

A Microstrip Printed Band-Notched UWB Antenna Using Modified CSRR Structure

Di Jiang, Yuehang Xu, and Ruimin Xu

School of Electronic Engineering University of Electronic Science and Technology of China,
Chengdu, China
merryjiangdi@163.com, yhxu@uestc.edu.cn, rmxu@uestc.edu.cn

Abstract ─ A compact triple band-notch ultra-wideband (UWB) antenna with microstrip-feed is presented. The desired band-notch antenna is achieved by etching a narrowband triple complementary split-ring resonator into the radiating element of an existing UWB antenna. By attenuation of the measured return, the new antenna reduces interference from UWB in the C-band (3.7 GHz - 4.2 GHz) satellite communication systems and wireless local area network (5.15 GHz - 5.35 GHz, 5.725 GHz - 5.825 GHz bands). The built prototypes have a compact size of 25 × 27.9 mm^2 including the ground plane. This miniature size also delivers advantageous radiation patterns with good mono-polar characteristics across the UWB band with the gain attenuated within the desired notch bands. The antenna demonstrates omnidirectional and stable radiation patterns across all the relevant bands. Moreover, a prototype of the proposed antenna is fabricated, and the measured results are shown to be in good agreement with the simulated results.

Index Terms ─ Multiband, notch bands, printed slot antenna, and ultra-wideband (UWB).

I. INTRODUCTION

As the need for high-data-rate wireless communication becomes more urgent, various solutions have been suggested. Ultra-wide band (UWB) radio is a good candidate technology that has the advantages of higher data rates; good immunity to multi-path cancellation; a possible increase in communication operational security and low interference into legacy systems [1]. As they are required to be small and operate relative bandwidths, antennas are a particularly challenging aspect of UWB technology. The Federal communications commission (FCC) version of UWB radio has within its spectrum (3.1 GHz – 10.6 GHz), C-band (3.7 GHz – 4.2 GHz) satellite communication systems and the IEEE802.11a frequency band (5.15 GHz – 5.825 GHz), which are also a low-power technology. Therefore FCC UWB may be seen as an interferer for both the IEEE802.11a and C-band satellite communication systems. To address this problem, various UWB antennas with multi-notch band-stop characteristics have been proposed [2-5].

In this paper, a new band-notched printed monopole antenna with good gain characterization over a wide bandwidth is presented. By using a co-directional hexagon complementary split-ring resonators strip and by inserting a wave strip in the ground plane, the gain of the square antenna is enhanced, and also much wider impedance bandwidth can be produced, especially at the higher band. Different from the conventional structure, the notched band, covering the 3.68 GHz - 4.25 GHz, 5.05 GHz - 5.38 GHz, 5.7 GHz - 6.12 GHz band, is provided by electromagnetically adjusting coupling between a pair of co-directional hexagon complementary split-ring resonators strips protruded inside the swallow radiation pattern in our model. Experimental and simulated results of the constructed prototype are presented. The size of the designed antenna is smaller than the UWB antennas with band-notched function reported recently [6-9].

II. ANTENNA DESIGN

Microstrip antennas are key components in 1 GHz - 50 GHz frequency range. Compared with normal microwave antennas, the microstrip

antennas have several advantages, including low loss, high integration, low profile, and compact size. To fabricate swallow-shaped microstrip triple band-notched antenna mentioned in this paper, a half ellipse is cut from a rectangle shape radiating patch firstly and then moved into the bottom side of the radiating patch. This new shape with a gradient structure has the same area as the rectangle shape. In addition, the ground of the antenna has wave-like shape so that this ground also has a gradient structure. Since both the swallow-shaped radiating patch and the wave-like shape ground have a gradient structure, the antenna can ensure a smooth transition from one mode to another. In this case, the antenna will have a good impedance matching within a broad bandwidth.

The quarter wavelength corresponding to the lowest cutoff frequency can be derived using equation (1)

$$\frac{\lambda}{4} = \frac{c}{4f} \ , \qquad (1)$$

where λ represents the wavelength in free space, f is the frequency, and c is the speed of light. In this case, the radiating patch is similar to a disk. The lowest cutoff frequency of the corresponding quarter wavelength is equal to twice the radius of this disk,

$$2R = \frac{\lambda_p}{4} \ . \qquad (2)$$

Therefore, the width of the antenna W < 2R.

According to earlier research, the band-notched can be introduced by the complementary split ring resonator (CSRR) structures in the radiating patch. If the length of the CSRR is roughly the same as the half wavelength of the corresponding central band-notched frequency, the currency is restricted around the CSRR, resulting in a no radiating antenna, which is due to band-notched [10-12]. In order to achieve three bands, three co-directional hexagon complementary split-ring resonators, are embedded into the radiating patch in the antenna. This can be expressed by,

$$L = \frac{c}{2\,f_{notch}\,\sqrt{\varepsilon_r}} \qquad (3)$$

where c represents the speed of light, f is the central frequency of the notched band, and ε_r is the effectively dielectric constant.

In order to reduce the interference from the UWB in the C-band (3.7 GHz – 4.2 GHz) satellite communication systems and wireless local area network (5.15 GHz – 5.35 GHz, 5.725 GHz – 5.825 GHz). Parameters like the radius of the complementary split ring resonator (CSRR), position of the CSRR, and the width of the CSRR have been optimized. These optimization works were managed by using commercial 3-D electromagnetic software HFSS [13-15].

The geometry of the proposed antenna is shown in Fig. 1. The overall antenna size is 25× 27.9 mm². As can be seen, it consists of the following major parts: main radiation patch with a microstrip feed and a wave shape conductor ground plane in the back. The radius of the swallow radiating patch is fixed at 12.5 mm. The width of the feeding microstrip line is 1.55 mm, and its characteristic impedance is 50 Ω. Meanwhile, the conducting ground plane has size of 25 × 10.78 mm². The modified wave shape ground plane is applied to achieve broadband characteristics over the entire UWB band because the truncation creates a capacitive load that neutralizes the inductive nature of the patch to produce nearly pure resistive input impedance. An SMA is connected to the port of the feeding microstrip line [16]. The specified characteristics of this substrate are 0.508 mm in thickness and 2.2 in relative permittivity (ε_r). Good performance of multiple band-notched characteristic is simply accomplished by embedding a common direction hexagon CSRR to the swallow patch.

Figure 2 shows the current distributions at three center notched bands. The dimensions of the three co-directional hexagon CSRR are corresponding to three notched bands. When the antenna is working at the center of the lower notched band near 3.9 GHz, the outer complementary SRR behaves as a separator in Fig. 2 (a), which almost has no relation to the other band-notches [17]. Similarly, the middle complementary SRR operates as a second separator for the center of the middle notched band near 5.2 GHz in Fig. 2 (b). From Fig. 2 (c), the upper notched band near 5.9 GHz is ensured by the inner complementary SRR [18]. Additionally, as a certain current crowded on the ground plane near the microstrip feed line would affect the antenna performance, we take simulation and find that the dimension of the ground plane, especially,

has a significant effect on the triple band-notches performance, as well as the impedance bandwidth.
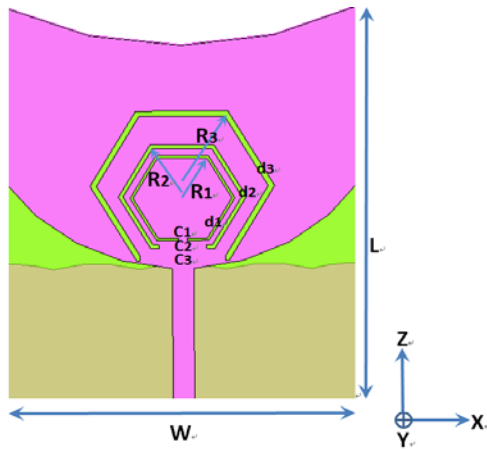

Fig. 1. Geometry of the antenna, having $R_1 = 4.01$ mm, $R_2 = 4.83$ mm, $R_3 = 6.98$ mm, $C_1 = 0.6$ mm, $C_2 = 3.35$ mm, $C_3 = 6$ mm, $d_1 = 0.2$ mm, $d_2 = 0.32$ mm, $d_3 = 0.45$ mm, $W = 25$ mm, and $L = 27.9$ mm.

III. RESULTS AND DISCUSSION

With the optimal parameters demonstrated in Fig. 1, an example monopole antenna was fabricated, which is shown in Fig. 3. As illustrated in Fig. 4, the proposed antenna has an impedance bandwidth (VSWR < 2) from 2.4 GHz to 11.8 GHz, which covers the entire UWB frequency band. Basically, this broad bandwidth is mainly determined by a conventional UWB antenna. By attaching co-directional hexagon complementary split-ring resonators, it is clearly observed from the measured results that the designed antenna exhibits triple stop bands of 3.68 GHz – 4.25 GHz, 5.05 GHz – 5.38 GHz, 5.7 GHz – 6.12 GHz. The center frequencies of the notched bands are 3.9 GHz, 5.2 GHz, and 5.9 GHz, respectively [19]. There is good agreement between simulated and measured results; the little difference between them may be caused by the soldering effects of an SMA connector, which have been neglected in our simulations [20].

The far-field radiation characteristics at 3.5 GHz, 5.5 GHz, and 7.5 GHz are given in Fig. 5, respectively. Nearly, omnidirectional radiation patterns in the xy-plane and dipole-like radiation patterns in the yz-plane are obtained at these frequencies [21]. Due to the limitations of laboratory instruments, the radiation patterns above 12 GHz were not measured. All the

obtained radiation patterns accord with those of the conventional printed UWB monopole antennas. The proposed antenna has proved to be capable of providing favorable spatial-independent band-notched characteristics [22].


(a)

(b)

(c)
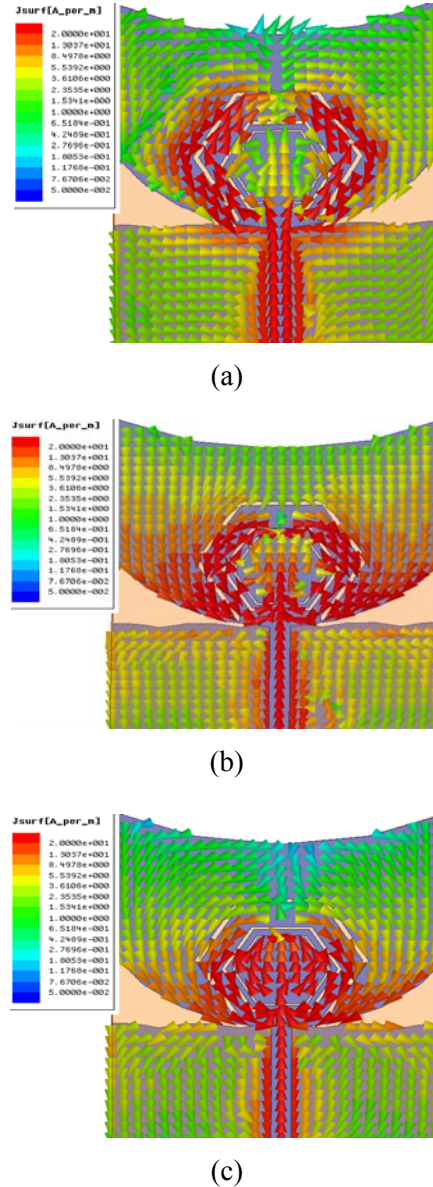
Fig. 2. The current distribution of the proposed antenna at (a) 3.9 GHz, (b) 5.2 GHz, and (c) 5.9 GHz.

Figure 6 shows the measured radiation efficiency of the antenna. The proposed antenna features an efficiency between 50 % and 70 % over the whole UWB frequency and lower than 5 % in the notch band. The features of about 60 %

average radiation efficiency is good enough to satisfy an acceptable variation for practical power transmission [23]. The measured gain of the proposed antenna is illustrated in Fig. 7. It can be seen that stable antenna gain with a variation of less than 3 dBi is achieved except for smaller values in the notched band, within which the smallest one is as low as -12 dBi. This confirms that the proposed antenna provides a high level of rejection to signal frequencies within the notched band [24-25].
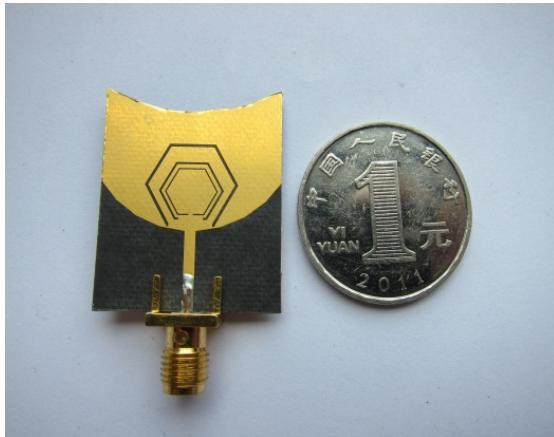
(a)
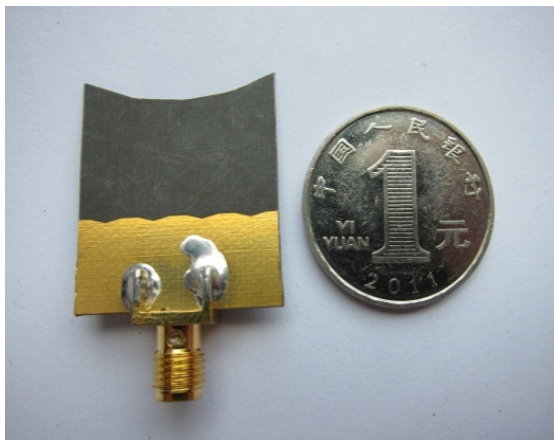
(b)

Fig. 3. Photograph of the proposed antenna; (a) front view and (b) bottom view.
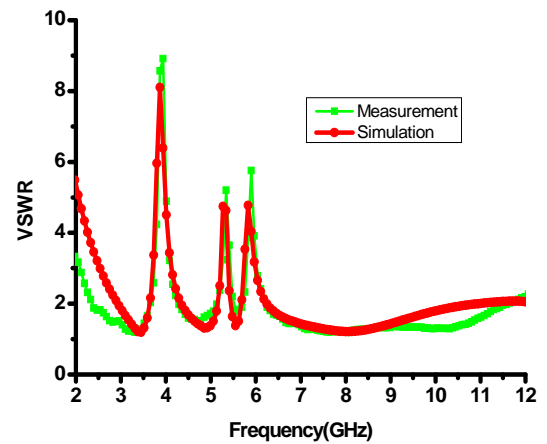
Fig. 4. Comparison of simulated and measured VSWR of the proposed antenna.

F=3.5GHz

F=5.5GHz

F=7.5GHz

(a)

F=3.5GHz

F=5.5GHz

F=7.5GHz

(b)
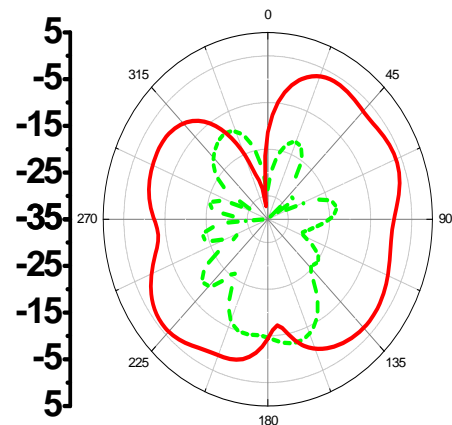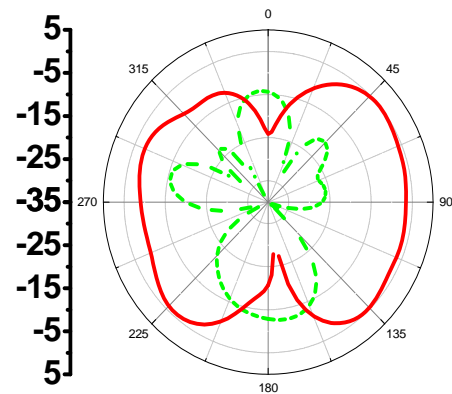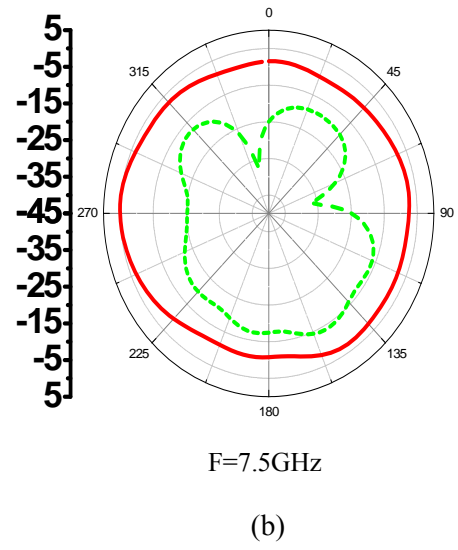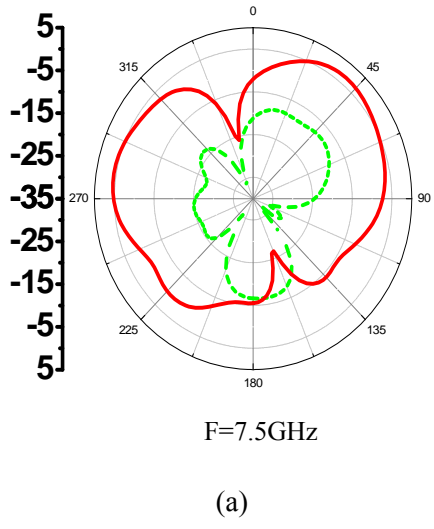
Co-polar: ▬▬▬   Cross-polar: ▬ ▬ ▬

Fig. 5. Measured radiation patterns at (a) yz -plane and (b) xy-plane.
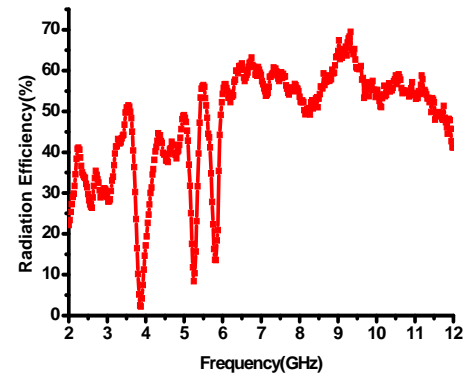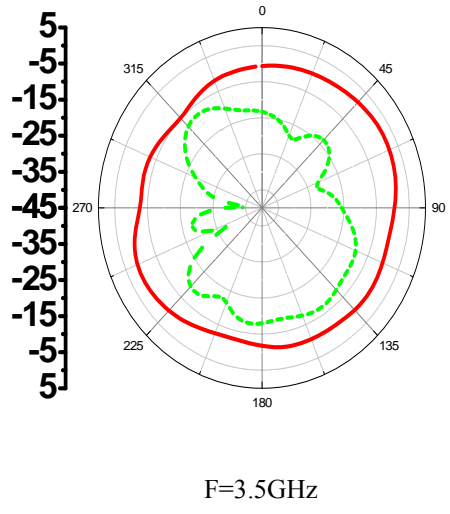
Fig. 6. Measured radiation efficiency of the proposed antenna.
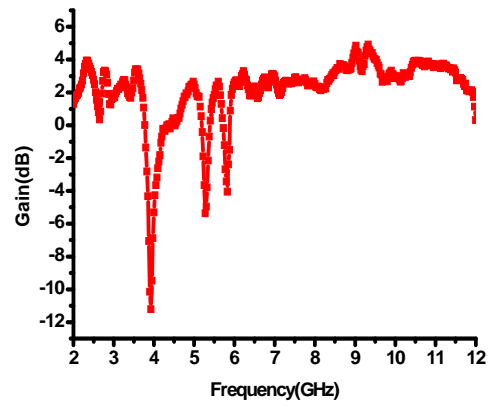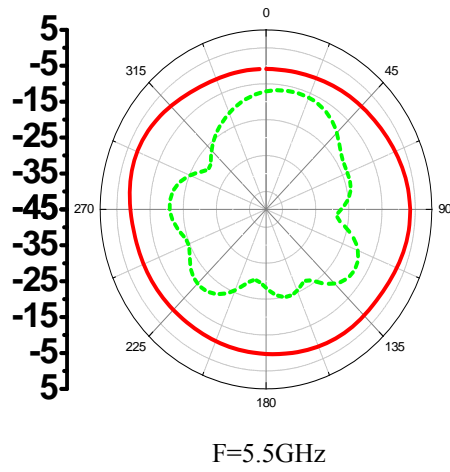
Fig. 7. Measured gain of the proposed antenna.

IV. CONCLUSIONS

A novel compact printed microstrip-fed monopole antenna with band-notched characteristics has been proposed for UWB applications. We showed that by embedding co-directional hexagon complementary split-ring resonators slots with proper dimensions and position in the radiation pattern, triple more resonances are excited, and as a result, wide impedance bandwidth from 2.4 GHz to 11.8 GHz is achieved, and also a rejection band around 3.68 GHz – 4.25 GHz, 5.05 GHz – 5.38 GHz, 5.7 GHz – 6.12 GHz can be achieved with the wave shape structures on the backside of the substrate. The designed antenna has a simple configuration and easy fabrication process. The experimental results show that the realized antenna with a very compact size, simple structure, and wide bandwidth can be a good candidate for UWB application. Therefore, the results of the work are useful for short-range wireless communication systems.

REFERENCES

[1] Federal Communications Commission, Washington, DC, "Revision of part 15 of the commission's rules regarding ultra-wideband transmission systems, First note and order," ET-Docket 98-153, 2002.

[2] N. Farrokh-Heshmat, J. Nourinia, and C. Ghobadi, "Band-notched ultra-wideband printed open-slot antenna using variable on-ground slits," *Electron. Lett.*, vol. 45, no. 21, pp. 1060-1061, Oct. 2009.

[3] G. Zhang, J. S. Hong, B. Z. Wang, and G. Song, "Switched band-notched UWB/ WLAN monopole antenna," *Appl. Comp. Electro. Society (ACES) Journal*, vol. 27, no. 3, pp. 256-260, March 2012.

[4] C. Yu, W. Hong, L. Chiu, G. Zhai, C. Yu, W. Qin, and Z. Kuai, "Ultra-wideband printed log-periodic dipole antenna with multiple notched bands," *IEEE Trans. Antennas Propag.*, vol. 59, no. 3, pp. 725-732, March 2011.

[5] M. T. Partovi, N. Ojaroudi, and M. Ojaroudi, "Small slot antenna with enhanced bandwidth and band-notched performance for UWB applications," *Appl. Comp. Electro. Society (ACES) Journal*, vol. 27, no. 9, pp. 772-778, Sep. 2012.

[6] F. Wei, L. Xu, X.-W. Shi, and B. Liu, "Compact UWB bandpass filter with two notch bands based on folded SIR," *Electron. Lett.*, vol. 46, no. 25, pp. 1679-1680, Dec. 2010.

[7] A. M. Montaser, K. R. Mahmoud, and H. A. Elmikati, "Integration of an optimized E-shaped patch antenna into laptop structure for bluetooth and notched-UWB standards using optimization techniques," *Appl. Comp. Electro. Society (ACES) Journal*, vol. 27, no. 10, pp. 786-794, Oct. 2012.

[8] A. A. Eldek, "Numerical analysis of a small ultra wideband microstrip fed tap monopole antenna," *Prog. Electromagn. Res.*, vol. 65, pp. 59-69, 2006.

[9] B. H. Siahkal-Mahalle, M. Ojaroudi, and N. Ojaroudi, "Enhanced bandwidth small square monopole antenna with band-notched functions for UWB wireless communications," *Appl. Comp. Electro. Society (ACES) Journal*, vol. 27, no. 9, pp. 759-765, Sep. 2012.

[10] Y. D. Dong, W. Hong, Z. Q. Kuai, C. Yu, Y. Zhang, J. Y. Zhou, and J. Chen, "Development of ultra wideband antenna with multiple band-notched characteristics using half mode substrate integrated waveguide cavity technology," *IEEE Trans. Antennas Propag.*, vol. 57, no. 12, pp. 2894-2902, Dec. 2009.

[11] M. Ojaroudi, N. Ojaroudi, and Y. Ebazadeh, "Dual band-notch small square monopole antenna with enhanced bandwidth characteristics for UWB applications," *Appl. Comp. Electro. Society (ACES) Journal*, vol. 27, no. 5, pp. 420-426, May 2012.

[12] A. Valizade, Ch. Ghobadi, J. Nourinia, N. Ojaroudi, and M. Ojaroudi, "Band-notch slot antenna with enhanced bandwidth by using Ω-shaped strips protruded inside rectangular slots for UWB applications," *Appl. Comp. Electro. Society (ACES) Journal*, vol. 27, no. 10, pp. 816-822, Oct. 2012.

[13] D. Jiang, Y. Xu, R. Xu, and W. Lin, "Compact dual-band-notched UWB planar monopole antenna with modified CSRR," *Electro. Lett.*, vol. 48, no. 20, pp. 1250-1252, Sep. 2012.

[14] K. S. Ryu and A. A. Kishk, "UWB antenna with single or dual band- notches for lower WLAN band and upper WLAN band," *IEEE Trans. Antennas Propag.*, vol. 57, no. 12, pp. 3942-3950, Dec. 2009.

[15] X. N. Low, Z. N. Chen, and T. S. P. See, "A UWB dipole antenna with enhanced impedance and gain performance," *IEEE Trans. Antennas*

Propag., vol. 54, no. 10, pp. 2959-2966, Oct. 2009.

[16] X. L. Ma, W. Shao, and G. Q. He, "A novel dual narrow band-notched CPW-fed UWB slot antenna with parasitic strips," *Appl. Comp. Electro. Society (ACES) Journal*, vol. 27, no. 7, pp. 581-586, July 2012.

[17] A. Nouri and G. R. Dadashzadeh, "A compact UWB band-notched printed monopole antenna with defected ground structure," *IEEE Antennas and Wireless Propagation Letters*, vol. 10, pp. 1178-1181, 2011.

[18] C.-M. Wu, Y.-L. Chen, and W.-C. Liu, "A compact ultra wideband slotted patch antenna for wireless USB dongle application," *IEEE Antennas and Wireless Propagation Letters*, vol. 11, pp. 596-599, 2012.

[19] Z. L. Zhou, L. Li, and J. S. Hong, "A novel compact monopole antenna with triple high quality rejected bands for UWB applications," *Appl. Comp. Electro. Society (ACES) Journal*, vol. 27, no. 8, pp. 654-659, August 2012.

[20] M. Mighani, M. Akbari, and N. Felegari, "A CPW dual band notched UWB antenna," *Appl. Comp. Electro. Society (ACES) Journal*, vol. 27, no. 4, pp. 352-359, April 2012.

[21] W. Jiang and W. Che, "A novel UWB antenna with dual notched bands for WiMAX and WLAN applications," *IEEE Antennas and Wireless Propagation Letters*, vol. 11, pp. 293-5296, 2012.

[22] C.-T. Chuang, T.-J. Lin, and S.-J. Chung, "A band-notched UWB monopole antenna with high notch-band-edge selectivity," *IEEE Trans. on Antennas and Propagation*, vol. 60, no. 10, pp. 4492-4499, Oct. 2012.

[23] S. W. Wong, T. G. Huang, C. X. Mao, Z. N. Chen, and Q. X. Chu, "Planar filtering ultra-wideband (UWB) antenna with shorting pins," *IEEE Trans. on Antennas and Propagation*, vol. 61, no. 2, pp. 948-953, Feb. 2013.

[24] Y. Sung, "Triple band-notched UWB planar monopole antenna using a modified H-shaped resonator," *IEEE Trans. on Antennas and Propagation*, vol. 61, no. 2, pp. 953-957, Feb. 2013.

[25] F. Wei, Z. D. Wang, F. Yang, and X. W. Shi, "Compact UWB BPF with triple-notched bands based on stub loaded resonator," *Electro. Lett.*, vol. 49, no. 2, Jan. 2013.

Di Jiang received the B.Sc. degree with Communication Engineering in 2004, and is currently pursuing the Ph.D. degree in Electromagnetic Field and Microwave Technology at the University of Electronic Science and Technology of China (UESTC), Chengdu, China. His research interest includes miniature antenna, RF circuit, and metamaterial design and its application.

Yuehang Xu received the B.Sc. degree, Master degree, and Ph.D degree in 2004, 2007, and 2010 in electromagnetic field and microwave technology from the University of Electronic Science and Technology of China (UESTC), respectively. He was a visiting scholar in Columbia University working on graphene RF devices during Sep. 2009 to Sep. 2010. He has been a lecture in UESTC since 2010. His research interests include wide band-gap semiconductor material and graphene based RF devices.

Ruimin Xu received the Ph.D. degree in Electrical Engineering from the University of Electronic Science and Technology of China (UESTC), Chengdu, China. At present as a University of Electronic Science and Technology extremely high frequency complex system, deputy director of the national defense key discipline laboratory. The main research fields including microwave millimeter-wave circuits and systems, microwave monolithic integrated circuit.

Disc-Shaped Monopole Antenna with Dual Band-Notched Function for UWB Applications

Nasser Ojaroudi [1], Mohammad Ojaroudi [2], and Noradin Ghadimi [2]

[1] Department of Electrical Engineering
Germi Branch, Islamic Azad University, Germi, Iran
n.ojaroudi@iaugermi.ac.ir

[2] Young Researchers Club
Ardabil Branch, Islamic Azad University, Ardabil, Iran
m.ojaroudi@iauardabil.ac.ir, noradin.ghadimi@gmail.com

Abstract ─ In this paper, we present a novel design of dual band-notched printed monopole antenna for UWB applications. By cutting an anchor-shaped slit in the disc-shaped radiating patch a single frequency band-stop performance can be achieved, also in order to create dual band-notched function, we use a T-shaped strip protruded inside a rectangular slot in the ground plane that with this design, a dual band-notched operation has been obtained. Simulated and measured results obtained for this antenna show that the proposed monopole antenna offers two notched bands, covering all the 5.2/5.8 GHz WLAN, 3.5/5.5 GHz WiMAX and 4 GHz C bands range. Good antenna gains and radiation behavior within the UWB frequency range have also been obtained. The antenna has a small dimension of 12×18 mm^2.

Index Terms ─ Anchor-shaped slit, disc-shaped radiating patch, dual band-notched function, T-shaped protruded strip structure, and ultra wide band (UWB) systems.

I. INTRODUCTION

In UWB communication systems, one of the key issues is the design of a compact antenna while providing wideband characteristic over the whole operating band. Consequently, a number of printed monopole antennas with different geometries have been experimentally characterized and automatic design methods have been developed to achieve the optimum planar shape. Moreover, other strategies to improve the impedance bandwidth have been investigated [1-4]. The frequency range for UWB systems between 3.1 GHz to 10.6 GHz will cause interference to the existing wireless communication systems, such as, the wireless local area network (WLAN) for IEEE 802.11a operating in 5.15 GHz – 5.35 GHz and 5.725 GHz – 5.825 GHz bands, WiMAX (3.3 GHz – 3.6 GHz) and C-band (3.7 GHz – 4.2 GHz), so the UWB antenna with a single and dual band-stop performance is required. Lately to generate the frequency band-notch function, modified planar monopoles several antennas with band-notch characteristic have been reported [5-7]. In [5], and [6], different shapes of the slots (i.e., SIR and folded trapezoid) are used to obtain the desired band notched characteristics. Half wavelength U-shaped slots are embedded in the radiating patch to generate the single and multiple band-notched functions [7].

In this paper, a novel and compact microstrip-fed monopole antenna with dual band-notched characteristic for UWB applications has been designed and manufactured. In the proposed structure, single frequency band-notched characteristics is obtained by applying the anchor-shaped slit in the disc-shaped radiating patch and also by creating the T-shaped strip protruded inside the rectangular slot in the ground plane, dual band-notched function can be provided. The dual notch bands, covering 5.02 GHz – 5.97 GHz WLAN band, 3.3 GHz – 3.8 GHz WiMAX, and

3.7 GHz – 4.2 GHz C- Band. Details of the proposed design and experimental results are also presented and discussed. Good return loss and radiation pattern characteristics are obtained in the frequency band of interest.

II. ANTENNA DESIGN

The presented small monopole antenna fed by a microstrip line is shown in Fig. 1, which is printed on an FR4 substrate of thickness 1.6 mm, permittivity 4.4, and loss tangent 0.018. The basic monopole antenna structure consists of a disc-shaped radiating patch, a feed line, and a ground plane. The proposed antenna is connected to a 50-Ω SMA connector for signal transmission.


(a)

(b)
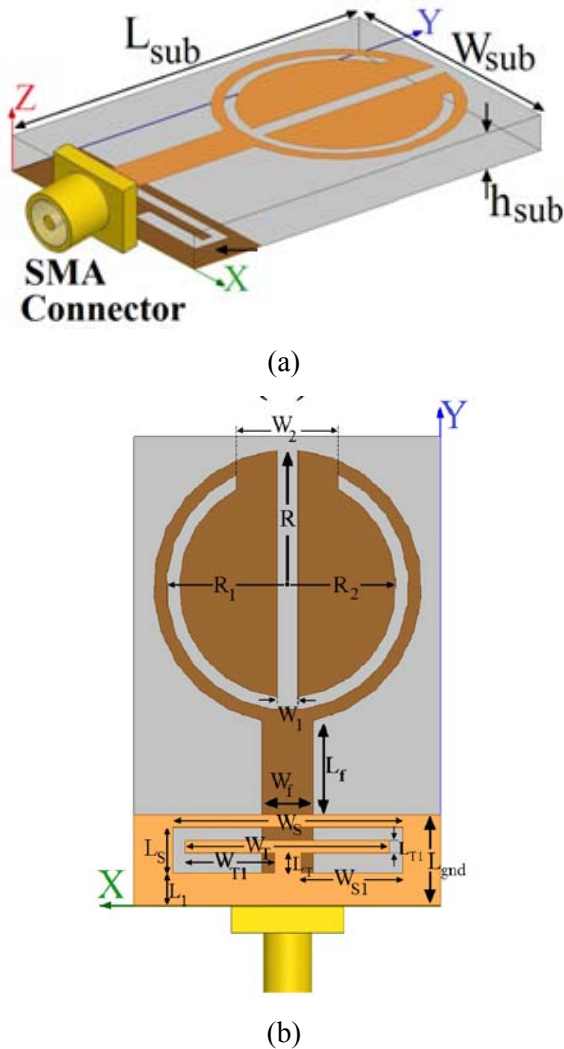
Fig. 1. Geometry of the proposed monopole antenna; (a) side view and (b) bottom view.

In this study, the anchor-shaped slit in the radiating patch perturbs the resonant response and also acts as a half-wave resonant structure [8-9]. At the notch frequency, the current concentrated on the edges of the interior and exterior of this slit [8]. Additionally, based on Defected Ground Structure (DGS), the rectangular slot with a T-shaped protruded strip inside the slot act as a filtering element to create a new band notch function of the proposed antenna, because it can create additional surface current path in the ground plane. At the notch frequency, the current flows are more dominant around the modified slot, and they are oppositely directed between the protruded strip and the ground plane [10]. As a result, the desired high attenuation near the notch frequency can be produced, in addition to the modified inverted T-shaped coupled strip.

In this work, we start by choosing the dimensions of the designed antenna. These parameters, including the substrate, are $W_{Sub} \times L_{sub}$ = 12 $mm \times$ 18 mm or about $0.15\lambda \times 0.25\lambda$ at 4.2 GHz (the first resonance frequency). Next step, we have to determine the radius of the radiating patch R. This parameter is approximately λ_{lower} / 4, where λ_{lower} is the lower bandwidth frequency wavelength. λ_{lower} depends on a number of parameters, such as the radiating patch length as well as the thickness and dielectric constant of the substrate on which the antenna is fabricated [11]. The important step in the design is to choose L_{notch} (the length of the filter). L_{notch} is set to band-stop resonate at $0.5\lambda_g$, where $L_{notch1}=R+0.5\prod \times(R_1+R_2)$, and $L_{notch2}=0.5W_S+W_{S1}+L_S+L_T+W_T$, λ_{g1} and λ_{g2} correspond to the notched band frequencies wavelength (3.8 GHz is the first notched frequency and 5.5 GHz is the second notched frequency). The optimized values of the proposed antenna design parameters are as follows:

W_{sub} = 12 mm, L_{sub} = 18 mm, h_{sub} = 1.6 mm, W_f = 2 mm, L_f = 3.5 mm, R = 10 mm, R_1 = 4.75 mm, R_2 = 4.5 mm, W_1 = 0.5 mm, L_1 = 1.5 mm, W_2 = 4 mm, W_S = 10 mm, L_S = 1.75 mm, W_{S1} = 4.5 mm, W_T = 9.5 mm, L_T = 0.75 mm, W_{T1} = 4.25 mm, L_{T1} = 0.5 mm, and L_{gnd} = 3.5 mm.

III. RESULTS AND DISCUSSIONS

The proposed microstrip-fed monopole antenna with various design parameters were

constructed, and the numerical and experimental results of the input impedance and radiation characteristics are presented and discussed. The Ansoft simulation software high-frequency structure simulator (HFSS) [12] version 13, with frequency sweep from 2 GHz to 12 GHz, is used to optimize the design and agreement between the simulation and measurement is obtained. The parameters of this proposed antenna, such as W_2 and W_S, are studied by changing one parameter at a time and also changing the others. In the HFSS by default, the antenna excited by wave port that is renormalized to a 50-Ohm full port impedance. The proposed antenna is connected to a 50-Ohm SMA connector for signal transmission.

The structure of various antennas used for simulation studies is shown in Fig. 2. Return loss characteristics for the ordinary disc-shaped monopole antenna (Fig. 2 (a)), disc-shaped monopole antenna with anchor-shaped slit (Fig. 2 (b)), and the proposed antenna structure (Fig. 2 (c)) are compared in Fig. 3. As shown in Fig. 3, to generate single frequency band-notched function (3.3/4.2 GHz), we insert anchor-shaped slit in the radiating patch of the ordinary disc-shaped monopole antenna, and also by using a rectangular slot with a T-shaped protruded inside the rectangular slot in the ground plane, the dual band-notch function can be achieved, that covering all the 5.2/5.8 GHz WLAN, 3.5/5.5 GHz WiMAX and 4-GHz C band. Also the input impedance of the proposed monopole antenna structure that is shown in Fig. 1, on a Smith chart is shown in Fig. 4.

Fig. 3. Simulated return loss characteristics for the various monopole antennas shown in Fig. 2.
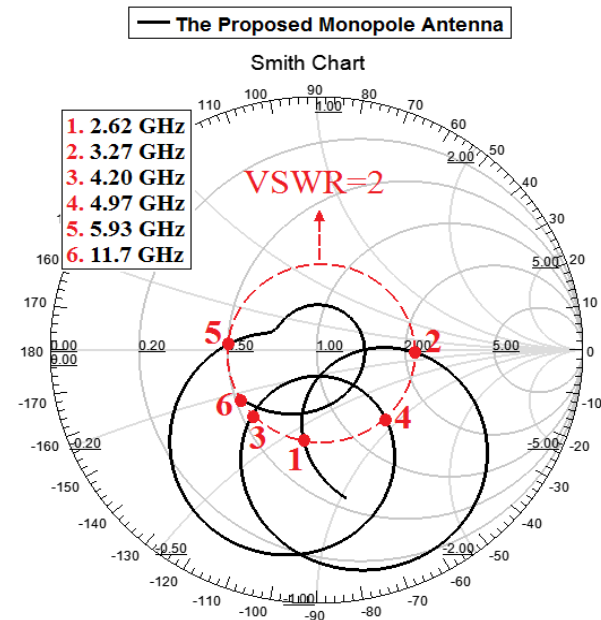
Fig. 4. Smith chart demonstration of the simulated input impedance for the proposed antenna.

In order to know the phenomenon behind this additional resonance performance, the simulated current distributions on the patch for the proposed antenna at 3.8 GHz are presented in Fig. 5 (a). It can be observed in Fig. 5 (a), that the current is concentrated on the edges of the interior and exterior of the anchor-shaped slit at 3.8 GHz. Another important design parameter of this structure is the rectangular slot with a T-shaped protruded strip inside the rectangular slot, used in


Fig. 2. The structure of the (a) ordinary disc-shaped monopole antenna, (b) disc-shaped monopole antenna with anchor-shaped slit, and (c) the proposed antenna structure.

the ground plane. Figure 5 (b) presents the simulated current distributions on the modified ground plane at the second notch frequency (5.5 GHz). As shown in Fig. 5 (b), at the second notch frequency the current flows are more dominant around the slot with T-shaped protruded strip. As a result, the desired high attenuation near the second notch frequency can be produced [13-14].

(a)   (b)
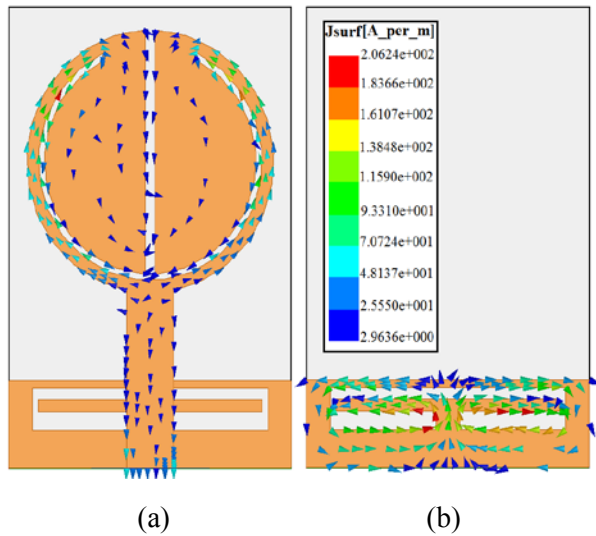
Fig. 5. Simulated surface current distributions for the proposed antenna (a) on the radiating patch at 3.8 GHz and (b) on the ground plane at 5.5 GHz.

Figure 6 shows the conceptual equivalent circuit model for the proposed antenna, which has two RLC band-stop filters. When the current path in the T-shaped strip protruded inside the rectangular slot in the ground plane, which is equal to a half-wavelength at 5.5 GHz as shown in Fig. 6 (b), and in the anchor-shaped slit inside the disc shaped radiating patch, which is equal to a half-wavelength at 3.8 GHz as shown in Fig. 6 (c); the input impedance at the feeding point is equal to zero (short circuit).

Figure 7 shows the simulated VSWR curves with different values of W_2 and W_S. As shown in Fig. 6, when the width W_2 increases from 2 *mm* to 6.5 *mm*, the center of the first notch frequency decreases from 4.17 GHz to 3.26 GHz, also when the exterior width of the rectangular slot W_S increases from 8 *mm* to 11 *mm*, the center of the second notch frequency decreases from 5.93 GHz to 4.79 GHz. From these results, we can conclude

that the centers of the notch frequencies are controllable by changing these parameters [15].


(a)

(b)

(c)
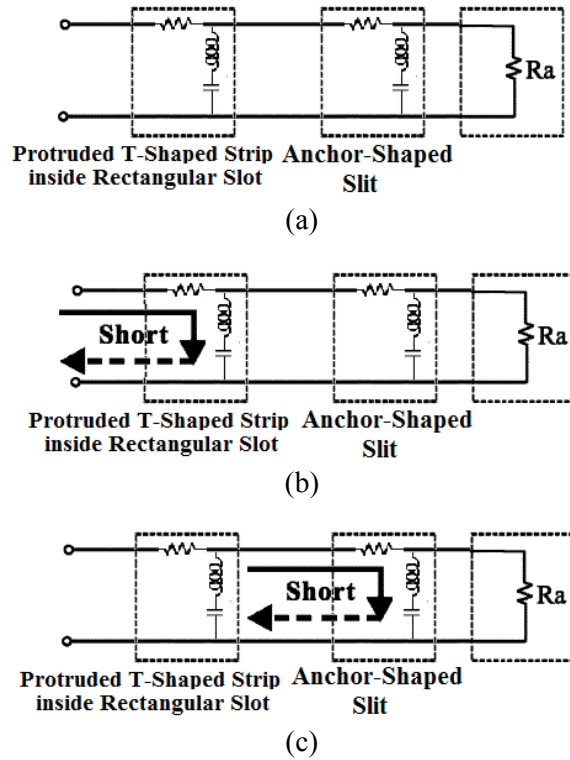
Fig. 6. Conceptual equivalent-circuit model for (a) the proposed antenna, (b) at the second notched frequency, (c) at the first notched frequency.
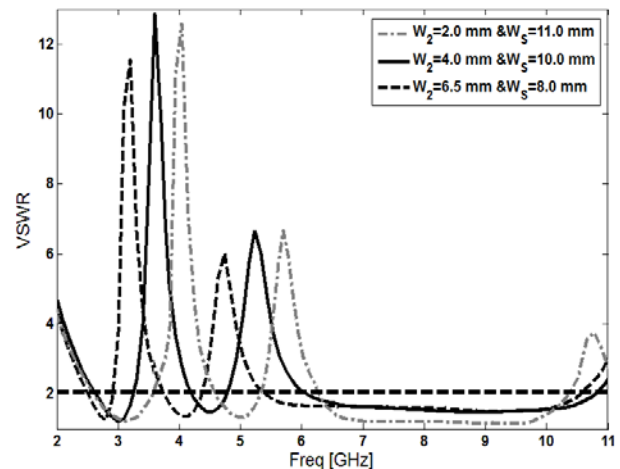

Fig. 7. Simulated VSWR characteristics for the proposed antenna with different values of W_2 and W_S.

The proposed antenna was built and tested. The measured and simulated VSWR characteristics of the proposed antenna are shown in Fig. 8. The fabricated antenna has the frequency band of 2.77 GHz to over 11.63 GHz with two notched-band function, covering all the 5.2/5.8 GHz WLAN, 3.5/5.5 GHz WiMAX and 4 GHz C-Band range. As shown in Fig. 8, there exists a discrepancy between the measured data and the simulated results. Figure 9 illustrates the measured radiation patterns, including the co-polarization and cross-polarization, in the H-plane (xz plane) and E-plane (yz plane). It can be seen that the radiation patterns in the xz plane are nearly omni-directional for the three frequencies.

Figure 10 shows the effects of the anchor-shaped slit and the rectangular slot with a T-shaped protruded strip inside the rectangular slot, on the maximum gain in comparison to the same antenna without them. As shown in Fig. 10, the ordinary disc-shaped monopole antenna has a gain that is low at 3 GHz and increases with frequency. It can be observed in Fig. 10 that by using a disc-shaped radiating patch with an anchor-shaped slit and the rectangular slot with a T-shaped protruded strip inside the rectangular slot in the ground plane, two sharp decreases of maximum gain in the notched frequencies band at 3.8 GHz and 5.5 GHz are shown in Fig. 10. For other frequencies outside the notched frequency band, the antenna gain with the filters is similar to those without it.
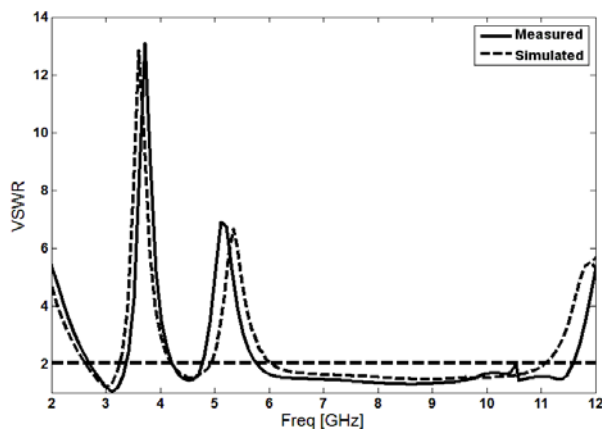
(a)

(b)

(c)
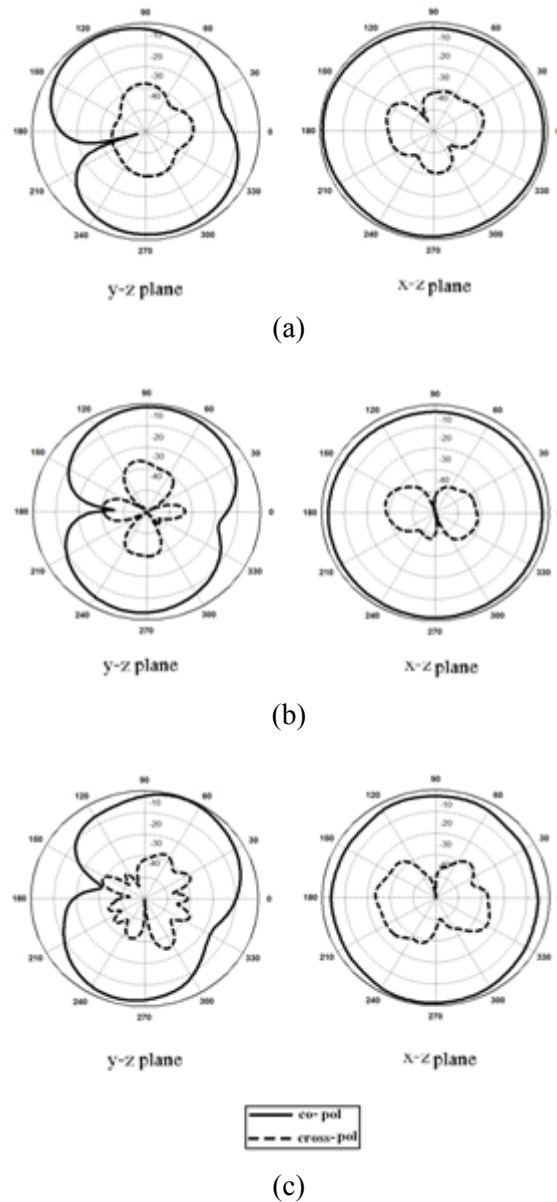
Fig. 9. Measured radiation patterns of the proposed antenna at (a) 4.5 GHz, (b) 7.3 GHz, and (c) 9.5 GHz.

Fig. 8. Measured and simulated VSWR characteristics for the proposed antenna.

IV. CONCLUSION

In this paper, we propose a novel design of ultra wide band monopole antenna with dual band-notch function. The presented disc-shaped monopole antenna can operate from 2.77 GHz to 11.63 GHz with two rejection bands around 3.3 GHz – 4.2 GHz and 5.01 GHz – 5.9 GHz. By inserting the anchor-shaped slit structure in the disc-shaped radiating patch a single band-stop performance can be achieved, also in order to

generate a dual band-notched function, we use the rectangular slot with a T-shaped protruded strip inside the rectangular slot in the ground plane. The proposed antenna has a simple configuration and is easy to fabricate. Simulated and experimental results show that the proposed antenna could be a good candidate for UWB applications.
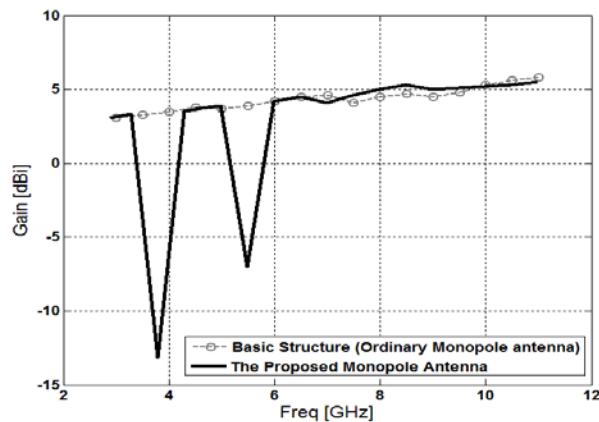
Fig. 10. Maximum gain comparisons for the ordinary disc-shaped monopole antenna (simulated) and the proposed antenna (measured).

ACKNOWLEDGMENT

REFERENCES

[1] N. Ojaroudi, M. Ojaroudi, and N. Ghadimi, "UWB omnidirectional square monopole antenna for Use in circular cylindrical microwave imaging systems," *IEEE Antennas Wireless Propag. Lett.*, vol. 11, pp. 1350-1353, 2012.

[2] N. Ojaroudi, M. Ojaroudi, and S. Amiri, "Enhanced bandwidth of small square monopole antenna by using inverted U-shaped slot and conductor-backed plane," *Applied Computational Electromagnetics Society (ACES) Journal*, vol. 27, no. 8, pp. 685-690, August 2012.

[3] J. Jung, W. Choi, and J. Choi, "A small wideband microstrip-fed monopole antenna," *IEEE Microwave Letters*, vol. 15, no. 10, pp. 703-705, October 2005.

[4] J. Jung, W. Choi, and J. Choi, "A compact broadband antenna with an L-shaped notch,"

IEICE Trans. Commun.., vol. E89-B, no. 6, pp. 1968-1971, June 2006.

[5] N. Ojaroudi, M. Ojaroudi, and S. Amiri, "Compact UWB microstrip antenna with satellite down-link frequency rejection in X-band communications by etching an E-shaped step-impedance resonator slot," *Microw. Opt. Technol. Lett.*, vol. 55, pp. 922-926, 2013.

[6] M. Ojaroudi, N. Ojaroudi, and Y. Ebazadeh, "Dual band-notch small square monopole antenna with enhanced bandwidth characteristics for UWB applications," *Appl. Comp. Electro. Society (ACES) Journal*, vol. 27, no. 5, pp. 420-426, May 2012.

[7] Y. Li, W. Li, and W. Yu, "A switchable UWB slot antenna using SIS-HSIR and SIS-SIR for multi-mode wireless communications applications," *Appl. Comp. Electro. Society (ACES) Journal*, vol. 27, no. 4, pp. 340-351, April 2012.

[8] G. Zhang, J. S. Hong, B. Z. Wang, and G. Song, "Switched band-notched UWB/WLAN monopole antenna," *Appl. Comp. Electro. Society (ACES) Journal*, vol. 27, no. 3, pp. 256-260, March 2012.

[9] N. Ojaroudi and M. Ojaroudi, "A novel design of reconfigurable small monopole antenna with switchable band notch and multi-resonance functions for UWB applications," *Microw. Opt. Technol. Lett.*, vol. 55, no. 3, pp. 652-656, March 2013.

[10] M. Mighani, M. Akbari, and N. Felegari, "A CPW dual band notched UWB antenna," *Appl. Comp. Electro. Society (ACES) Journal*, vol. 27, no. 4, pp. 352-359, April 2012.

[11] J. William and R. Nakkeeran, "A new UWB slot antenna with rejection of WiMax and WLAN bands," *Appl. Comp. Electro. Society (ACES) Journal*, vol. 25, no. 9, pp. 787-793, September 2010.

[12] Ansoft High Frequency Structure Simulation (HFSS), ver. 13, Ansoft Corporation, 2010.

[13] M. Ojaroudi, N. Ojaroudi, and N. Ghadimi, "Dual band-notched small monopole antenna with novel coupled inverted U-ring strip and novel fork-shaped slit for UWB applications," *IEEE Antennas Wireless Propag. Lett.*, vol. 12, pp. 182-185, 2013.

[14] N. Ojaroudi, M. Ojaroudi, and N. Ghadimi, "Dual band-notched small monopole antenna with novel W-shaped conductor backed plane and novel T-shaped slot for UWB applications," *IET Microw. Antennas Propag.*, vol. 7, pp. 8-14, 2013.

[15] N. Ojaroudi and M. Ojaroudi, "Dual band-notch square monopole antenna with a modified ground plane for UWB applications," *Microw. Opt. Technol. Lett.*, vol. 54, pp. 2743-2747, 2012.

Nasser Ojaroudi was born on 1986 in Germi, Iran. He received his B.Sc. degree in Electrical Engineering from Azad University, Ardabil Branch. From 2011, he is working toward the M.Sc. degree in Telecommunication Engineering at Shahid Rajaee Teacher Training University. Since March 2009, he has been a Research Fellow in the Microwave Technology Company (MWT), Tehran, Iran. His research interests include ultra-wideband (UWB) and small microstrip antennas for wireless communications, microstrip filters, reconfigurable structures, design and modeling of microwave devices and circuits, and electromagnetics theory. He is author and coauthor of more than 60 journal and international conference papers.

Mohammad Ojaroudi was born on 1984 in Germi, Iran. He received his B.Sc. degree in Electrical Engineering from Azad University, Ardabil Branch and M.Sc. degree in Telecommunication Engineering from Urmia University. From 2010, he is working toward the Ph.D. degree at Shahid Beheshti University. From 2007 until now, he is a Teaching Assistant with the Department of Electrical Engineering, Islamic Azad University, Ardabil Branch, Iran. Since March 2009, he has been a Research Fellow (Chief Executive Officer) in the Microwave Technology Company (MWT), Tehran, Iran. From 2012, Mr. Ojaroudi is a member of the IEEE Transaction on Antennas and Propagation (APS) reviewer group. From 2013 he is a student member of the IEEE. His research interests include analysis and design of microstrip antennas, design and modeling of microwave structures, radar systems, and electromagnetic theory. He is author and coauthor of more than 100 journal and international conferences papers. His papers have more than 300 citations with 10 h-index.

Noradin Ghadimi was born in ardabil-Iran in 1985, and received the B.Sc. degree in Electrical Engineering from the Islamic Azad University, Ardabil Branch, Ardabil, Iran, in 2009 and the M.Sc. degree in Electrical Engineering from the Islamic Azad University Ahar Branch, Ahar, Iran, in 2011. His research interests include power system protection, modeling and analysis of distributed generations, renewable energy and communications systems.

Calculation and Analysis of Shielding Effectiveness of the Rectangular Enclosure with Apertures

Chuan-Chuan Wang[1], Chang-Qing Zhu[1], Xing Zhou[2], and Zhi-Feng Gu[1]

[1] Department of Electrical Engineering
Shi Jia Zhuang Mechanical Engineering College, Shi Jia Zhuang, 050003, P.R.China
wangchuan1083@126.com, zhuneil@163.com, gzfgohappy@163.com

[2] Electrostatic and Electromagnetic Research Institute
Shi Jia Zhuang Mechanical Engineering College, Shi Jia Zhuang, 050003, P.R.China
zxlwbh@126.com

Abstract ─ Based on transmission line theory, an approach which combines the analytical model developed by Robinson *et al.* and the model which analyses the shielding effectiveness (SE) of enclosure with an off-centre aperture or aperture array is presented. The model is more general than other methods and includes the incident wave with varied polarization angles and incident angles. It is quicker to calculate the SE with this model, which on the other hand enables to investigate the effect of important design parameters on SE. This model is validated by comparing the SE predictions with those from literatures. Different aspects' effect on the SE are investigated such as aperture dimension, enclosure dimension, position of observation point, number of apertures, polarization angles, and incident angles, etc.

Index Terms ─ Analytical method, numerical method, rectangular enclosure, shielding effectiveness, and transmission line theory.

I. INTRODUCTION

Shielding is a useful and simple technique in EMC field. As to common electronic equipment, its metallic enclosure usually has one or more apertures, which break the completeness of metallic enclosure. How to evaluate the shielding effectiveness (SE) of the enclosure and analyze the factors that affect the SE, becomes a practical problem.

At present, there are three kinds of methods that can be utilized to investigate the SE, including methods based on Bethe's small hole theory, numerical methods, and analytical methods. As early as 1970's, Mendez [1, 2] proposed an analytic shielding formulation for rectangular enclosures excited by internal sources. Using the well-known Bethe's small hole theory [3], Mendez replaced the apertures by equivalent electric and magnetic dipoles. However, this approach is limited to small holes/apertures and is only valid for frequencies below the first resonance. To overcome the limitation of the small hole theory approximation, Wallen *et al.* [4] employed cavity Green's functions to extend Mendez's approach to include the cavity resonance region. Audone and Balma [5] also considered a similar analysis to [4] for a rectangular enclosure with an aperture using MOM along with a network formulation. However, these analyses were still limited to frequencies below the first resonance.

More recently, numerical methods such as transmission line method (TLM), finite-element method(FEM), moment method (MOM), finite-difference time-domain method (FDTD), and the hybrid methods are used in the calculation of SE [6-11]. Numerical methods can offer good accuracy over a broad frequency band but at the cost of large memory and computational time. Hence, numerical methods are severely limited when it comes to analyzing practical enclosures with large number of small holes.

Another analytical method proposed by Robinson *et al.* [12], is based on transmission line theory and used in the calculating of SE. Although the accuracy, this method can be only applied to simple geometries with use of approximations, while it can be used to analyze the effects of many factors on SE. The computation time and computer memory are also saved, which are very useful for the engineers that design the metallic enclosure.

In this paper, for an enclosure with apertures, an accurate aperture array admittance for use in the waveguide equivalent circuit model of Robinson *et al.* is presented. The enclosure is modeled as a short-circuited waveguide, the aperture array is characterized by an admittance. Additionally, the incident wave is modeled by a voltage source and free-space impedance in the equivalent circuit. Using this circuit model, SE for an off-center aperture, aperture array, high-order modes, enclosure loss, arbitrary incident angles, and polarization angles can be calculated. Then, main factors that affect the SE are analyzed, which can be referenced for the design and EMC of electronic equipment's enclosure.

II. TRANSMISSION LINE METHOD OF CALCULATING SE OF RECTANGULAR ENCLOSURE WITH APERTURE(S)

A. Enclosure with only one aperture

Based on Robinson *et al*'s method [12], the enclosure with one aperture (Fig. 1 (a)) can be modeled in Fig. 1 (b). The electric shielding at a distance p from the aperture is obtained from the voltage at a point P in the equivalent circuit, while the current at P gives the magnetic shielding. The radiating source is represented by voltage V_0 and impedance $Z_0 = 377$ Ω, and the enclosure by the shorted waveguide whose characteristic impedance and propagation constant are Z_{mg} and k_{mg}, respectively. The load impedance Z_l is included in this circuit model, which represents the loss of enclosure.
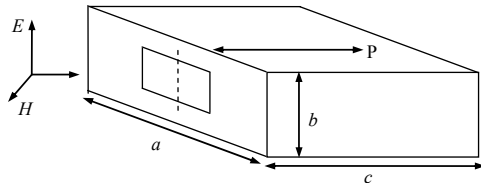
(a) Rectangular enclosure with one aperture.
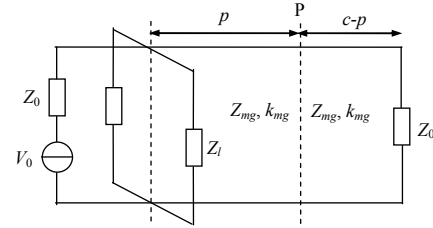

(b) Equivalent circuit.

Fig. 1. Rectangular enclosure with one aperture and its equivalent circuit.

The aperture is represented as a length of coplanar strip transmission line. According to Gupta's theory [13], the characteristic impedance of the transmission line can be given by,

$$Z_{os} = 120\pi^2 \left[\ln\left(2\frac{1+\sqrt[4]{1-(w_e/b)^2}}{1-\sqrt[4]{1-(w_e/b)^2}} \right) \right]^{-1} . \quad (1)$$

The effective width is given by

$$w_e = w - \frac{5t}{4\pi}\left(1+\ln\left(\frac{4\pi w}{t}\right)\right), \quad (2)$$

where t is the thickness of enclosure wall, w is the width of the aperture.

To calculate the aperture impedance Z_{ap}, we transform the load impedance Z_l at the end of the aperture in considering a distance $l/2$ to the centre,

$$Z_{ap} = \frac{1}{2}C_m Z_{os} \frac{Z_l + jZ_{os}\tan(k_0 l/2)}{Z_{os} + jZ_l \tan(k_0 l/2)}. \quad (3)$$

Figure 2 shows the coordinate system of the aperture, where l and w are the length and width of the aperture, respectively. X and Y are the aperture positions from the origin to the centre of the aperture, respectively. According to field continuity at the aperture, the coupling coefficient C_m [14] is introduced to account for higher-order modes and the coupling between the aperture and the enclosure, so the SE for off-centre aperture and higher order modes can be calculated.
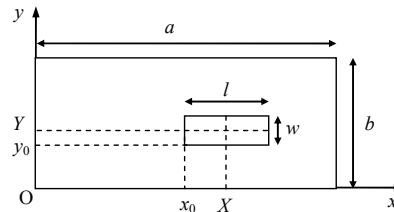

Fig. 2. Coordinate system of the aperture.

In many studies, the enclosure is modeled as a perfect conductor, whose conductivity is infinite, then $Z_l = 0$. But for a practical material, its impedance should be described as

$$Z_l = (1+j)\sqrt{\pi f \mu_1 / \sigma_1}, \qquad (4)$$

where μ_1 and σ_1 are magnetic permeability and conductivity of the enclosure, respectively.

Based on Thevenin's theorem, combining Z_0, V_0 and Z_{ap} gives an equivalent voltage and its impedance

$$V_1 = V_0 Z_{ap} / (Z_0 + Z_{ap}), \qquad (5)$$

$$Z_1 = Z_0 Z_{ap} / (Z_0 + Z_{ap}). \qquad (6)$$

Now transform V_1, Z_1 at the end of the waveguide to P, giving equivalent voltage V_2 and source impedance Z_2

$$V_2 = \frac{V_1}{\cos(k_{mg}p) + j(Z_1/Z_{mg})\sin(k_{mg}p)}, \qquad (7)$$

$$Z_2 = Z_{mg} \frac{Z_1 + jZ_{mg}\tan(k_{mg}p)}{Z_{mg} + jZ_1\tan(k_{mg}p)}. \qquad (8)$$

For the TE_{mn} mode of propagation, the waveguide's characteristic impedance and propagation constant respectively are

$$\begin{cases} Z_{mg} = Z_0 / \sqrt{1 - (m\lambda/2a)^2 - (n\lambda/2b)^2}, \\ k_{mg} = k_0 \sqrt{1 - (m\lambda/2a)^2 - (n\lambda/2b)^2}, \end{cases} \qquad (9)$$

where $k_0 = 2\pi/c$, and c is velocity of light in free space.

Now transform the equivalent impedance of the enclosure wall to P, giving load impedance Z_3,

$$Z_3 = Z_{mg} \frac{Z_l + jZ_{mg}[k_{mg}(c-p)]}{Z_{mg} + jZ_l[k_{mg}(c-p)]}. \qquad (10)$$

Then we can get the voltage at P by

$$V_{pm} = \frac{V_2 Z_3}{Z_2 + Z_3}. \qquad (11)$$

The current at P is

$$I_{pm} = \frac{V_2}{Z_2 + Z_3}. \qquad (12)$$

For all the wave modes in the enclosure, the total voltage at P is

$$V_{ptotal} = \sum V_{pm}. \qquad (13)$$

And the total current at P is

$$I_{ptotal} = \sum I_{pm}. \qquad (14)$$

In the absence of the enclosure, the load impedance at P is Z_0, the voltage and current at P are $V_p = V_0/2$ and $I_p = V_0/2Z_0$, respectively. Then the electric shielding and the magnetic shielding are given by

$$SE = 20\lg|V_{ptotal}/V_p| = 20\lg|V_0/2V_p|, \qquad (15)$$

$$SM = 20\lg|I_{ptotal}/I_p| = 20\lg|V_0/2Z_0V_p|. \qquad (16)$$

B. Enclosure with an array of apertures

(1) *With an array of rectangular apertures*

Sometimes, the enclosure has an array of identical rectangular apertures, as shown in Fig. 3.
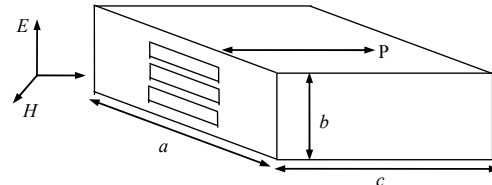
Fig. 3. Enclosure with an array of rectangular apertures.

If the apertures are distant from each other, the aperture array's impedance Z'_{ap} is calculated by

$$Z'_{ap} = kZ_{ap}, \qquad (17)$$

where k is the number of apertures. Equation (17) shows that the aperture array's impedance is the sum of that of each aperture. By replacing Z_{ap} in section A with Z'_{ap}, the SE is derived.

(2) *With an array of round apertures*

Sometimes, the enclosure may have an array of round apertures, as shown in Fig. 4.
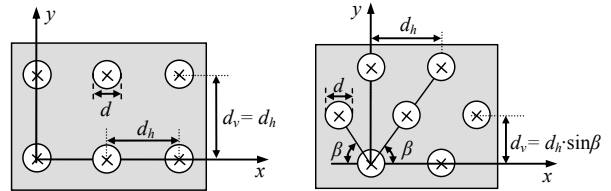
Fig. 4. Geometry of the enclosure with an array of round apertures arranged in the center of enclosure wall (square arrangement or at an angle of β).

In Fig. 4, the array of apertures can be represented by an appropriate admittance. Taking the mutual coupling between apertures into account and the normalized shunt admittance for both configurations is [15, 16],

$$\frac{Y_{ap}}{Y_0} = -j\frac{3d_h d_v \lambda_0}{\pi d^3} + j\frac{288}{\pi \lambda_0 d^2}$$

$$\cdot \left[\sum_{\substack{m=0 \\ m \neq odd}}^{\infty} \sum_{\substack{n=0 \\ n \neq odd}}^{\infty} \left(\frac{\varepsilon_m n^2}{d_v^2} + \frac{\varepsilon_n m^2}{d_h^2} \right) J_1^2(X) \right], \quad (18)$$

where λ_0 and Y_0 are the free-space wavelength and intrinsic admittance, respectively, d_v and d_h are the vertical and horizontal aperture separations assuming that aperture's diameter d is smaller than the separations.

In equation (18), $X = \frac{[\pi d(m^2/d_h^2 + n^2/d_v^2)/2]^{1/2}}{(m^2/d_h^2 + n^2/d_v^2)^{5/2}}$,

and the primes denote summation on even integers only, J_1 is the Bessel function of the first kind of the first order, and $\varepsilon_{m,n} = 1$ if m, $n = 0$ and 2 if m, $n \neq 0$. The second term in equation (18) can be neglected when d_v, d_h and d are much smaller than the wavelength.

In Fig. 4, the effective wall impedance Z'_{ap} is a fraction of Z_{ap}. Using an impedance ratio concept, Z'_{ap} becomes

$$Z'_{ap} = Z_{ap} \times \frac{l \times w}{a \times b}, \quad (19)$$

where l and w are the length and width of the array, respectively, and they are given by

$$l = d/2 + (k_1 - 1)d_h + d/2, \quad (20)$$

$$w = d/2 + (k_2 - 1)d_v + d/2, \quad (21)$$

where k_1 and k_2 are the number of apertures in length and width direction of the array, respectively. If the apertures are staggered arranged by an angle β, then $d_v = d_h \cdot \sin\beta$.

C. SE for any polarization angles and incident angles plane wave

It is worth noting that polarization angles are not considered in Robinson *et al.*'s method in the earlier analysis, and the plane wave is supposed as perpendicularly illuminating the enclosure wall with aperture(s).

If the plane wave is polarized at an angle φ, then the incident plane wave E can be divided into two components, which are vertical polarization component $E_v = E \cdot \sin\varphi$ and horizontal polarization component $E_h = E \cdot \cos\varphi$. Based on electromagnetic theory, the electric field propagation coefficient is

$$T = \frac{2Z_2}{Z_2 + Z_1}. \quad (22)$$

Equation (22) shows that when the wave illuminates a dividing boundary of two mediums, one part is reflected, and one part penetrates into the other medium. As to E_v, the penetration part is calculated as follows. The equivalent impedance can be calculated as that in section A for single aperture and section B for aperture array.

When the plane wave obliquely illuminates the enclosure wall with aperture(s) at an angle θ, Z_2 in equation (22) is given by $Z_2 = Z_{ap}/\cos\theta_T$, and $\cos\theta_T = \sqrt{1 - (\varepsilon_1 \sin^2\theta)/\varepsilon_2}$. Here, ε_1 and ε_2 are the electric permeability of the two medias. When the plane wave propagates from air into the enclosure, ε_1 is the electric permeability of air, and ε_2 is the equivalent electric permeability of aperture(s), $\varepsilon_2 = \mu_0/Z_{os}^2$. μ_0 is the equivalent magnetic permeability of the aperture(s), and it's equivalent to that of air. Z_1 in equation (22) is given by $Z_1 = Z_0/\cos\theta$. Then, the vertical electric field propagation coefficient T_v is given by,

$$T_v = \frac{2Z_2}{Z_2 + Z_1} = \frac{2Z_{ap}/\cos\theta_T}{Z_0/\cos\theta + Z_{ap}/\cos\theta_T}. \quad (23)$$

The vertical polarization component of electric field after penetrating the aperture(s) is given by $E_v^1 = T_v E_v$. As to E_h, Z_1 and Z_2 in equation (22) are respectively given by $Z_1 = Z_0 \cos\theta$ and $Z_2 = Z_{ap}\cos\theta_T$. Then, the horizontal electric field propagation coefficient T_h is given by,

$$T_h = \frac{2Z_2}{Z_2 + Z_1} = \frac{2Z_{ap}\cos\theta_T}{Z_0\cos\theta + Z_{ap}\cos\theta_T}. \quad (24)$$

The horizontal polarization component of electric field penetrating the aperture(s) is given by $E_h^1 = T_h E_h$. The equivalent circuits of the vertical polarization and horizontal polarization components of electric field propagating in the enclosure are given by Figs. 5 (a) and 5 (b), respectively.
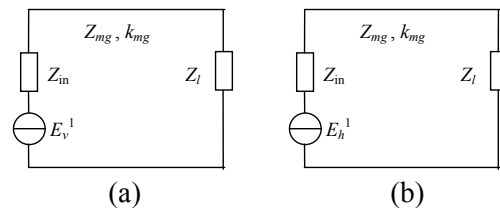

Fig. 5. Equivalent circuits of vertical polarization and horizontal polarization components of electric field propagating in the enclosure.

The electric voltage at P can be calculated as that in section A. For vertical polarization and horizontal polarization components of electric field, the total voltage are respectively given by $V_v^{total} = \sum V_v^{pm}$ and $V_h^{total} = \sum V_h^{pm}$. Then the total voltage at P is given by $V_{total} = \sqrt{(V_v^{total})^2 + (V_h^{total})^2}$, and the SE can be calculated using equations (15) and (16).

III. EXAMPLE AND ANALYSIS

Unless other specified, the simulation parameters are characterized as: the dimensions of enclosure is $300 \times 120 \times 300 \ mm^3$, thickness of enclosure wall made of copper is $t = 1.5 \ mm$. The coordinate of observation point P is $x = 225 \ mm$, $y = 60 \ mm$ and $z = 140 \ mm$. The plane wave perpendicularly illuminates the enclosure wall with aperture(s).

A. Single aperture case

For the validation of the proposed method, we consider a rectangular aperture, whose dimensions are $50 \times 5 \ mm^2$ (unless other specified, the aperture dimensions in the following is stationary). From Fig. 6, it can be observed that the calculated result using the proposed method is in well agreement with the results from [17].
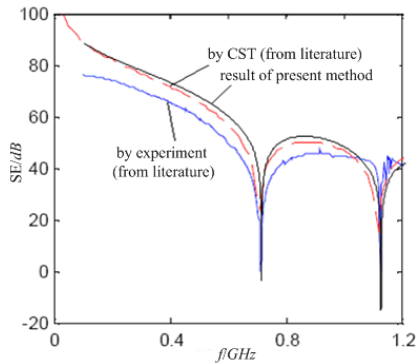

Fig. 6. Validation of present method for single aperture case.

(1) *Effect of aperture dimensions on SE*

Figure 7 shows that the SE becomes worse when the dimension of the aperture is enlarged. When the frequency is about 707 MHz and 1.12 GHz, the SE is negative, which is caused by resonance. The resonance frequency is calculated by,

$$f = \frac{1}{2\sqrt{\mu\varepsilon}} \sqrt{\left(\frac{m}{a}\right)^2 + \left(\frac{n}{b}\right)^2 + \left(\frac{l}{c}\right)^2}, \qquad (25)$$

where m, n, and l are determined by the wave modes in the enclosure. Using equation (25), we can get the resonance frequency point is 707 MHz for TE_{101} mode, and 1.12 GHz for TE_{201} mode. Based on microwave theory, it is known that the SE at resonance frequency will become negative which leads to the least value of SE.
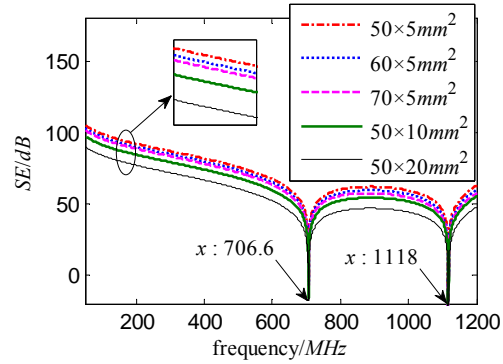
Fig. 7. Effect of aperture dimensions on SE.

(2) *Effect of enclosure dimension on SE*

The thickness of enclosure wall is $1 \ mm$, Fig. 8 shows SE for different enclosure dimensions.
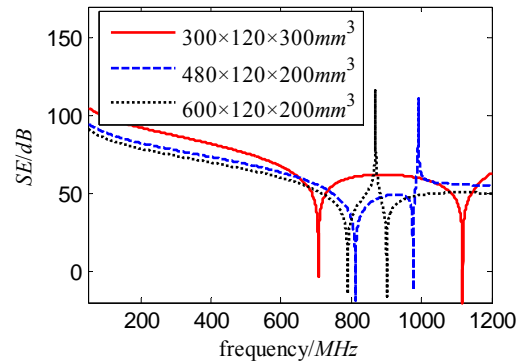
Fig. 8. Effect of enclosure dimensions on SE.

Using equation (25), we can deduce that in the frequency band of 0~1.2 GHz, the three enclosures all have two resonance frequencies. The resonance frequencies of first enclosure are about 707 MHz and 1.12 GHz, those of the second are about 312.3 MHz and 624.6 MHz, and those of the third are about 249.9 MHz and 499.7 MHz. All the upper resonance frequencies can be found from Fig. 8. The SE is negative at resonance frequencies, and

does not change monotonously as the enclosure is enlarged.

(3) *Effect of observation point's position on SE*

When the frequencies of the plane wave is $f = 0.75$ GHz, 0.90 GHz or 1.20 GHz, as p changes, the SE at point P is shown in Fig. 9.
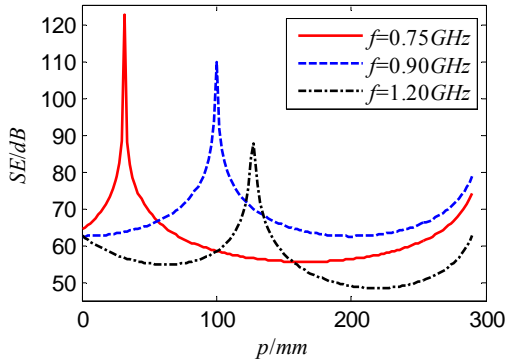
Fig. 9. Effect of observation point's position on SE.

It is shown that the SE does not change as intuition or literatures [18, 19]: the SE is better when p is larger. The SE does not monotonously reduce or increase as p changes. When the frequency of the incident plane wave is $f = 0.75$ GHz, there is only TE_{10} mode in the enclosure, the SE is best when $p = 32$ mm, and worst when $p = 164$ mm. When $f = 0.90$ GHz, there is also only TE_{10} mode in the enclosure, the SE is best when $p = 100$ mm, and worst when $p = 201$ mm. When $f = 1.20$ GHz, there are TE_{10} and TE_{20} modes in the enclosure, the SE is best when $p = 128$ mm, and worst when $p = 216$ mm. So we know that the SE is not only related with p, but also with frequency of incident plane wave. Based on electromagnetic theory, we can get the following laws.

For the TE_{mn} or TM_{mn} mode in the enclosure, the SE is worst when

$$p_{\min} = c - i\lambda_y / 4, \ \ i = 1,3,5,\cdots,$$

and the SE is best when

$$p_{\max} = c - i\lambda_y / 2, \ \ i = 0,1,2,\cdots,$$

where $\lambda_y = 2 / \sqrt{(2f/c)^2 - (m/a)^2 - (n/b)^2}$.

It can be observed that the sensitive component can be set based on the upper laws.

(4) *Effect of aperture's position on SE*

Figure 10 shows the SE for the same aperture at three different positions. In conclusion, the SE

of the middle aperture is the worst. The nearer the aperture is to the edge the better SE is obtained. This model allows us to determine the SE not only in the centre of the enclosure but also for any other positions, which is impossible with Robinson *et al*'s model. Based on the results, electronic engineers should place apertures at the edges of the enclosure.
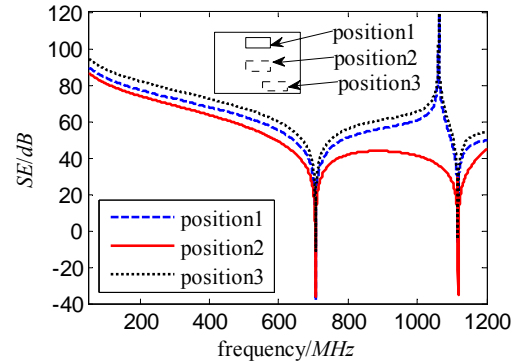

Fig. 10. Effect of aperture's position on SE.

(5) *Effect of enclosure wall's thickness and material conductivity on SE*

When the enclosure wall's thickness t and material conductivity are changed, respectively, the SE are shown in Figs. 11 (a) and 11 (b). Figure 11 (a) shows that the SE is better as t is increased. This is because when t is increased, electromagnetic energy penetrating into the enclosure is decreased. But t only has a little effect on SE. Figure 11 (b) shows when increasing the material conductivity, the SE is stationary.

(6) *Effect of ratio between aperture's length and width*

The thickness of enclosure wall is 1 mm. The area of aperture is 250 mm^2, and the dimensions of aperture is 50×5 mm^2, 15.8×15.8 mm^2 or 5×50 mm^2, respectively. Figure 12 shows that SE is better when the ratio of aperture's length and width is reduced. This is because electromagnetic energy transmitted into the enclosure is decreased when decreasing the ratio.

B. An array of apertures case

For the validation of the proposed method in the case of apertures array, we consider an enclosure with one large aperture or three smaller ones located at center of its side wall. The three

smaller apertures are identical, with dimensions of $10 \times 1.0\ cm^2$ and their vertical separation d is $2\ cm$. The area of the large aperture is equal to the total areas of the three apertures. Figure 13 shows that the results calculated by present method are in well agreement with the results from [20].
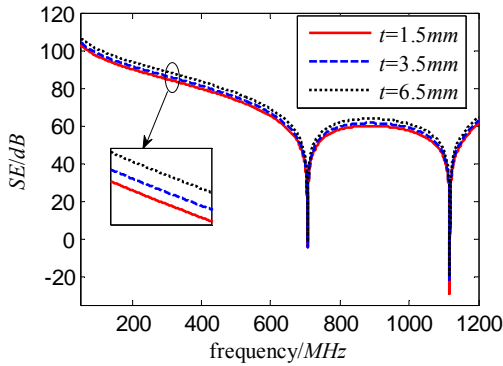
(a) Effect of enclosure wall's thickness.
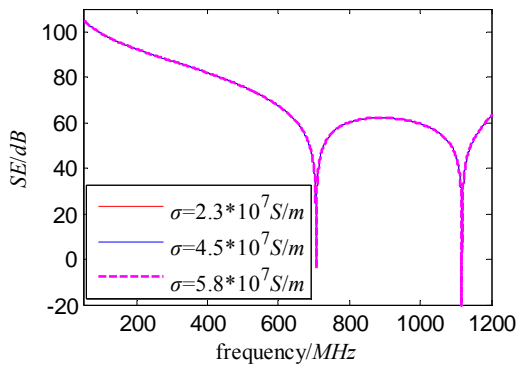
(b) Effect of material conductivity.

Fig. 11. Effect of enclosure wall's thickness and material conductivity on SE.
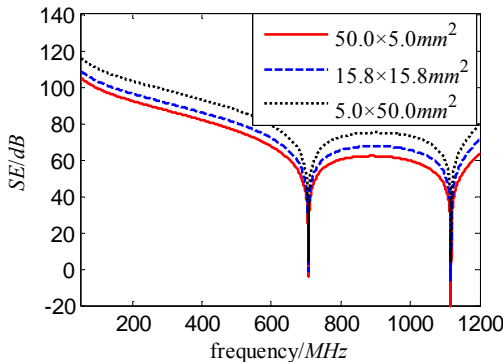

Fig. 12. Effect of ratio of aperture's length and width.
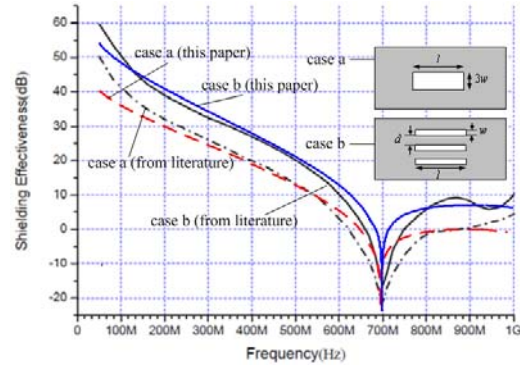
Fig. 13. Validation of present method for aperture array case.

(1) *Effect of aperture shape on SE*

Case 1: the number of rectangular apertures is $k = 3$, and the dimensions of each aperture is $50 \times 10\ mm^2$. Case 2: the number of square arrangement round apertures shown in Fig. 4 is 5×3, the distance between two adjacent apertures is $d_v = d_h = 20\ mm$, the radius of each aperture is about 5.64 mm in order to guarantee that the total area of round apertures is equivalent to that of rectangular apertures in case 1. Figure 14 shows that if the area of rectangular and round apertures are equivalent, the SE is better for round apertures.
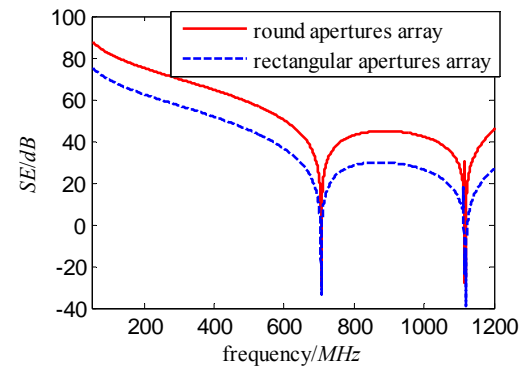
Fig. 14. Effect of aperture shape on SE.

(2) *Effect of number of round apertures on SE*

An enclosure wall has an array of round apertures, when d_v, d_h, and the total area of apertures S_1 are stationary, only the diameter of aperture d is variable, Fig. 15 (a) shows the SE for three cases. When the area of apertures array S_2 and the diameter of aperture d are stationary, only the number of apertures is variable, Fig. 15 (b) shows the SE for this case.

(a) d_v, d_h and S_1 are stationary, only the number of apertures is variable.

(b) S_2 and d are stationary, only the number of apertures is variable.

Fig. 15. Effect of number of round apertures on SE.

Figure 15 (a) shows that when d_v, d_h and S_1 are stationary, by reducing the diameter of round aperture, the SE can be improved. Figure 15 (b) shows that when S_2 and d are stationary, by reducing the distance d_v and d_h, and increasing the number of apertures, the SE is reduced.

(3) *Effect of rectangular apertures' number on SE*

The enclosure has an array of rectangular apertures, and there are three cases of the array. Case 1: dimensions of aperture is $l \times w = 50 \times 5$ mm^2, the apertures' number k is variable. Case 2: total area of apertures and aperture length l are stationary, aperture width w and number of apertures k are variable. Case 3: total area of apertures and aperture width w are stationary, the aperture length l and number of apertures k are variable. Figures 16 (a), (b), and (c) shows the SE for the three cases, respectively.

(a) The area of single aperture is stationary, and number of apertures is variable.
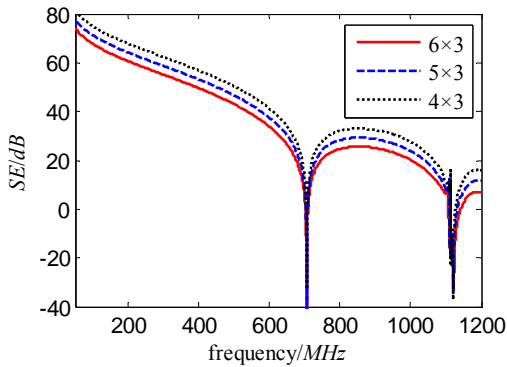
(b) Total area of apertures is stationary, the width of aperture and number of apertures are variable.
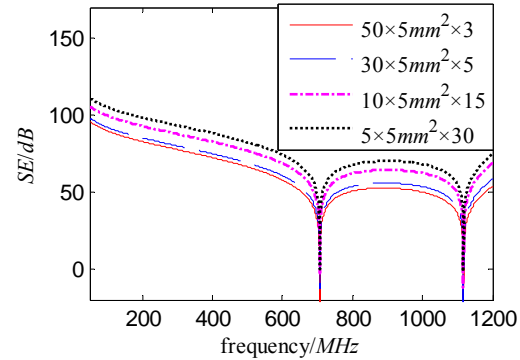
(c) Total area of apertures is stationary, the length of aperture and number of apertures are variable.

Fig. 16. Effect of rectangular apertures' number.

Figure 16 (a) shows that if the area of single aperture and ratio of aperture length and width are stationary, the SE is reduced with increasing the number of apertures. Figure 16 (b) shows that if the area of apertures and aperture length are stationary, by reducing the aperture width, the

number of apertures is increased, but the SE is not changed monotonously for this case. Figure 16 (c) shows that if the area of apertures and aperture width are stationary, by reducing the aperture length, the number of apertures is increased, then the SE is improved.

(4) *Effect of aperture array's arrangement on SE*

There is an aperture array that contains square and round apertures, and it is arranged by two styles. The radius of round aperture is $r = 5$ *mm*, and the length of square aperture is $w = 1$ *cm*. The adjacent apertures are distant from each other. Figure 17 shows the SE is stationary when the arrangement of apertures is changed.
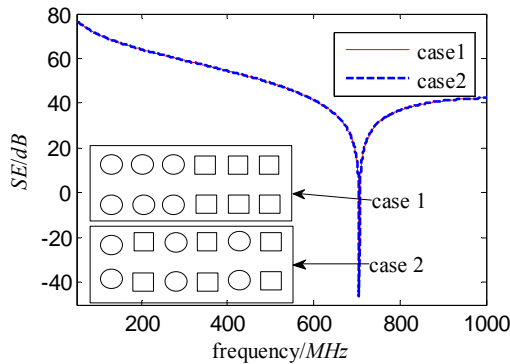
Fig. 17. Effect of aperture array's arrangement on SE.

## C. Effect of polarization angles and incident angles on SE

Suppose that there is an aperture at the center of the enclosure wall. The dimensions of the aperture are 100×5 *mm*^{2}. The frequency and incident angle θ of incident plane wave is 700 MHz and 90^0, respectively, when polarization angle φ varies from 0^0 to 88^0, the SE is depicted in Fig. 18 (a). It can be observed that the results calculated by present method and that from [21] are consistent, which validates the proposed method.

Figure 18 (b) shows the SE for the case that polarization angle φ of incident plane wave is 30^0, 45^0, and 60^0, respectively, and incident angle θ changes from 0^0 to 180^0. It's shown that when θ changes from 0^0 to 90^0, the SE is improved. When θ changes from 90^0 to 180^0, the SE is reduced.
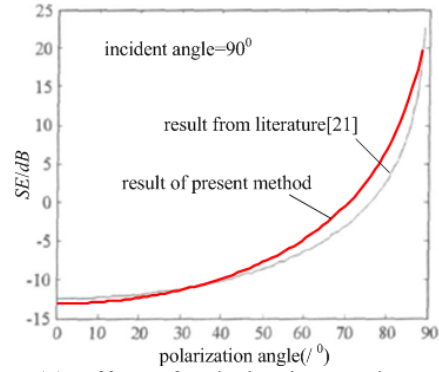
(a) Effect of polarization angles.
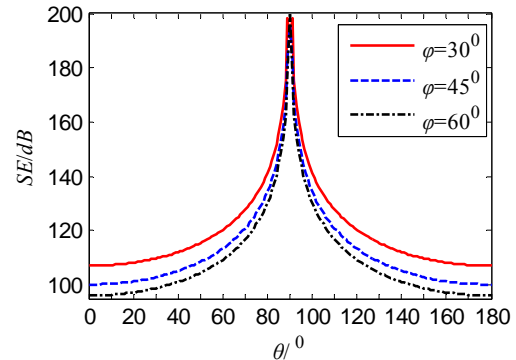
(b) Effect of incident angles.

Fig. 18. Effect of polarization angles and incident angles on SE.

IV. CONCLUSION

In this paper, an efficient analytical approach based on Robinson *et al.*'s model has been presented to predict the SE of enclosures with off-centre apertures, numerous apertures, and for any polarization angles and incident angles plane wave. The calculation of the electric shielding depends on the frequency, polarization, and incident angles of the incident wave, the dimensions of the enclosure and the aperture(s), the number of apertures, the degrees of closeness, the position of aperture(s), etc. The method described in this paper has good agreement with other methods over a wide frequency range. The estimation of the SE based on the proposed method has offered a cost-effective alternative to the numerical techniques through saving computing resources. Solution time is the key advantage of the proposed model. Therefore, this study may be helpful in designing an effective shield to achieve better shielding performance.

REFERENCES

[1] H. A. Mendez, "On the theory of low-frequency excitation of cavity resonances," *IEEE Trans. Microwave Theory Tech.*, vol. 18, pp. 444-448, 1970.

[2] H. A. Mendez, "Shielding theory of enclosures with apertures," *IEEE Trans. Electromagn. Compat.*, vol. 20, pp. 296-305, May 1978.

[3] H. A. Bethe, "Theory of diffraction by small holes," *Phys. Rev.* II, vol. 66, pp. 163-182, 1944.

[4] W. Wallyn, D. De Zutter, and E. Laermans, "Fast shielding effectiveness prediction for realistic rectangular enclosures," *IEEE Trans. Electromagn. Compat.*, vol. 45, no. 4, pp. 639-643, 2003.

[5] B. Audone and M. Balma, "Shielding effectiveness of apertures in rectangular cavities," *IEEE Trans. Electromagn. Compat.*, vol. 31, no. 1, pp. 102-106, 1989.

[6] Jr. W. P. Carpes, G. S. Ferreira, and A. Raizer, *et al*, "TLM and FEM methods applied in the analysis of electromagnetic coupling," *IEEE Trans. Magn.*, vol. 36, no. 4, pp. 982-985, 2000.

[7] V. Rajamani, C. F. Bunting, and M. D. Deshpande, *et al*, "Validation of modal/ MoM in shielding effectiveness studies of rectangular enclosures with apertures," *IEEE Trans. Electromagn. Compat.*, vol. 46, no. 2, pp. 348-353, 2006.

[8] J. Chen and A. X. Zhang, "A Subgridding scheme based on the FDTD method and HIE-FDTD method," *Appl. Comp. Electro. Society (ACES) Journal*, vol. 26, no. 1, pp. 1-7, 2011.

[9] W. Abdelli, X. Mininger, and L. Pichon, *et al*, "Impact of composite materials on the shielding effectiveness of Enclosures," *Appl. Comp. Electro. Society (ACES) Journal*, vol. 27, no. 4, pp. 369-375, 2012.

[10] P. Dehkhoda, A. Tavakoli, and M. Azadifar, "Shielding effectiveness of an enclosure with finite wall thickness and perforated opposing walls at oblique incidence and arbitrary polarization by GMMoM," *IEEE Trans. Electromagn. Compat.*, vol. 54, no. 4, pp. 792-805, 2012.

[11] N. Fichtner and P. Russer, "A hybrid TLM-integral equation method using time–domain plane-waves for shielding effectiveness computations," *26th Annual Review of Progress in Appl. Comp. Electro. Society (ACES)*, Tampere, Finland, pp. 404-409, April, 2010.

[12] M. P. Robinson, T. M. Benson, and C. Christopoulos, *et al*, "Analytical formulation for the shielding effectiveness of enclosures with apertures," *IEEE Trans. Electromagn. Compat.*, vol. 40, no. 3, pp. 240-248, 1998.

[13] K. C. Gupta, R. Garg, and I. J. Bahl, *Microstrip Lines and Slot Lines*, Artech House, Norwood, MA, 1979, Ch.7.

[14] D. Shi, Y. Shen, and Y. Gao, "3 High-order mode transmission line model of enclosure with off-center aperture," *IEEE Int. Symp. on Electromagn. Compat.*, pp. 361-364, October, 2007.

[15] T. Y. Otoshi, "A study of microwave leakage through perforated flat plates," *IEEE Trans. Microw. Theory Tech.*, vol. 20, no. 3, pp. 235-236, 1972.

[16] W. Culshaw, "Reflectors for a microwave Fabry–Perot interferometer," *IEEE Trans. Microw. Theory Tech.*, vol. 7, no. 2, pp. 221-228, 1959.

[17] X. H. Chen, "Research on composite shielding effectiveness computing method and equipments electromagnetic protection envelope," *Doctoral Thesis of Shi Jia Zhuang, Mechanical Engineering College*, China, 2011.

[18] H. Song, D. F. Zhou, and D. T. Hou, *et al*, "Hybrid algorithm for slot coupling of double layer shielding cavity," *High Power Laser and Particle Beams*, vol. 20, no. 11, pp. 1892-1898, 2008.

[19] L. Wang and Y.Gao, "Analysis of shielding effectiveness for rectangular cavity with apertures and resonance suppression," *Chinese Journal of Radio Science*, vol. 23, no. 3, pp. 560-564, 2008.

[20] G. Wu, X. Zhang, and B. Liu, "A Hybrid method for predicting the shielding effectiveness of rectangular metallic enclosures with thickness apertures," *J. of Electromagn. Waves and Appl.*, vol. 24, pp. 1157-1169, 2010.

[21] X. F. Zhang, Y. Li, and G. Y. Ni, *et al*, "Hybrid model to evaluating shielding effectiveness of cavity with apertures," *Chinese Journal of Radio Science*, vol. 26, no. 1, pp. 25-29, 2011.

Chuan-Chuan Wang received the B. A. and M. Sc. degrees in Electrical Engineering from Shi Jia Zhuang, Mechanical Engineering College, China, in 2007 and 2009, respectively. He is currently working toward the Ph.D. degree in electromagnetic protection engineering in Shi Jia Zhuang, Mechanical Engineering College. His research interests include transmission-line theory, EMC, and EM protection.

Chang-Qing Zhu received the M.Sc. degree in Measurement Engineering from the North University of China, Shan xi, China, in 1987, and the Ph.D. degree in electromagnetic protection engineering from Shi Jia Zhuang, Mechanical Engineering College, China, in 2005.

He is currently a Professor in the Mechanical Engineering College. His current research interests include Test of Electromagnetic field, Automation of electrical system, and EMC.

Xing Zhou received the M.Sc. degree in Electrical Engineering from National University of Defense Technology, Hunan, China, in 2002, and the Ph.D. degree in electromagnetic protection engineering from Shi Jia Zhuang, Mechanical Engineering College, China, in 2006.

She is currently a Lecturer in Shi Jia Zhuang, Mechanical Engineering College. Her research interests include transmission-line theory, EMC, and EM protection.

Zhi-Feng Gu received the B. A. and M. Sc. degrees in Electrical Engineering from Hebei University of Technology, Tian jin, China, in 2002 and 2005, respectively.

He is currently a Lecturer and working toward the Ph.D. degree in control engineering at the Shi Jia Zhuang, Mechanical Engineering College. His research interests include control theory and techniques, and automation of electrical system.

Multi-Resonance Monopole Antenna with Variable Band-Notch Performance for UWB Applications

Nasser Ojaroudi[1], Mohammad Ojaroudi[2], and Noradin Ghadimi[2]

[1]Department of Electrical Engineering
Germi Branch, Islamic Azad University, Germi, Iran
n.ojaroudi@yahoo.com

[2]Young Researchers Club
Ardabil Branch, Islamic Azad University, Ardabil, Iran
m.ojaroudi@iauardabil.ac.ir, noradin.ghadimi@gmail.com

Abstract — In this paper, a novel multi-resonance monopole antenna with frequency band-notched function is presented. By cutting a pair of rotated Ω-shaped slots in the ground, the bandwidth is improved, that achieves a fractional bandwidth with multi resonance performance of more than 160 %. In order to achieve single band-rejected function an S-shaped parasitic structure was inserted in the ground plane and a frequency notched band of 5.03 GHz – 5.98 GHz has been received. The measured results reveal that bandwidth of proposed antenna is from 2.75 GHz to 18.73 GHz for VSWR < 2. Simulated and experimental results obtained for this antenna show that it exhibits good radiation behavior within the UWB frequency range. The designed antenna has a small size of 12×18 mm^2.

Index Terms — Band-notched performance, square monopole antenna, S-shaped parasitic structure, and ultra-wideband systems.

I. INTRODUCTION

In UWB communication systems, one of the key issues is the design of a compact antenna while providing wideband characteristic over the whole operating band. Consequently, a number of planar monopoles with different geometries have been experimentally characterized [1-2]. Moreover, other strategies to improve the impedance bandwidth have been investigated [3-7].

The federal communication commission (FCC)'s allocation of the frequency range 3.1 GHz – 10.6 GHz for UWB systems, which will cause interference to the existing wireless communication systems, such as, the wireless local area network (WLAN) for operating in 5.15 GHz – 5.35 GHz and 5.725 GHz – 5.825 GHz bands. Thus, the UWB antenna with a single band-stop performance is required. Lately to generate the frequency band-notch function, several modified planar antennas with band-notch characteristic have been reported [8-11]. In [8-10], different shapes of the slits (i.e., square ring, W-shaped, and folded trapezoid) are used to obtain the desired band notched characteristics. Single and multiple half-wavelength U-shaped slits are embedded in the radiation patch to generate the single and multiple band-notched functions, respectively [11].

In this paper, a new multi-resonance small square monopole antenna with a frequency-notch function is presented. In the proposed structure, by inserting two rotated Ω-shaped slots in the ground plane, multi-resonance characteristic can be achieved where the proposed antenna can operate from 2.75 GHz to 18.73 GHz. In order to generate a single notch function we insert an S-shaped parasitic structure in the ground plane. The designed antenna has a small size of 12×18 mm^2. Good VSWR and radiation pattern characteristics are obtained in the frequency band of interest.

II. ANTENNA DESIGN

Figure 1 shows the geometry of the proposed planar monopole antenna that fed by a microstrip line, which is printed on an FR4 substrate of thickness 1.6 mm, permittivity 4.4, and loss tangent 0.018. As shown in Fig. 1, the presented antenna consists of a square radiating patch and modified ground plane with a pair of rotated Ω-shaped slots and an S-shaped parasitic structure. The basic antenna structure consists of a square patch, a feed line, and a ground plane. The square patch has a width W. The patch is connected to a feed line of width W_f and length $L_f + L_{gnd}$. On the other side of the substrate, a conducting ground plane of width W_{sub} and length L_{gnd} is placed. The proposed antenna is connected to a 50 Ω SMA connector for signal transmission.

In this design, to achieve a multi-resonance function and provide a bandwidth enhancement performance, two rotated Ω-shaped slots are inserted in the ground plane. By adding an S-shaped parasitic structure in the ground plane, frequency band notch function (5.03 GHz -5.98 GHz WLAN) is generated. Regarding defected ground structures (DGS), the creating slots in the ground plane provide an additional current path. Moreover, this structure changes the inductance and capacitance of the input impedance, which in turn leads to change in bandwidth. The DGS applied to a microstrip line causes a resonant character of the structure transmission with a resonant frequency controllable by changing the shape and size of the slots [10]. Therefore, by cutting two rotated Ω-shaped slots at the ground plane and carefully adjusting its parameters, much enhanced impedance bandwidth may be achieved. As illustrated in Fig. 1, the S-shaped conductor-backed plane is placed under the radiating patch. The conductor-backed plane perturbs the resonant response and also acts as a parasitic half-wave resonant structure electrically coupled to the square monopole [9]. At the notch frequency, the current flows are more dominant around the parasitic element, and they are oppositely directed between the parasitic element and the radiation patch. As a result, the desired high attenuation near the notch frequency can be produced. The variable band-notch characteristics can be achieved by carefully choosing the parameter (W_S and L_S) for the S-shaped conductor-backed plane. In this structure, the length W_S, is the critical

parameter to control the filter bandwidth. On the other hand, the center frequency of the notched band is insensitive to the change of W_S. The resonant frequency of the notched band is determined by L_S.

In this work, we start by choosing the dimensions of the designed antenna. These parameters, including the substrate, is $W_{Sub} \times L_{Sub}$ = 12 mm $\times$ 18 mm or about 0.15 $\lambda \times$ 0.25 λ at 4.2 GHz (the first resonance frequency). We have a lot of flexibility in choosing the width of the radiating patch. This parameter mostly affects the antenna bandwidth. As W_X decreases, so does the antenna bandwidth, and vice versa. Next step, we have to determine the length of the radiating patch L_X. This parameter is approximately $\lambda_{lower}/4$, where λ_{lower} is the lower bandwidth frequency wavelength. λ_{lower} depends on a number of parameters such as the radiating patch width as well as the thickness and dielectric constant of the substrate on which the antenna is fabricated [12]. The important step in the design is to choose $L_{resonance}$ (the length of the resonators), L_{notch} (the length of the filter). $L_{resonance}$ is set to resonate at $0.25\lambda_g$, where $L_{resonance3} = 2(L_X-L_{X1})+W_{X1}+W_{X2}$, and $L_{resonance4} = L_{X1}+W_X$, λ_g corresponds to the resonance frequencies wavelength (11.2 GHz is the third resonance frequency and 17.1 GHz is the fourth resonance frequency). L_{notch} is set to band-stop resonate at $0.5\lambda_g$, where $L_{notch} = L_{S1}+W_S+2W_{S1}$, λ_g corresponds to notched band frequency wavelength (5.5 GHz is the notched frequency).

The optimized values of the proposed antenna design parameters are as follows: W_{sub} = 12 mm, L_{sub} = 18 mm, h_{sub} = 1.6 mm, W_f = 2 mm, L_f = 3.5 mm, W = 10 mm, W_S = 1.25 mm, L_s = 14 mm, W_{S1} = 0.25 mm, L_{S1} = 13.5 mm, W_{S2} = 0.5 mm, W_X = 4.5 mm, L_X = 2 mm, W_{X1} = 4 mm, L_{X1} = 1.25 mm, W_{X2} = 0.25 mm, L_{X2} = 0.25 mm, and L_{gnd} = 3.5 mm.

III. RESULTS AND DISCUSSIONS

In this section, the microstrip monopole antenna with various design parameters were constructed, and the numerical and experimental results of the input impedance and radiation characteristics are presented and discussed. The proposed microstrip-fed monopole antenna was fabricated and tested to demonstrate the effect of the presented. The parameters of this proposed

antenna are studied by changing one parameter at a time and fixing the others. Ansoft HFSS simulations are used to optimize the design and agreement between the simulation and measurement is obtained [13].


(a)

(b)
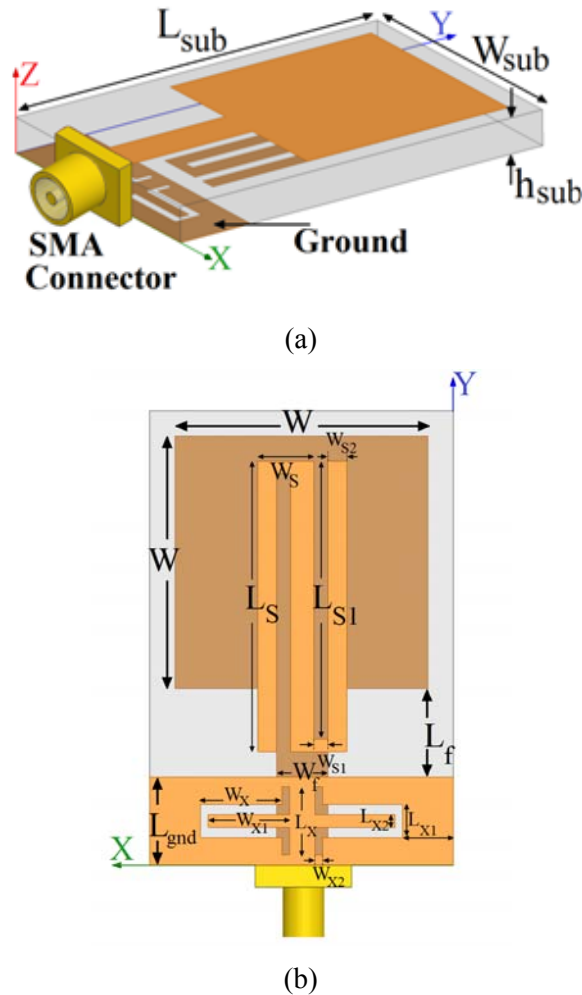
Fig. 1. Geometry of the proposed square monopole antenna; (a) bottom view and (b) side view.

The configuration of the various antennas structures were shown in Fig. 2. VSWR characteristics for ordinary square patch antenna, square antenna with two rotated Ω-shaped slots in the ground plane and the proposed antenna structure are compared in Fig. 3. As shown in Fig. 3, it is observed that the upper frequency bandwidth is affected by using a pair of rotated Ω-shaped slots in the ground plane and the notch frequency, which is sensitive to the S-shaped parasitic structure.
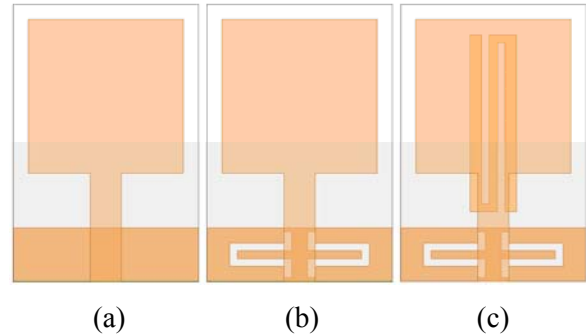

Fig. 2. (a) The ordinary square monopole antenna, (b) antenna with a pair of rotated Ω-shaped slots in the ground plane, and (c) the proposed square monopole antenna.
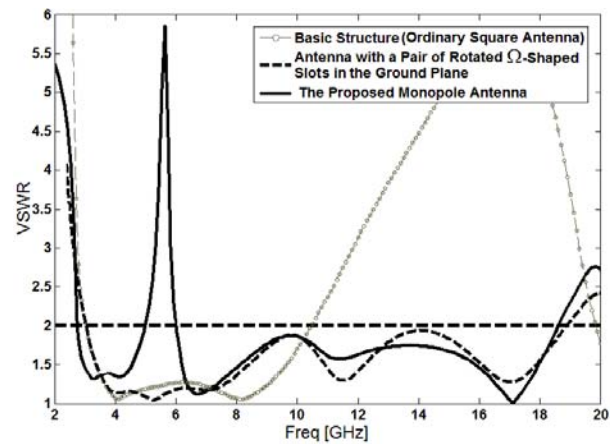
Fig. 3. Simulated VSWR characteristics for the various square monopole antenna structures shown in Fig. 2.

To understand the phenomenon behind this multi resonance performance, the simulated current distributions on the ground plane for the square antenna with two rotated Ω-shaped slots at 11.2 GHz and 17.1GHz are presented in Figs. 4 (a) and (b). It can be observed in Figs. 4 (a) and (b) that the current is concentrated on the edges of the interior and exterior of the two rotated Ω-shaped slots at 11.2 GHz and 17.1 GHz. Therefore, the antenna impedance changes at these frequencies due to the resonant properties of the rotated Ω-shaped slots. It is found that by using these slots, third and fourth resonances are generated at 11.2 GHz and 17.1 GHz, respectively [14]. Another important design parameter of this structure is the S-shaped parasitic structure used in the ground plane. Figure 4 (c) presents the simulated current distributions on the modified ground plane at the

notch frequency (5.5 GHz). As shown in Fig. 4 (c), at the notch frequency the current flows are more dominant around of the S-shaped parasitic structure. As a result, the desired high attenuation near the notch frequency can be produced [11].


(a)   (b)   (c)
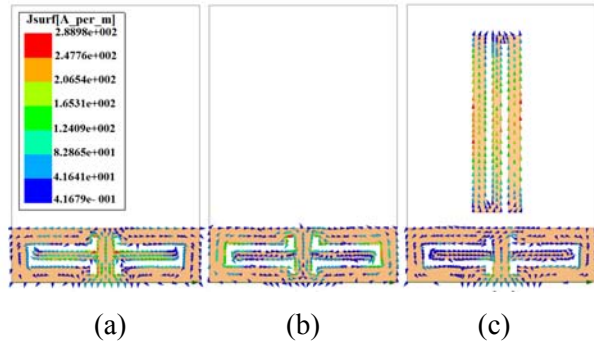
Fig. 4. Simulated surface current distributions on the ground plane for (a) the square antenna with a pair of Ω-shaped slots in the ground plane at a third resonance frequency (11.2 GHz), (b) at fourth resonance frequency (17.1 GHz), and (c)) for the proposed antenna at the notch frequency (5.5 GHz).

The simulated VSWR curves with different values of L_S are plotted in Fig. 5. As shown in Fig. 5, when the height of the L_S increases from 12.5 mm to 15 mm, the centre of the notch frequency decreases from 6.4 GHz to 4.9 GHz and from these results, we can conclude that the notch frequency is controllable by changing the interior height of the L_S. The simulated VSWR curves with different values of W_S are plotted in Fig. 6. As shown in Fig. 6, when the width of W_S increases from 0.75 mm to 2 mm, the filter bandwidth has a various size and with $W_S = 1.25$ mm, we provide a good bandwidth of the notch frequency.

The simulated input signal and impulse response for the proposed antenna is shown in Fig. 7. A first-order Rayleigh pulse is used as the source signal to drive the transmitter [8]. One of the characteristics of UWB signals is pulse distortion, which is inherently determined by their huge bandwidth. Good impedance matching over the operating frequency band is desired to minimize the reflection loss and to avoid pulse distortion [8]. Therefore, the signal distortions shown in Fig. 7 are mainly due to the bandwidth mismatch between the source pulse and the antenna. As a result, some frequency components

of the pulse cannot be transmitted effectively by the monopole, leading to the distortions of the received signal.
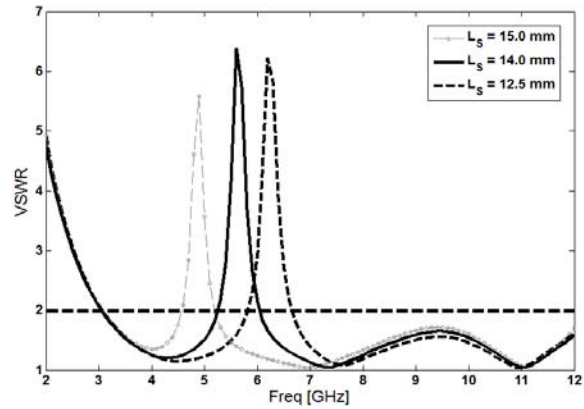

Fig. 5. Simulated VSWR characteristics for the proposed antenna with different values of L_S.
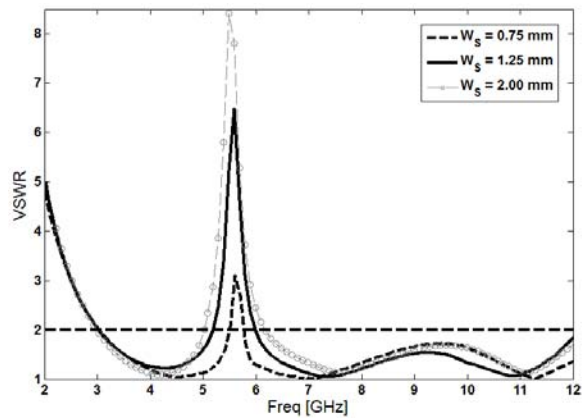
Fig. 6. Simulated VSWR characteristics for the proposed antenna with different values of W_S.
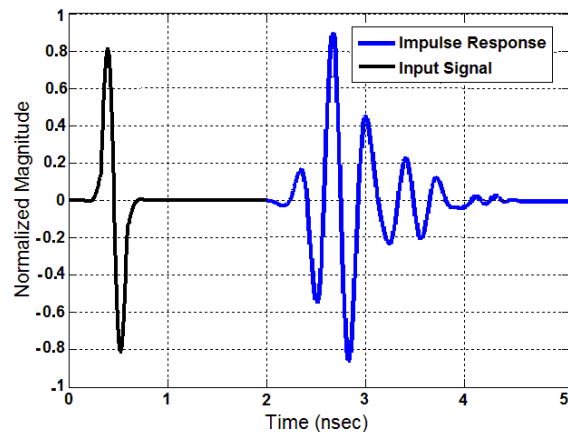
Fig. 7. Simulated time-domain analysis (input signal and impulse response).

A prototype of the proposed monopole antenna was fabricated and tested in the antenna laboratory at the Microwave Technology Company (MWT), and the VSWR were measured using an HP 8720ES network analyzer in an anechoic chamber. The measured and simulated VSWR characteristics of the proposed antenna are shown on Fig. 8. The fabricated antenna has a frequency band of 2.75 GHz to over 18.73 GHz with notched-band function around 5.03-5.98. As shown in Fig. 8, there exists a discrepancy between measured data and simulated results.

The radiation patterns have been measured inside an anechoic chamber using a double-ridged horn antenna as a reference antenna placed at a distance of 2 m. Figure 9 illustrates the measured radiation patterns, including the co-polarization and cross-polarization, in the H–plane (x-z plane) and E-plane (y-z plane). It can be seen that the radiation patterns in the x-z plane are nearly omnidirectional for three frequencies.
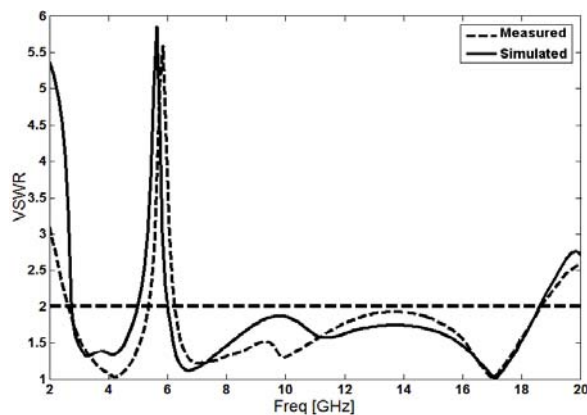

Fig. 8. Measured and simulated VSWR for the proposed antenna.

Figure 10 shows the effects of the rotated Ω-shaped slots and the S-shaped parasitic structure in the ground plane on the maximum gain in comparison to the ordinary slot antenna without them. A two-antenna technique using an Agilent E4440A spectrum analyzer and a double-ridged horn antenna as a reference antenna placed at a distance of 2 m, is used to measure the radiation gain in the z-axis direction (x-z plane). As shown in Fig. 10, the ordinary antenna has a gain that is low at 3 GHz and increases with frequency. It is found that the gain of the ordinary monopole antenna is decreased with the use of the

rotated Ω-shaped slots and the S-shaped parasitic structure in the ground plane. It can be observed in Fig. 10 that by using these structures, a sharp decrease of maximum gain in the notched frequency band at 5.5 GHz are shown. For other frequencies outside the notched frequencies band, the antenna gain with the filter is similar to those without it.
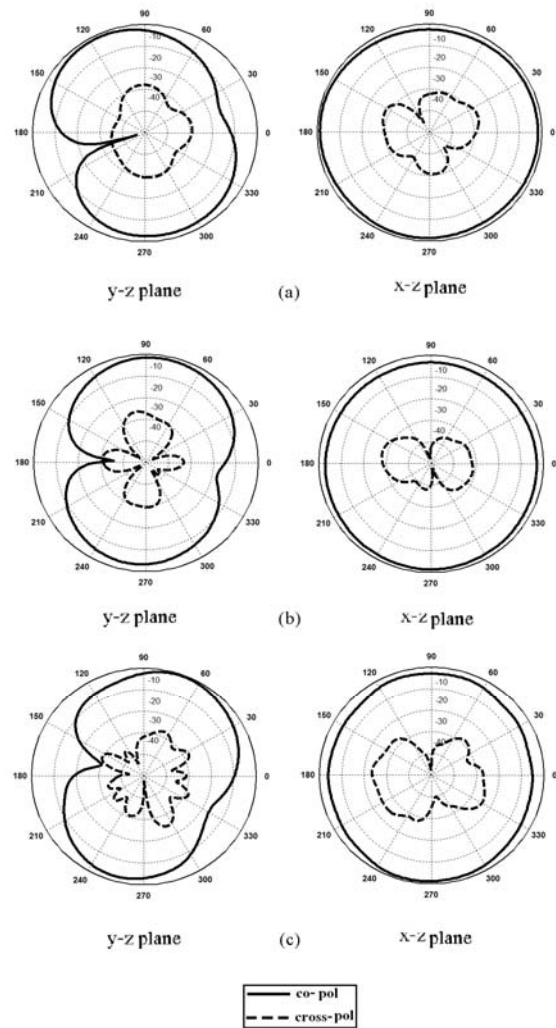

Fig. 9. Measured radiation patterns of the proposed antenna at (a) 4 GHz, (b) 7 GHz, and (c) 10 GHz.

IV. CONCLUSION

In this paper, we present a novel multi-resonance microstrip-fed square monopole antenna for UWB applications with band-notch performance. The proposed antenna can operate from 2.75 GHz to 18.73 GHz with WLAN

rejection band around 5.03 GHz – 5.98 GHz. In order to enhance the bandwidth we cut two rotated Ω-shaped slots in the ground plane, and also by inserting an S-shaped parasitic structure, a frequency band-notch function can be achieved. The designed antenna has a small size of 12×18 mm². Simulated and experimental results show that the proposed antenna could be a good candidate for UWB application.
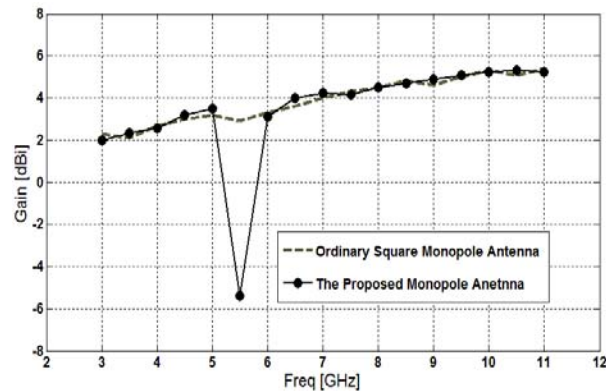

Fig. 10. Maximum gain comparisons for the ordinary monopole antenna (simulated), and the proposed antenna (measured) in the z-axis direction (x-z plane).

ACKNOWLEDGMENT

REFERENCES

[1] M. Ojaroudi, Sh. Yzdanifard, N. Ojaroudi, and M. Nasser-Moghaddasi, "Small square monopole antenna with enhanced by using inverted T-shaped slot and conductor-backed plane," *IEEE Transactions on Antenna and Propagation*, vol. 59, no. 2, pp. 670-674, Feb. 2011.

[2] M. Ojaroudi, G. Kohneshahri, and Ja. Noory, "Small modified monopole antenna for UWB application," *IET Microw. Antennas Propag.*, vol. 3, no. 5, pp. 863-869, August 2009.

[3] M. Ojaroudi, Ch. Ghobadi, and J. Nourinia, "Small square monopole antenna with inverted T-shaped notch in the ground plane for UWB application," *IEEE Antennas and Wireless Propagation Letters*, vol. 8, no. 1, pp. 728-731, 2009.

[4] Y. Li, W. Li, and W. Yu, "A switchable UWB slot antenna using SIS-HSIR and SIS-SIR for multi-mode wireless communications

applications," *Applied Computational Electromagnetics Society (ACES) Journal*, vol. 27, no. 4, pp. 340-351, April 2012.

[5] M. T. Partovi, N. Ojaroudi, and M. Ojaroudi, "Small slot antenna with enhanced bandwidth and band-notched performance for UWB applications," *Applied Computational Electromagnetics Society (ACES) Journal*, vol. 27, no. 9, pp. 772-778, Sep. 2012.

[6] J. William and R. Nakkeeran, "A new UWB slot antenna with rejection of WiMax and WLAN bands," *Applied Computational Electromagnetics Society (ACES) Journal,* vol. 25, no. 9, pp. 787-793, Sep. 2010.

[7] J. Jung, W. Choi, and J. Choi, "A compact broadband antenna with an L-shaped notch," *IEICE Trans. Commun.*, vol. E89-B, no. 6, pp. 1968–1971, June 2006.

[8] M. Ojaroudi, Sh. Yzdanifard, N. Ojaroudi, and R. A. Sadeghzadeh, "Band-notched small square-ring antenna with a pair of T-shaped strips protruded inside the square ring for UWB applications," *IEEE Antennas and Wireless Propagation Letters*, vol. 10, pp. 227-230, 2011.

[9] Sh. Yazdanifard, R. A. Sadeghzadeh, and M. Ojaroudi, "Ultra-wideband small square small monopole antenna with variable frequency function," *Progress In Electromagnetics Research C*, vol. 15, pp. 133-144, 2010.

[10] M. Ojaroudi, "Printed monopole antenna with a novel band-notched folded trapezoid for ultra-wideband applications," *Journal of Electromagnetic Waves and Application (JEMWA)*, vol. 23, pp. 2513–2522, 2009.

[11] M. Ojaroudi, Gh. Ghanbari, N. Ojaroudi, and Ch. Ghobadi, "Small square monopole antenna for UWB applications with variable frequency band-notch function," *IEEE Antennas and Wireless Propagation Letters*, vol. 8, pp. 1061-1064, 2009.

[12] M. Ojaroudi, N. Ojaroudi, and Y. Ebazadeh, "Dual band-notch small square monopole antenna with enhanced bandwidth characteristics for UWB applications," *Applied Computational Electromagnetics Society (ACES) Journal*, vol. 27, no. 5, pp. 420-426, May 2012.

[13] Ansoft High Frequency Structure Simulation (HFSS), ver. 13, Ansoft Corporation, 2010.

[14] B. H. Siahkal-Mahalle, M. Ojaroudi, and N. Ojaroudi, "Enhanced bandwidth small square monopole antenna with band-notched functions for UWB wireless communications," *Applied Computational Electromagnetics Society (ACES) Journal*, vol. 27, no. 9, pp. 759-765, Sep. 2012.

Nasser Ojaroudi was born on 1986 in Germi, Iran. He received his B.Sc. degree in Electrical Engineering from Azad University, Ardabil Branch. From 2011, he is working toward the M.Sc. degree in Telecommunication Engineering at Shahid Rajaee Teacher Training University. Since March 2008, he has been a Research Fellow in the Microwave Technology Company (MWT), Tehran, Iran. His research interests include monopole antenna, slot antennas, microstrip antennas for radar systems, ultra-wideband (UWB) and wireless communications, microwave passive devices and circuits, and microwave/millimeter systems.

Mohammad Ojaroudi was born on 1984 in Germi, Iran. He received his B.Sc. degree in Electrical Engineering from Azad University, Ardabil Branch and M.Sc. degree in Telecommunication Engineering from Urmia University. From 2010, he is working toward the Ph.D. degree at Shahid Beheshti University. From 2007 until now, he is a Teaching Assistant with the Department of Electrical Engineering, Islamic Azad University, Ardabil Branch, Iran. Since March 2008, he has been a Research Fellow (Chief Executive Officer) in the Microwave Technology Company (MWT), Tehran, Iran. His research interests include analysis and design of microstrip antennas, design and modeling of microwave structures, radar systems, and electromagnetic theory. He is author and coauthor of more than 100 journal and international conference papers.

Noradin Ghadimi was born in Ardabil-Iran in 1985, and received the B.Sc. degree in Electrical Engineering from the Islamic Azad University, Ardabil Branch, Ardabil, Iran, in 2009 and the M.Sc. degree in Electrical Engineering from the Islamic Azad University Ahar Branch, Ahar, Iran, in 2011. His research interests include Power System Protection, modeling and analysis of distributed generations, renewable energy, and communications systems.

High-Resolution and Jamming-Resistant Adaptive Synthetic Aperture Radar Imaging System based on UWB-OFDM Waveform

Md Anowar Hossain, Ibrahim Elshafiey, and Majeed A. S. Alkanhal

Department of Electrical Engineering
King Saud University, Riyadh, Kingdom of Saudi Arabia
ahossain@ksu.edu.sa, ishafiey@ksu.edu.sa, majeed@ksu.edu.sa

Abstract — A novel approach for jamming-resistant and high-resolution synthetic aperture radar (SAR) imaging technique is explored based on ultra-wideband orthogonal frequency division multiplexing (UWB-OFDM) waveform. Suitable waveforms for both friendly and hostile environment are proposed based on various random sequences and tested for SAR imaging in presence of a digital radio frequency memory (DRFM) repeat jammer. Adaptivity factor is introduced to make the system consistent in both environments. Wide-band ambiguity function (WAF) has been derived and the effect of sub-carrier composition in UWB-OFDM waveform as SAR signal is analyzed to avoid ambiguity in image reconstruction. Appropriate UWB-OFDM pulse shaping is introduced for SAR imaging in jamming scenarios and in hostile environments to solve the susceptibility of conventional linear frequency modulated (LFM) chirp signal, Gaussian pulses and any other constant pulse shape to avoid the possibility of false target introduced by jammer and to achieve secured imaging in jamming scenarios. The peak side-lobe performance is examined in terms of number of OFDM sub-carriers and sub-carrier orientation.

Index Terms — Orthogonal frequency division multiplexing (OFDM), synthetic aperture radar (SAR), SAR jamming and anti-jamming, and ultra-wideband (UWB).

I. INTRODUCTION

Synthetic aperture radar (SAR) is used to obtain high resolution images of a large target area. It involves transmitting signals at spaced intervals called pulse repetition interval (PRI). The responses at each PRI are stored and processed to reconstruct a radar image of the terrain [1]. Recently, achievement of high resolution SAR images has been investigated depending on transmission of ultra-wideband (UWB) waveform as radar signals [2]. UWB technology has double advantages: good penetration capability and high resolution target detection for radar applications [3] and [4].

Conventional LFM chirp signal experiences high susceptibility to jammer because of the linear nature of the intermediate frequency (IF). Gaussian pulse exhibits constant pulse-shape make these pulses susceptible to certain forms of deception jamming. These radars may be susceptible to certain types of jammer in scenarios where multiple pulse transmissions are mandatory, as in SAR imaging. Constant pulse shape also prevents using multiple radars in same location as they could interfere with each other. Therefore, it is necessary to explore radar signals that employ wide bandwidths and have the ability to quickly adjust to any adverse situations.

Orthogonal frequency division multiplexing (OFDM) is a method of digital modulation commonly used in commercial communications, shows great potential to be used in radar pulse shaping. Although OFDM has been frequently studied and commercialized in the digital communication field, it has not so widely been studied by radar communities rather than a few efforts [5-10]. An OFDM signal consists of several orthogonal sub-carriers that are simultaneously passed over a single transmission path. Each sub-carrier contains a small portion of the entire signal bandwidth [11]. Spectral components in OFDM signals are orthogonal to each other; therefore, by

controlling the sub-carriers we can ensure that any two waveforms emitted simultaneously will have minimum interference. Essentially, the subcarriers partition the bandwidth of the signal into several smaller orthogonal blocks. The system has control over the sub-carriers and, therefore, control over the spectrum of the waveform. In radar scenarios, the spectrum can be manipulated to avoid any interference that may be introduced from hostile environments. Moreover, OFDM signals can be formed in an attempt to eliminate all forms of jamming and interference.

In some scenarios, enemy combatants may use specific electronic countermeasures (ECM) to confuse the radar by altering the radar received signal characteristics resulting in a poor reconstructed image [12]. Pulse diversity of radar signals is an effective electronic counter-countermeasures (ECCM) technique against deception jammers. Advances in sampling technology have increased sampling speed allowing for OFDM waveforms employing UWB (500 MHz and above) to be generated accurately and at relatively low costs. The wide bandwidth along with excellent pulse diversity shows clear potential for UWB-OFDM signal to be used as radar pulse in jamming scenarios. The advantages of using OFDM waveform in radar application are: a) waveforms are generated digitally with pulse-to-pulse shape variation, b) ease of jamming/interference mitigation, and c) noise-like waveforms provide low probability of interception (LPI) and low probability of detection (LPD).

The structure of the paper is as follows. UWB-OFDM signal generation is described in section II, while the proposed multi-modulation technique is presented in section III. Detailed analysis of DRFM repeat jammer is discussed in section IV. Target model based on different scenarios is presented in section V. Section VI presents the comparison of auto-correlation and cross-correlation of different pulses in radar perspective. SAR imaging in jamming scenarios is investigated in section VII and wideband ambiguity function is derived in section VIII. Conclusions are provided in section IX.

II. UWB-OFDM SIGNAL GENERATION

UWB-OFDM signal is generated according to the scheme shown in Fig. 1 by randomly populating the digital frequency domain vector as,

$$\Psi_\omega = \begin{bmatrix} \Pi_{ns} \ \Pi_0 \ \Pi_{ps} \end{bmatrix} \tag{1}$$

where, Π_{ps} and Π_{ns} represent the positive and negative sub-carriers, respectively, whereas Π_0 represents the baseband DC value. Inverse discrete Fourier transform (IDFT) is then applied to Ψ_ω to get the discrete time domain OFDM signal as,

$$\Psi_{tx}(t) = F^{-1}[\Psi_\omega] \tag{2}$$
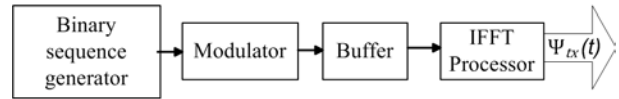
Fig. 1. UWB-OFDM signal generator.

UWB-OFDM waveforms are generated using the following parameters: number of OFDM sub-carriers = 256, sampling time, Δt_s = 1ns results in baseband bandwidth, $B_0 = 1/2\Delta t_s$ = 500 MHz, dividing by a factor of two to satisfy Nyquist criterion. Observing Fig. 2 (a) we see that when Π_{ps} is populated with all 1's and modulation scheme is chosen as BPSK, UWB-OFDM waveform becomes a short spike i.e., delta pulse, which can provide the best possible range resolution and exact position of the target in radar application. Hardware limitations can be an obstacle to generate this waveform, however, similar performance can be achieved by employing the samples of an LFM chirp in OFDM context as shown in Fig. 2 (b). We can consider these signals for the SAR imaging in friendly environment to obtain high resolution images. However, the constant pulse shape causes the system to suffer in jamming scenarios. Figure 3 shows an UWB-OFDM waveform when Π_{ps} populated randomly with 1's and 0's and modulation scheme is chosen as BPSK. It is observed that the signal is noise-like and provides a unique signal at each PRI, ideal for the SAR system in jamming scenarios.


(a)

(b)
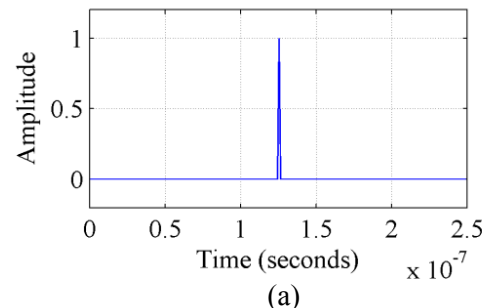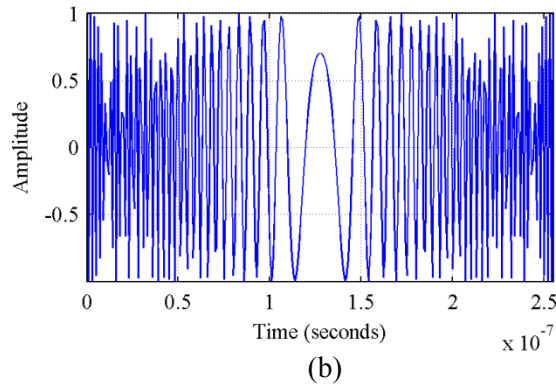
Fig. 2. UWB radar signal a) OFDM waveform with all sub-carriers and b) OFDM-LFM chirp.
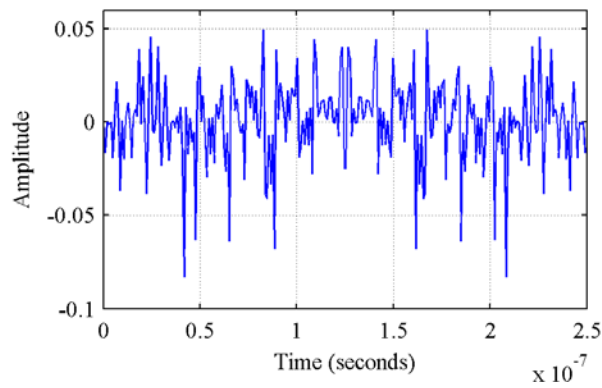

Fig. 3. UWB-OFDM signal with random sub-carrier orientation.

III. RANDOM MODULATION

Random modulation or multi-modulation modem modulates and demodulates signals using multiple modulation schemes. It includes a modulation selector unit that selects respective ones of the set of modulations to modulate the signals. Figure 4 shows the block diagram of the multi-modulated UWB-OFDM signal generator. The modulation selector fixed an arbitrary M-ary PSK from $M = 2^n$ and the random data generator generates a sample between 0 to (M-1). The sample is then modulated according to the selected modulation scheme and stored in a buffer. IFFT is then applied to the frequency domain vector to obtain the discrete time-domain UWB-OFDM signal.

Figure 5 shows an UWB-OFDM waveform using multi-modulation technique in which different modulation schemes are employed for the individual OFDM sub-carriers. It is observed that the signal is noise-like and provides high degree of randomness, suitable for the SAR system in hostile environments. Even jammer cannot identify the modulation scheme used in generating the waveform because the signal is inherently multi-modulated.
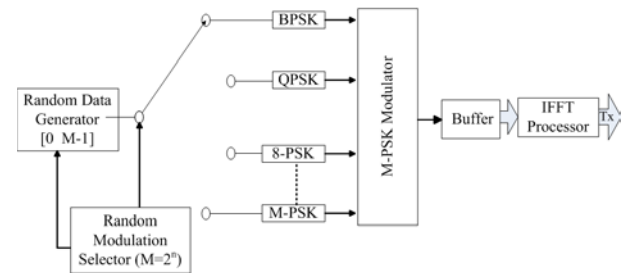
Fig. 4. UWB-OFDM signal generator with multi-modulation.
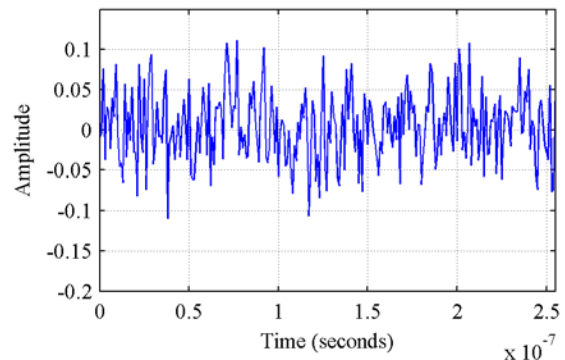
Fig. 5. Multi-modulated UWB-OFDM signal.

IV. DRFM JAMMER CONCEPTS

Deception jammers attempt to manipulate transmitted SAR signals in order to introduce false target into the reconstructed SAR image. This type of jamming can be accomplished by using a digital radio frequency memory (DRFM) repeat jammer [12] as shown in Fig. 6. The radar transmitted signal is received and converted to baseband. Analog–to-digital conversion is then performed to produce the discrete signal. A delay is then introduced to the discrete signal creating a false range offset by means of a controller and stored in memory until the next predicted PRI.

The discrete delayed signal is then passed through a digital-to-analog (DAC) converter and is mixed with an exponential at the known center frequency results in the transmitted jammer signal (received signal for radar) given by,

$$J_{tx}(t, u) = \sum_{n=1}^{N_j} \Psi_{txj}(t - t_{dj}) \qquad (3)$$

where, $t_{dj} = \frac{2}{c}\sqrt{(X_j - x_j) + (y_j - u)^2}$ denotes the jammer introduced time delay and (x_j, y_j) is the position of the false target. X_j and u represents the jammer distance to swath and the synthetic aperture positions respectively while $j = 1, 2, 3, \ldots N_j$ are the number of false target reflections at any given synthetic aperture position and c is the speed of light. The term Ψ_{txj} is the cyclic shifted version of the radar transmitted signal.
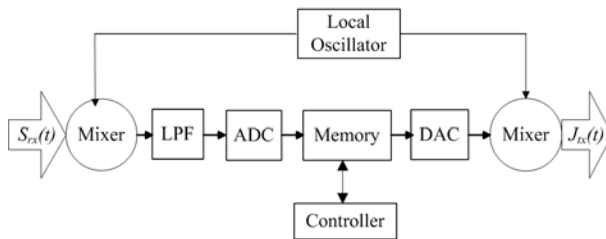

Fig. 6. DRFM repeat jammer.

If center frequency is known to the jammer and it is capable to form exact replicas of the transmitted SAR signal, the received signal for radar in jamming scenarios is given by

$$\Psi_{rxj}(t, u) =$$
$$\sum_{n=1}^{N_a} \sigma_n \Psi_{tx}(t - t_{dn}) + J_{tx}(t, u) + \eta(t), \qquad (4)$$

where, $t_{dn} = \frac{2}{c}\sqrt{(X_c - x_n)^2 + (y_n - u)^2}$ denotes the time-delay associated with the actual target position (x_n, y_n) and X_c is the range distance to center of the swath. Where, $n = 1, 2, 3 \ldots N_a$ are the number of actual target reflections at any given synthetic aperture position while σ_n denotes the reflectivity of the target. The term Ψ_{tx} is the radar transmitted signal and $\eta(t)$ denotes the additive white Gaussian noise, respectively.

V. TARGET MODEL

In practice, reflection from a point target is not a single peak as shown in Fig. 7 (a); the radar received signal is the combination of reflection from the target and closely surrounded scatterers of radar cross section (RCS) of a target as shown in Fig. 7 (b). Other important parameters that can be considered in target model are surface clutter and free space path loss. Table 1 shows the parameters used for simulation of the point target.

Surface clutter refers to reflections of a radar signal from land, sea or any other surfaces [13]. To detect targets above the surface, the radar must be able to distinguish between clutter and the targets of interest. For example, the radar should detect targets on the ground while accounting for radar reflections from trees or houses. Fig. 7 (c) shows the target profile based on surface clutter.

Propagation environments have significant effects on the amplitude, phase, and shape of propagating space-time wave-fields. If we consider a system that propagates signals through free space, we can model the free space path loss as,

$$L = \frac{(4\pi R)^2}{\lambda^2} \qquad (5)$$

where, R represents the one-way distance between the target and the radar in meters, and λ is the signal wavelength. The target profile using free space path loss is shown in Fig. 7 (d). We observe that the maximum peak of the point target decreases as the distance increases. Figure 8 shows the clutter returns based on constant gamma model for different types of surface such as flat land, rugged mountain and sea-state.

Table 1: UWB-OFDM SAR simulation parameters.

| Parameter	Symbol	Value
Pulse repetition frequency	PRF	300 Hz
Flight Duration	Dur	3 sec
Velocity of platform	V_p	200 m/s
Carrier frequency	f_c	7.5 GHz
Distance to target area	X_c	1Km
Half target area width	X_0	600 m
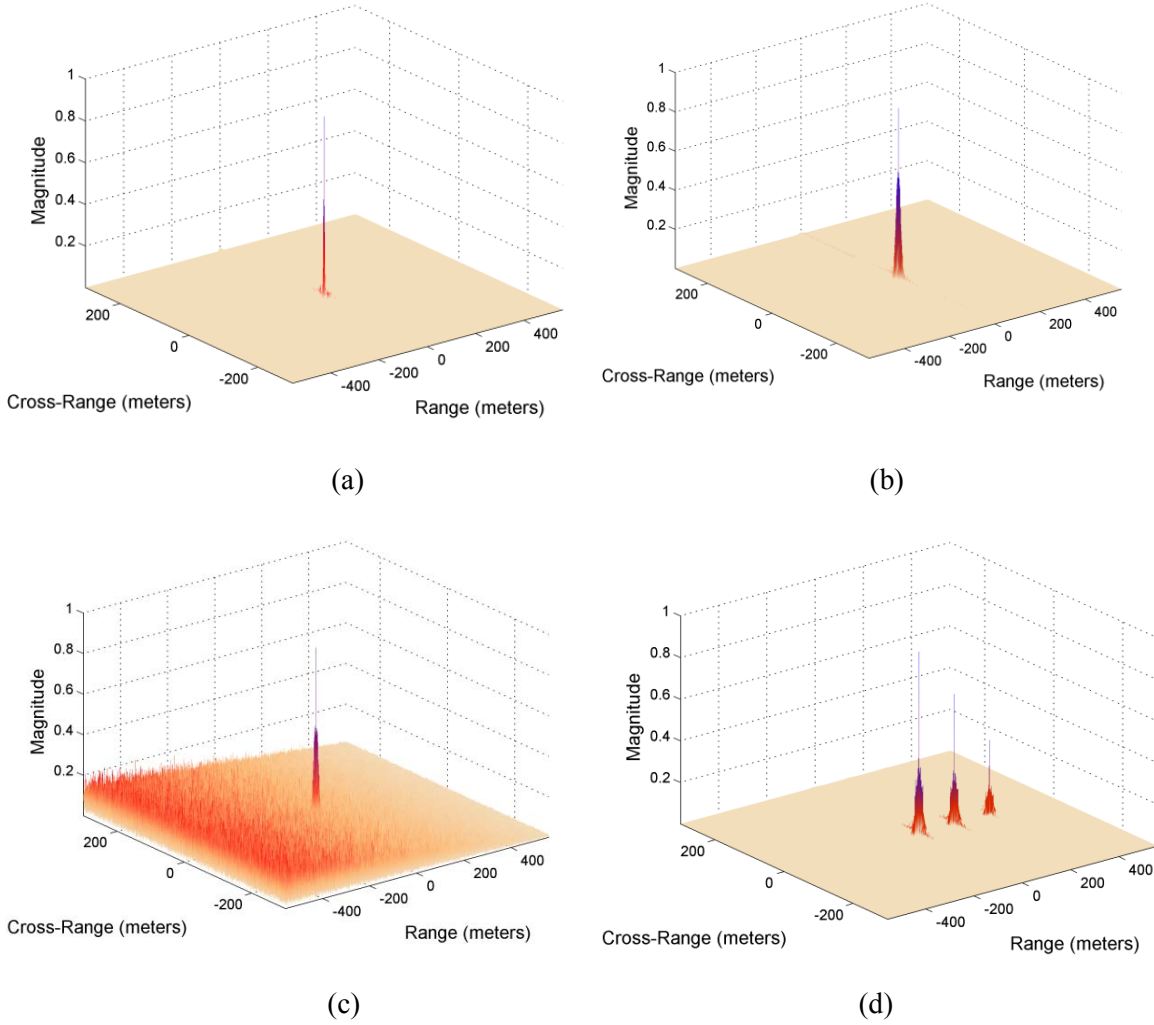
Fig. 7. Target profile for (a) ideal model, (b) RCS model, (c) clutter model, and (d) path loss model.

VI. WAVEFORM ANALYSIS

Analysis of waveforms is presented in terms of their auto-correlation function (ACF) and cross-correlation function (CCF). The auto-correlation and cross-correlation properties of the sequences used in generating the transmitted waveform play an important role in high resolution SAR imaging and in false target rejection. Cross-correlation is the measure of similarity between two different sequences and can be expressed as,

$$R_{xy}(m) = \begin{cases} \sum_{n=0}^{N-m-1} x_{n+m} y_n^* & m \geq 0 \\ R_{yx}^*(-m) & m < 0 \end{cases} \quad (6)$$

where, x_n and y_n are the elements of two different sequences with period N. Auto-correlation shows the measure of similarity between the sequence and its cyclic shifted copy, which can be obtained from equation (6) as a special case (x = y) [14].

The sequences with better auto-correlation properties provide high resolution target detection and lower cross-correlation properties provide degradation of false target. So, our objective is to find the waveform that provides the lowest cross-correlation properties among all types of sequences. The auto-correlation is measured as the correlation between the received signal and the transmitted signal while cross-correlation is measured as the correlation between received signal and transmitted signal at previous PRI. The auto-correlation and cross-correlation properties are examined for all types of UWB-OFDM pulses in the following subsections assuming a point target at the center of the target area.

A. Constant pulses

The delta pulse and LFM chirp shown in Figs. 2 (a) and 2 (b) before providing the highest auto-correlation as shown in Figs. 9 (a) and 9 (b), respectively with a main lobe width of 0.32 meters, which almost matches the theoretical range resolution, $\Delta R = c/2B_0 = 0.30$ meters. These pulses are best suited for the SAR system in friendly environment to obtain high resolution images. However, both pulses also exhibits highest cross-correlation makes them imperfect for the SAR system in jamming scenarios.
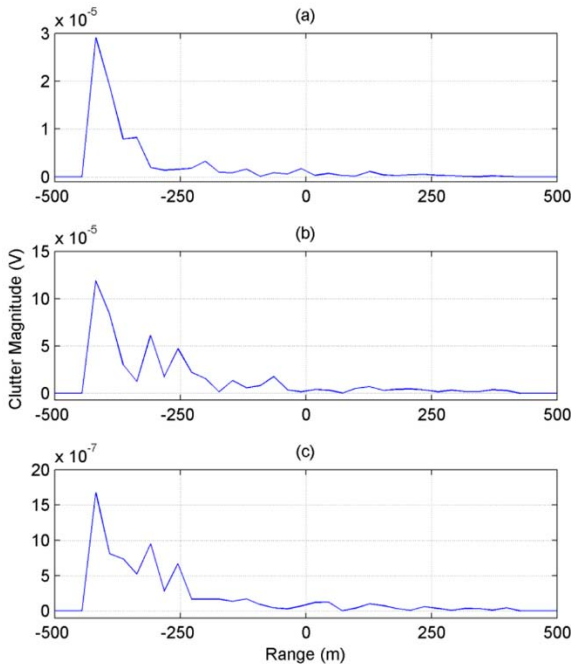

Fig. 8. Clutter return versus the range for (a) flat land, (b) rugged mountain, and (c) sea-state.

B. Random sequences

Random sequences such as Pseudo-noise (PN) sequences, Gold sequences and Kasami sequences are used extensively in spread-spectrum communication system [14]. We can consider these sequences for noise-like UWB-OFDM waveform generation to be used as SAR transmitted pulse in jamming scenarios. The parameter used in generating the sequences is shown in Table 2. The generator polynomial has been chosen so that the balance between number of 1's and 0's is maintained.

The PN sequences are almost ideal when viewed in terms of their autocorrelation function

as shown in Fig. 10 (a). Unfortunately, the cross-correlation between any pair of PN sequences of the same period can have relatively high peaks that are undesirable as shown in Fig. 10 (b). A particular class of PN sequences called Gold sequences provides better cross-correlation properties and is generated by modulo-2 addition of two PN sequences of the same length. The auto-correlation and cross-correlation of Gold sequences is shown in Figs. 10 (c) and 10 (d), respectively.
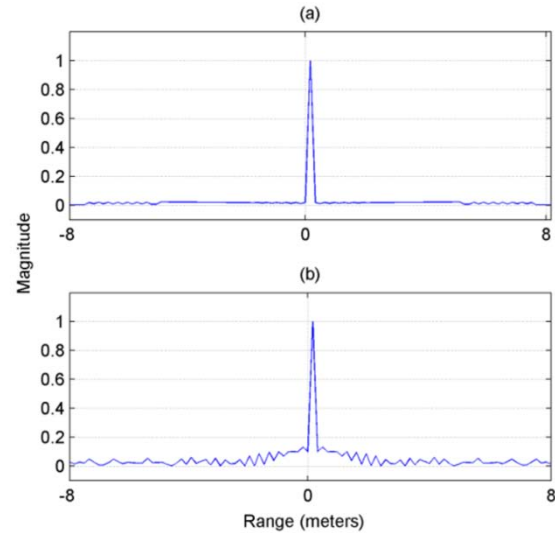
Fig. 9. Point target profile for a) UWB-OFDM pulse with all sub-carriers (ACF) and b) UWB OFDM-LFM chirp (ACF).

Table 2: Sequence generator parameters.

Sequence Generator	Generator polynomial	Initial states
PN	[53 6 2 0]	[53 41 28 15 1]
Gold	[11 2 0]	[11 8 4]
	[11 8 5 2 0]	[11 7 3]
Kasami	[12 6 4 0]	[12 8 2 0]

Kasami sequences are one of the important types of binary sequences because of their very low cross-correlation. Kasami sequences provide better cross-correlation as compared to PN sequences and Gold sequences. Figures 10 (e) and 10 (f) show the ACF and CCF of Kasami sequences, respectively.
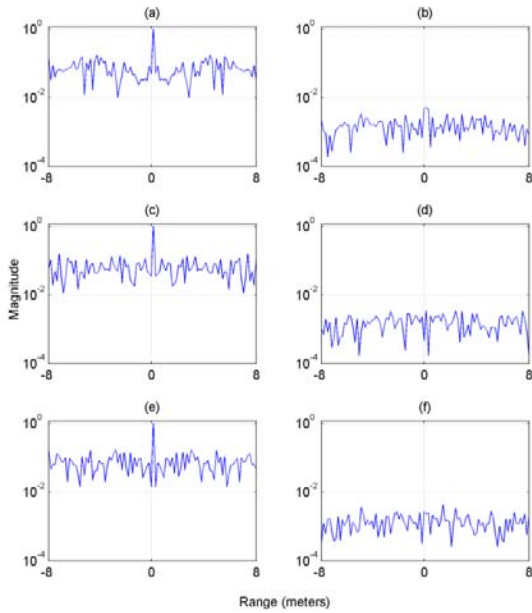
Fig. 10. Point target profile using (a) PN seq. (ACF), (b) PN seq. (CCF), (c) Gold seq. (ACF), (d) Gold seq. (CCF), (e) Kasami seq. (ACF), and (f) Kasami seq. (CCF).

C. Orthogonal sequences

Orthogonality is the most important properties of Walsh-Hadamard sequences. Because of this property, the cross-correlation between any two codes of the same set is zero, when the system is perfectly synchronized as shown in Fig. 11. Unfortunately, these sequences have non-zero off-peak auto-correlations and cross–correlation in asynchronous case. Figures 12 (a) and 12 (c) show the auto-correlation and cross-correlation in terms of a point target using Walsh-Hadamard sequences without spreading. By spreading Walsh sequences with a PN sequence using specific spreading factor better performance can be achieved.

The spreading uses a waveform that appears random to anyone except the intended receiver of the transmitted signal. The waveform is actually pseudo-random in the sense that it can be generated by precise rules yet has the statistical properties of a truly random sequence. Figures 12 (b) and 12 (d) show the auto-correlation and cross-correlation in terms of a point target using Walsh-Hadamard sequences with spreading by a factor of 4.
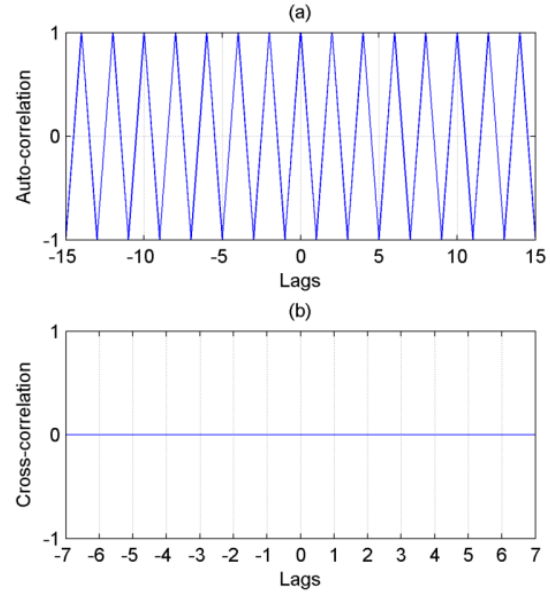
Fig. 11. Ideal Walsh-Hadamard sequences, (a) ACF and (b) CCF.
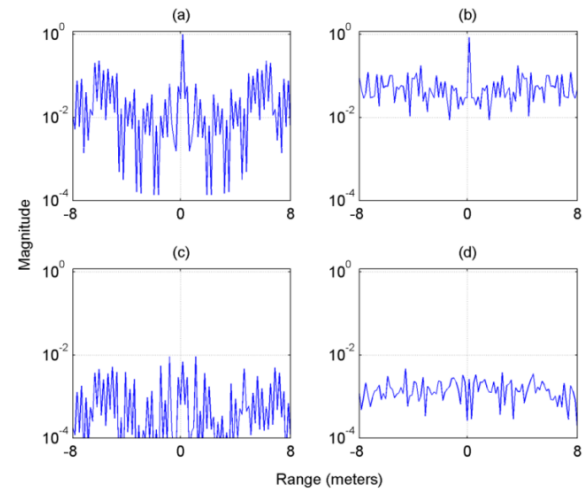
Fig. 12. Point target profile using Walsh-Hadamard sequences showing (a) ACF without spreading, (b) ACF with spreading, (c) CCF without spreading, and (d) CCF with spreading.

D. Multi-modulated pulse

The proposed multi-modulated UWB-OFDM pulse provides reasonable auto-correlation properties with increased main-lobe width but exhibits lowest cross-correlation as shown in Fig. 13 among all types of pulses makes this pulse ideal for the SAR system for false target rejection.
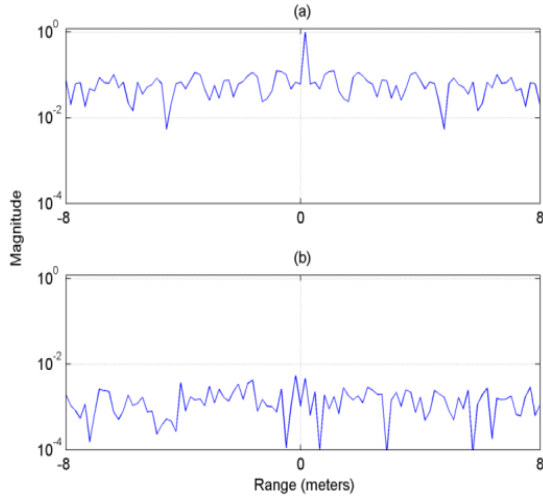
Fig. 13. Point target profile of Multi-modulation (a) ACF and (b) CCF.

Since all cross-correlation values, not just peak values, affect the system performance, we should consider the measure as the mean cross-correlation value. Figures 14 and 15 summarize the peak auto-correlation values in terms of width of the main lobe i.e., range resolution and normalized mean cross-correlation values of different pulses, respectively.
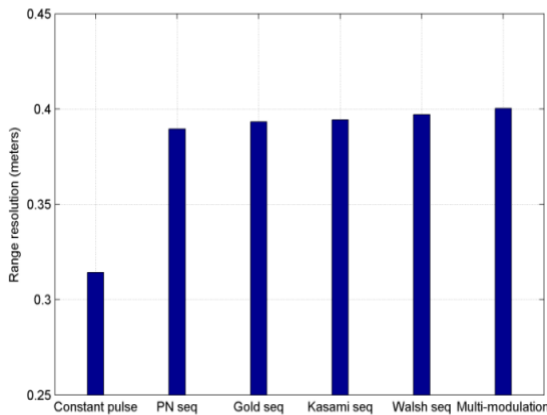
Fig. 14. Range resolution in terms of ACF.

VII. SAR IMAGING IN JAMMING SCENARIOS

The scenario involves the SAR imaging in jamming scenarios by considering three distinct UWB-OFDM waveforms as SAR transmitted pulse. A DRFM repeat jammer will receive the radar transmitted pulse from the previous PRI, introduce a false delay and retransmit to radar at next expected PRI to introduce false target in reconstructed SAR image. The objective is to investigate the performance of the UWB-OFDM waveform with constant pulse, noise-like pulses based on random sequences and multi-modulated waveform as SAR transmitted pulse in jamming scenarios.
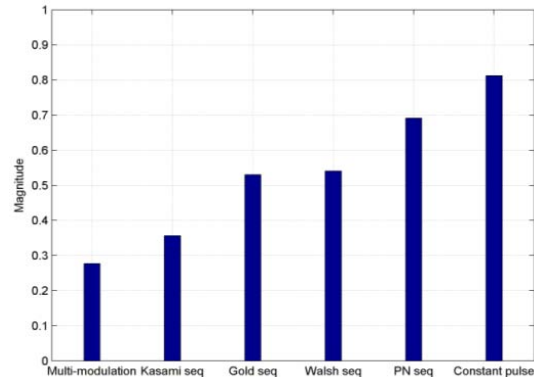
Fig. 15. Mean cross-correlation values.

Let us consider 2 point targets as actual target at the positions (x_n, y_n) = [(-300m, 80m), (300m, 80m)] and 2 point target as false target introduced by jammer at the positions (x_j, y_j) = [(-300m, -80m), (300m, -80m)]. Stripmap SAR topology is considered and UWB-OFDM waveform is used as transmitted pulse to perform the SAR raw data generation using while Range-Doppler algorithm (RDA) is used for SAR image reconstruction [15]. The details of SAR configuration can be found in [5]. Although different techniques exist in literature for SAR image reconstruction [16] RDA is chosen to achieve exact SAR transfer function.

Reconstructed SAR image with resolved point targets in jamming scenarios is shown in Fig. 16. Because of using UWB-OFDM waveform with constant pulse shape shown in Fig. 2 (a) as transmitted SAR signal at each PRI, the signal had strong correlation with the jammer transmitted signals causing both false targets presence at their respective positions in the reconstructed SAR image.

Point targets are also resolved by using UWB-OFDM waveform with random sub-carrier compositions shown in Fig. 3 as SAR transmitted pulse in jamming scenarios. Fig. 17 shows the reconstructed SAR image using a random waveform at each PRI. Because of transmitting a

unique UWB-OFDM signal at each PRI, the signal has weaker correlation with the jammer transmitted signals causing degraded false target appears in the reconstructed SAR image. Figure 18 shows the reconstructed SAR image using a unique UWB-OFDM waveform at each PRI employing multi-modulation technique as shown in Fig. 5. Because of transmitting a unique multi-modulated UWB-OFDM signal with high degree of randomness at each PRI, the signal has much weaker correlation with the jammer signals causing no false target appears in the reconstructed SAR image.
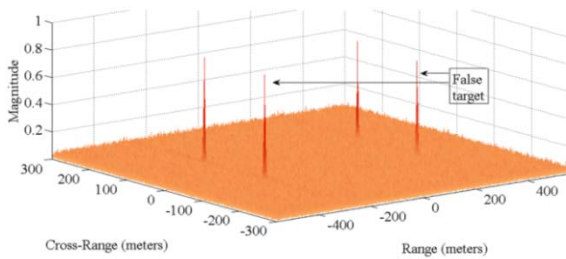

Fig. 16. SAR image showing two false targets.
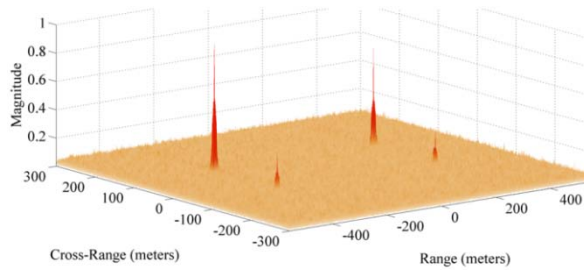
Fig. 17. SAR image showing degraded false targets.
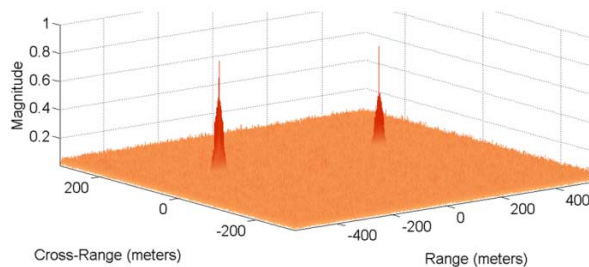
Fig. 18. SAR image without false targets.

The degradation of false targets using different sequences can be analyzed in terms of entropy [17] by analyzing SAR images i.e., degradation of

false targets will have reduction in entropy of the SAR image. Figure 19 shows the degradation of the false target in terms of entropy for different sequences as well as multi-modulation technique for different adaptivity factor. The adaptivity factor is the ratio of randomness of an UWB-OFDM waveform i.e., the ratio of 0's and 1's within the data vector that is used for waveform generation and is given by,

$$\eta = \frac{N_{0s}}{N_{sub}} \times 100 \qquad (7)$$

where, N_{0s} is the number of zeros in the data vector and N_{sub} is the number of sub-carrier used in generating the waveform. As we are using BPSK modulation in case of random sequences, we should increase the number of 0's within the data vector to increase the adaptivity factor and vice versa.

In Fig. 19, we observe that as long as we increase the adaptivity factor, the entropy is increased. This is because the increment in the adaptivity factor increases the correlation of a pulse with the pulse at previous PRI. On the other hand, increment in the adaptivity factor increases the occupied bandwidth by the pulse, which in turns enhances the range resolution as shown in Fig. 20. We observe that multi-modulated UWB-OFDM waveform is the best choice for false target rejection but Kasami sequences exhibits a good balance between false target degradation as well as resolution among all random sequences.
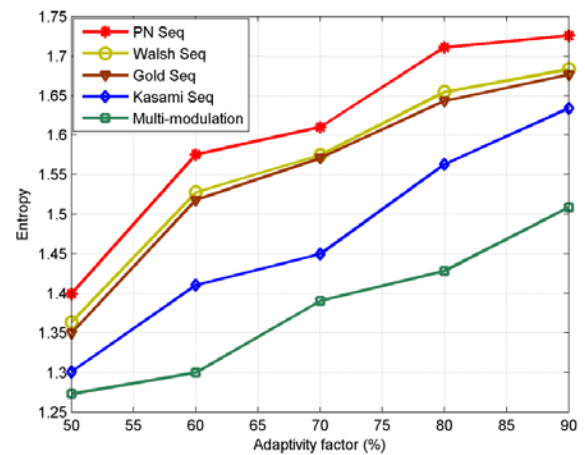

Fig. 19. Estimation of false target degradation.

UWB-OFDM waveform with constant pulse shape provides high-resolution SAR image but not effective for rejecting false target while UWB-

OFDM waveform with random sub-carrier orientation is capable of rejecting false target in jamming scenarios. On the other hand, UWB-OFDM waveform with multi-modulation technique is capable of rejecting false target completely. This waveform is evidently hardest to predict and intercept for the jammer because the signal is inherently multi-modulated. The high degree of randomness in SAR transmitted signal also rejects any reflected energy arrived from previous PRI during cross-correlation process as part of matched filtering, which in turns allow us to increase the swath. However, the trade-off is the increased target ambiguity i.e., increased main lobe width. This problem can be analyzed in terms of wide-band ambiguity function.
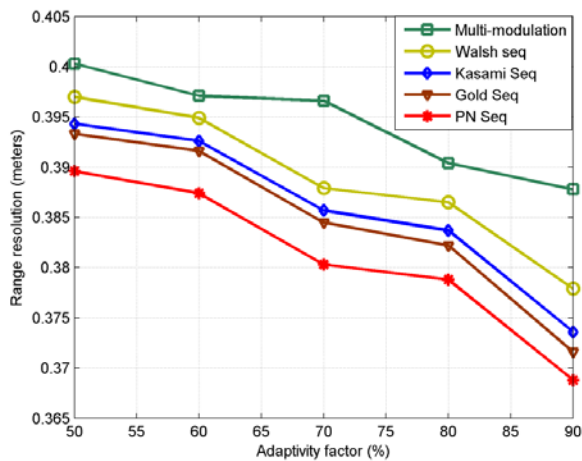

Fig. 20. Estimation of range resolution.

VIII. WIDE-BAND AMBIGUITY FUNCTION (WAF)

Radar ambiguity function is used to evaluate the performance limitations of the chosen radar waveform. The ambiguity function (AF) for any waveform contains a main lobe whose maximum lies at AF (0, 0) with a spread in both Doppler and delay. The spread is determined by the signal duration (TP) and baseband bandwidth (B_0). The delay spread is $\tau = 1/B_0$ while the Doppler spread, $v_0 = 1/T_P$. In our case, T_P depends on the number of sub-carriers used in the OFDM signal. So, an OFDM signal with larger number of sub-carriers can produce a main lobe with a reduced Doppler ambiguity while increased sampling rate increases the baseband bandwidth, which in turns reduces main lobe delay ambiguity. The wideband

ambiguity function [18] suitable for UWB-OFDM radar signal is given by,

$$AF_{wb}(\alpha,t) = \sqrt{|\alpha|} \int_{-\frac{T_p}{2}}^{\frac{T_p}{2}} \Psi(t)\,\Psi^*(\alpha(t-\tau))\mathrm{dt} \quad (8)$$

where, $\alpha = \frac{c-v}{c+v}$ and v is the radial velocity of the radar platform to the target and c is the speed of light. Equation (8) considers the Doppler shift of each sub-carrier individually whereas the narrowband AF considers only one sub-carrier causing incorrect Doppler shift for other sub-carriers. The continuous time analytical OFDM waveform [11] is given by,

$$\Psi(t) = \sum_{k=1}^{N} x(k) e^{j\left(\frac{2\pi kt}{T_p} + \varphi_0(t)\right)} \quad 0 < t < T_p \quad (9)$$

where, x(k) is the kth data symbol, N is the number of sub-carriers and T_P is the pulse duration. By substituting the analytical form of OFDM signal into equation (8), WAF for a UWB-OFDM signal is given by,

$$AF_{OFDM}(\alpha,\tau) =$$
$$T_P\sqrt{|\alpha|} \sum_{l=1}^{N} \sum_{k=1}^{N} x(k)\,x(l)\,e^{j2\pi l\Delta f\alpha\,\tau} sinc(\pi\Delta f(k - l\alpha)T_P)$$
$$(10)$$

where, sub-carrier spacing $\Delta f = 1/T_P$ has been substituted and $\varphi_0 = 0$ is assumed. Equation (10) shows the dependence of the AF on not only number of sub-carrier but also the orientation of the sub-carriers in the OFDM signal.

The range ambiguity can be reduced by increasing the adaptivity factor in UWB-OFDM SAR transmitted signal and is shown in Fig. 21. The reason behind this reduction in mainlobe width is that as long as we increase the adaptivity factor, the UWB-OFDM waveform approaches to the constant pulse shape as shown in Fig. 2. Figure 22 shows that the ambiguity in cross-range decreases as the number of sub-carrier increases. Increasing the number of sub-carrier in the signal has no effect on the main-lobe width because the bandwidth remains constant for any number of sub-carriers. However, increasing the number of sub-carriers will increase the size of raw SAR data, which should be minimized for radar processing purposes to reduce the computation time.
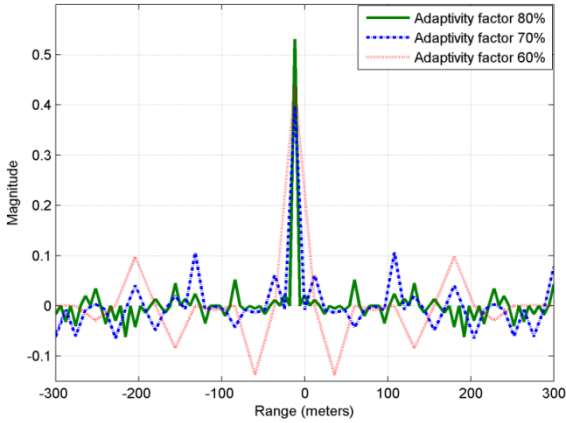
Fig. 21. Range ambiguity versus adaptivity factor.
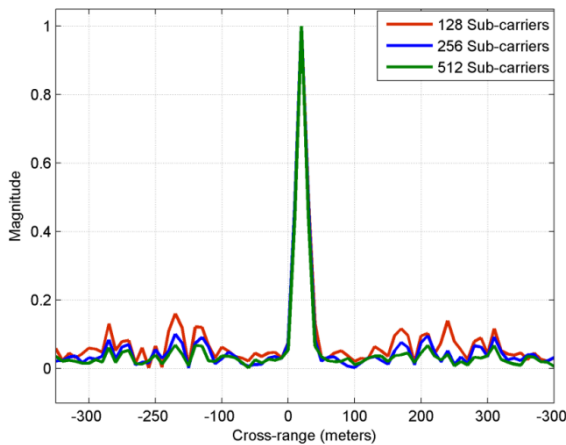
Fig. 22. Cross-range ambiguity versus number of OFDM sub-carriers.

Peak side-lobe (PSL) performance of a radar signal is a crucial part in determining whether a signal will be acceptable for high resolution imaging. PSL refers the maximum value residing outside the main-lobe. We are concerned with the difference between main-lobe peak and the highest side-lobe peak. Table 3 shows the normalized PSL performance for a varying number of sub-carriers and adaptivity factor. As expected, the PSL decreases as the number of sub-carriers and adaptivity factor increases.

IX. CONCLUSION

Performance of UWB-OFDM based SAR imaging has been investigated in jamming scenarios. UWB-OFDM based SAR can be adapted with both friendly environments and with jamming scenarios just by changing the transmitted waveform. The adaptivity factor can

Table 3: OFDM sub-carrier versus PSL.

OFDM Sub-carriers	Peak side-lobe (dB)		
	Adaptivity factor 60%	Adaptivity factor 70%	Adaptivity factor 80%
128	-13.24	-16.14	-17.26
256	-16.02	-18.12	-21.04
512	-17.62	-19.03	-22.32

be used to handle mutual exclusion between resolution and false target rejection. The performance of the SAR system in both environments can easily be controlled by changing the number and composition of the OFDM sub-carriers. Wideband ambiguity function has been derived and the effect of adaptivity factor in UWB-OFDM waveform has been analyzed. The results prove that UWB technology enhances the resolution of SAR images while randomness of noise-like OFDM waveform improves the anti-jamming capabilities of SAR system. UWB-OFDM waveform with in addition with multi-modulation technique is an excellent choice to be used as SAR transmitted pulse in hostile environments to achieve secured SAR imaging.

ACKNOWLEDGMENT

REFERENCES

[1] M. Soumekh, *Synthetic Aperture Radar Signal Processing with MATLAB Algorithms*, 2nd ed. New York, USA: Wiley, 1999.
[2] D. Garmatyuk and M. Brenneman, "Slow-time SAR signal processing for UWB OFDM radar system," *IEEE Radar Conf.*, Washington, USA, pp. 853-858, 2010.
[3] R. Aiello and S. Wood, *Essentials of UWB*, 1st ed. New York: Cambridge, 2008.
[4] K. P. Prokopidis and T. D. Tsiboukis, "Modeling of ground-penetrating radar for detecting buried objects in dispersive soils," *Appl. Comp. Electro. Society (ACES) Journal*, vol. 22, no. 2, pp. 287-294, 2007.
[5] Md A. Hossain, I. Elshafiey, M. Alkanhal, and A. Mabrouk, "Adaptive UWB-OFDM synthetic aperture radar," *Proc. of Saudi Int. Electronics, Comm. and Photonics Conf. (SIECPC)*, Riyadh, Saudi Arabia, pp. 1-6, 2011.

[6] Md A. Hossain, I. Elshafiey, and M. Alkanhal, " High resolution UWB SAR based on OFDM architecture," *Proc. of 3rd Asia-Pacific Int. Conf. on Synthetic Aperture Radar (APSAR)*, Seoul, South Korea, pp. 1-4, 2011.

[7] Md A. Hossain, I. Elshafiey, M. Alkanhal, and A. Mabrouk, "Anti-jamming capabilities of UWB-OFDM SAR," *Proc. of European Radar Conf. (EuRad)*, Manchester, United Kingdom, pp. 313-316, 2011.

[8] Md A. Hossain, I. Elshafiey, M. Alkanhal, and A. Mabrouk, "Real-time implementation of UWB-OFDM synthetic aperture radar imaging," *IEEE Int. Conf. on Signal and Image Processing Applications (ICSIPA)*, Kuala lumpur, Malaysia, pp. 450-455, 2011.

[9] D. Garmatyuk, "Simulated imaging performance of UWB SAR based on OFDM," *Proc. of the IEEE Int. Conf. on Ultrawideband*, Waltham, MA, pp. 237-242, Sep. 24 - 27, 2006.

[10] J. Schueger and D. S. Garmatyuk, "Multi-frequency OFDM SAR in presence of deception jamming," *EURASIP Journal on Adv. in Signal Processing*, pp. 1-13, 2010.

[11] L. Hanzo and T. Keller, *OFDM and MC-CDMA*, 2nd ed. United Kingdom: Wiley, 2006.

[12] M. Soumekh, "SAR-ECCM using phase-purturbated LFM chirp signals and DRFM repeat jammer penalization," *IEEE Trans. on Aerospace and Electronic Systems*, vol. 42, no. 1, pp. 191-205, Nov. 2006.

[13] M. Richards, "Evaluating the radar cross section of maritime radar reflectors using computational electromagnetics," *Appl. Comp. Electro. Society (ACES) Journal*, vol. 24, no. 4, pp. 403-406, 2009.

[14] D. U. Ke-lin and M. N. Swamy, *Wireless Communication Systems*, Cambridge University Press, New York, 2010.

[15] I. G. Cumming and F. H. Wong, *Digital Processing of Synthetic Aperture Radar Data*, 2nd ed. United Kingdom: Artech House, 2004.

[16] A. Capozzoli, C. Curcio, A. Liseno, and P. Vinetti, "Fast interpolation accelerated on GPU for SAR back projection," *Proc. of the 28th Annual Rev. of Progress in Appl. Comp. Electro. Society (ACES)* , Columbus, OH, pp. 305-310, Apr. 2012.

[17] R. C. Gonzalez and R. E. Woods, *Digital Image Processing*, 2nd Ed., Pearson Education, Inc. New Jersey, USA, 2008.

[18] L. G. Weiss, "Wavelets and wideband correlation processing," *IEEE Signal Processing Magazine*, vol. I, no. 11, pp. 13-32, Jan. 1994.

Md Anowar Hossain received his B.Sc. degree in Computer and Communication Engineering from International Islamic University Chittagong (IIUC), Bangladesh in 2005 and M.Sc. degree in Electrical Engineering from King Saud University, Saudi Arabia in 2012. He has been working as a researcher in the department of Electrical Engineering, King Saud University, from October 2008 to till now. Currently, he is pursuing PhD in Electrical Engineering at King Saud University. His research interests include UWB radar; synthetic aperture radar (SAR) imaging; radar jamming and anti-jamming; radar signal processing and FPGA based real-time signal processing.

Ibrahim Elshafiey received his B.Sc. degree in Communications and Electronics Engineering from Cairo University in 1985. He obtained his M.Sc. and PhD degrees from Iowa State University in 1992 and 1994, respectively. He is currently a professor in the Electrical Engineering Department, King Saud University, on loan from the Electrical Engineering Department, Fayoum University, Egypt. His research interests include computational electromagnetics, biomedical imaging and nondestructive evaluation.

Majeed A. S. Alkanhal received the B.Sc. and M.Sc. degrees from King Saud University, Riyadh, Saudi Arabia, in 1984 and 1986 respectively, and the PhD from Syracuse University, Syracuse, NY, in 1994, all in Electrical Engineering. He is presently a Professor and Chairman of the Electrical Engineering Department at King Saud University, Riyadh, Saudi Arabia. His research interests are in antennas and propagation, computational electromagnetics, and microwave engineering.

2013 INSTITUTIONAL MEMBERS

DTIC-OCP LIBRARY
8725 John J. Kingman Rd, Ste 0944
Fort Belvoir, VA 22060-6218

AUSTRALIAN DEFENCE LIBRARY
Northcott Drive
Canberra, A.C.T. 2600 Australia

BEIJING BOOK CO, INC
701 E Linden Avenue
Linden, NJ 07036-2495

DARTMOUTH COLLEGE
6025 Baker/Berry Library
Hanover, NH 03755-3560

DSTO EDINBURGH
AU/33851-AP, PO Box 830470
Birmingham, AL 35283

SIMEON J. EARL – BAE SYSTEMS
W432A, Warton Aerodome
Preston, Lancs., UK PR4 1AX

ENERGY KEN LIBRARY
PO Box 300613
Jamaica, NY, 11430

ENGINEERING INFORMATION, INC
PO Box 543
Amsterdam, Netherlands 1000 Am

ETSE TELECOMUNICACION
Biblioteca, Campus Lagoas
Vigo, 36200 Spain

GA INSTITUTE OF TECHNOLOGY
EBS-Lib Mail code 0900
74 Cherry Street
Atlanta, GA 30332

TIMOTHY HOLZHEIMER
Raytheon
PO Box 1044
Rockwall, TX 75087

HRL LABS, RESEARCH LIBRARY
3011 Malibu Canyon
Malibu, CA 90265

IEE INSPEC
Michael Faraday House
6 Hills Way
Stevenage, Herts UK SG1 2AY

INSTITUTE FOR SCIENTIFIC INFO.
Publication Processing Dept.
3501 Market St.Philadelphia, PA
19104-3302

LIBRARY – DRDC OTTAWA
3701 Carling Avenue
Ottawa, Ontario, Canada K1A OZ4

LIBRARY of CONGRESS
Reg. Of Copyrights
Washington DC, 20559

LINDA HALL LIBRARY
5109 Cherry Street
Kansas City, MO 64110-2498

MISSOURI S&T
400 W 14th Street
Rolla, MO 56409

MIT LINCOLN LABORATORY
244 Wood Street
Lexington, MA 02420

NATIONAL CHI NAN UNIVERSITY
Lily Journal & Book Co, Ltd
20920 Glenbrook Drive
Walnut, CA 91789-3809

JOHN NORGARD
UCCS
20340 Pine Shadow Drive
Colorado Springs, CO 80908

OSAMA MOHAMMED
Florida International University
10555 W Flagler Street
Miami, FL 33174

NAVAL POSTGRADUATE SCHOOL
Attn:J. Rozdal/411 Dyer Rd./ Rm 111
Monterey, CA 93943-5101

NDL KAGAKU
C/0 KWE-ACCESS
PO Box 300613 (JFK A/P)
Jamaica, NY 11430-0613

OVIEDO LIBRARY
PO BOX 830679
Birmingham, AL 35283

DAVID PAULSEN
E3Compliance
1523 North Joe Wilson Road
Cedr Hill, TX 75104-1437

PENN STATE UNIVERSITY
126 Paterno Library
University Park, PA 16802-1808

DAVID J. PINION
1122 E Pike Street #1217
SEATTLE, WA 98122

KATHERINE SIAKAVARA
Gymnasiou 8
Thessaloniki, Greece 55236

SWETS INFORMATION SERVICES
160 Ninth Avenue, Suite A
Runnemede, NJ 08078

YUTAKA TANGE
Maizuru Natl College of Technology
Maizuru, Kyoto, Japan 625-8511

TIB & UNIV. BIB. HANNOVER
Welfengarten 1B
Hannover, Germany 30167

UEKAE
PO Box 830470
Birmingham, AL 35283

UNIV OF CENTRAL FLORIDA
4000 Central Florida Boulevard
Orlando, FL 32816-8005

UNIVERSITY OF COLORADO
1720 Pleasant Street, 184 UCB
Boulder, CO 80309-0184

UNIVERSITY OF KANSAS –
WATSON
1425 Jayhawk Blvd 210S
Lawrence, KS 66045-7594

UNIVERSITY OF MISSISSIPPI
JD Williams Library
University, MS 38677-1848

UNIVERSITY LIBRARY/HKUST
Clear Water Bay Road
Kowloon, Honk Kong

CHUAN CHENG WANG
8F, No. 31, Lane 546
MingCheng 2nd Road, Zuoying Dist
Kaoshiung City, Taiwan 813

THOMAS WEILAND
TU Darmstadt
Schlossgartenstrasse 8
Darmstadt, Hessen, Germany 64289

STEVEN WEISS
US Army Research Lab
2800 Powder Mill Road
Adelphi, MD 20783

YOSHIHIDE YAMADA
NATIONAL DEFENSE ACADEMY
1-10-20 Hashirimizu
Yokosuka, Kanagawa,
Japan 239-8686

INFORMATION FOR AUTHORS

PUBLICATION CRITERIA

Each paper is required to manifest some relation to applied computational electromagnetics. **Papers may address general issues in applied computational electromagnetics, or they may focus on specific applications, techniques, codes, or computational issues.** While the following list is not exhaustive, each paper will generally relate to at least one of these areas:

1. **Code validation.** This is done using internal checks or experimental, analytical or other computational data. Measured data of potential utility to code validation efforts will also be considered for publication.

2. **Code performance analysis.** This usually involves identification of numerical accuracy or other limitations, solution convergence, numerical and physical modeling error, and parameter tradeoffs. However, it is also permissible to address issues such as ease-of-use, set-up time, run time, special outputs, or other special features.

3. **Computational studies of basic physics.** This involves using a code, algorithm, or computational technique to simulate reality in such a way that better, or new physical insight or understanding, is achieved.

4. **New computational techniques** or new applications for existing computational techniques or codes.

5. **"Tricks of the trade"** in selecting and applying codes and techniques.

6. **New codes, algorithms, code enhancement, and code fixes.** This category is self-explanatory, but includes significant changes to existing codes, such as applicability extensions, algorithm optimization, problem correction, limitation removal, or other performance improvement. **Note: Code (or algorithm) capability descriptions are not acceptable, unless they contain sufficient technical material to justify consideration.**

7. **Code input/output issues.** This normally involves innovations in input (such as input geometry standardization, automatic mesh generation, or computer-aided design) or in output (whether it be tabular, graphical, statistical, Fourier-transformed, or otherwise signal-processed). Material dealing with input/output database management, output interpretation, or other input/output issues will also be considered for publication.

8. **Computer hardware issues.** This is the category for analysis of hardware capabilities and limitations of various types of electromagnetics computational requirements. Vector and parallel computational techniques and implementation are of particular interest.

Applications of interest include, but are not limited to, antennas (and their electromagnetic environments), networks, static fields, radar cross section, inverse scattering, shielding, radiation hazards, biological effects, biomedical applications, electromagnetic pulse (EMP), electromagnetic interference (EMI), electromagnetic compatibility (EMC), power transmission, charge transport, dielectric, magnetic and nonlinear materials, microwave components, MEMS, RFID, and MMIC technologies, remote sensing and geometrical and physical optics, radar and communications systems, sensors, fiber optics, plasmas, particle accelerators, generators and motors, electromagnetic wave propagation, non-destructive evaluation, eddy currents, and inverse scattering.

Techniques of interest include but not limited to frequency-domain and time-domain techniques, integral equation and differential equation techniques, diffraction theories, physical and geometrical optics, method of moments, finite differences and finite element techniques, transmission line method, modal expansions, perturbation methods, and hybrid methods.

Where possible and appropriate, authors are required to provide statements of quantitative accuracy for measured and/or computed data. This issue is discussed in "Accuracy & Publication: Requiring, quantitative accuracy statements to accompany data," by E. K. Miller, *ACES Newsletter,* Vol. 9, No. 3, pp. 23-29, 1994, ISBN 1056-9170.

SUBMITTAL PROCEDURE

All submissions should be uploaded to ACES server through ACES web site (http://aces.ee.olemiss.edu) by using the upload button, journal section. Only pdf files are accepted for submission. The file size should not be larger than 5MB, otherwise permission from the Editor-in-Chief should be obtained first. Automated acknowledgment of the electronic submission, after the upload process is successfully completed, will be sent to the corresponding author only. It is the responsibility of the corresponding author to keep the remaining authors, if applicable, informed. Email submission is not accepted and will not be processed.

EDITORIAL REVIEW

In order to ensure an appropriate level of quality control, papers are peer reviewed. They are reviewed both for technical correctness and for adherence to the listed guidelines regarding information content and format.

PAPER FORMAT

Only camera-ready electronic files are accepted for publication. The term **"camera-ready" means that the material is neat, legible, reproducible, and in accordance with the final version format listed below.**

The following requirements are in effect for the final version of an ACES Journal paper:

1. The paper title should not be placed on a separate page.

The title, author(s), abstract, and (space permitting) beginning of the paper itself should all be on the first page. The title, author(s), and author affiliations should be centered (center-justified) on the first page. The title should be of font size 16 and bolded, the author names should be of font size 12 and bolded, and the author affiliation should be of font size 12 (regular font, neither italic nor bolded).

2. An abstract is required. The abstract should be a brief summary of the work described in the paper. It should state the computer codes, computational techniques, and applications discussed in the paper (as applicable) and should otherwise be usable by technical abstracting and indexing services. The word "Abstract" has to be placed at the left margin of the paper, and should be bolded and italic. It also should be followed by a hyphen (─) with the main text of the abstract starting on the same line.

3. All section titles have to be centered and all the title letters should be written in caps. The section titles need to be numbered using roman numbering (I. II. ….)

4. Either British English or American English spellings may be used, provided that each word is spelled consistently throughout the paper.

5. Internal consistency of references format should be maintained. As a guideline for authors, we recommend that references be given using numerical numbering in the body of the paper (with numerical listing of all references at the end of the paper). The first letter of the authors' first name should be listed followed by a period, which in turn, followed by the authors' complete last name. Use a coma (,) to separate between the authors' names. Titles of papers or articles should be in quotation marks (" "), followed by the title of journal, which should be in italic font. The journal volume (vol.), issue number (no.), page numbering (pp.), month and year of publication should come after the journal title in the sequence listed here.

6. Internal consistency shall also be maintained for other elements of style, such as equation numbering. Equation numbers should be placed in parentheses at the right column margin. All symbols in any equation have to be defined before the equation appears or right immediately following the equation.

7. The use of SI units is strongly encouraged. English units may be used as secondary units (in parentheses).

8. Figures and tables should be formatted appropriately (centered within the column, side-by-side, etc.) on the page such that the presented data appears close to and after it is being referenced in the text. When including figures and tables, all care should be taken so that they will appear appropriately when printed in black and white. For better visibility of paper on computer screen, it is good to make color figures with different line styles for figures with multiple curves. Colors should also be tested to insure their ability to be distinguished after black and white printing. Avoid the use of large symbols with curves in a figure. It is always better to use different line styles such as solid, dotted, dashed, etc.

9. A figure caption should be located directly beneath the corresponding figure, and should be fully justified.

10. The intent and meaning of all text must be clear. For authors who are not masters of the English language, the ACES Editorial Staff will provide assistance with grammar (subject to clarity of intent and meaning). However, this may delay the scheduled publication date.

11. Unused space should be minimized. Sections and subsections should not normally begin on a new page.

ACES reserves the right to edit any uploaded material, however, this is not generally done. It is the author(s) responsibility to provide acceptable camera-ready files in pdf and MSWord formats. Incompatible or incomplete files will not be processed for publication, and authors will be requested to re-upload a revised acceptable version.

COPYRIGHTS AND RELEASES
Each primary author must execute the online copyright form and obtain a release from his/her organization vesting the copyright with ACES. Both the author(s) and affiliated organization(s) are allowed to use the copyrighted material freely for their own private purposes.

Permission is granted to quote short passages and reproduce figures and tables from and ACES Journal issue provided the source is cited. Copies of ACES Journal articles may be made in accordance with usage permitted by Sections 107 or 108 of the U.S. Copyright Law. This consent does not extend to other kinds of copying, such as for general distribution, for advertising or promotional purposes, for creating new collective works, or for resale. The reproduction of multiple copies and the use of articles or extracts for commercial purposes require the consent of the author and specific permission from ACES. Institutional members are allowed to copy any ACES Journal issue for their internal distribution only.

PUBLICATION CHARGES
All authors are allowed for 8 printed pages per paper without charge. Mandatory page charges of $75 a page apply to all pages in excess of 8 printed pages. Authors are entitled to one, free of charge, copy of the printed journal issue in which their paper was published. Additional reprints are available for $ 50. Requests for additional re-prints should be submitted to the managing editor or ACES Secretary.

Corresponding author is required to complete the online form for the over page charge payment right after the initial acceptance of the paper is conveyed to the corresponding author by email.

ACES Journal is abstracted in INSPEC, in Engineering Index, DTIC, Science Citation Index Expanded, the Research Alert, and to Current Contents/Engineering, Computing & Technology.